

UC Santa Barbara

UC Santa Barbara Electronic Theses and Dissertations

Title

Mechanistic Studies of Ion Transport in Organic Solid Electrolytes

Permalink

<https://escholarship.org/uc/item/9b76t5cz>

Author

Jones, Seamus Dylan Summerville

Publication Date

2022

Peer reviewed|Thesis/dissertation

UNIVERSITY OF CALIFORNIA

Santa Barbara

Mechanistic Studies of Ion Transport in Organic Solid Electrolytes

A dissertation submitted in partial satisfaction of the
requirements for the degree Doctor of Philosophy
in Chemical Engineering

by

Seamus Dylan Summerville Jones

Committee in charge:

Professor Rachel Segalman, Co-Chair

Professor Glenn Fredrickson, Co-chair

Professor Craig Hawker

Professor Todd Squires

September 2022

The dissertation of Seamus Dylan Summerville Jones is approved.

Craig Hawker

Todd Squires

Rachel Segalman, Committee Co-Chair

Glenn Fredrickson, Committee Co-Chair

June, 2022

Mechanistic Studies of Ion Transport in Organic Solid Electrolytes

Copyright © 2022

by

Seamus Dylan Summerville Jones

ACKNOWLEDGEMENTS

I am thankful for the help and support of many friends and colleagues.

Firstly, I would like to acknowledge the support of my advisors. I was in close contact with Rachel throughout my thesis and I think she is the individual person who is responsible for most of my personal and professional growth over the past half decade. Rachel is a person who truly awed me with her dedication and focus the first time I met her and has continued to live up to this impression for the entirety of my time working with her. Rachel and I have an excellent working rapport and I will probably forever find myself hoping to work with other scientists with her style. Rachel challenged me not to compare myself to peers, but to always push for the best I can do, without shying away from the challenges that come along with that. I am so glad to continue my work with Rachel, as she always sees the big picture and helps me to not get lost in the details. I am really thankful for all the effort she has put into my development; I truly do not think there are many advisors who invest so much in the people they develop. In Glenn, I had a mentor who always brought a pragmatic perspective and a genuine interest in the work. I was impressed with the simultaneous breadth and depth that Glenn brought to every conversation.

I also would like to thank my other committee members – Craig and Todd. Craig became quite involved in my thesis through the interdisciplinary research group I was involved in early on at UCSB and it was always a joy to work with him. Craig has more fun doing science than anyone I have ever met and the simultaneous high quality of the work and the levity of Craig's attitude makes it that much easier to dig in and be productive. Craig was always willing to lend a synthetic hand when needed to help me focus my time on the

big picture. Todd also brings a great attitude to his work, and I was glad to interact with him, especially in classes.

I have had opportunities to interact closely with several other PIs at UCSB and they have taken an active role in shaping my thesis. Professor Clemente was an amazing mentor and nearly another advisor. Chris Bates was always available for discussion and had a ton of enthusiasm for every project I talked to him about.

I would also like to thank some of the important mentors who have shaped who I am scientifically. Andy Ubel was influential to me very early on in my career and helped me obtain my first job working in science at the Valspar Corporation. Andy brought a lot of enthusiasm for work and was always making people he worked with happy through his bright attitude, a skill I have not mastered yet but very much admire. At Valspar I also met Keith, who turned out to be an excellent boss and mentor to me. Keith was very flexible with me but also always led by an excellent example. Keith even encouraged me to pursue mentorship opportunities that were for my best interest, even if they were against his best interest, which I valued greatly. This selflessness in mentorship proved to be an excellent lesson for me. I also want to thank Jeff Ting, who mentored me through projects at the University of Minnesota. Jeff was another very early influence for me who taught me to perform academic research. Jeff was an excellent presenter of our work, teaching me that presentation is equally as important as doing great work. Jeff also taught me to think dynamically – when we worked together, we were carving out a new space and we didn't always know what to do, but Jeff was always willing to learn something and try something. This is something I love about the space that academic science provides to this day. Finally, I was mentored by Michael Maher in my last summer before UCSB. Michael initially

intimidated me because he seemed to know more than anybody in the room, but eventually we got to know each other and worked well together. Ultimately, Michael treated me as an equal which was refreshing and gratifying because I felt I had earned this privilege. We had an amazingly productive summer with the team of Michael, Aristotelis, and myself. I learned the real power of working in a small team, when chemistry, circumstance, and personality all align. I also thank Frank Bates for his mentorship in my early studies. I came in to UCSB with great preparation to do research and that is largely due to the contributions of Frank, who taught me so much. I had the privilege of returning to his lab to do some more chemistry just this last year, so I appreciate that his support continues years after my time as an undergraduate in his lab. I know his recommendation was a large part of the reason I was even awarded the chance to do my research here at UCSB and so I feel he is owed great thanks from me.

Finally, I want to thank my many collaborators who worked with me here at UCSB. When I joined the Segalman group I was amazed by the expertise of the research team working here, including members such as Scott Danielsen, Nicole Schauer, and Beihang Yu who I had the opportunity to learn a lot from throughout my time. Scott is still someone I want to talk to at every conference as his perspective is almost always interesting and insightful on almost any topic. Nicole was a great mentor who combined great productivity with a work life balance I still struggle to attain. I am truly impressed by her productivity in the time she was here. Beihang always impressed me for being such a dedicated scholar of the literature and the fundamentals. She truly read every theory with gusto and approached every endeavor methodically. I also want to thank some collaborators who came along later in Shuyi Xie and Oscar Nordness. Shuyi is also an impressive and methodical researcher

who is truly dedicated to his work, and I've enjoyed his company greatly. Oscar and I intuitively clicked on a research level nearly right away. We both have a lot of creativity and willingness to speculate. Oscar is a truly generous and fun person – I am grateful to call him a colleague and close friend.

Other members of the community at UCSB have also been excellent collaborators and mentors. I want to thank the Fredrickson group for being so welcoming to me, despite the fact I do experiments and sometimes seemed like an outsider. Daniel Vigil from this group became a great friend of mine throughout my work, and though we never really worked together, we always took a keen interest in each other's work. Daniel is an excellent scientist and a great hiking partner. Max Berkow and Greg Zakem also came in with me and have remained close friends throughout. Walking dogs with Greg and playing soccer with Max have been welcome diversions for me throughout my time here. David Goldfeld also became a great friend to me near the end of my time at UCSB. David and I knew each other from Minnesota and quickly reformed a connection in his time here. David is a dedicated and brilliant chemist as well as a lover of the same media and humor style as me.

Finally, I would like to thank some of the other noncolleagues who have contributed to my development and helped me accomplish this thesis. This includes countless associates and everyone I played sports with, plus so many administrators and others. I want to thank Rich Enderton for the influence he had on me at an early age. Some friends from my younger years: Karl, Sandy, Haley, David, Anthony, and others.

I am also so thankful to my partner Leslie for her role. Leslie came into my life at a crossroads for me professionally and helped me to view the salient facts of the decisions that I had to make – something that contributed hugely to my success. Drs. Leslie and Piper have

also physically been the person/dog combo who have been most present for me as I wrote this thesis. The life we have shared as I vigorously try to convert research results into tangible words and figures has been what got me through this process. I am lucky to have someone so intelligent and accomplished in my life and if I could make half the academic splash she makes I would call it a resounding success.

I want to thank my family. My mother and father kept me alive when I was an infant, without them I would have died as a child and could never have written a thesis at all. Their support has continued throughout my life, and I am grateful for the inexpressible commitment they have made to my development. I think they are both wonderful people and I am proud of the work they have done and to call myself their son. My younger sister Isobel is a kindred spirit who understands and sees me in a way that few others ever have. I am impressed with the progress she has made in her life, and it was always fun to have another polymer scientist and chemical engineer in my family. These parallels between us gave me enthusiasm to redouble my efforts, in part due to my naturally competitive spirit with my sibling.

VITA OF SEAMUS DYLAN SUMMERVILLE JONES

June 17 2022

EDUCATION

University of Minnesota, Twin Cities
Bachelor of Chemical Engineering, June 2017

University of California, Santa Barbara
PhD. Chemical Engineering, Anticipated Summer 2022

PUBLICATIONS

1. “Design of Polymeric Zwitterionic Lithium Conductors – Impact of Tethered Ion Identity,” Seamus D. Jones, Yan-Qiao Chen, Craig J. Hawker, Raphaële J. Clément, Glenn H. Fredrickson, Rachel A. Segalman, *In press*
2. “Chain Conformation of Zwitterionic Polymers in Bulk and Solvated Environments,” Seamus D. Jones, Yan-Qiao Chen, Craig J. Hawker, Shuyi Xie, Glenn H. Fredrickson, Rachel A. Segalman, *In preparation*
3. “Eutectic Behavior of Zwitterion/Salt Blends,” Seamus D. Jones, James T. Bamford, Oscar A. Nordness, Shuyi Xie, Raphaële J. Clément, Glenn H. Fredrickson, Rachel A. Segalman, *In preparation*
4. “Decoupled Conduction Modes in Polymer Electrolytes” Seamus D. Jones, James T. Bamford, Glenn H. Fredrickson, Rachel A. Segalman. *In press*
5. “Ion Transport of Deep Eutectic Zwitterion/Salt Blends,” Seamus D. Jones, James T. Bamford, Oscar A. Nordness, Shuyi Xie, Raphaële J. Clément, Glenn H. Fredrickson, Rachel A. Segalman, *In preparation*
6. “Role of Electron-Deficient Imidazoles in Ion Transport and Conductivity in Solid-State Polymer Electrolytes,” Andrei Nikolaev, Peter M Richardson, Shuyi Xie, Luana Canzian Llanes, Seamus D Jones, Oscar Nordness, Hengbin Wang, Guillermo C Bazan, Rachel A Segalman, Raphaële J Clément, Javier Read de Alaniz, *Macromolecules* 2022, 55, 3, 971–977, DOI: 10.1021/acs.macromol.1c01979
- 7.* “Design of Polymeric Zwitterionic Solid Electrolytes with Superionic Lithium Transport,” Seamus D. Jones, Howie Nguyen, Peter M. Richardson, Yan-Qiao Chen, Kira E. Wyckoff, Craig J. Hawker, Raphaële J. Clément, Glenn H. Fredrickson, Rachel A. Segalman, *ACS Central Science* 2022, 8, 2, 169–175, DOI:10.1021/acscentsci.1c01260
8. “Polycation Radius of Gyration in a Polymeric Ionic Liquid (PIL): The pure PIL is not a Theta Solvent” Lucas Wong, Seamus Jones, Kathleen Wood, Liliana de Campo, Michael Moir, Tamim Darwish, Hua Li, Rachel A Segalman, Gregory Warr, Rob Atkin, *Phys. Chem. Chem. Phys.* 2022, 24, 4526–4532 DOI:10.1039/D1CP05354J
9. “Interfacial Nanostructure and Friction of a Polymeric Ionic Liquid-Ionic Liquid Mixture as a Function of Potential at Au(111) Electrode Interface,” Hua Li, Yunxiao Zhang, Seamus D. Jones, Rachel A. Segalman, Gregory G. Warr, Rob Atkin, *Journal of Colloid and Interface Science*, 606:2.1170–1178 DOI:10.1016/j.jcis.2021.08.067
10. “Electronic, Ionic, and Mixed Conduction in Polymeric Systems,” Elayne M. Thomas, Phong H. Nguyen, Seamus D. Jones, Michael L. Chabinyk, Rachel A. Segalman, *Annual Review of Materials Research*, 1:2.1–2.20 DOI: 10.1146/annurev-matsci-080619-110405

11. “Light-Switchable and Self-Healable Polymer Electrolytes Based on Dynamic Diarylethene and Metal-Ion Coordination,” Hui Nie, Nicole S. Schauser, Jeffrey L. Self, Tarnuma Tabassum, Saejin Oh, Zhishuai Geng, Seamus D. Jones, Manuel S. Zayas, Veronica G. Reynolds, Michael L. Chabiny, Craig J. Hawker, Songi Han, Christopher M. Bates, Rachel A. Segalman, and Javier Read de Alaniz, *J. Am. Chem. Soc.* 2021, 143, 3, 1562–1569, DOI: 10.1021/jacs.0c11894
- 12.* “The Role of Polymer–Ion Interaction Strength on the Viscoelasticity and Conductivity of Solvent-Free Polymer Electrolytes,” Seamus D. Jones, Nicole S. Schauser, Glenn H. Fredrickson, and Rachel A. Segalman, *Macromolecules*, 2020, 53, 23, 10574–10581, DOI: 10.1021/acs.macromol.0c02233
13. “Physical Aging of Polylactide Based Graft Block Polymers,” Ingrid J. Haugan, Bongjoon Lee, Michael Maher, Aristotelis Zografos, Haley Schibur, Seamus D. Jones, Marc Hillmyer, Frank Bates, *Macromolecules*, 2019, 52, 22, 8878–8894, DOI: 10.1021/acs.macromol.9b01434
14. “Photocrosslinking polymeric ionic liquids via anthracene cycloaddition for organic electronics,” Bhooshan C. Popere, Gabriel E. Sanoja, Elayne M. Thomas, Nicole S. Schauser, Seamus D. Jones, Joshua M. Bartels, Matthew E. Helgeson, Michael L. Chabiny and Rachel A. Segalman, *J. Mater. Chem. C*, 2018,6, 8762-8769, DOI: 10.1039/C8TC02561D
10. “The Order–Disorder Transition in Graft Block Copolymers,” Michael J. Maher, Seamus D. Jones, Aristotelis Zografos, Jun Xu, Haley J. Schibur, and Frank S. Bates, *Macromolecules* 2018, 51, 1, 232-241 DOI: 10.1021/acs.macromol.7b02262
15. “Tuning PNIPAm self-assembly and thermoresponse: roles of hydrophobic end-groups and hydrophilic comonomer,” Monica L. Ohnsorg, Jeffrey M. Ting, Seamus D. Jones, Seyoung Jung, Frank S. Bates and Theresa M. Reineke, *Polymer Chem.* 2019, DOI: 10.1039/C9PY00180H
16. “Deconstructing HPMCAS: Excipient Design to Tailor Polymer–Drug Interactions for Oral Drug Delivery,” Jeffrey M. Ting, Tushar S. Navale, Seamus D. Jones, Frank S. Bates, and Theresa M. Reineke, *ACS Biomater. Sci. Eng.* 2015, 1, 10, 978-990, DOI: 10.1021/acsbiomaterials.5b00234 (ACS Editors’Choice)
17. “High-Throughput Excipient Discovery Enables Oral Delivery of Poorly Soluble Pharmaceuticals,” Jeffrey M. Ting, Swapnil Tale, Anatolii A. Purchel, Seamus D. Jones, Lakmini Widanapathirana, Zachary P. Tolstyka, Li Guo, Steven J. Guillaudeu, Frank S. Bates, and Theresa M. Reineke, *ACS Cent. Sci.* 2016, 2, 10, 748-755, DOI: 10.1021/acscentsci.6b00268 (ACS AuthorChoice)

PATENTS

1. “Polymer Zwitterionic Liquids with High Conductivity and Transport Number,” Seamus D. Jones, Glenn H. Fredrickson, Rachel Segalman, UC Case 2021-875
2. “Ionic Liquid Inspired Zwitterions with High Conductivity and Transport Number,” Seamus D. Jones, Yanqiao Chen, Peter Richardson, Raphael Clement, Craig Hawker, Glenn H. Fredrickson, Rachel A. Segalman, Docket 30794.0800USP2

AWARDS

Best Talk Award, Clorox-Amgen Graduate Student Symposium 2021
 Presidential Scholar, University of Minnesota, 2013-2017 (awarded yearly)

National Masonic Scholar, National Masonic Foundation, 2013-2017 (awarded yearly)
George T. Walker Prize for Excellence in Chemical Research, Sigma Xi, May 2016

CONFERENCE ORAL PRESENTATIONS

1. “The Role of Ion Size and Electronic Character in Zwitterionic Electrolytes for Transport of Lithium-Metal Ions,” Seamus D. Jones, Yan-Qiao Chen, Craig Hawker, Glenn Fredrickson, Rachel Segalman
2. “Polymer-Ion Interaction Strength and Conductivity in Polymer Electrolytes,” Seamus D. Jones, Nicole S. Schauer, Glenn H. Fredrickson, Rachel A. Segalman; Dillon Medal Award Symposium, American Physical Society: March Meeting, March 2021
3. “From Discovery to Design: Enabling Functional Drug and Nucleic Acid Transport Through Controlled Polymer Synthesis,” Jeff M. Ting, Swapnil Tale, Anatoli A. Purchel, Seamus D. Jones, Lakmini Widanapathirana, Gao Li, Stevem J. Guillaudeu, Frank S. Bates, Theresa M. Reineke, Gordon Research Conference: Drug Carriers in Medicine & Biology, Aug. 2016.
4. “Design of Tunable Polymers as Modular Excipients for Oral Drug Delivery” Ting, J. M.; Navale, T. S.; Jones, S. D.; Bates, F. S.; Reineke, T. M., American Institute of Chemical Engineering (AIChE) ChEnected Graduate Student Research Spotlight Series, Jan. 2016. URL: aiche.org/chenected
5. “Generation of Complex Morphologies in Diblock Copolymers via Blending” Lewis R., Schulze M., Jones S. D., Beech H., Hickey R., Lettow, J., Bates F.S., American Physical Society: March Meeting, March 2018.
6. “Mechanics and Ion Transport in Dynamic Polymer Networks based on Metal-Ligand Coordination in Polymeric Ionic Liquids,” Segalman R. A., Michenfelder-Schauser N., Jones S. D., Seshadri R., American Physical Society: March Meeting, March 2018.

CONFERENCE POSTER PRESENTATIONS

1. “Simultaneous Transient Gel Behavior and Multivalent Ionic Mobility in Polymeric Ionic Liquid-Ligand Gels,” Jones S. D., Michenfelder-Schauser N., Fredrickson, G. H., Segalman R. A., American Physical Society: March Meeting, March 2019.
2. “High-throughput Polymer Screening for Oral Administration: From Discovery to Design,” Ting, J. M.; Tale, S.; Widanapathirana, L.; Jones, S. D.; Guillaudeu, S. J.; Li, G.; Bates, F. S.; Reineke, T. M., Polymers Gordon Research Conference, June 2015. URL: grc.org
3. “Strategic, High-throughput Excipient Synthesis and Screening for Poorly-soluble Pharmaceuticals in Oral Drug Delivery,” Ting, J. M.; Tale, S.; Purchel, A. A.; Jones, S. D.; Widanapathirana, L.; Tolstyka, Z. P.; Li, G.; Guillaudeu, S. J.; Bates, F. S.; Reineke, T. M., Gordon Research Conference: Drug Carriers in Medicine & Biology, Aug. 2016. URL: grc.org

ABSTRACT

Mechanistic Studies of Ion Transport in Organic Solid Electrolytes

by

Seamus Dylan Summerville Jones

The efficient and safe storage of electrochemical energy is critical for emerging technologies such as electric vehicles and portable electronic devices. Practical requirements for next-generation secondary Lithium-ion batteries include higher energy densities and charge-discharge rates, which hinge on new cathode materials and electrolytes with higher ionic conductivities (σ). Further, higher energy densities can only be reached if Lithium-ion cells are operated over a wide potential range that exceeds the electrochemical stability window of current organic solvent-based electrolytes. Next generation Lithium-ion cells require the development of more stable and nonflammable electrolytes. Solid polymer electrolytes (SPEs) have attracted interest due to their stability and mechanical robustness, but it remains challenging to attain SPEs with both high ionic conductivity and lithium selectivity.

This thesis explored the limitations that govern the design of SPEs based on metal-ligand coordination. In such SPEs, the metal-ligand bond between the polymer-bound ligand and the free cation of an added salt promotes dissociation of the salt, enabling conductivity in the solid state. These interactions simultaneously act as reversible crosslinks, promoting salt dissociation and enabling conductivity in the solid state. Oscillatory rheology was used to

probe the timescale of these crosslinking interactions. A scaling relation was established which demonstrated the inverse relationship between bond lifetime and ionic conductivity, suggesting a hierarchical conduction mechanism that involves an interplay of polymer segmental motion and the dissociation of metal-ligand bond lifetimes. Overall, this relationship suggests a limitation for homogeneous conduction whereby ion conductivity is inherently limited by the sluggish relaxation dynamics of polymers.

This problematic coupling of polymer relaxation and ion dynamics was overcome by designing a prearranged pathway of free volume elements along which an ion can opportunistically hop, much like in superionic ceramic electrolytes. Polymers with a zwitterionic functionality tethered to each monomer were designed to leverage this conduction mechanism. These polymers self-assemble into superionically conductive domains, permitting the decoupling of ion motion and polymer segmental rearrangement. Although crystalline domains are conventionally detrimental to ion conduction in SPEs, I demonstrated that these electrolytes displayed excellent lithium conductivity and selectivity. I proceeded to investigate design rules for these materials – finding that large ion size is critical in promoting fast, activated ion transport.

TABLE OF CONTENTS

I.	Introduction.....	1
A.	The Liquidlike Transport Model in Polymeric Electrolytes.....	1
B.	Amorphous Polymer Electrolyte Designs	6
C.	Superionic Ceramics Support a Solidlike Transport Mechanism.....	9
D.	Analysis of Transport Mechanisms	13
E.	Measurement Methods.....	16
F.	Leveraging Alternative Conduction Mechanisms in Organic Electrolytes	
	20	
	F.1 Zwitterionic Electrolytes	20
	F.2 Packing Frustration and Intrinsic Free Volume.....	29
	F.3 Transport of Ions Through Nanostructured Channels	31
II.	The Role of Polymer-Ion Interaction Strength on the Viscoelasticity and Conductivity of	
	Solvent-Free Polymer Electrolytes	41
A.	Abstract.....	41
B.	Introduction.....	41
C.	Experimental	43
D.	Results and Discussion	49
E.	Conclusion.....	64
F.	Appendix	65
	F.1 NMR Spectra.....	65

1.2 NMR Spectrum of Di-Imidazole Poly(methyl acrylate)	66
1.3 NMR of Mono-bromo Poly(methyl acrylate).....	67
F.2 Size Exclusion Chromatography	69
F.3 Small- and Wide-Angle X-Ray Scattering	70
F.4 Rheology Fitting.....	73
F.5 Monofunctional Control Experiments:.....	76
F.6 Estimation of Glassy Dynamics:	77
F.7 Electrochemical Impedance Spectroscopy Sample Spectra	78
F.8 Differential Scanning Calorimetry	80
III. Design of Polymeric Zwitterionic Solid Electrolytes with Superionic Lithium Transport	
.....	81
A. Abstract.....	81
B. Introduction.....	81
C. Results and Discussion.....	86
C.1 PZILs Display a Faster-than-Vehicular Conduction Mechanism .	86
C.2 The PZIL Ion Conduction Mechanism Arises from Ordered Subdomains	
that Promote Superionic Mobility	88
C.3 Conduction Through Superionic Lattices Promotes High Cation	
Selectivity	91
D. Appendix.....	93
D.1 Materials and Methods.....	93
1.9 Quaternization of PDMAEA to Polyzwitterion with TFSI Anion (Am-TFSI-	
PZIL).....	99

D.2 Limiting Current Fraction Analysis Using Symmetric Li/Li Cells	113
D.3 Solid-State NMR	127
D.4 Additional Structural Analysis of the Zwitterion	156
D.5 Room temperature stability of Im-TFSI PZIL $r=0.9$ versus Lithium	157
D.6 Evaluating the High-Salt Limit	160
D.7 Thermal Analysis	163
D.8 Stress Relaxation Experiment	167
D.9 Raw Dielectric Spectroscopy Data	169
D.10 NMR Spectra	176
D.11 Size Exclusion Chromatography	190
IV. Design of Polymeric Zwitterionic Solid Electrolytes with Superionic Lithium Transport	192
A. Abstract	192
B. Introduction	192
C. Results and Discussion	197
Tethered Ion Size Plays a Crucial Role in PZIL Conduction	197
Electron Withdrawing Nature of TFSI is Key to the Anion Design	203
D. Appendix	208
D.1 Materials and Methods	208
D.2 NMRs	224
D.3 Chromatography Analysis of Polymers	238
D.4 IR Spectrum of Im-c3-TFSI	242

V: Conclusions and Outlook.....	242
References.....	251

LIST OF FIGURES

Figure 1: Cartoon of ion dissociation in an electrolyte medium.	2
Figure 2: Cartoon Illustrating ion transport in a superionic ceramic.....	11
Figure 3: A representative model Walden plot containing some typical electrolytes.	13
Figure 4: A diagram of an ionic conductivity setup and typical response curves for blocking and nonblocking electrodes.	17
Figure 5: Zwitterionic polymers and small molecules display superionic transport and break the upper-bound set by Robison plot analysis.	22
Figure 6: Zwitterionic molecules display 3 universal phase behaviors.	24
Figure 7: Zwitterions analyzed by NMR show diffusion of the zwitterion and both ions.	26
Figure 8: Polymer fragility correlates with the degree of decoupling.	30
Figure 9: Crystalline complexes exhibiting superionic transport.	32
Figure 10: Superionic transport is attained in layered liquid crystal assemblies.....	35
Figure 11: Layered structures studied by Winey show superionic transport.....	38
Figure 12: End functionalized polymers made by ATRP.....	52
Figure 13: Rheology curves of telechelic polymers.	54
Figure 14: Rheological shift factors as a function of inverse temperature.	57
Figure 15: Conductivity analysis of telechelic polymers	60
Figure 16: Timescale analysis of the telechelic polymers.	63
Figure 17: NMR Spectrum of Di-bromo Poly(methyl acrylate)	65
Figure 18: NMR Spectrum of Di-Imidazole Poly(methyl acrylate).....	66
Figure 19: NMR of Mono-bromo Poly(methyl acrylate)	67

Figure 20: Mono-Imidazole Poly(methyl acrylate)	68
Figure 21: Molecular masses of the telechelic and monofunctional polymers before (red) and after (blue) functionalization with the imidazole thiol.	69
Figure 22: Representative WAXS for the lithium containing telechelic and nonfunctional polymer.	70
Figure 23: WAXS analysis of all salt-containing polymers.	71
Figure 24: Small angle x-ray scattering analysis of salt-containing polymers.	72
Figure 25: Control experiments of the monofunctional, nonfunctional, and telechelic polymer viscoelastic response in the presence of the copper(II) TFSI salt.	76
Figure 26: A representative sample spectrum for an EIS experiment.	78
Figure 27: EIS experiments in the absence of added salts.....	79
Figure 28: Differential scanning calorimetry curves for the samples tested in this study.	80
Figure 29: Transport of ions through the ZIL resembles ceramic transport.....	84
Figure 30: Structural analysis of the PZIL.	90
Figure 31: A) A Robeson-inspired plot of the PZIL.....	91
Figure 32: Rheology analysis of the PZIL.....	102
Figure 33: Limiting current measurement setup.....	111
Figure 34: The Equivalent circuit model used to fit the EIS data in the Bruce-Vincent cell.	114
Figure 35: The EIS spectrum of the polymers before (red circle) and after (black square) polarization of the cell.	116
Figure 36: Normalized current versus time graph of the cell undergoing polarization.	117

Figure 37: The Equivalent circuit model used to fit the EIS data in the Bruce-Vincent cell.
..... 120

Figure 38: The EIS spectrum of the polymers before (red circle) and after (black square) polarization of the cell. 121

Figure 39: Normalized current versus time graph of the cell undergoing polarization. 122

Figure 40: The EIS spectrum of the polymers before (red circle) and after (black square) polarization of the cell. 124

Figure 41: Normalized current versus time graph of the cell undergoing polarization. 125

Figure 42: Solid State NMR Data for the PZILs. 130

Figure 43: Lineshape fitting example. 133

Figure 44: The normalized intensity versus time curve for a ^{19}F T_1 experiment on the Im-TFSI PZIL with $r=0.9$ at a temperature of 355 K. The black squares correspond to measured data and the red curve is a single exponential fit (Equation 19). 134

Figure 45: The normalized intensity versus time curve for a ^{19}F T_1 experiment on the Im-TFSI PZIL with $r=0.9$ at a temperature of 346 K. The black squares correspond to measured data and the red curve is a single exponential fit (Equation 19). 134

Figure 46: The normalized intensity versus time curve for a ^{19}F T_1 experiment on the Im-TFSI PZIL with $r=0.9$ at a temperature of 337 K. The black squares correspond to measured data and the red curve is a single exponential fit (Equation 19). 135

Figure 47: The normalized intensity versus time curve for a ^{19}F T_1 experiment on the Im-TFSI PZIL with $r=0.9$ at a temperature of 328 K. The black squares correspond to measured data and the red curve is a single exponential fit (Equation 19). 136

Figure 48: The normalized intensity versus time curve for a ^7Li $T_{1\rho}$ experiment on the Im-TFSI PZIL with $r=0.9$ at a temperature of 355 K.	138
Figure 49: The normalized intensity versus time curve for a ^7Li $T_{1\rho}$ experiment on the Im-TFSI PZIL with $r=0.9$ at a temperature of 346 K.	139
Figure 50: The normalized intensity versus time curve for a ^7Li $T_{1\rho}$ experiment on the Im-TFSI PZIL with $r=0.9$ at a Temperature of 337 K.	140
Figure 51: The normalized intensity versus time curve for a ^7Li $T_{1\rho}$ experiment on the Im-TFSI PZIL with $r=0.9$ at a temperature of 328 K.	141
Figure 52: The normalized intensity versus time curve for a ^7Li $T_{1\rho}$ experiment on the Im-TFSI PZIL with $r=0.9$ at a temperature of 320 K.	141
Figure 53: The normalized intensity versus time curve for a ^7Li $T_{1\rho}$ experiment on the Im-TFSI PZIL with $r=0.9$ at a temperature of 311 K.	142
Figure 54: The normalized intensity versus gradient strength curve obtained from a ^7Li PFG NMR measurement on the Im-TFSI PZIL with $r=0.9$ at a temperature of 355 K.	144
Figure 55: The normalized intensity versus gradient strength obtained from a ^{19}F PFG NMR measurement on the Im-TFSI PZIL with $r=0.9$ at a temperature of 355 K.	146
Figure 56: The normalized intensity versus gradient strength obtained from a ^{19}F PFG NMR measurement on the Im-TFSI PZIL with $r=0.9$ at a temperature of 346 K.	147
Figure 57: The normalized intensity versus gradient strength obtained from a ^{19}F PFG NMR measurement on the Im-TFSI PZIL with $r=0.9$ at a temperature of 337 K.	148
Figure 58: The normalized intensity versus gradient strength obtained from a ^{19}F PFG NMR measurement on the Im-TFSI PZIL with $r=0.9$ at a temperature of 328 K.	149

Figure 59: The normalized intensity versus gradient strength curve for a ^7Li PFG NMR experiment of the Im-TFSI PZIL with $r=0.9$ at a Temperature of 355 K.....	153
Figure 60: The normalized intensity versus gradient strength curve for a ^{19}F PFG NMR experiment of the Im-TFSI PZIL with $r=0.9$ at a Temperature of 355 K.....	154
Figure 61: Microscopy and scattering analysis of the single crystal.	157
Figure 62: The Voltage against lithium versus the capacity for the cell described above.	159
Figure 63: Conductivity versus ‘r’ for the PZILs over a larger range of salt concentrations.	160
Figure 64: Ionic conductivity (normalized by glass transition temperature) plotted against the salt concentration as parameterized by r.....	162
Figure 65: The decomposition profiles of the ZIL and PZILs.....	163
Figure 66: Calorimetric studies of $\text{Li}^+/\text{bTFSI}^-$	164
Figure 67: Calorimetric studies of the ZI.	165
Figure 68: Calorimetric studies of the PZI.	166
Figure 69: Stress relaxation of the PZI.	168
Figure 70: The real part of the conductivity is plotted against frequency for the salt-free polymer.	169
Figure 71: The real component of the conductivity is provided for the $r=0.1$ sample at temperatures ranging from -30 to $110\text{ }^\circ\text{C}$	170
Figure 72: The loss tangent is provided as a function of frequency for the $r=0.1$ sample at temperatures ranging from -35 to $110\text{ }^\circ\text{C}$	171

Figure 73: The real component of the conductivity is provided for the $r=0.3$ sample at temperatures ranging from -35 to 110 °C.....	172
Figure 74: The loss tangent is provided as a function of frequency for the $r=0.3$ sample at temperatures ranging from -35 to 110 °C.....	173
Figure 75: The real component of the conductivity is provided for the $r=0.9$ sample at temperatures ranging from -35 to 110 °C.....	174
Figure 76: The loss tangent is provided as a function of frequency for the $r=0.3$ sample at temperatures ranging from -35 to 110 °C.....	175
Figure 77: Crude ^1H NMR of the NHS ester acrylate after polymerization.....	176
Figure 78: ^1H NMR of Purified NHS Acrylate Polymer.....	177
Figure 79: ^1H NMR of TFSI-Bromide compound after washes.....	178
Figure 80: ^{19}F NMR of TFSI Br.....	179
Figure 81: ^1H of imidazole functionalized polymer poly(Im).....	180
Figure 82: ^1H NMR of poly(Im-c3-TFSI).....	181
Figure 83: ^1H NMR of EthIm-c3-TFSI.....	182
Figure 84: ^{13}C NMR of EthIm-c3-TFSI.....	183
Figure 85: ^{19}F NMR of EthIm-c3-TFSI.....	184
Figure 86: ^1H NMR of Crude PDMAEA.....	185
Figure 87: ^1H NMR of Purified PDMAEA.....	186
Figure 88: ^1H NMR of Purified Am-TFSI PZIL.....	187
Figure 89: ^1H NMR of Cl-c3-SI-C6F5.....	188
Figure 90: ^{19}F NMR of Cl-c3-SI-C6F5.....	189

Figure 91: The normalized intensity is plotted against the calibrated equivalent mass of a narrow polystyrene standard.....	190
Figure 92: ZIs synthesized with bulky and nonbulky ions.....	198
Figure 93: Ionic conductivity studies of bulky and compact PZIs.....	200
Figure 94: NMR and selectivity studies of bulky and compact PZIs.....	203
Figure 95: Electron withdrawing groups ranked by their withdrawing strength.....	204
Figure 96: Conductivity studies of PZIs with electron withdrawing groups.....	207
Figure 97: ¹ H NMR of Cl-C3-SI-Me.....	225
Figure 98: ¹ H NMR of Cl-C3-SI-Bu.....	226
Figure 99: ¹ H NMR of Cl-C3-SI-C2F5.....	226
Figure 100: ¹⁹ F NMR of Cl-C3-TFS-C2F5.....	227
Figure 101: NMR spectrum of Cl-C3-TFS-Ph(CF ₃) ₃	228
Figure 102: NMR Spectrum of Cl-C3-TFS-Ph.....	229
Figure 103: NMR spectrum of of EthIm-C3-SO ₃	230
Figure 104: NMR Spectrum of EthIm-C3-SO ₃	231
Figure 105: NMR Spectrum of TEA-C3-SO ₃	232
Figure 106: NMR Spectrum of TEA-C3-SO ₃	233
Figure 107: NMR Spectrum of EthIm-C3-TFSI.....	234
Figure 108: NMR Spectrum of EthIm-C3-SO ₃	235
Figure 109: NMR Spectrum of EthIm-C3-SO ₃	236
Figure 110: ¹⁹ F NMR spectrum of EthIm-C3-SO ₃	237
Figure 111: SEC of Pyr(MA).....	238
Figure 112: SEC analysis of PDMAEA.....	240

Figure 113: IR Spectrum of Im-c3-TFSI	242
Figure 114: State diagram of a blend of EthIm-c3-TFSI and LiTFSI	245

I. Introduction

A. *The Liquidlike Transport Model in Polymeric Electrolytes*

The operating principles of electrochemical devices require electrolytes that promote high flux of redox reactive species, typically metal cations¹⁻⁴. Although maximizing the flux of reactive species is ultimately of primary interest for operation of high-power electrochemical devices, ion transport within an electrolyte is often parameterized by its ionic conductivity (σ), which is the transport coefficient relating the ionic current density from *all* charged species (i_n) to the voltage drop (ΔV) per unit distance (L) (Figure 1). The ionic conductivity fails to capture the complexity of engineered devices, which must have high ionic conductivity as well as high voltage stability (to operate at sufficient ΔV values) and mechanical robustness (ability to make defect-free and processable films with small L). Nonetheless, σ is a useful parameter to evaluate electrolytes as it can be easily measured using widely available impedance techniques, where more precise transport coefficients often require techniques only available to experts. Another complexity in real cells is that much of the current parameterized by the ionic conductivity may be transient conductivity that is not maintained during cell operation – since redox inactive ions will accumulate at the electrode-electrolyte interface in the absence of electrochemical reactions that can consume the charged species^{1,5}. Thus, full characterization of electrolyte performance for electrochemical applications must simultaneously consider the species-dependent mobilities of all mobile ions in the electrolyte or the selectivity of the electrolyte for the redox active ions, which are often metal cations such as Li^+ , Mg^{2+} , Na^+ , or others.

$$\sum_n i_n = \sigma \frac{\Delta V}{L}$$

Equation 1

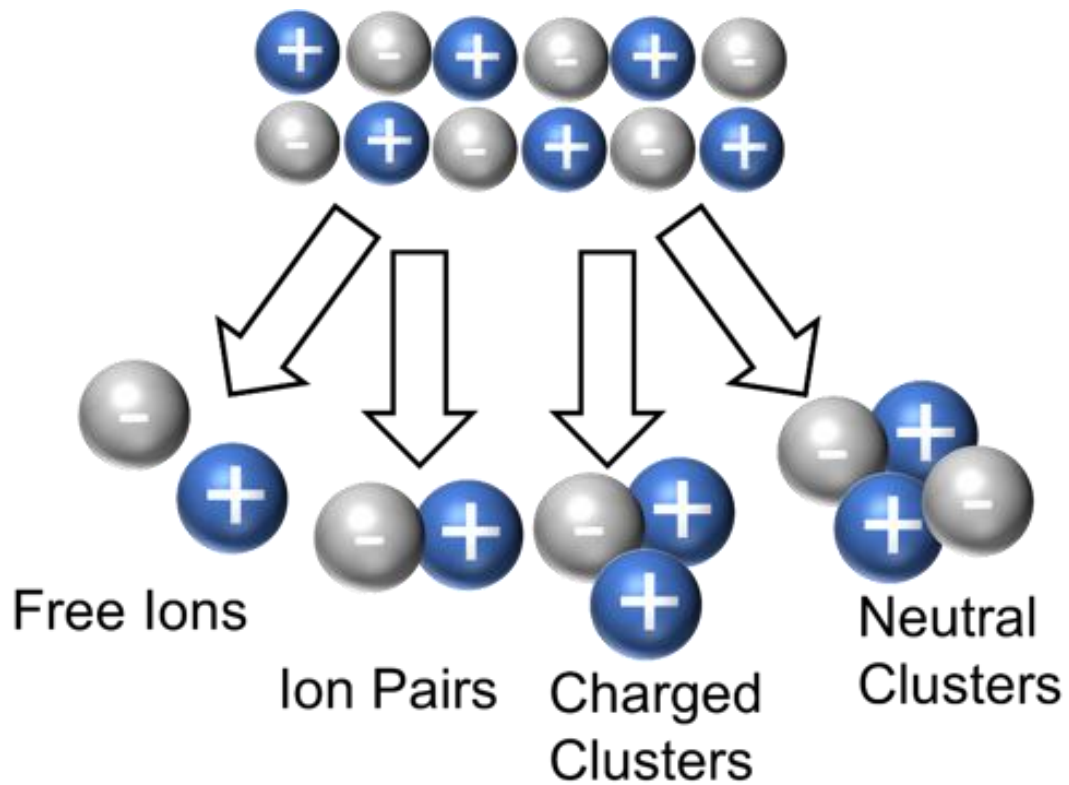


Figure 1: Cartoon of ion dissociation in an electrolyte medium.

When a salt is introduced into an electrolyte medium it can undergo a complex equilibrium between 'free' ions, associated ion pairs, and charged or neutral clusters/aggregates of >2 ions. This equilibrium plays an important role in dictating the conductive properties of an electrolyte. Similar equilibria exist for ion pairs of differing valency.

Ionic conductivity is broadly governed by two interconnected factors: ion concentration and ion mobility. The mobile ion concentration is set by both the total salt concentration and the ability of the electrolyte to dissociate the relevant salt. Within an electrolyte, ions exist in equilibrium as ‘free ions’ (dissociated, charged ions), ion pairs (associated, neutral pairs of ions), and ionic clusters (consisting of >2 ions and may be charge neutral or charged)⁶⁻¹³, as illustrated in Figure 1. When ions are associated, their motions become correlated over the lifetime of the ion association, impacting both the flow of charge and the species-specific flow of ions. Although numerous equilibria are required to describe the full population of aggregates, generally only the equilibrium between dissociated ions and ion pairs/clusters is captured as the extent of ion dissociation (ξ) (sometimes also called the ionicity), defined in Equation 22^{7, 14}. This dissociation extent is a function of both the identity of the ionic species as well as the properties of the background medium, including ion-electrolyte specific interactions and the overall dielectric properties of the background¹⁵⁻²¹.

The generation of dissociated ions generally occurs through solvation of added salts where the mobile ionic species are added to the electrolyte, generally through salt-doping. In so-called single ion-conductors, which are typically comprised of a polycation or polyanion with a corresponding small-molecule counterion, the generation of mobile species occurs through dissociation of the charged polymer-small molecule ion pairs. In either case, high extents of complete ion dissociation (ξ) are favorable in promoting high conductivity. Since ξ can be dependent upon both the salt and the host polymer identity, it is commonly necessary to independently optimize the salt loading for each polymer/salt combination, where a typical trend of salt concentration versus conductivity displays a local maximum that is a consequence of competing effects of ion mobility and concentration.

$$\xi = \frac{[free\ ions]}{[total\ ions]} \quad \text{Equation 2}$$

The ionic conductivity (σ) accounts for the net charge motion of all clusters and dissociated ions. This is seen in Equation 3, where e is the elementary charge, μ_n is the specific mobility, c_n is the concentration, and z_n is the charge of cluster 'n'. Since ion pairs and neutral clusters do not contribute to the ionic conductivity of the electrolyte ($z_n=0$), Equation 3 only requires two terms, which correspond to the contributions of dissociated cations and anions (Equation 4), where c_{salt} is the total salt concentration.

$$\sigma = \sum_n e c_n |z_n|^2 \mu_n \quad \text{Equation 3}$$

$$\sigma = e c_{salt} \xi (|z_+|^2 \mu_+ + |z_-|^2 \mu_-) \quad \text{Equation 4}$$

In addition to generating mobile ionic species, an effective electrolyte must also facilitate the transport of these species. The standard perspective of ion motion through SPEs is derived from theories of ion transport through standard, small-molecule liquids, whereby the molecular scale (<1nm) dynamics controls ion motion. At this lengthscale, the mobility of dissociated ions is primarily dictated by the local frictional environment of the liquid. The strength of the frictional force opposing ion transport is typically dictated by the segmental relaxation timescale, τ_α ^{14, 22-23}, leading to the relation $\mu \sim \tau_\alpha^{-1}$.

Due to the coupling of ion mobility and τ_α , theories of glassy dynamics in polymers can be used to model conductivity trends in SPEs. Although the glass transition is not precisely

defined in polymers, the semi-phenomenological Williams-Landau-Ferry (or equivalent Vogel-Tamman-Fulcher) equation (Equation 5) can be modified to model ion dynamics. Equation 5 describes the temperature dependent dynamics of the glassy timescale of a glass forming fluid or polymer. By substituting this expression for mobility into Equation 4, I obtain Equation 6, which provides a proportionality expression for the molar ionic conductivity (Λ , $\Lambda \equiv \sigma/c_{salt}$) as a function of temperature. This can be calibrated using the ionic conductivity of a reference system to obtain values for A , which depends on the salt identity. Although this elegant means of relating the temperature-dependent ion dynamics to the glass transition is established, it is commonplace within the field of SPEs to instead treat all constants as totally phenomenological, thus omitting any possibility to make a fundamental connection between the polymer dynamics and the glass transition.

$$\mu^{-1} \sim \tau_{\alpha} = \tau_{\alpha}(T = T_g) \cdot 10^{\frac{-C_{1g} \cdot (T - T_g)}{C_{2g} + T - T_g}} \quad \text{Equation 5}$$

$$\Lambda = \frac{\sigma}{c_{salt}} = \xi A [\tau_{\alpha}(T = T_g)]^{-1} \cdot 10^{\frac{C_{1g} \cdot (T - T_g)}{C_{2g} + T - T_g}} \quad \text{Equation 6}$$

The coupling of ion dynamics to the glass transition presents a conundrum for designers of amorphous SPEs. Typically, molar conductivities on the order of $\sim 1 \text{ Scm}^2/\text{mol}$ are required to provide a viable replacement to liquid electrolytes. Consequently, a segmental relaxation rate of $\tau_{\alpha} \sim 10^{-9} \text{ s}$ is required, suggesting that liquidlike transport of SPEs can only provide sufficient ionic conductivities at temperatures $\sim 90^\circ\text{C}$ above their glass transition temperatures (if typical values of $C_{1g} = 17.44$ and $C_{2g} = 51.6\text{K}$ are used). Although it is

possible to design sufficiently low- T_g polymers to achieve this temperature window, balancing the low T_g as well as other requirements of an electrolyte presents a major challenge, particularly since mechanical robustness is generally a major attribute and reason for choosing a polymer over a liquid electrolyte. Furthermore, the liquidlike transport mechanism generally results in poor selectivity for ions of interest relative to other ions in the system.

The selectivity of the electrolyte in the fully dissociated limit is a consequence of the unequal diffusion of the cations and anions of the system. The cation transport number, t_+ , is computed according to the self-diffusion coefficients all mobile ionic species/clusters in the electrolyte (shown in Equation 7 for the simplified equilibrium of Equation 2). Although Equation 7 is subject to the same approximations as the previous expression and has the same limitations as a descriptor for a real system, this expression demonstrates the principle that selectivity is difficult to attain in a liquidlike transport mechanism since both $\tau_\alpha^{-1} \sim \mu_+$ and $\tau_\alpha^{-1} \sim \mu_-$. This further motivates the design of systems where ion dynamics are unrelated to segmental relaxation since alternative modes of conduction typically display much greater selectivity for cations of interest.

$$t_+ = \frac{|z_+|^2 \mu_+}{|z_+|^2 \mu_+ + |z_-|^2 \mu_-} \quad \text{Equation 7}$$

B. Amorphous Polymer Electrolyte Designs

Standard strategies towards improving SPE conductivity primarily rely on either improving the solubility of salts within the electrolyte (increasing $\zeta_{C_{salt}}$) and increasing the mobility of salts by reducing the glass transition temperature of the electrolyte. Linear

polyethylene oxide (PEO) has become a model polymer host for lithium conduction as the coordination of ether-oxygens with lithium have been shown to yield high salt solubilities of lithium salts such as Lithium bis(trifluoromethanesulfonyl)imide (LiTFSI) or Lithium Hexafluorophosphate (LiPF₆) and the relatively low glass transition temperature of the polymer promotes ion mobility via the liquidlike conduction mechanism^{3, 24}. These properties have made PEO the most highly studied SPE host despite its relatively poor mechanical and selectivity properties. Although PEO is a semicrystalline polymer, its conductivity in the amorphous state is of primary relevance for most applications since the ionic conductivity in this state is typically much higher than below the melting temperature²⁵⁻²⁶, except in exceptional cases²⁷. Many detailed reports have investigated the transport mechanism for this polymer²⁸⁻³⁰, finding it to mainly display liquidlike transport at low salt compositions and above its melting temperature.

Although amorphous PEO is known to generally follow a liquidlike mechanism, several factors can result in cases where trends in glass transition temperature do not result in expected trends in conductivity. This suggests that conductivity in these systems may also depend on solvation site dynamics and percolation. For example, Hawker and coworkers studied the impact of PEO-based materials with linear and cyclic ether side chains, finding that the ionic conductivity of the linear and cyclic polyethers were similar despite significant differences between the glass transition temperatures of these two polymers³¹. Similarly, work by Patel and coworkers has experimentally and theoretically studied side-chain polyethers and found that ionic conductivity differences between linear and side-chain polyethers of differing lengths cannot be explained by differences in segmental mobility of the system³²⁻³³. They found that the conductivity trends of these systems could only be

accounted for by considering both solvation site connectivity differences and differences in the dynamics of the solvation sites, which were found to differ depending on the distance of the chelating groups from the backbone.

Attempts to surpass the performance of PEO primarily focus on reducing its crystallinity, further reducing the T_g , and improving its salt solvation ability. The crystallinity of PEO can be reduced by designing nonlinear architectures³¹⁻³⁴, addition of additives that inhibit crystallization³⁵⁻³⁷, crosslinking³⁸⁻⁴⁰, and using copolymerization to reduce the ordering of the PEO⁴¹⁻⁴². Small molecule additives can play various roles including as plasticizers⁴³⁻⁴⁵, dielectricizers⁴⁶⁻⁴⁷. In general, PEO is poorly selective ($t_+ < 0.2$) and the addition of anion traps seem to modestly increase selectivity⁴⁸⁻⁵¹. A variety of other amorphous hosts based on other coordinating groups have also been reported, however none of these candidates reliably surpass the benchmarks set by PEO^{24, 52}. Indeed, it appears in most cases that as conductivity is increased, selectivity is sacrificed resulting in a practical upper bound in performance¹.

Another relevant amorphous ion conduction system is the metal-ligand polymers that have been studied and developed in the Segalman laboratory. These materials comprise polymers with tethered ligands that act to dissociate salts and promote ion conduction of these dissociated pairs through exchange of cations between ligand sites. These materials have been the focus of significant study in the Segalman laboratory, ranging from studies of their design in polyethers for Nickel conduction to their application as competitive lithium transport materials. Interestingly, the controlled nature of the metal-ligand bond allows for these materials to also act as transiently crosslinked materials enabling the characterization of the metal-ligand bond by rheology. These nominally amorphous polymer electrolytes also

display coupling of ion transport with segmental dynamics in a similar fashion to PEO and other polyethers. The mechanism of ion transport in these polymers is the topic of the second chapter of this thesis.

C. Superionic Ceramics Support a Solidlike Transport Mechanism

While the discussion of SPE conductivity up to this point has focused on the liquidlike mechanism of transport, whereby ion transport is coupled to fluid relaxation, some materials display relatively fast transport of ions despite having very slow relaxation dynamics. Diverse materials ranging from carefully-designed ceramics⁵³ to commonplace materials such as ice at extreme pressure and temperature conditions⁵⁴⁻⁵⁵ can display high decoupling of ion transport from their relaxation rates. Mechanisms for charge transport in these solid systems do not involve fluidlike motion of the electrolyte since the atomic coordinates of crystalline or amorphous ceramics are strongly confined by steep energy wells, yet high ionic conductivities above 10^{-2} S/cm have been reported⁵⁶. So-called superionic transport in ceramic electrolytes relies upon immobile percolated pathways of free volume, allowing ions to opportunistically hop along a pathway of sites comprising vacancies, interstitials, or voids at rates that can exceed those attainable in simple or polymeric fluids. Moreover, the fixed nature of the sites enables greater size-based selectivity of ion transport in these electrolytes (often approaching $t_{+}=1$)⁵⁶⁻⁵⁷.

Ion transport decoupled from matrix motion has been demonstrated in many ceramic materials, which often are crystalline in nature and yet, display ionic conductivities on par with simple fluids. Extensive work detailing the design of these materials are already published⁵⁸⁻⁶⁵, so here I summarize some key findings from this field that may be applicable to solid polymer systems. Firstly, it is known that a percolating network of free volume sites

must be present to promote sufficiently rapid ionic motion. In these cases, the energy to hop between sites is often conceptualized to follow an Arrhenius-type process where energy for an ion jump process in isolation is controlled by factors such as the free volume of the sites and the interactions between the ion and the matrix. These two features require that the equilibrium packing of the electrolyte be loosely spaced to accommodate the mobile ion and that the chemical properties of the matrix are sufficiently labile such that ions can dissociate from their local interactions to allow for fast hopping rates. This resembles the solvation strength tradeoffs which can be present in SPEs and prevent the activated hopping of ions between sites in these materials. Another relevant feature is the collective nature of motions in these types of materials (Figure 2, adapted from⁶⁵). It has been shown that a significant amount of the motions in such materials are stringlike motions where the presence of nearby ions can lower the energy barrier for ion transport in these materials. This type of mechanism can only occur at sufficiently high ion loadings, and ion concentrations in these materials typically exceed levels seen in polymer or liquid electrolytes.

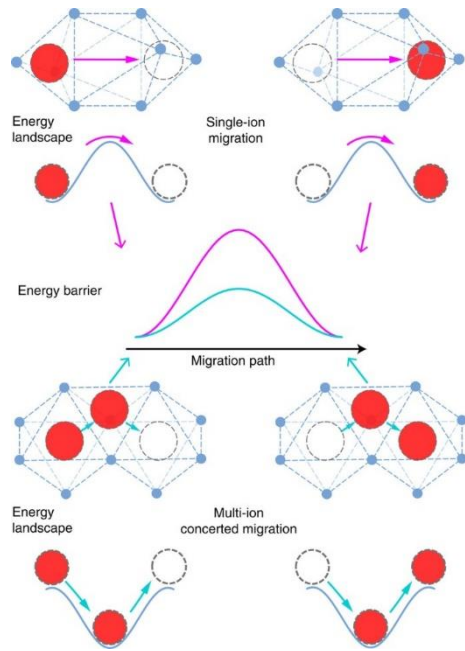


Figure 2: Cartoon Illustrating ion transport in a superionic ceramic.

Transport pathways in superionic ceramics can be dominated by cooperative hopping events. In the case of a discrete ion (pink) the ion experiences a larger energy barrier for hopping than in the case of the cooperative event (green) where the correlation of the ion motions results in a lower overall energy barrier that these ions must overcome.

Reproduced with permission.

Another crucial design principle is the requirement of mobility within superionic crystals. In both inorganic glasses⁶⁶ and crystalline inorganic solids⁶⁷, crankshaft-like motions of the matrix are crucial in driving the motion of lithium, this effect is often called the ‘paddlewheel’ effect⁶⁶⁻⁶⁷. These types of microscopic motion typically consist of rotation and vibrational modes and thus do not truly correspond to rearrangement of the crystal, but nonetheless can set temperature floors for operation of ceramic crystals and devices. These motions arise below the melting temperature of the material – phenomenologically it has been observed that they arise at $T \sim 2/3 T_m$ ⁵⁹. Although ion transport is often still Temperature-dependent in these electrolytes, the temperature dependence of this phonon-assisted

transport in rigid ceramics is typically much than glass-forming liquids, allowing excellent ion transport performance over a range of temperatures.

Another remarkable aspect of ceramic ion conductors is their near-universal high selectivity for ions of interest in many applications. Indeed, in lithium-conducting ceramics the transport number of lithium often approaches unity, suggesting almost complete exclusion of counterion motion and perfect selectivity for ions of interest. This is attained based on the precise size-selectivity of these structures. Since alkali metal ions such as lithium are typically much smaller than their counterions the size selective nature of these structures can prevent counterion motion altogether, leading to t_+ approaching unity.

Although the design principles of ceramic materials are inarguably different than SPEs, some design principles from such systems are likely to be maintained. The free-volume pathway for ion motion is likely to be a necessary design feature of either class of material. This free volume pathway can be realized in ordered crystalline solids, fragile glasses, or through nanoscale ordering of soft materials. Additionally, it is seen that ion-ion correlations between mobile ions can play a positive role in promoting the concerted motions of ions. This type of motion is likely to be rarely implemented in organic polymeric electrolytes since common ion loadings are too low, however in systems like polymer-in-salt electrolytes these concerted motions may play a larger role. Finally, the ion solvation of SPEs can be a great concern, attaining high salt loadings is crucial to leverage superionic effects, but it can be challenging to simultaneously impart high solubility while maintaining labile electrolyte-ion interactions^{16, 68}.

D. Analysis of Transport Mechanisms

Although it is straightforward to identify the dominant transport mechanism for fluids well above their melting or glass transition temperature (liquidlike) and highly constrained inorganic solids (solidlike), polymers represent a more complicated case where the dominant mechanism of transport may be system-dependent and nonintuitive. As such it is necessary to analyze the transport behavior of soft-matter electrolytes to determine the dominant modes of ion mobility. Most techniques for determining the mechanism of transport involve analysis of the fluid/matrix relaxation rate and a comparison with the observed transport rate. A useful means of analyzing this behavior is Walden plot analysis^{22-23, 69}.

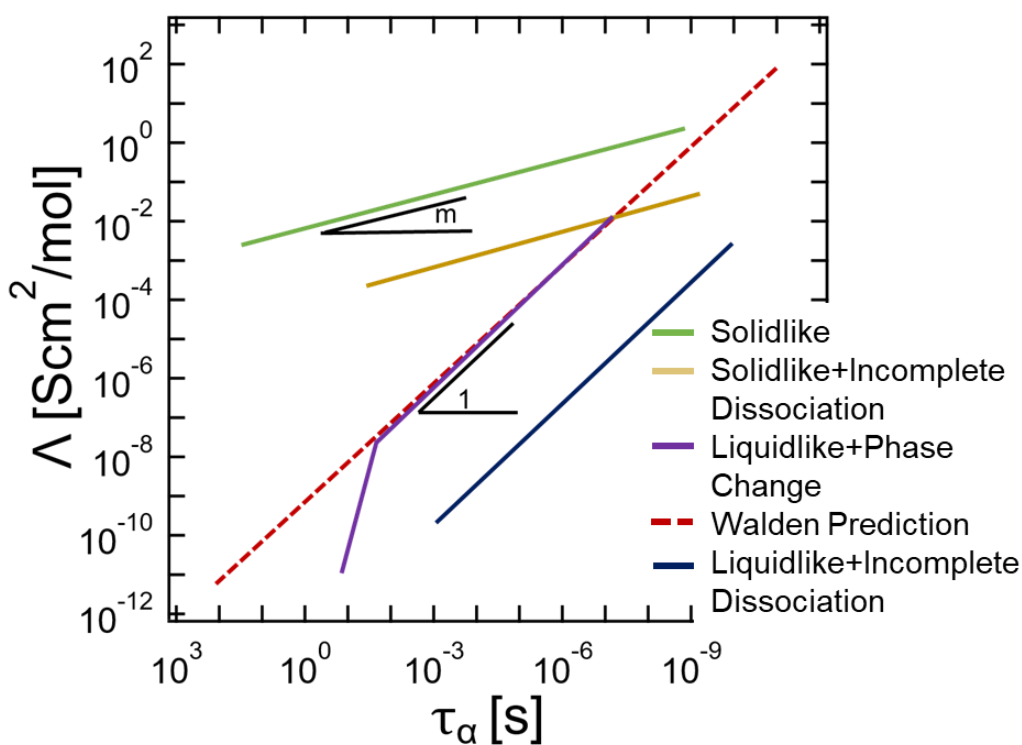


Figure 3: A representative model Walden plot containing some typical electrolytes.

This figure shows a representative Walden plot where the red dashed line shows the Walden prediction line applicable to most ideal liquidlike electrolytes, the blue line is a fluid with

partial ion aggregation resulting in suppressed ionic conductivity, the green line is superionic material with decoupled transport, the yellow line is a superionic material with partial ion aggregation, and the purple line represents a material undergoing a crystallization transition. The slope 'm' < 1 represents decoupling of matrix dynamics and ion transport.

Walden plot analysis compares the average mobility of the ionic species within an electrolyte to the anticipated ionic mobility based on the liquidlike transport mechanism. Figure 3 shows a representative Walden plot^{14, 22-23, 69}, where the red line indicates the Walden prediction that is dictated by the scaling relation $\Lambda \sim \tau_{\alpha}^{-1}$ and the absolute magnitude of the line is calibrated based on the conductivity of a dilute solution. This line is typical of a simple fluid with $\xi=1$ (complete salt dissociation) and represents complete coupling of segmental motion of the polymer matrix to ionic transport. This line is the Walden prediction, and it separates the region of superionic behavior from that of subionic behavior. One source of departure from this line can come from incomplete ion dissociation i.e. $\xi < 1$. This case is highlighted by the blue line and commonly arises in ionic liquids or concentrated electrolytes. The line still is parallel to the Walden line with $\Lambda \sim \tau_{\alpha}^{-1}$, however the ionic conductivity is reduced compared to this line due to a fraction of electrochemically inactive, charge-neutral species. The green line represents another strong deviation from the Walden line typical of structured solid electrolytes such as ceramics and certain inorganic glasses. Typically, these electrolytes display a region of power-law behavior where $\Lambda \sim \tau_{\alpha}^{-m}$. The value of this 'm' parameter is called the decoupling index and often ranges from zero to unity, where 'm' values approaching zero represent complete decoupling of ionic transport from matrix motion and a decoupling exponent of unity represents completely coupled ion and matrix motion or the 'Nernst-Einstein' behavior. Voronel²³ has shown that 'm' values for typical fluids fall from 0.8-1, suggesting only slight decoupling of ion and momentum

transport. Experimental studies and theoretical models have yielded ‘ m ’ values exceeding unity for some materials, although these cases are uncommon and not fully understood. In some cases, both effects of incomplete salt dissociation and breakdown of Stokes-Einstein dynamics can occur, resulting in behavior where both superionic and subionic behavior occur in the same system as represented by the yellow line. Additionally, thermodynamic transitions such as crystallization can impact the ion conduction mechanism. The purple line is representative of PEO, which typically follows the Walden relation above T_m , but becomes subionic upon crystallization.

Utilizing the Walden plot requires accurate measurement of both the molar conductivity of the ions in the electrolyte as well as the segmental timescale of the electrolyte. Most frequently the ionic conductivity as determined from dielectric spectroscopy is used to determine the molar conductivity, although this can lead to complications in cases of incomplete ion dissociation since a portion of the ions will not contribute to the measured ionic conductivity. This can be corrected by renormalizing the conductivity to reflect the concentration of dissociated ions in cases where the ion dissociation extent can be determined. Alternatively, it is possible to utilize direct measurements of ion diffusion coefficients from NMR-based measurements⁷⁰⁻⁷¹. In this case the Nernst-Einstein relation can be used to convert the Walden prediction to a prediction of diffusivity. Although the framing of the Walden relation is classically formulated as a prediction of the molar conductivity, it may be more fundamentally useful to frame this relation in terms of a diffusivity axis or to renormalize based on the fraction of dissociated ions⁷².

The determination of the segmental time requires grappling with the complex nature of fluid relaxation, especially near the glass transition temperature. Experimentally the

segmental relaxation can be determined via a variety of means including scattering techniques, broadband dielectric spectroscopy, rheology, and via NMR; however, these techniques are specialized and are often not reported for SPEs. In a recent review, Sokolov proposes that the experimentally measured glass transition temperature², which is much more standardized in its measurement, may provide a good way to estimate glassy dynamics in the literature using the relation $\tau_\alpha(T = T_{g,calorimetric}) \approx 100 \text{ s}$. This expression provides a single point to compare dynamics, however polymers cannot be placed on a Walden plot using this information unless the variation of dynamics with temperature is known.

Extrapolation based on the “universal” form of the WLF equation is in principle a means to tackle this issue. However, such an approach suffers from difficulties in fitting the universal function. Computationally, the measurement of glassy dynamics also comes with its own challenges. While atomistic molecular dynamics simulations can access picosecond to microsecond relaxation phenomena, this timescale range is still insufficient to capture matrix dynamics relevant for the calorimetric glass transition, which involves geologically-relevant timescales⁷³⁻⁷⁴. Furthermore, glass formation behavior is typically dynamically heterogeneous, wherein the relaxation is highly spatially dependent. This dynamic heterogeneity can cause additional issues when collecting particle-by-particle statistics as a larger ensemble of particles may be necessary to capture the average behavior.

E. Measurement Methods

While the total ionic conductivity is the most commonly reported metric of ionic transport in polymer electrolytes, actual electrolyte performance in energy storage and conversion devices heavily depends on a more comprehensive view of ion conduction. For example, in lithium-ion batteries, the ionic current carried by Li^+ ions is of primary interest and counter-

ion motion can be detrimental to cell performance. Consequently, the transport number is an important parameter to approximate the fraction of the total current carried by the ion of interest (see Equation 7)⁶⁹.

The complex impedance measured by electrochemical impedance spectroscopy (EIS), or AC impedance, is widely used to measure contributions of ionic transport (Figure 4A).

These contributions are determined through construction of an equivalent circuit model to fit the impedance data (Figure 4B). Generally, the equivalent circuit is designed with physical phenomena in mind to connect the circuit elements with the physical behavior in the sample. In a cell with blocking electrodes it is typical to model the behavior according to the circuit inset in Figure 4B, which models the electrolyte as a resistor/capacitor (R2 and Q1) with additional contributions from the interfacial polarization impedance (Q2) and net resistance of the circuit (R1).

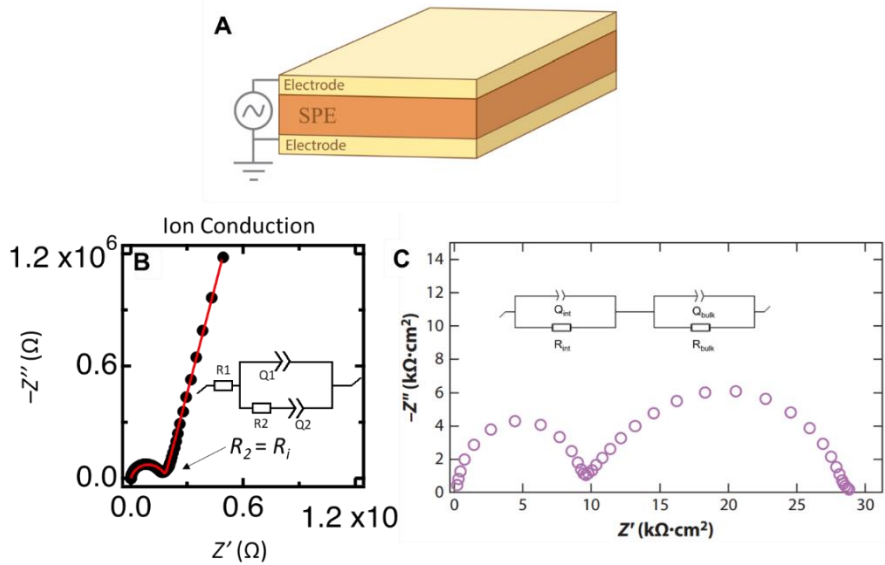


Figure 4: A diagram of an ionic conductivity setup and typical response curves for blocking and nonblocking electrodes.

A) The setup for an AC-impedance experiment sandwiches an electrolyte between two electrodes. A potentiostat is used to apply an oscillatory voltage and the current response is measured by the instrument. B) A typical curve for a pure ion conductor in a 'blocking electrode' setup has contributions from circuit resistance (R1) interfacial polarization (Q2) as well as the RC circuit of the electrolyte (R2 and Q1). C) For a pure ion conductor in a symmetric metal cell in the presence of redox reactions an additional semicircle arises due to interfacial polarization. It is typical to model these circuits as having an RC mode from the Solid-electrolyte interphase layer as well as from the bulk electrolyte layer as seen in the inset.

The Bruce-Vincent method is a cell-based method frequently employed in the literature to determine the species-dependent transport number¹². This method employs a symmetric electrochemical cell and can relate the steady-state DC voltage of the cell to the transport of a specific species under dilute conditions. Consequently, this method does not give a true transport number under conditions relevant for many applications. The dilute approximation generally only applies at low ionic strengths (< 0.01), which is much less than the ionic strength typical for an electrolyte¹⁸. Despite the inability to extract relevant transport numbers under common conditions, the ease of implementation has resulted in wide propagation of this method and it has become standard in the field of ionically conducting polymers. Therefore, the results of this experiment are important for benchmarking purposes and to compare between materials systems. Recent developments in cell-based methods may allow better estimation in concentrated solutions, including direct measurement of the concentration gradient along the transport direction and analysis based on concentrated solution theory⁸³.

An alternative family of techniques to examine ion-specific transport utilizes measurements of ion self-diffusion constants and their contribution to conductivity is again calculated based upon the assumptions of the Nernst-Einstein equation (Equation 3).

Techniques such as pulsed-field gradient NMR can measure the self-diffusion constants of ions^{84, 85}. Neglecting intermolecular interactions, the ionic conductivity contributions from individual species is directly related to this constant, their concentration, and valency allowing for facile computation of their contribution to the total conductivity. However, experimental reconstructions of the net ionic conductivity based on these results often fail to reproduce the measured ionic conductivity.

A quantity known as the Haven ratio (Equation 8) is used to characterize the ratio of the measured ionic conductivity and the ionic conductivity reproduced from the Nernst-Einstein relation (Equation 3).

$$H = \frac{\sigma_{NE}}{\sigma_{electrochem}} = \frac{\sum_i n_i z_i^2 D_i}{kT \sigma_{electrochem}} \quad \text{Equation 8}$$

In Equation 8, H is the Haven ratio, σ_{NE} is the Nernst-Einstein conductivity, $\sigma_{electrochem}$ is the electrochemically-determined conductivity, n_i is the number of charge carriers i , z_i is the integer charge of the charge carrier, D_i is the diffusion coefficient, k is the Boltzmann constant, and T is the temperature.

The Haven ratio often takes on a value of greater than unity for ionic liquids or molten salts,⁷⁰ but can take on values greater than unity for superionic conductors⁷¹. In some concentrated polymer electrolytes, Haven ratios of nearly unity are observed, but authors should take care to note that deviations from the Nernst-Einstein relation are likely to arise, particularly at high ionic strengths or in the presence of crystalline regimes. As such, Haven ratio values far from unity are indicative of intermolecular interactions that lead to differences between ionic diffusivity and charge diffusivity – such as ion aggregation.

F. Leveraging Alternative Conduction Mechanisms in Organic Electrolytes

A limited but growing number of polymeric systems have been demonstrated to have deviation from liquidlike transport, some with aspects of solidlike behavior and others approaching superionic transport similar to ceramics, as described below.

F.1 Zwitterionic Electrolytes

Crystalline zwitterionic (ZI) compounds with bulky and diffuse ion groups show great promise as solid-state ion conductors due to their charge neutrality, excellent dielectric properties, and unique self-assembly behaviors. ZIs are comprised of an anion and cation that are connected by a short tether, typically consisting of a 3-4 carbon alkyl spacer. Due to this covalent ion attachment, ZIs are charge-neutral molecules with extreme values of the dielectric constant, ranging up to 270 in the amorphous state⁷⁶. These properties make for useful ion transport hosts as the charge-neutral molten or solid ZI will not migrate in an electric field, but can act as a highly polar background to promote ion transport of ions when blended with salt⁷⁶⁻⁷⁷. Indeed, the excellent dielectric properties of ZIs promote ultra-high salt solubilities without ion pair formation, even up to equimolar salt/ZI loadings^{76, 78}. Furthermore, ZIs display a broad range of ordering motifs (e.g., fluid, liquid crystal, crystal) due to the strong intermolecular interactions among the charged groups. Interestingly, zwitterions display significantly more ordering than their ionic liquid counterparts even when they are comprised of the same ionic components, with significantly wider windows of stability for the crystalline phase.

Incorporation of zwitterions onto polymers results solidlike mechanisms of the small molecule zwitterions without the disadvantages of purely crystalline electrolytes such as

poor contact with electrodes⁷⁹, brittleness and cracking⁸⁰⁻⁸¹, and limited chemical/electrochemical stability against a metal anode or high energy cathode⁸² that are typical of purely crystalline ion conductors. Chapter 3 discusses a ZI (Figure 5A) and ZI polymers tethered to linear polymer chains such that the cation of the zwitterion was connected to the dangling amide group attached to each monomer⁸³. I used Walden plot analysis to show that these polymers displayed transport behavior strongly decoupled from the segmental relaxation behavior (Figure 5B). This decoupling suggests a solid-like structural motif that enables superionic behavior. The polymers were analyzed by calorimetry and x-ray scattering and were found to be semicrystalline, possessing structural similarity between the PZI and the equivalent ZI in structural motif I. I believe that a similar hopping-type transport mechanism may be present in both the polymeric and nonpolymeric versions of this zwitterion, accounting for the observed superionic transport behavior.

The excellent performance of polymeric zwitterions as solid and Li^+ selective hosts for ion transport has inspired further investigation of these compounds. Both small-molecule and polymeric ZIs are surpass a phenomenological upper-bound proposed by Balsara and coworkers² when analyzed in terms of their selectivity and transport properties. This suggests the excellent promise of these semi-crystalline electrolytes as ion transport materials. In recent work I have further elucidated structure-property relationships for these materials, finding that the effective bulkiness of the tethered ion species closely correlates with the ionic conductivity of the electrolyte. This suggests that both the nanoscale ordering of the zwitterion as well as the strength of zwitterion-salt interactions are crucial in promoting efficient ion transport in ZI materials. In the proceeding text I further review

work on ZI electrolyte materials, focusing on recent work that characterizes the simpler case of small-molecule ZIs.

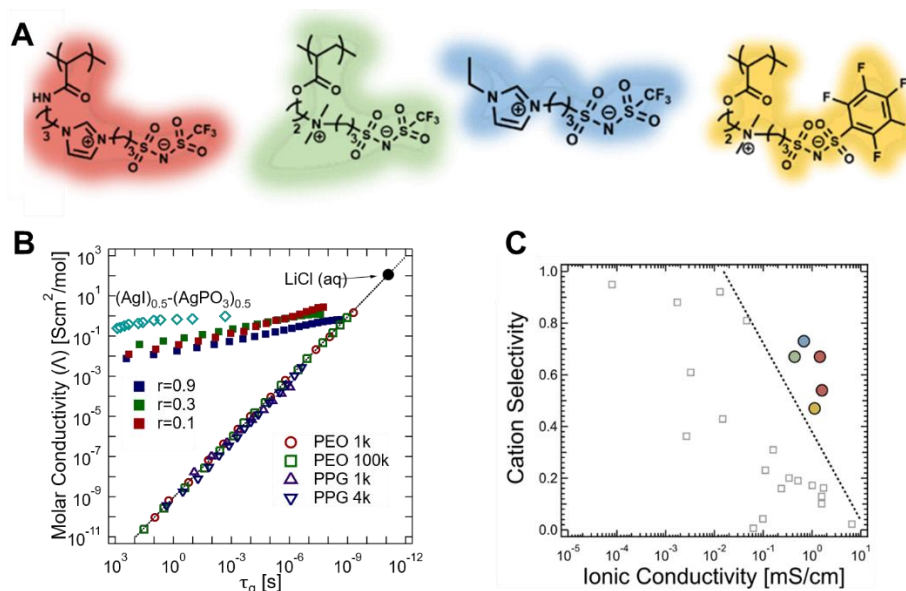


Figure 5: Zwitterionic polymers and small molecules display superionic transport and break the upper-bound set by Robison plot analysis.

A) ZI polymers (red, green, yellow) and ZI-small molecule (blue) that were studied as Li^+ electrolytes in Chapter 3. B) A Walden plot analysis of the ZI polymers at various salt loadings (r =moles of salt/mole of ZI) shows strongly superionic behavior of the ZI polymers. ZI Polymer behavior is nearly competitive with superionic ceramic materials in terms of decoupling from liquidlike conduction mechanism. C) Analysis of ZI polymer conductivity and selectivity performance surpasses a phenomenological ‘upper-bound’ for SPE performance as proposed by Balsara and coworkers.²

As in ceramic materials, the structure of ZIs is hypothesized to intimately relate to their ion transport properties and mechanism, suggesting the importance of understanding zwitterion phase behavior. Though ZIs and ionic liquids are composed of the same ions, distinct differences arise in the phase behavior of ZIs due to the tethered nature of these ions. For instance, while imidazolium and sulfonamide ions constitute some of the most common

room temperature IL's such as 1-Ethyl-3-methylimidazolium bis(trifluoromethylsulfonyl) imide ($T_m = -16\text{ }^\circ\text{C}$), when they are joined together by a relatively short tether, they form a ZI with a relatively high melting point ($T_m = 131\text{ }^\circ\text{C}$ ⁸⁴). The structure of ZI/salt blends is particularly important in electrolyte applications as the addition of salt is required to generate charge carriers for the electrolyte. Ohno has observed that the addition of equimolar salt to a crystalline ZI results in the disappearance of a crystalline melting peak and the appearance of a glass transition when analyzed in calorimetry⁸⁴, suggesting a liquidlike structure of ZI/salt blends at high salt loadings. This is studied in greater detail by Pringle and coworkers, who have found solid phases at both the high and low salt concentration extrema and a liquid phase at intermediate composition⁸⁵. I have investigated the composition-dependent phase behavior of zwitterion-salt mixtures, suggesting eutectic-like behavior at intermediate compositions that is heavily dependent upon both the structure of the zwitterion and the added salt identity, with bulkier salts generally being more disruptive to the crystallization of the zwitterionic electrolyte. Zwitterion/salt blends studied in the literature appear to universally behave as eutectic mixtures with three major structural motifs: (Figure 6A) I) a zwitterion-rich crystalline regime that exists at low salt concentrations II) a disordered liquid regime that exists at intermediate concentrations of salt and zwitterion, and III) a salt-rich crystalline phase that contains some zwitterion. In the following, I will discuss the structure and ion conduction properties within each regime.

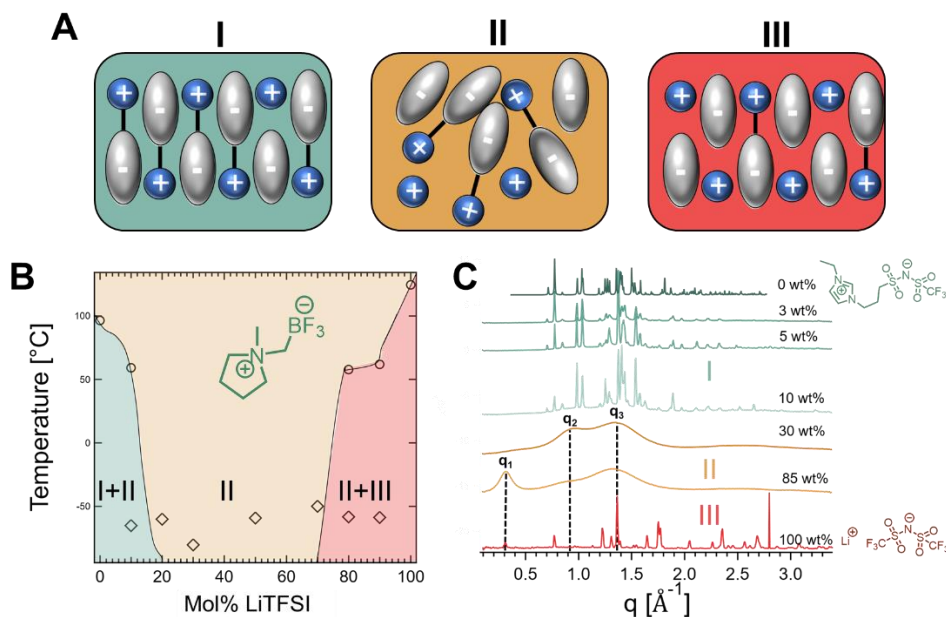


Figure 6: Zwitterionic molecules display 3 universal phase behaviors.

A) The three regimes of zwitterion behavior that seem apparent include (I) a zwitterionic crystal regime (II) a liquid consisting of zwitterion and salt, and (III) a salt crystal regime. B) Pringle and coworkers measured the calorimetry of a zwitterion/salt blend. Based on their measurements a preliminary phase diagram can be prepared, this diagram has coexistence regimes at both extrema and a large liquid window in the center of the phase diagram. C) Blends of a zwitterion consisting of IL-like ion pairs is found to display solidlike behavior at low salt concentrations indicated by sharp Bragg peaks. Then at intermediate salt loadings the Bragg peaks give way to liquidlike structuring with an ion-ion correlation peak (q_2) and a liquidlike packing peak (q_3). At higher salt loadings the presence of a third peak q_1 that likely corresponds to salt aggregates emerges.

At low concentrations of salt, the ZI retains its crystalline nature and displaying solidlike transport properties. Pringle and coworkers studied a pyrrolidinium/boron trifluoride ZI (Figure 6B inset structure) in the presence of lithium/TFSI salt. They found (Figure 6B) a T_m (indicating motif I) and a T_g (indicating motif II) at 10mol% salt loading. This suggests a

coexistence of ZI crystals (motif I) with a disordered fluid (motif II) that is present at appreciable salt concentrations. Similarly, I studied the structure of blends of Li/TFSI salt and ZIs comprised of ethyl-imidazolium/TFSI ion pairs with a propyl spacer between the ions (Figure 6C). I also found that 10wt% salt blends maintain Bragg reflections that coincide with the Bragg reflections of the pure crystal, again suggesting coexistence of crystal (motif I) and liquid regions (motif II). Another universal feature of both blends is the reduction of the melting temperature as salt is added. Pringle and coworkers observe a T_m reduction of $\sim 40^\circ\text{C}$ at 10% salt where I see a similar reduction of about 60°C at a similar salt composition. This reduction is typical of eutectic mixtures and is commonly observed in metallurgical systems where it can suggest the formation of ‘alloys’ where two components are cocrystallized together into one structure. More work is required to understand the thermodynamics of zwitterions and whether similar alloys can form, as this alloying may have profound implications on the ionic transport of these structures.

ZI/salt blends in motif I closely resemble superionic ceramics wherein zwitterionic crystallites may promote long-range transport of ionic species through a hopping mechanism. I have investigated the ionic conductivity of zwitterions with a smaller composition of salt added to the electrolyte such that the structure of the zwitterion remains dominated by crystallites. Despite the crystalline nature of the resulting electrolyte, there is significant ionic conductivity consistent with superionic transport. I find that a significant portion of the ionic conductivity can be attributed to lithium motion with a calculated lithium selectivity of 0.73. Similarly, the ZIs studied by Pringle and coworkers also displayed significant lithium conductivity despite their crystalline nature. They also observe

mobility of both Li and TFSI, however they see significantly reduced selectivity for lithium ($t_+ = 0.29$, determined by PFG as shown in Figure 7).

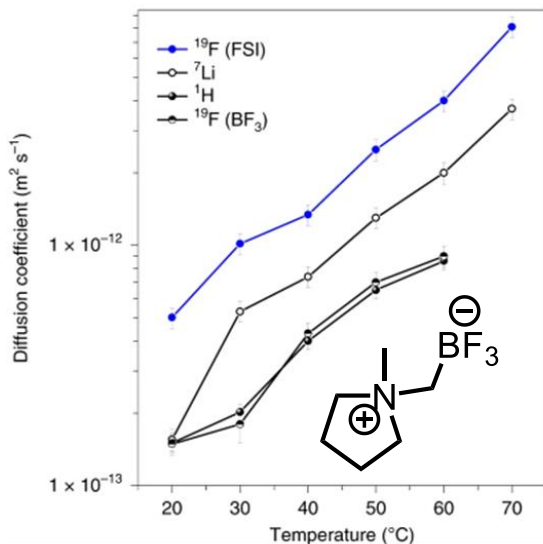


Figure 7: Zwitterions analyzed by NMR show diffusion of the zwitterion and both ions.

The ZI electrolyte from Pringle and coworkers shows mobility of the zwitterion (^1H and ^{19}F) and the salts (^{19}F and ^7Li). Based on their NMR measurements they compute a selectivity of $t_+ \sim 0.29$, which exceeds the typical transport number of PEO ($t_+ \sim 0.2$).

At higher salt loadings, only a T_g is seen, suggesting a glass-forming fluid (motif II) with distinct conduction and mechanical properties from the zwitterionic crystal (motif I). The behavior of ZI displaying structural motif I has been extensively characterized by Ohno who primarily studied nearly-equimolar blends of ZI/salt in a wide variety of zwitterion and salt identities^{77, 84, 86}. Ohno typically found that these blends displayed a T_g that is relatively insensitive to salt loading, but can vary significantly based on salt and ZI identity. Pringle and coworkers (Figure 6B) found that motif II is present across the salt concentration region of 20 to 70 mol% with coexistence of motif I+II at 10mol% salt and coexistence of motifs

II+III at 80-90mol%. I (Figure 6C) also found similar behavior in blends of ZI/LiTFSI through x-ray scattering studies. Motif II is evident in the x-ray scattering data from the disappearance of ordered, Bragg-like reflections and their replacement with broad, liquid-like peaks. I show that multiple characteristic lengthscales exist in motif II (Figure 6C): two correlation lengthscales of $q_2 \sim 7 \text{ \AA}$ and $q_3 \sim 4.5 \text{ \AA}$ correspond to the packing of the disordered electrolyte. These two separate correlation peaks may arise from large differences in ion diameters, leading to slight ordering within the liquid phase, though more investigation is required to understand the liquidlike packing of these materials. At higher salt concentrations I find that another correlation lengthscale arises at longer lengthscale $q_1 \sim 20 \text{ \AA}$, this may correspond to nanoscale aggregation of salts that commonly arises in salt/polymer blends, though this nanoscale aggregation is likely driven by differences in ion chemistry, rather than the poor dielectric properties of the ZI.

It is anticipated that when disordered, these ZI materials will display liquidlike mechanical and transport properties, this appears to be mostly true, however some gaps in the understanding of conduction in this region remain. Ohno and coworkers have extensively investigated the ionic conductivity of these disordered pseudo-solid electrolytes^{77, 84, 86}. They find that conductivity roughly follows a WLF-like trend and appears to collapse based on glass transition temperatures across various zwitterions. These observations suggest that local ion dynamics play a critical role in promoting ionic conductivity. Nonetheless, these materials exhibit much greater values of t_+ ($t_+ > 0.5$) than is typical for the liquidlike transport mechanism⁸⁶, suggesting that further work may be needed to fully understand the transport mechanism in these disordered ZI/salt electrolytes. Future work investigating the Walden-plot behavior of these materials may be useful in

determining the transport mechanism of these electrolytes. Further, despite being low molecular weight fluids above their glass transition temperatures, these materials display tremendous rigidity that approaches glassy behavior. The origin of this rigidity is not yet understood, but it may also have implications for their application as solid electrolytes.

At high salt concentrations, the zwitterionic composition is small and the behavior is dominated by the added salt, which is typically crystalline and nonconductive, resulting in transport behavior that is dominated by regimes of motif II. This situation resembles polymer-in-salt electrolytes or high concentrations of salts in ILs where the majority of the electrolyte is comprised of crystalline salts with small disordered regions with very high carrier concentrations. Pringle observes the coexistence of motifs II+III at salt compositions ranging from 80-90 mol%. Although I do not observe this region for the blends of ZI/LiTFSI, I do see a wide region of this behavior for other salts such as NaCl and LiCl. Ion transport in the coexistence region of motifs II+III is likely to resemble transport of salt and ionic liquid blends at high salt concentrations, though no studies have sufficiently probed this region. Pringle observed that the conductivity in this high salt region can also be quite high, though the transport mechanism and selectivity are not currently known in this region. I believe that these solid electrolytes could be fruitful ion transport hosts and I suggest that this area requires additional study.

Ordering of zwitterions also occurs at a longer lengthscale in zwitterions with a significant nonpolar fraction. This ordering has been shown to have useful properties for promoting proton mobility, however, the relevance of these channels for other carrier ions is yet unknown. ZIs comprised of a highly polar head group and nonpolar tail can assemble into thermodynamically favored states that display order over the 1-3 nm lengthscale⁸⁷⁻

⁸⁹.The structure resembles those seen in ionic liquids with hydrophobic tails, where a variety of liquid crystalline (smectic, nematic etc.) and long-range ordered (micellar, cubic, hexagonal, gyroidal) structures are observed at characteristic lengthscales of ~10nm. Ordered morphologies such as double-gyroid and aligned cylinder mesostructures may provide conduction pathways for ions – allowing ion motion even as fluidlike relaxation of the electrolyte is arrested. These ion-carrying pathways may promote superionic conduction. To my knowledge, there have not been any attempts to leverage a similar mechanism for the transport of larger ions than protons, but this could potentially provide an alternative mechanism for superionic transport in zwitterions by engineering larger lengthscale voids.

F.2 Packing Frustration and Intrinsic Free Volume

Packing frustration, especially the frustrated packing of rigid polymers can also promote decoupled transport by imparting free volume through which ions can opportunistically hop. This has already been well appreciated in membrane gas transport applications; work from the Freeman group⁹⁰ and others⁹¹ has shown that glassy polymers with very high fractional free volume exhibit exceptionally high permeabilities with selectivity determined by the chemical affinity of the polymer to the solute. In these materials, transport occurs through a static percolated network of free volume sites, enabling diffusion without the need for rearrangement of the membrane. Sokolov and coworkers have demonstrated that similar concepts apply in ion conducting polymers⁹². They have shown (**Figure 8A**) that the fragility (a measure of packing frustration defined as $fragility = \left[\frac{\partial \log \tau_{\alpha}}{\partial (T_g/T)} \right]_{T=T_g}$) inversely correlates with the coupling exponent ‘m’ (See section 1.4 for the definition of ‘m’). This relationship suggests that materials with greater extents of packing frustration may exhibit

significant decoupling of ion transport from the liquid relaxation of the electrolyte. This may be rationalized by considering the free volume of fragile polymers, where more fragile, packing frustrated chains are unable to efficiently pack, leaving significant unstructured free volume in the material. Although frustrated, fragile chains are typically less able to create free volume for ion motion via a relaxation mechanism, the static free volume in these systems can be sufficient to enable hopping-like transport of ions as illustrated in Figure 8B. While demonstrated ionic conductivities in these glassy systems are still modest, they have the potential for both high performance and less temperature-sensitivity than liquidlike electrolytes.

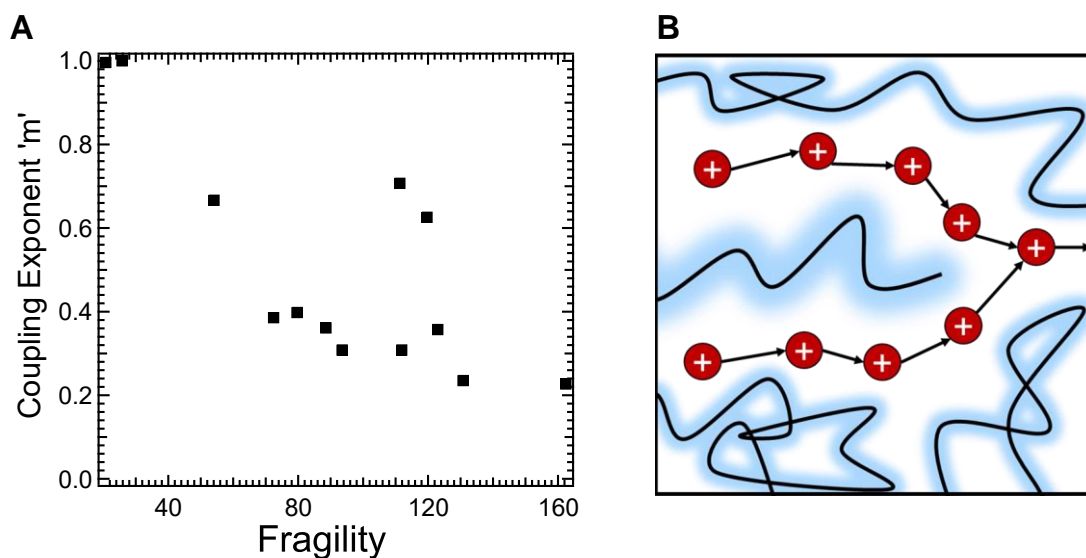


Figure 8: Polymer fragility correlates with the degree of decoupling.

A) Sokolov and coworkers studied a variety of SPE hosts and found a positive correlation between the decoupling exponent (m , where m is defined in Section 1.4 to be the slope of the Walden-plot curve) and polymer fragility. This suggests that more packing-frustrated materials display less coupling between conductivity and segmental motion. B) The free volume channels of an electrolyte provide a network of vacancies through which ions can opportunistically hop.

This perspective of motion through intrinsically porous or polymers is a promising means to impart superionic transport, however the limited solubility of dissociated ions in many packing-frustrated polymers can limit their potential application. For instance it has been shown that while semi-rigid styrene-derived polymer electrolytes have very high decoupling ($m \sim 0.67^{23}$), they do not demonstrate superionic conductivity under most conditions, due to poor salt solubility which reduces the effective ion concentration. Many such rigid polymer electrolytes indeed show evidence of decoupling, however this decoupling often only results in superionic transport when the ion concentration is renormalized by the extent of ion dissociation. Nonetheless, packing frustration presents an excellent opportunity to generate SPEs with high conductivity and rigidity, providing these solubility limitations can be overcome. Several authors report rigid SPEs that have attained conductivities suitable for applications based on this principle, demonstrating the potential promise of this approach⁹³⁻⁹⁶. Further, many design principles for these electrolytes are in parallel to materials used in gas transport such as polymers of intrinsic microporosity and metal-organic frameworks – the well-developed literature in these areas could be used to further inspire materials design in this area⁹⁷⁻⁹⁸.

F.3 Transport of Ions Through Nanostructured Channels

Although the liquidlike mechanism of conductivity requires dynamical creation of free volume elements to generate a pathway for ion transport and ordering is typically associated with reduced mobility within electrolytes, proper arrangement of ion solvation sites and free volume can lead to high ionic conductivity. In particular, the constrained nature of diffusion in channels, the highly correlated nature of charge transport, and the prevention of ion backflow in channels may all lead to improved performance in materials with nanoscale

structure. Furthermore, transport in constrained channels can lead to selectivity rules that are sensitive to ion size. This provides an opportunity to improve selectivity for alkali metal ions since these ions are typically smaller than their counterions.

Cocrystalline Structures of Salts and Ions

Although PEO conventionally displays its highest conductivity in the amorphous state, even this canonical electrolyte can display fast ion transport rates in a carefully engineered crystalline state. Reports by Bruce and coworkers^{28,99} indicate that systems comprised of low-molecular weight PEO and salts (LiXF_6 where $X = \text{P, As, Sb}$ or LiClO_4) can cocrystallize to generate well-defined ionic channels whereby the ether oxygens of PEO wrap around lithium ions in tubelike formations with the anions excluded from these channels. These structures are confirmed with x-ray crystallography of the polymer-salt complexes, finding that well defined Bragg reflections corresponding to the tubelike structure can be attained.

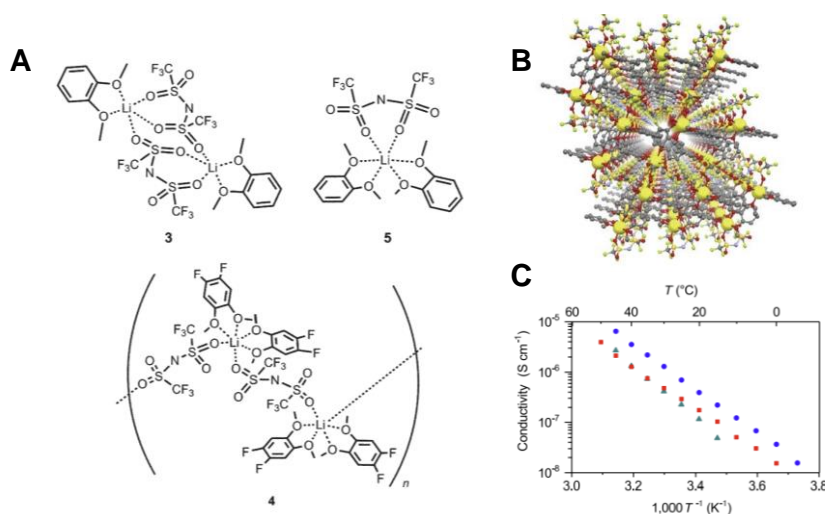


Figure 9: Crystalline complexes exhibiting superionic transport.

A) Complexes consisting of dimethoxybenzene compounds and Lithium bis(trifluoromethanesulfonyl)imide form lithium coordination environments. B) These complexes crystallize into solid materials with long range-order and high melting

temperatures. C)The crystalline form of these electrolytes promotes moderate ionic conductivities, despite the immobile nature of the frozen crystal structure. This behavior is representative of nearly complete decoupling of ionic transport and segmental motion.

Furthermore, they demonstrate appreciable ionic conductivity of these crystallites, despite the evident arrested segmental motion of the polymers. It is further shown that the ionic conductivity of this electrolyte even exceeds the conductivity of the equivalent amorphous-phase PEO – demonstrating the efficacy of this method to generate mechanically robust SPEs. A further advantage of these electrolytes is their excellent selectivity. Since the ion channels of the electrolyte effectively exclude anion motion, there is no free path for anion motion, resulting in excellent selectivity for lithium. Bruce and coworkers confirm this observation by NMR measurements, finding no evidence of anion mobility, corresponding to $t_+ = 1$.

Similar to this polymeric case, some reports indicate that crystalline complexes of salt and small organic molecules may also promote fast, selective transport of ions through crystallites¹⁰⁰. For example, complexes of lithium bis(trifluoromethanesulfonimide) with dimethoxy benzene groups¹⁰¹, boron-containing molecules with glyme side chains¹⁰², and diamines¹⁰³ crystallize to form compounds with lithium and its counterion included in the crystal structure of the resulting electrolyte (Figure 9A). These cocrystals display long-range transport pathways as illustrated in Figure 9B that conduct ions in the absence of segmental relaxation. These complexes have been shown to attain moderately high ionic conductivities $\sim 10^{-5}$ S/cm at 60°C despite being totally crystalline (Figure 9C).

2.4 Liquid Crystals and Liquid Crystalline Polymers

Liquid crystalline (LC) moieties offer an excellent opportunity to simultaneously promote order and high conductivity, due to the structured nature of the mesogenic units and

packing frustration from the rigid nature of these moieties. The simplest examples are nematic or smectic mesophases formed by rigid rod-like small molecules. However, solid-like bicontinuous cubic structures with high degrees of percolation for ion transport can be accessed through many design choices including lengths of alkyl linkers or tails, placement and strength of ionic or polar functionality, and selection of solvent or polymer environment^{87, 104}. For practical implementation in electrochemical devices, LCs exhibit the most useful nanostructures when they are imbedded in SPE systems. Here I focus on the ion conductive properties of polymers that are structured by small molecule LC additives and side chain liquid crystalline polymers.

Ionic interactions between LC additives and SPEs result in ionophilic channels capable of promoting ion conduction without relaxation of the polymer chain. In one manifestation, ionophilic head groups of LCs align near polymer backbones creating a 1-D layered structure that promotes conductivity when the layers are well aligned¹⁰⁵⁻¹⁰⁷. For example, Yang et al.¹ observed the formation of ionic nanochannels through complexation of biphenyl benzoate based pyridinium cationic stiff mesogens (Figure 10A inset) and the anionic functionalities of poly(styrene sulfonate) (Figure 10A). Evidence of a hopping mechanism through the nanochannels is obtained from both the relatively high conductivity of protons through the system at the polymer T_g (139°C) and the increase in conductivity when channels were aligned (Figure 10B). Interestingly these authors find that a change in the scaling of conductivity with temperature in the unaligned system occurs at ~190C, which is coincident with the observed transition from nematic (Cr) to smectic (S_A), further emphasizing the importance of the alignment of these channels.

This approach has primarily been applied to proton conductors; however, application to metal ion conduction has also been demonstrated. For example, mixtures of PEO with the LC salt Sodium Tetracyanoquinodimethane has been reported to have a sodium ion conductivity above 3 mS/cm at room temperature, much higher than PEO under the same conditions, even when prepared in the amorphous state. Similar to the protic cases, the conductivity of the film shows alignment-dependent conductivity, suggesting that the percolation of nanochannels plays a crucial role in ion transport performance. In another approach, polymeric LCs drive the nanostructural formation of ionic liquid crystalline grains leveraged between rigid-rod polyamide chains¹⁰⁸. This lyotropic LC assembly of the polyamide effectively templates the formation of a percolated nanocrystalline network. Lithium ions were shown to migrate via a hopping mechanism through defect structures in the alloy.

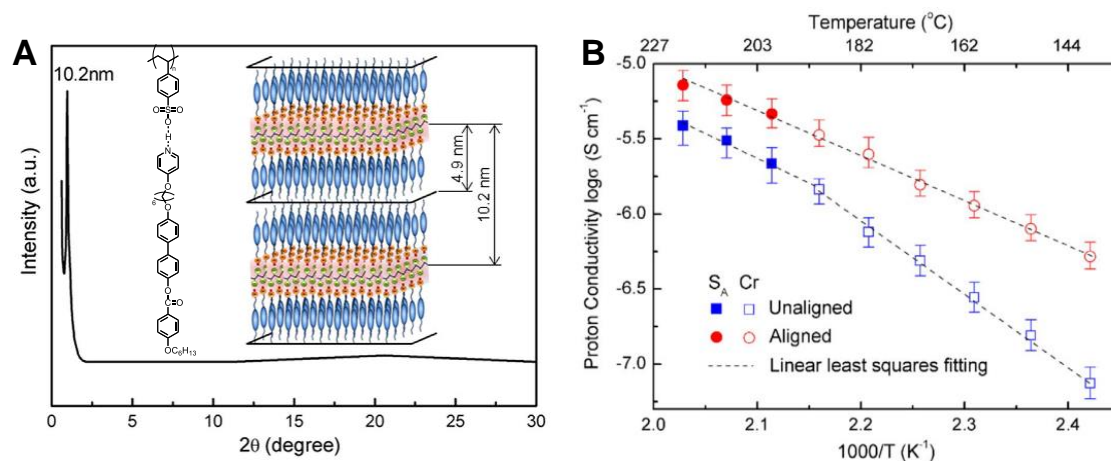


Figure 10: Superionic transport is attained in layered liquid crystal assemblies.

A) Structural analysis of a liquid crystal/polymer adduct indicates chain packing where the anionic liquid crystalline moieties preferentially pack near the polymer backbones to form layered sheets. B) The proton conductivity of this liquid crystal adduct shows alignment

dependence, suggesting the importance of a non-homogeneous transport mechanism. Adapted with permission from Yang et al.¹

Another approach is to utilize polymer-bound liquid-crystalline moieties to organize ionophilic domains capable of transporting ions. Wright and coworkers have studied polymers comprised of polyether backbone chains with regularly spaced alkyl side chains pendant to the backbone¹⁰⁹⁻¹¹¹. The alkyl sidechains of these materials can cocrystallize inter and intramolecularly with other side chains within the electrolyte, resulting in nonconductive alkyl crystallites with ethylene oxide chains located at the crystal periphery. Although these electrolytes are very rigid due to their high crystallinities, they exhibit high ionic conductivities up to 10^{-2} S/cm. Ion transport is hypothesized to occur through the 2-dimensional interface layers, rather than through the crystallites. The highly anisotropic conductivity (10^{-4} S/cm along ion channels and $<10^{-12}$ perpendicular to the channels) of the aligned electrolyte confirms this conductivity mechanism. A similar mechanism and approach was employed by McHattie et al.¹¹²⁻¹¹⁴ who studied polyethers with regularly spaced mesogenic groups which align in a similar fashion to the alkyl chains employed by Wright and coworkers. These materials also display highly anisotropic conduction that occurs at fast rates in spite of the frozen structure of the electrolyte, displaying no significant change in conductivity, below the T_g of the polymer. These authors hypothesize that the ion transport in these electrolyte is also highly selective, however I are not aware of any measurements of selectivity for these systems.

2.5 Pathways Created by Ionic Aggregation

While ionic aggregation of the mobile cations is deleterious to conduction, ionic aggregation of the charged components of the SPE can lead to nanostructured channels that conduct ions without relaxation of the bulk material.–The mechanism of ion transport

depends strongly on the morphology and percolated nature of the aggregates which are in turn impacted by factors such as polymer architecture, ion diameters, and polymer and ion chemistries. Molecular dynamics simulations suggest that extended string-like aggregates that percolate through the material¹¹⁵⁻¹¹⁹ may eliminate the need for ions to hop between ion clusters and instead promote high conductivity if the clusters present a locally fluid-like environment for ion movement. Partial decoupling of ion transport from the segmental dynamics of the nonpolar domains of the SPE is possible under these conditions.

This mechanism of intra-aggregate transport has led to concerted efforts to generate percolated aggregate shapes and higher ionic conductivities. One strategy to generate percolated structures has focused on the nature of the ion attachment. It has been shown that ‘ionenes’ (polymers with the ion included in the backbone rather than being tethered to it) display faster Tg-normalized ion transport than their ionomer counterparts¹²⁰⁻¹²¹. Studies have also demonstrated that these ionenes result in more percolated ionic structures¹¹⁶. Ion aggregation is also intimately tied to the dielectric constant of the electrolyte; however, joint experimental-simulation studies have shown that the dielectric constant, while impacting the extent of ion aggregation, has a limited impact on the rate of ion transport as long as the aggregates are percolated through the electrolyte¹⁶.

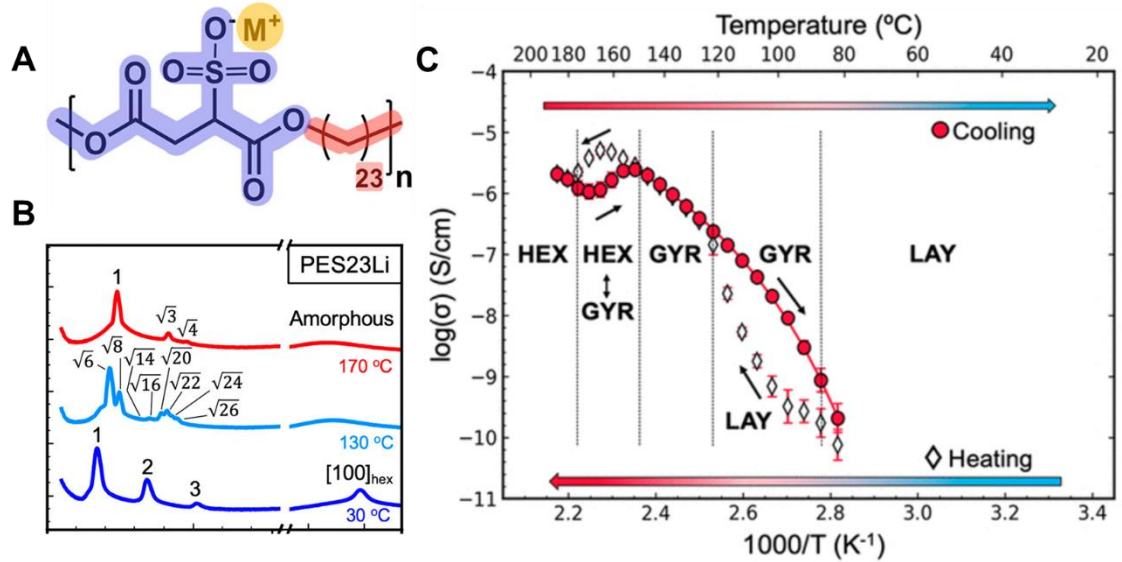


Figure 11: Layered structures studied by Winey show superionic transport.

A) Winey and coworkers used condensation polymerization to prepare materials with precise spacing between ionic groups. B) Small Angle Xray scattering experiments reveal the presence of layered, gyroidal and hexagonally close-packed morphologies. The wide-angle experiments show crystallinity of the polyethylene chains at low temperature. C) The ionic conductivity was measured at on a heating cooling cycle of this electrolyte. The ionic conductivity increases significantly during the transition between layered structures and gyroidal structures. At higher temperatures, the transition between gyroid and hexagonally close packed cylinders results in a reduction in the ionic conductivity. The same trend is seen upon cooling.

Tuning the structure of aggregates to generate highly percolated structures greatly enhances the degree of decoupled transport in these electrolytes. SPEs consisting of ionic groups separated by a nonpolar alkyl chain (Figure 11A)¹²²⁻¹²⁵ have been studied by Winey and coworkers. The combination of high polarity contrast and the regular ion spacing of these materials results in ordered packings of ionic domains that can conduct free ions. Winey and coworkers have demonstrated a variety of morphologies, including layered, hexagonal, and gyroid structures (Figure 11B). They found that these materials exhibit

morphology-dependent ionic conductivity trends (Figure 11C), consistent with the described mechanism whereby ionic conductivity depends on the connectivity of the ion-transporting channels. Similarly, Abbott and coworkers demonstrated with molecular dynamics simulations that well-defined side-chain polymers could self-assemble into precise ionic layer structures¹²⁶. Their results were experimentally validated in collaboration with McCloskey and coworkers who generated PAGE-based materials with well-defined ionic layer structures¹²⁷. Although these aggregates are structurally percolated, they do not display intra-aggregate ion transport due to the rigid nature of the ionic aggregates in the system.

The ion aggregates formed in such systems can be locally fluid, amorphous solid, or crystalline. In most systems demonstrating high ionic conductivity, the aggregates are fluid-like. However, conceptually it is possible for a SPE to support high conductivity if the ion aggregates are amorphous solids or crystals with sufficient free volume, vacancies, or interstitial sites to enable rapid ion motion. The nature of the aggregates can also be influenced by the addition of plasticizing molecules or polymers that retain the shape of the aggregate while enabling faster fluid-like transport. For instance Paren et al.¹²⁸ recently reported on styrene-based lithium single-ion conductors that strongly aggregate. Although the aggregates in this system are expected to structurally percolate, the transport through the ion channels in the absence of plasticizer is slow due to strong ion-polymer interactions and collapsed ion channels, however the addition of plasticizing, low molecular weight PEO broadens the ion channels and allows for greater ion dissociation. In this case the plasticizer acts to change the transport rate through the ion channels while minimally perturbing their structure. Similarly, the transport through ion channels in layered electrolytes consisting of a PEO backbone with alkyl side-chains could be improved by greater than two orders of

magnitude when blended with polar polymers¹²⁹⁻¹³⁰ or plasticizers¹³¹, which effectively swelled the ionic channels and increased their fluidity. This suggests that effective design of ion channels must effectively consider the connectivity of channels as well as the mobility in these channels, which relates to their size as well as the energy barrier for activated transport within these channels.

II. The Role of Polymer-Ion Interaction Strength on the Viscoelasticity and Conductivity of Solvent-Free Polymer Electrolytes

A. Abstract

Metal-ligand coordinating polymers utilize labile bonds between polymer-bound ligands and free cations to delocalize and conduct mono- and multi-valent metal ions in the solid state. These interactions simultaneously act as reversible cross-links, leading to delayed terminal relaxation as measured by oscillatory rheology. Well-controlled poly(methyl acrylate)s with imidazole chain ends are synthesized as model polymers to obtain metal-ligand bond lifetimes and to investigate design rules for solid polymer electrolytes. Through changes in identity of the metal species, metal-ligand bond lifetimes are varied over nearly two orders of magnitude. Scaling analysis demonstrates a correlation between bond lifetime and the ionic conductivity, suggesting a hierarchical conduction mechanism that involves an interplay of polymer segmental motion with the dissociation of metal-ligand bonds. This suggests an alternative means to enhance long-range ionic transport that is partially decoupled from efforts to enhance the segmental mobility of ionically conducting polymers.

B. Introduction

Synthetic polymers derive much of their mechanical properties from their mesoscale structure, chain topology, and monomer-monomer interactions. In most synthetic polymers, interactions among monomers are characterized by harsh short-ranged repulsions, such as

excluded volume interactions, and weak short-ranged attractions arising from dispersive interactions or polar moieties. However, polymers with strong and specific monomer-monomer associations such as hydrogen bonding⁷⁵⁻⁷⁷, metal-ligand coordination⁷⁸⁻⁸⁰, ionic forces⁸¹⁻⁸², or dynamic covalent chemistries⁸³⁻⁸⁴ display a rich array of network topologies and rheological features that have yet to be fully explored⁸⁵⁻⁸⁷. These so-called ‘associating polymers (APs)’ have attracted interest in both fundamental and applied contexts, where they have been considered as elastomers⁸⁴, delivery vehicles⁸⁸, and ion conductors⁸⁰.

Polymer electrolytes are distinguished by their high ionic concentrations and polymer-bound functionalities that assist in ionic solvation. The introduction of ions into polymeric materials often intrinsically causes AP behavior due to multifunctional interactions between polymer-bound solvating functionalities and ions. In poly(ethylene oxide) and related polyether-based materials, the ether oxygen coordinates with incorporated metal ions⁸⁹, leading to reduced segmental mobility especially in the presence of multivalent ions⁹⁰. A very different class of polymers, ionomers, display AP behavior driven by the mesoscale segregation of ionic and polar groups into dense clusters that dominate their viscoelastic and conductive properties⁹¹⁻⁹⁴. Though ionomers and polyether-based materials differ greatly in ion transport, both classes of materials display hindered chain relaxations due to ion-polymer interactions. Despite the salient influence of ion-polymer interactions on the dynamics of these materials, their impact on long-range ionic transport is not fully understood.

Ion transport in amorphous polymers is traditionally viewed as having a liquid-like mechanism whereby the friction exerted on an ion in a polymer electrolyte is dictated by the rate of polymer segmental relaxation (τ_α). This mechanism has been validated across many

polymer systems with techniques including rheology²⁰, dielectric spectroscopy²², and quasi-elastic neutron scattering²⁸. Although this mechanism of conductivity appears to apply within specific systems, it is clear from analysis across a wide range of literature that this liquidlike mechanism is an insufficient predictor of ionic conductivity⁹⁵⁻⁹⁶. The failure of this liquidlike mechanism to explain results from a diverse set of materials may be due in part to the insensitivity of this mechanism to ion-polymer interactions.

Herein I demonstrate that rheologically-determined ion-polymer association lifetimes dictate long-range ionic transport in polymers with specific ion-polymer associations. A model telechelic polymer doped with a series of mono-, di-, and trivalent metal bis(trifluorosulfonyl) imide (MTFSI) salts exhibits metal ligand (M-L) bond lifetimes varying over nearly two orders of magnitude, allowing a range of ion-polymer association energies to be studied within a single polymer system. These changes in M-L bond lifetime collapse temperature-dependent ionic conductivity measurements, suggesting a hierarchical conductivity mechanism in which ions dissociate from their local constraints before undergoing long-range diffusion. I anticipate that these findings will be generalizable across polymer electrolytes with specific interactions between polymer-bound chemical motifs and mobile ions. This mechanism motivates work to enhance the lability of metal-ligand bonds, offering a route to improve the ionic conductivity of polymer electrolytes that is partially decoupled from efforts to accelerate polymer segmental dynamics.

C. Experimental

Chemicals:

All chemicals were purchased from Sigma Aldrich unless otherwise specified. All salts were purchased from Alpha Aesar and were opened and stored in a nitrogen-containing

glovebox. Salts previously tested to monitor water uptake in this environment were found to have minimal uptake over a period of weeks as described in Schauser et al.⁸⁰

Preparation of Ethylene bis(2-bromoisobutyrate) (Eb2BiB):

An oven-dried round bottom flask was charged with ethylene glycol (5.6 mL, 100mmol), triethyl amine (24.3 mL 250mmol), dichloromethane (200mL), and a teflon-coated stir bar. The vessel was sealed with a rubber septum and purged with nitrogen. α -Bromoisobutyryl bromide (30 mL, 243 mmol) was added dropwise to the flask under high stirring speeds at 0°C. The reactor was allowed to reach room temperature and left to stir for 36 hours. During reaction, triethylamine hydrobromide precipitated from solution as a white solid and was removed via filtration. The filtrate was concentrated in vacuo and the resulting powder was washed with deionized water to remove any remaining triethylamine salts. This solid was recrystallized in ethanol and dried in vacuo before use, resulting in a white crystalline product. ¹H NMR (600 MHz, CDCl₃, δ): 1.93 (s, 12H, -CH₃), 4.42 (s, 4H, -O-CH₂-CH₂-O-). ¹³C NMR (600MHz, CDCl₃, δ): 171.38 (s, O-C(=O)-), 63.16 (s, -O-CH₂-CH₂-O-), 55.31 (s, -C-(CH₃)₂-Br), 30.67 (m, -CH₃).

Polymerization of bromine terminated telechelic polymer:

The synthesis and chain end modification strategies used in this study were adapted from Anastasaki et al.⁹⁷ Methyl acrylate (MA) monomer was purified by passing it through a column of basic alumina immediately before polymerization. A dried 100mL round bottom flask was charged with 15g of purified methyl acrylate, 1 gram of Eb2BiB, 27 mg of copper(II) bromide, 168 mg of tris[2-(dimethylamino)ethyl]amine, 30 mL of dimethyl sulfoxide (DMSO), and a teflon-coated stir bar. The reaction vessel was sealed with a rubber septum and sparged with nitrogen gas. During the sparging process, the solution in the flask

turned a pale green color due to formation of the copper-tris[2-(dimethylamino)ethyl]amine catalyst complex. After sparging, the reactor was placed in a pre-heated oil bath thermostated at 70°C.

Aliquots of the reaction mixture were taken periodically and monitored via ^1H NMR. After five hours, the reaction progress reached 95% and the reaction was terminated by cooling the solution in an ice bath and eventually exposing the reaction vessel to air. Copper and DMSO residues were removed from the reaction mixture by extraction into the aqueous phase of a 50 v/v% water and ethyl acetate mixture. The organic layer was washed five times with water until the extract contained no visually detectable copper residues and dried first over magnesium sulfate and subsequently in vacuo. This polymer was characterized via size exclusion chromatography (SEC) and ^1H NMR, for details see SI Sections 1 and 2.

Polymerization of monofunctional precursor polymer:

The monofunctional prepolymer was prepared and purified in the same manner as the telechelic material, except that the polymerization was initiated from Ethyl 2-bromo-2-methylpropanoate purchased from Sigma Aldrich. This initiator was recrystallized in anhydrous ethanol before use.

Synthesis of N-(2-(1H-Imidazol-1-yl)propyl)-4-mercaptobutanamide (Im-SH):

Im-SH was synthesized according to previous reports⁸⁰. The thiol was dried in vacuo and stored in a nitrogen-purged desiccator until use. ^1H NMR (600 MHz, DMSO d_6 , δ): 1.77 (dp, $J=30.0$, 7.1 Hz, 4H), 2.16 (t, $J=7.4$ Hz, 2H), 2.44 (t, $J=7.1$ Hz, 2H), 2.98 (q, $J=6.5$ Hz, 2H), 3.93 (t, $J=6.9$ Hz, 2H), 6.86 (s, 1H), 7.14 (s, 1H), 7.59 (s, 1H).

Functionalization of MA:

To prepare the thiolate Im-S⁻, the 4.36 g of dried Im-SH was added to a round bottom flask along with 20mL of dry THF and 2.67 mL of triethylamine. This was stirred for one hour without purging. In a separate round bottom flask, 14 grams of bromine-terminated poly(methyl acrylate) was dissolved in 30mL of THF. The thiolate solution was added dropwise to the polymer solution under rapid stirring. After complete addition of the thiolate mixture, the reactor was sealed and allowed to stir for two days at room temperature.

After two days of stirring, a white solid precipitate of triethylamine hydrobromide salt had formed. This solid was removed via filtration and washed with additional THF to remove any entrained product. The filtrate was concentrated via rotary evaporation and precipitated three times into a solution containing 80/20 v/v% water and methanol, each time redissolving the solid in THF. Polymer was dried under vacuum at 50°C for 48 hours in the presence of phosphorous pentoxide and immediately transferred to a nitrogen-containing glovebox to prevent water reuptake. This product was characterized via NMR and SEC, no traces of unreacted thiol or triethylamine salts were detectable on the final NMR. This same procedure was followed for the functionalization of the monofunctional precursor and the ratio of Im-Sh to bromine chain end was kept constant.

Molecular Characterization:

¹H NMR and ¹³C NMR spectra were collected on a Varian VNMRS 600 MHz instrument using chloroform or DMSO-d₆ as the solvent. Polymer molecular weight was determined via ¹H NMR end-group analysis as described in SI section 1. Size Exclusion Chromatography was performed on a Waters instrument using a refractive index detector and Agilent PL gel 5 μm MiniMIX-D column. THF at 35°C was used as the mobile phase

with a flow rate of 1.0 mL/min. Polydispersity was determined against narrow polystyrene standards (Agilent).

Ion Incorporation:

In a glovebox, a stock solution of salt was made by dissolving salt in anhydrous methanol. A micropipette was used to add the correct amount of stock solution to polymer to achieve desired salt/polymer ratios. If necessary, additional anhydrous chloroform was added to the polymer/salt solution to fully dissolve all polymer. The polymer/salt solution was removed from the glovebox and vortexed to fully homogenize the mixture. The solution was flash frozen at liquid nitrogen temperatures and the residual solvent was removed in vacuo. The polymer/salt solution was dried in a vacuum oven at $\sim 10^{-3}$ torr for >72 hours at 40°C to yield a solid material. These materials were subsequently transferred to an ultra-high vacuum system and dried for >24 hours at $< 10^{-8}$ torr and directly transferred into a nitrogen-containing glovebox.

X-ray Scattering:

Samples were placed on a Kapton film suspended across a stainless steel washer and were dried and annealed in an inert atmosphere at 80 °C. These samples were transferred to a glovebox where they were sealed under nitrogen. Measurements were conducted at the Advanced Light Source (ALS, beamline 7.3.3, Lawrence Berkeley National Laboratory) with X-ray energy 10 keV and at the National Synchrotron Light Source II (NSLS-II, beamline 11-BM, Brookhaven National Laboratory) with an X-ray energy of 13.5 keV. Measurements were taken at two detector distances. The sample to detector distance was calibrated via a silver behenate standard.

Rheology:

The rheology of samples was characterized using an TA Instruments AR-G2 rheometer using 8mm parallel plates. Samples were prepared with thicknesses ranging between 500-700 μm . Strain sweeps were conducted at the lowest operating temperature to confirm that measurements were taken in the linear viscoelastic regime. Frequency sweeps were conducted at various temperatures ranging between -5-75 $^{\circ}\text{C}$. After each temperature change, an oscillatory time sweep at a frequency of 10 rads/s was performed for at least 150s. The next temperature was measured only once this time sweep reached stable values for G' and G'' . Time-temperature superposition was performed with shifting in frequency only.

Ionic Conductivity Measurements:

Electrical impedance spectroscopy (EIS) measurements were performed on polymer samples between indium tin oxide (ITO) blocking electrodes. The thickness of the ITO electrodes on glass slides was measured via a micrometer prior to cleaning. ITO electrodes were cleaned via subsequent 5 minute sonications in detergent water, deionized water, acetone, and isopropanol followed by UV/ozone treatment. Double-sided Kapton tape with a hole defining the electrode area was adhered to the ITO side of one electrode. In a nitrogen glovebox, polymer-salt mixtures heated to 80 $^{\circ}\text{C}$ were coated onto the electrode in the area defined by the Kapton spacer. The second electrode was pressed down to form a sandwich containing polymer evenly coating the punched area. The thickness of the sandwich was measured via a micrometer to determine the final sample thickness, thicknesses ranged between 150 to 200 μm . EIS measurements were performed using a Biologic SP-200 potentiostat in a nitrogen glovebox. A sinusoidal voltage with a magnitude of 100mV was applied to the electrodes over a frequency range from 1 MHz to 10mHz at temperatures

ranging from 30 to 90 °C. The conductivity was calculated from the real component of conductivity at the maximum in $\tan(\delta)$ or an apparent plateau in the real conductivity at low temperatures where a maximum in $\tan(\delta)$ could not be resolved.

Differential Scanning Calorimetry:

Differential scanning calorimetry (DSC) measurements were performed on a TA Instruments Q2000 DSC. Around 8 mg of each polymer sample was weighed and loaded into aluminum ‘Tzero’ hermetic pans. All samples were heated to 150° on an initial heating cycle and cooled to -80°C. Glass transition measurements were recorded on the second heating cycle at a ramp rate of 20°C/minute. The glass transition temperature was analyzed via the midpoint analysis method of the calorimetric curve.

D. Results and Discussion

Conventional design rules for polymer electrolytes dictate that ion dissociation is controlled by bulk dielectric properties and the mobility of ions is regulated by the segmental relaxation timescale. However, “sticky Rouse” theories demonstrate that the association of stickers and their bulk motion through a sticky network is closely related to the energies/timescales of sticker dissociation⁹⁸. Evidence from prior studies of metal-ligand coordinating polymers indicate that conventional notions about the solvation and transport of metal salts through networks based on metal-ligand coordination do not hold. Specifically, the T_g -normalized ionic conductivity of metal-ligand polymers with highly variable dielectric constants is relatively constant across widely varying dielectric environments¹⁵, but changes dramatically when the identity of the ligand is slightly altered⁹⁶. These results indicate that ion solvation and dissociation are largely controlled by the

identity of the ligand functionality and suggest that dynamic network theories may better explain ion motion in these materials.

Dynamic networks with polymer-bound ligands comprise an ideal model system to examine the impact of ion-polymer association lifetimes on the bulk rheological and transport properties through disordered polymer electrolytes. Metal-imidazole bond chemistries are chosen due to their relative lability at application-relevant temperatures and their generalizability across a variety of metal species⁹⁹. The strength of the interaction is varied in this study by altering the identity of the metal ion, which is known from small-molecule studies to change the timescale and energies of metal-ligand association,¹⁰⁰ and from bulk studies of imidazole-containing polymeric materials, which exhibit nearly a thousand-fold variation in their zero-shear viscosity through metal-identity variation¹⁰¹. Telechelic, unentangled materials with imidazole ligands at their chain ends are selected to simplify analysis of rheological data. Poly(methyl acrylate) is selected as the backbone as prior studies have demonstrated that the ‘methyl-ester’ functionality does not compete with imidazole for transition metal coordination¹⁰² and for its moderate glass transition temperature.

The synthesis of telechelic polymers leveraged the reactivity of the halide chain ends obtained in atom-transfer radical polymerization (ATRP) to generate quantitatively end-functionalized polymers (Figure 12). Polymerization of methyl acrylate (MA) by a mono- or bi-functional bromoisobutyryl bromide initiator were catalyzed with copper(II) bromide, with Me₆tren as the ligand, ensuring high fidelities of the bromide chain end, even at high (>90%) conversions of MA. Purified polymers were modified to incorporate ligands via the reaction of bromide chain ends with an imidazole-containing thiol⁹⁷. Finally, the polymers

were doped with $M^{Z+}(\text{TFSI})_z$ salts via solution casting. A summary of the prepared polymers is given in Table 1, where ‘f’ indicates the number of imidazoles per chain of each material. Molecular masses are maintained roughly constant between polymers and were chosen to be nearly half the entanglement molar mass of this material¹⁰³. Polydispersities are typical of well-controlled radical polymerization techniques. Details of molecular characterization, including NMR, SEC, and X-ray scattering are provided in the section F. Metal salts were introduced at an equimolar ratio of metal cation to imidazole functionality, a concentration that was found to fall below the solubility limit of the salts within the polymer matrix, yet sufficiently high to produce transient gelation effects.

Table 1: ^aDetermined via analysis of initiator group protons to backbone protons. ^bDetermined via SEC using tetrahydrofuran (THF) as the eluent at 35°C. Deviation from NMR-determined molar masses are expected since no absolute molecular weight calibration was used.

Polymer Identity	$M_{n, \text{NMR}}^a$ [kg/mol]	$M_{n, \text{SEC}}^b$ [kg/mol]	\mathcal{D}^b
PMA f=0	4.5	5.6	1.13
PMA f=1	4.6	5.8	1.11
PMA f=2	4.8	5.9	1.14

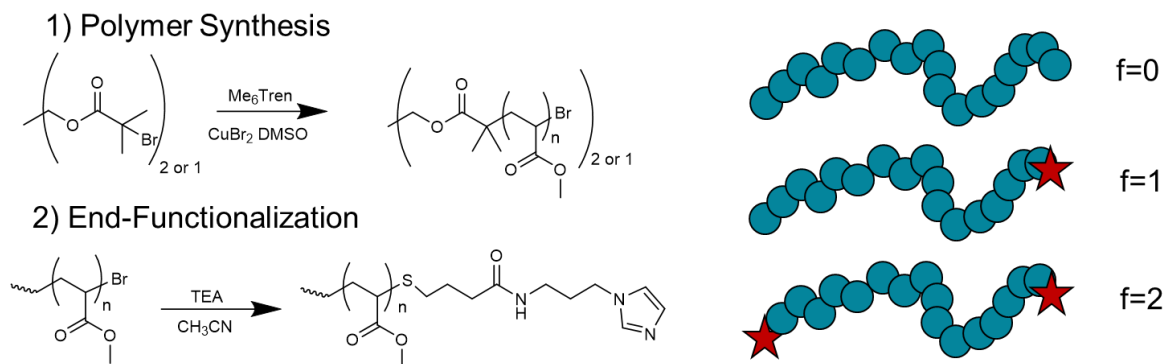


Figure 12: End functionalized polymers made by ATRP.

Polymers are synthesized via ATRP to generate materials with functionalizable alkyl-halide chain ends, which are further reacted under basic conditions to generate chain-end functionalized materials. Polymers with imidazoles on zero, one, and two chain ends were synthesized in this way.

Metal-ligand coordination has a dramatic impact on the bulk mechanical properties of these transient networks demonstrated by shifts of terminal relaxation towards lower frequencies as metals are doped into the polymer network. Figure 13 compares the storage ($G'(\omega)$) and loss ($G''(\omega)$) moduli of telechelic polymers as a function of salt identity at an equimolar ratio of cations to imidazole ligands. These master curves are shown at an isofrictional reference temperature ($T_{\text{iso}}=T-T_g$) of $T_{\text{iso}}=20^\circ\text{C}$, where the T_g was determined calorimetrically (F.8). Though the principles of time-temperature superposition (TTS) may not be rigorously satisfied, TTS analysis provides an approximation of the mechanical behavior of the system and can be used to approximate relaxation timescales over an otherwise inaccessible broad frequency range, even for thermo-rheologically complex materials⁷⁵. The solid lines in Figure 13 are model fits to an ‘elastic dumbbell’ model described in F.4 Rheology Fitting¹⁰⁴. All samples display the same three characteristic rheological behaviors. At high frequencies, materials display characteristic glassy behavior

with a modulus in the gigapascal range, a plateau in the storage modulus, and a broad peak in the loss modulus. At moderate frequencies, the polymer undergoes glass transition and displays Rouse-like behavior characterized by a drop in both storage and loss moduli into the megapascal regime. At low effective frequencies, the polymer undergoes terminal relaxation with the scalings predicted by the Maxwell model, $G' \sim \omega^2$ and $G'' \sim \omega^1$.

The presence of 'sticky' modes indicates a dynamic percolating network comprised of telechelic chains bound together by intermolecular metal ligand bonds. These modes are evident from the delay in terminal relaxation upon addition of metal salts to the network (a downturn in modulus that occurs at lower effective frequencies). The lifetime of these sticker bonds (τ_s) varies over nearly two orders of magnitude across this series as can be observed both from the clear changes in terminal relaxation of the curves and from the corresponding fitting parameters (Table 2). Though other authors have observed that simultaneous fitting of Rouse and Sticky Rouse modes can lead to arbitrary parameter values⁹¹, this is not the case in these telechelic materials since Rouse and Sticky Rouse modes are decoupled (F.4) and because the salt free material provides a basis to estimate Rouse parameters in the absence of Sticky Rouse modes. Indeed, this can be observed from the relative consistency of the longest Rouse time (τ_0) compared to the sticky Rouse time (τ_s), which varies over nearly two orders of magnitude across this series of salts.

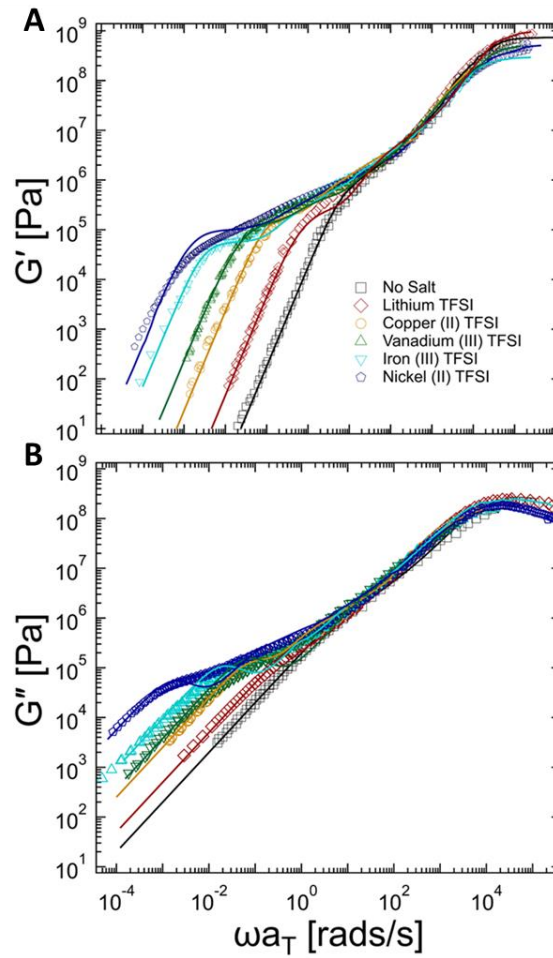


Figure 13: Rheology curves of telechelic polymers.

Apparent master curves for telechelic polymers with various salts at an isofrictional reference temperature of $T_{iso}=20$ °C. Solid lines indicate fits to the sticky dumbbell model described in F.4.

Table 2: Fitting parameters for relaxation times used to generate fits in Figure 13.

Additional fitting parameters can be found in F.4 Rheology Fitting.

	No Salt	Lithium	Copper	Vanadium	Iron	Nickel
τ_g [s]	$3.66 \cdot 10^{-5}$	$2.69 \cdot 10^{-5}$	$8.41 \cdot 10^{-5}$	$7.06 \cdot 10^{-5}$	$3.02 \cdot 10^{-5}$	$1.76 \cdot 10^{-5}$
τ_0 [s]	$9.52 \cdot 10^{-4}$	$7.11 \cdot 10^{-4}$	$4.50 \cdot 10^{-4}$	$8.53 \cdot 10^{-4}$	$8.28 \cdot 10^{-4}$	$3.85 \cdot 10^{-3}$
τ_s [s]	-	3.81	12.3	17.5	67.1	347

At elevated temperatures, the longer-lived process of metal-ligand bond dissociation dominates the dynamics of the transient network as polymeric relaxations such as Rouse modes and segmental reorganization occur quickly under these conditions. Consequently, analysis of shift factors (Figure 14) reveals a transition from Williams-Landau-Ferry (WLF) temperature dependence to an Arrhenius dependence at $\sim 40^\circ\text{C}$, suggesting a transition from a process dominated by segmental rearrangement to an activated dissociation process¹⁰⁵. The salt-free polymer appears to agree with the WLF relation for PMA (dotted line) throughout the tested temperature regime, however all salt containing materials diverge at slopes steeper than the salt free material and dependent upon the cation identity. Arrhenius fits to these deviations can be used to compute apparent activation energies for sticky bond dissociation ($E_{a,app}$) seen in Table 3. These sticky dissociation energies are anticipated to be overestimates of the true dissociation energies since the slope in this region also includes contributions from the segmental relaxation process. The activation energy for sticker dissociation ($E_{a,st}$) can be obtained by subtracting an estimate for the segmental activation energy ($E_{a,\alpha}$) from the apparent activation energy ($E_{a,app}$)⁹². The Arrhenius energies from shift factors can be compared to the estimated energy for crosslink dissociation by applying

the relation $\tau_s(T) = \tau_0(T) \exp\left(\frac{E_{ast}}{k_b T}\right)$ ⁹⁸. The activation energy is calculated at the region where dynamics appear to shift from WLF-controlled to Arrhenius-controlled (25C) and the anticipated contribution from glassy dynamics are subtracted as described in F.6. Although there is some disagreement in the methods indicated by overestimation of the activation energies from shift factor analysis there is apparent agreement in both the trend and values of activation energies calculated by both methods (Table 3). Activation energies of crosslink dissociation reactions varying from ~15-40 kJ/mol depending upon the metal identity are consistent with expectations from small-molecule characterization of M-L stabilities¹⁰⁶. The trend in M-L bond energies ($\text{Li}^+ < \text{Cu}^{2+} < \text{V}^{3+} < \text{Fe}^{3+} < \text{Ni}^{2+}$) is consistent with prior studies of metal-ligand bonding in a soft matter environment, which shows a slightly different trend than the dissociation kinetics of metal-imidazole complexes in aqueous solution¹⁰¹⁻¹⁰². This is unsurprising as M-L bond dissociation in an aqueous environment occurs via a solvent-assisted pathway¹⁰⁷⁻¹⁰⁸. The discrepancies between the values of the activation energies calculated in both ways may be the result of the failure of TTS to fully account for the viscoelasticity over a broad range of temperatures.

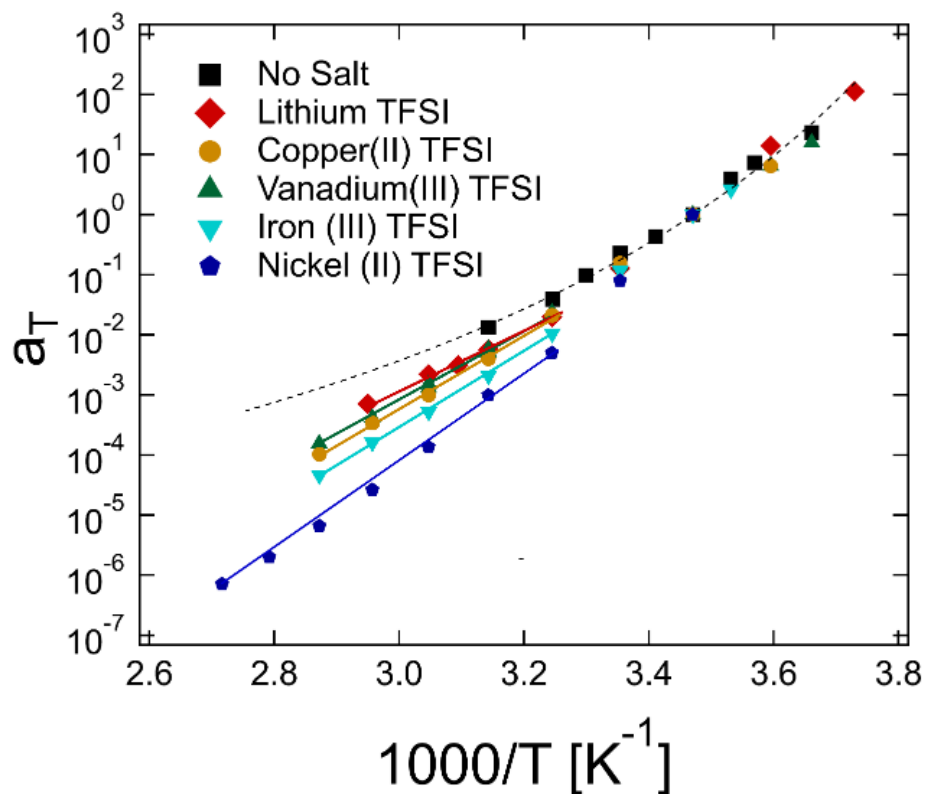


Figure 14: Rheological shift factors as a function of inverse temperature.

Horizontal shift factors (a_T 's) are plotted against temperature. The dotted line indicates a WLF correlation for low molecular weight PMA extracted from the literature¹⁰³. Colored solid lines indicate Arrhenius fits to the data points divergent from the literature trend. Arrhenius slopes are summarized in Table 3.

Table 3: Activation Energies

Sample	From Fitting		From Shift Factors	
	τ_s^a	$E_{a,st}$	$E_{a,app}^c$	$E_{a,st}^d$
Lithium	3.8	15.7	104	16.9
Copper	12.2	18.8	110	23.2
Vanadium	31.4	21.2	111	23.9
Iron	67.3	23.3	120	33.5
Nickel	348	27.7	125	37.9

^aDetermined via best fit of viscoelastic data at reference $T_{iso}=20^\circ\text{C}$ ^bDetermined from the relation $\tau_s(T) = \tau_0(T) \exp\left(-\frac{E_a}{k_b T}\right)$ ^cFrom fitting high-temperature ($T>45^\circ\text{C}$) regime of shift factor curves to the Arrhenius equation $E_a=E_{a,app}-E_{a,\alpha}$ with $E_{a,\alpha}=87$ kJ/mol

Though the experiments above demonstrate salient ‘sticky’ modes that are strongly ion-identity dependent, control experiments are required to demonstrate that these ‘sticky’ modes are the result of ion-ligand interactions. Two clear alternative possibilities exist: 1) that the ‘sticky’ modes are the result of crosslinking interactions between PMA monomers instead of exclusively between chain ends, and 2) that the measured relaxation is actually the relaxation of ionic clusters, rather than individual coordination events. I have addressed the first possibility through control experiments involving polymers with fewer than 2 imidazole moieties per chain in the presence of the same concentration of crosslinking salt (F.5). Viscoelastic measurements of these materials demonstrate that ‘sticky’ viscoelastic modes

occur only in the presence of the telechelic material, suggesting that ion-backbone interactions are not responsible for the observed ‘sticky modes.’ The presence of ionic clusters is probed via small and wide angle x-ray scattering (F.3) which do not feature the characteristic ‘ionomer peak’ that seems to be universally characteristic of ionically clustered materials, suggesting that large ionic aggregates are not a prominent feature of these materials¹⁰⁹. In aggregate, these results suggest that viscoelastic measurements probe the metal-ligand association lifetime rather than other viscoelastic contributions.

The polymeric relaxation processes characterized via rheology are anticipated to dictate the net ionic motion through the polymer electrolyte. Ionic conductivities of the polymer samples were measured as a function of temperature via electrochemical impedance spectroscopy (Figure 15A), which probes the collective ionic conductivity including contributions from both the cation and anion. Since the ionic conductivity contributions from the salt-free polymer are measured to be less than 10^{-11} S/cm at 90 °C and are undetectable at lower temperatures (F.7 Electrochemical Impedance Spectroscopy Sample Spectra), the ionic conductivity of all salt-containing materials is attributed to be wholly to the motion of ions from the added salts. The data in Figure 15A demonstrates that ionic conductivity is both temperature and ion-identity dependent.

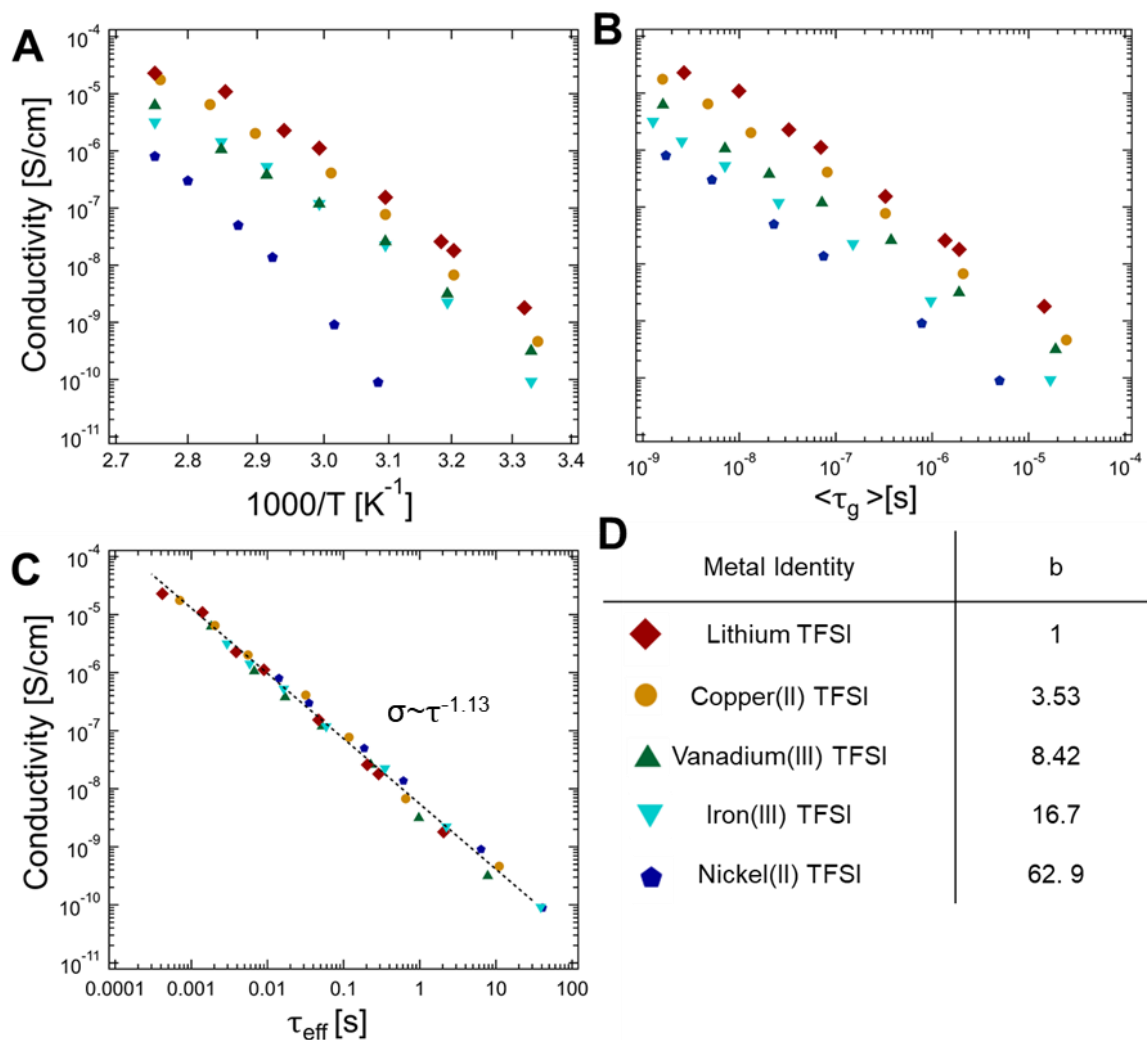


Figure 15: Conductivity analysis of telechelic polymers

A) The ionic conductivity of salt containing telechelics as a function of temperature and ion identity. The salt-free polymer is not included since no detectable ionic conductivity features could be resolved for this material. B) The ionic conductivity scaled against the effective mean glass transition time as determined from TTS of rheology data C) The ionic conductivity collapses into a master curve when shifted by the effective time as defined by Equation 8. The dashed line indicates a power-law correlation which has been applied to all data. D) The parameters required to collapse the ionic conductivity in frame (C).

The prevailing view of polymer electrolytes above their glass transition temperatures treats them as a uniform frictional environment for mobile ionic species²², a viewpoint

seemingly incongruent with the presence of specific interactions between ions and polymers. This perspective is the basis for the ‘polymeric Walden rule’, which posits that the product of molar conductivity and the segmental relaxation timescale (τ_g) of a fluid results in a temperature-independent constant. This perspective is evaluated in Figure 15B, which uses time-temperature superposition shift factors to plot ionic conductivity against the average glassy timescale, $\langle\tau_g\rangle$ ($\langle\tau_g\rangle \sim \tau_a$) (Figure 14). Evidently the Walden relation seems to linearize the ionic conductivity behavior for all metal species, suggesting that a common dynamic process is dictating the mechanics and conduction of these materials. However, the failure to collapse suggests, contrary to conventional design principles, that the segmental relaxation does not universally dictate the ionic conductivity behavior in these systems.

Since the segmental relaxation process does not appear to explain the long-range transport behavior, I hypothesize that an alternative process with the same temperature scaling must be crucial in dictating overall conductivity. In order to further elucidate the dynamic process underlying the overall ion conductivity of these materials, the temperature axis in Figure 14A, which was rescaled by the product of the rheological shift factors (a_T 's) and an ion-specific, temperature independent shift factor, b , that is determined empirically from best-fit shifting to generate a master curve (Equation 8). This shift factor (b) accounts for the ion-identity dependence of the conductivity, while the rheological shift factors account for all temperature-dependence of ionic conductivity, with the sticky timescale of the LiTFSI-containing polymer as a reference timescale (τ_{ref}). The result of this rescaling by τ_{eff} is a master curve where the conductivities of all materials display approximate power-law scaling with τ_{eff} with a power law exponent close to unity as indicated by the dotted ‘best-fit’ power law relation (Figure 15C). This master curve is analogous in form to a

Walden plot, where an additional ion-identity shift factor (b) is used to collapse the data. The slight deviation of the best fit line of Figure 15C from a scaling exponent of unity is attributed to failure of TTS to capture the temperature dependence of segmental, chain, and sticker relaxations.

$$\tau_{eff}(T) = a_T(T) \cdot b \cdot \tau_{ref} \quad \text{Equation 8}$$

This scaling analysis of viscoelastic timescales and the ion-identity shift factor (b) demonstrates that the sticky Rouse timescale is intimately linked with the ion-identity shift factor, suggesting that the dissociation of ion-polymer interactions universally dictates the ionic conductivity in this system. The dashed line of parity in Figure 16 indicates one-to-one correspondence of rheological and conductive timescales. While the glass transition and elementary Rouse timescales display limited dependence on the ion identity, the sticky timescales correspond well with these ion identity shift factors, suggesting that the ion-identity dependence of the ion motion in these materials is accounted for almost entirely by the differences in the dynamics of the metal-ligand bond strengths of these materials. Though the above analysis presented on the basis of total conductivity cannot account for mobility differences exhibited by the cations and anions, prior studies suggest that the 'ion transport numbers' of metal-ligand coordination based ion conductors is relatively insensitive to metal identity, a notion that suggests correlated motions of cations and anions.

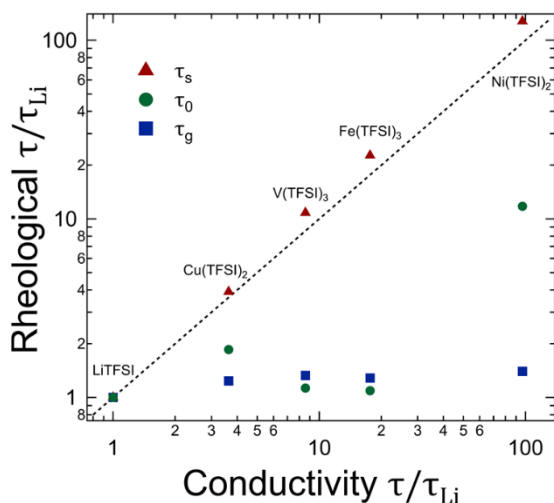


Figure 16: Timescale analysis of the telechelic polymers.

The relative timescales from the three rheological processes (glass transition, Rouse time, and sticker relaxation) are plotted against the timescale that appeared to collapse ionic conductivity. The lithium containing material is selected as a reference system. The dotted line of parity indicates perfect agreement between mechanical and conductive timescales.

The above results demonstrate that long-range transport of ions through a polymer network with specific ion-polymer interactions is intimately coupled to the exchange dynamics of the ion-ligand interaction. I propose that ion conduction occurs by a hierarchical process involving 1) thermal fluctuations which set a minimum ‘attempt timescale’ related to the glass transition process, 2) dissociation of ion-ligand bonds governed by an activation barrier, and 3) diffusion of dissociated ions through the matrix. This mechanism is analogous to the mechanisms of sticker motion proposed by Rubinstein⁹⁸ and the observations of Colby and Saalwaechter in ionomers⁹². However, in the present case the relevant mobile species are not polymer-bound and should explore space diffusively, rather than sub-diffusively.

E. Conclusion

This study investigated the relationship between polymer dynamical relaxation timescales and ionic conductivity in salt-doped, model telechelic polymers with M-L coordination bonds between the dynamic polymer network and the mobile cationic species. Through changes in the identity of the metal cation, the apparent imidazole-cation bond dissociation energy was modulated over nearly a factor of 2 (from ~15-30kJ/mol), resulting in changes in metal-ligand dynamic timescales of nearly two decades. These changes in bond dissociation energy and timescale were found to correlate well with the species-dependence of the ionic conductivity, indicating an inverse relationship between bond lifetime and ionic conductivity in fully dissociated salt systems. This result suggests that enhancing ion-polymer interaction lability can be used as an alternative means of enhancing ionic conductivity in polymer electrolytes, synergistic with conventional strategies to increase the rate of polymer segmental motion. This work motivates the design of labile ion-solvating functionalities to permit rapid dissociation of metal-ligand bonds and suggests that microscopic ligand design may be leveraged to increase ionic mobilities of M-L coordinating polymer electrolytes.

F. Appendix

F.1 NMR Spectra

1.1 NMR Spectrum of Di-bromo Poly(methyl acrylate)

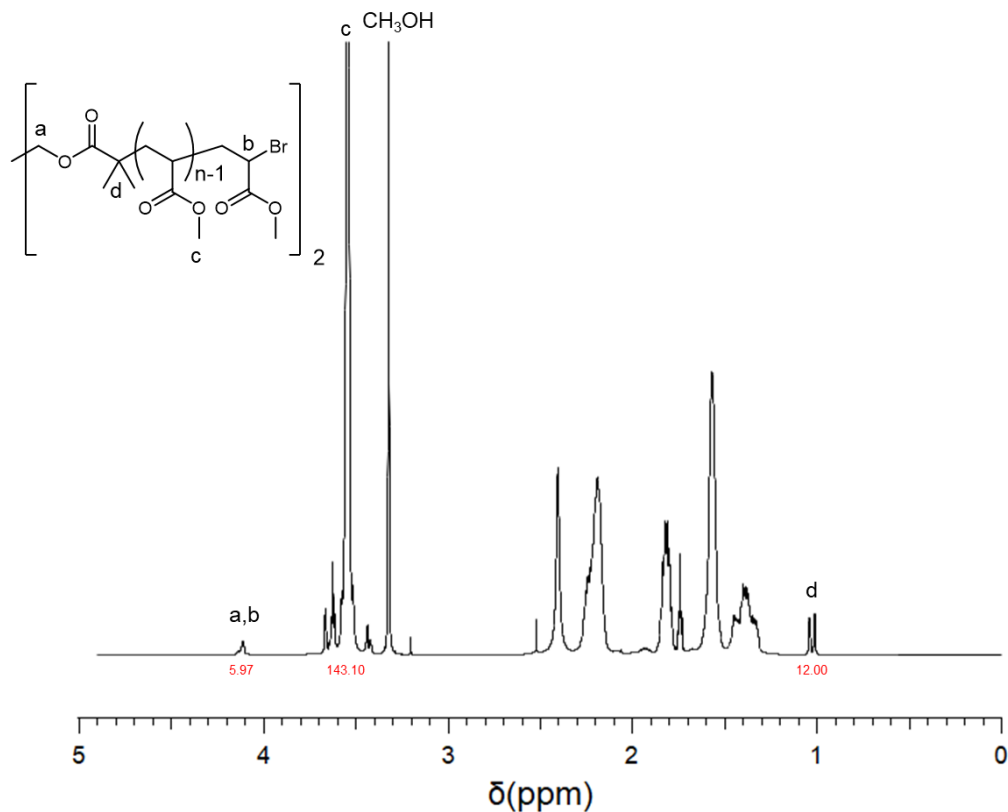


Figure 17: NMR Spectrum of Di-bromo Poly(methyl acrylate)

The degree of polymerization for this polymer was estimated by analysis of the ratio of the methyl peaks of the initiator (d) to the methyl backbone peaks alpha to the ester of the methyl acrylate functionality (c) via:

$$N_N = 4 \frac{I_c}{I_d} = 47.7$$

Quantitative retention of the bromine chain end is confirmed by comparison of the chain end peaks (b) corresponding to the protons alpha to the bromine chain end to the initiator

peaks (d). Though peaks (a) and (b) overlap, the integration is in correct proportions and the presence of chain ends is further confirmed after substitution of imidazole thiol onto the polymer chain ends.

1.2 NMR Spectrum of Di-Imidazole Poly(methyl acrylate)

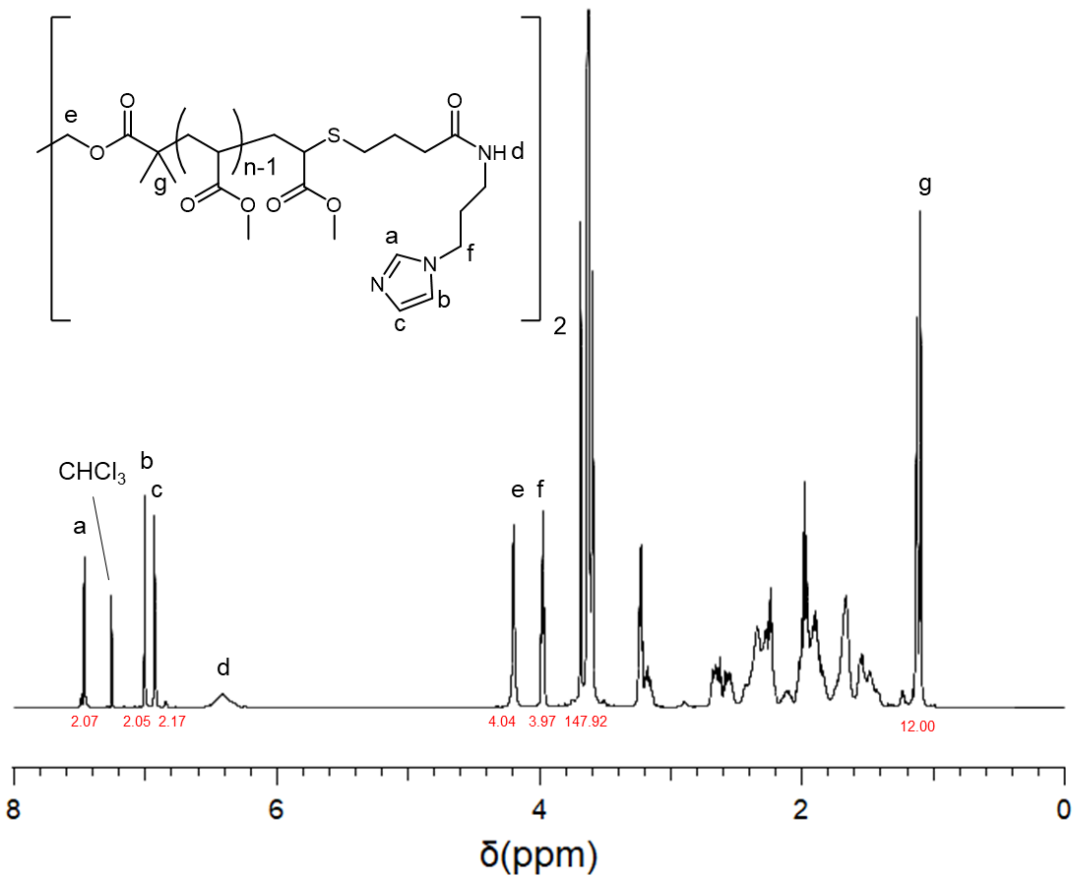


Figure 18: NMR Spectrum of Di-Imidazole Poly(methyl acrylate)

The degree of chain end functionalization was calculated by comparison of the aromatic imidazole peaks (a,b,c) to those corresponding to initiator methyl peaks (g). Chain-end functionalization appears to be quantitative.

1.3 NMR of Mono-bromo Poly(methyl acrylate)

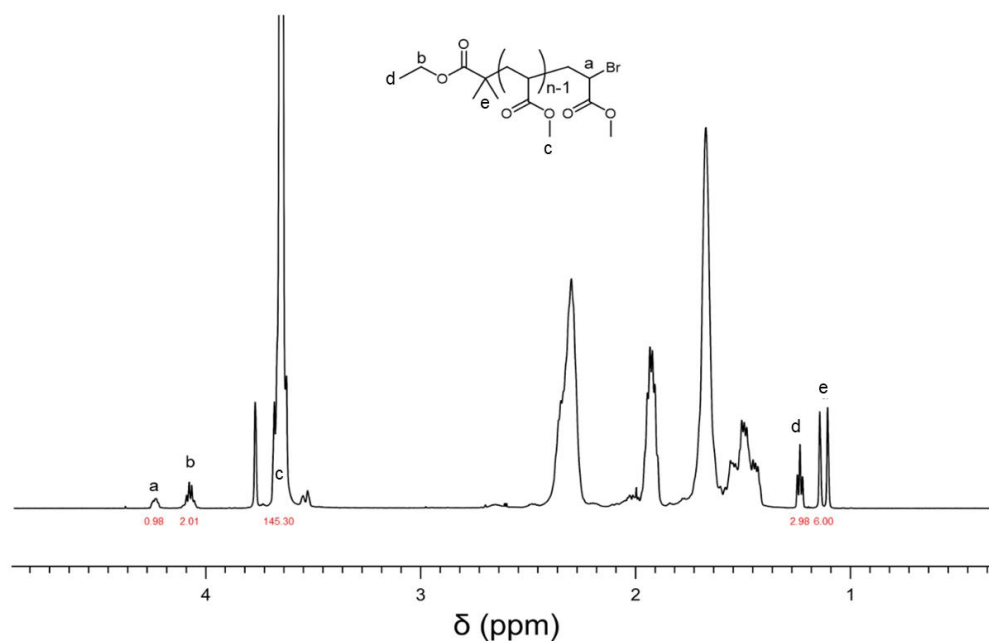


Figure 19: NMR of Mono-bromo Poly(methyl acrylate)

The degree of polymerization was calculated from the ratio of the methyl peaks alpha to the ester of the acrylate unit (c) to the methyl peaks of the initiator (e) via:

$$N_N = 2 \frac{I_c}{I_e}$$

Quantitative retention of the bromine chain end is confirmed via comparison of the proton signal from the hydrogen alpha to the bromine (a) and the initiator methyl peaks (e).

1.4 NMR of Mono-Imidazole Poly(methyl acrylate)

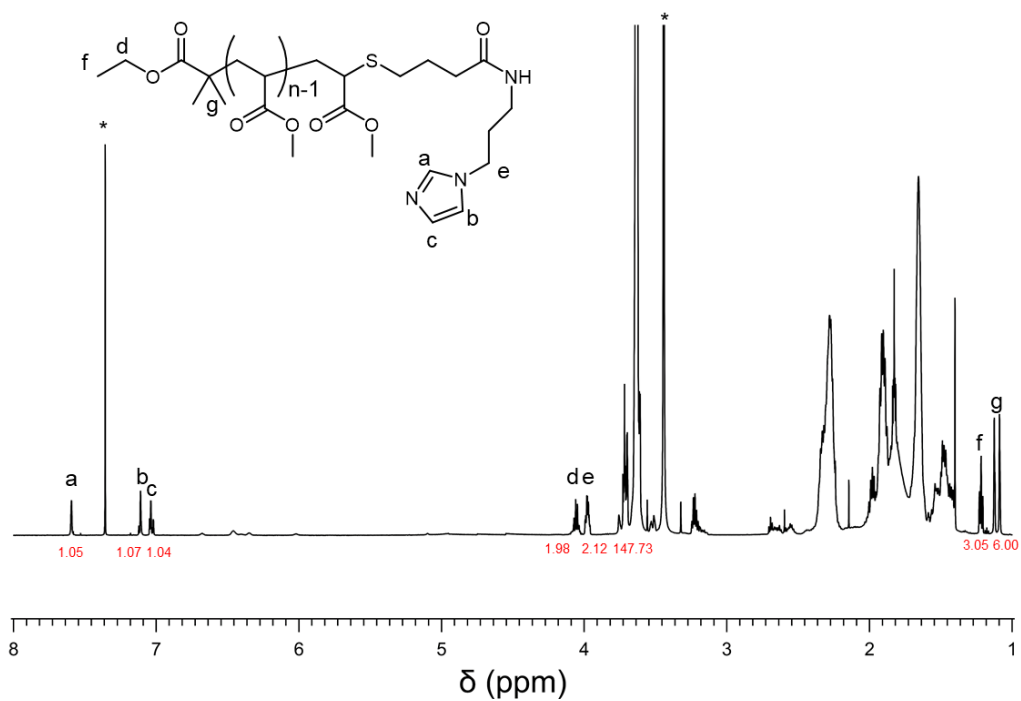


Figure 20: Mono-Imidazole Poly(methyl acrylate)

The degree of chain end functionalization was calculated by comparison of the aromatic imidazole peaks (a,b,c) to those corresponding to initiator methyl peaks (g). Chain-end functionalization is quantitative.

F.2 Size Exclusion Chromatography

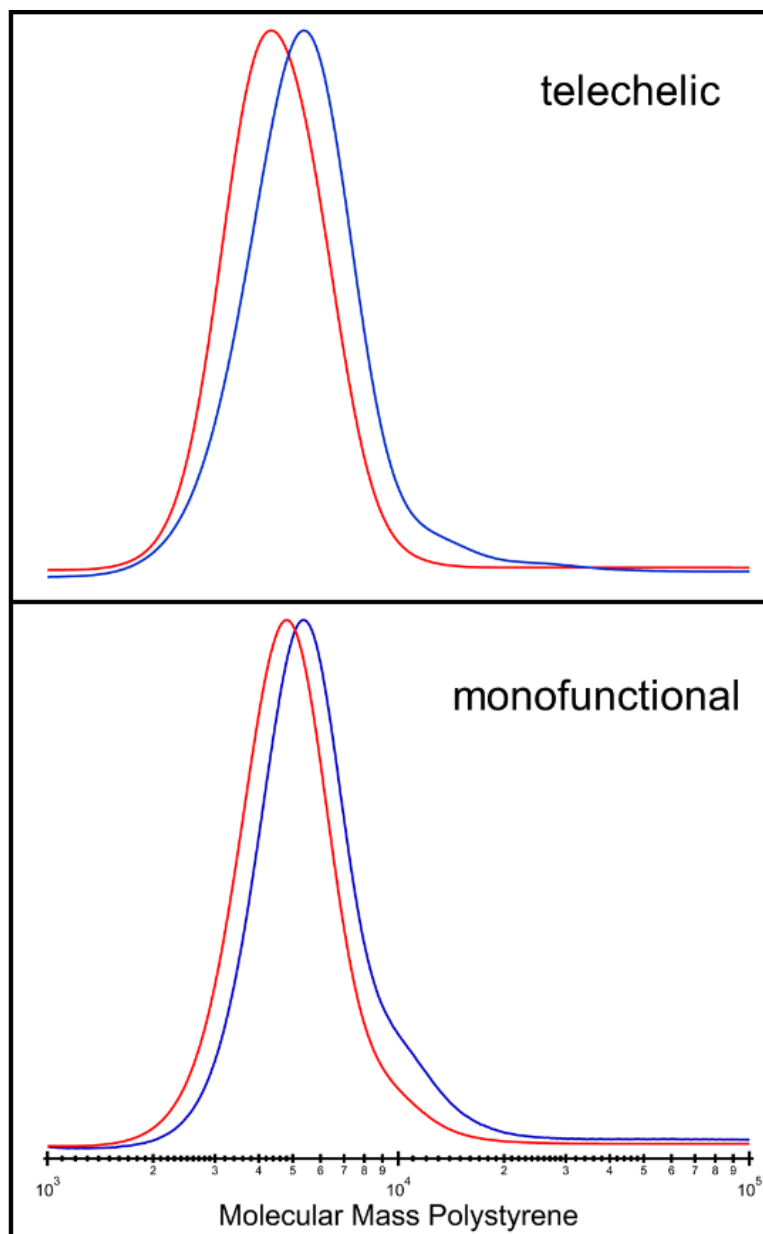


Figure 21: Molecular masses of the telechelic and monofunctional polymers before (red) and after (blue) functionalization with the imidazole thiol.

F.3 Small- and Wide-Angle X-Ray Scattering

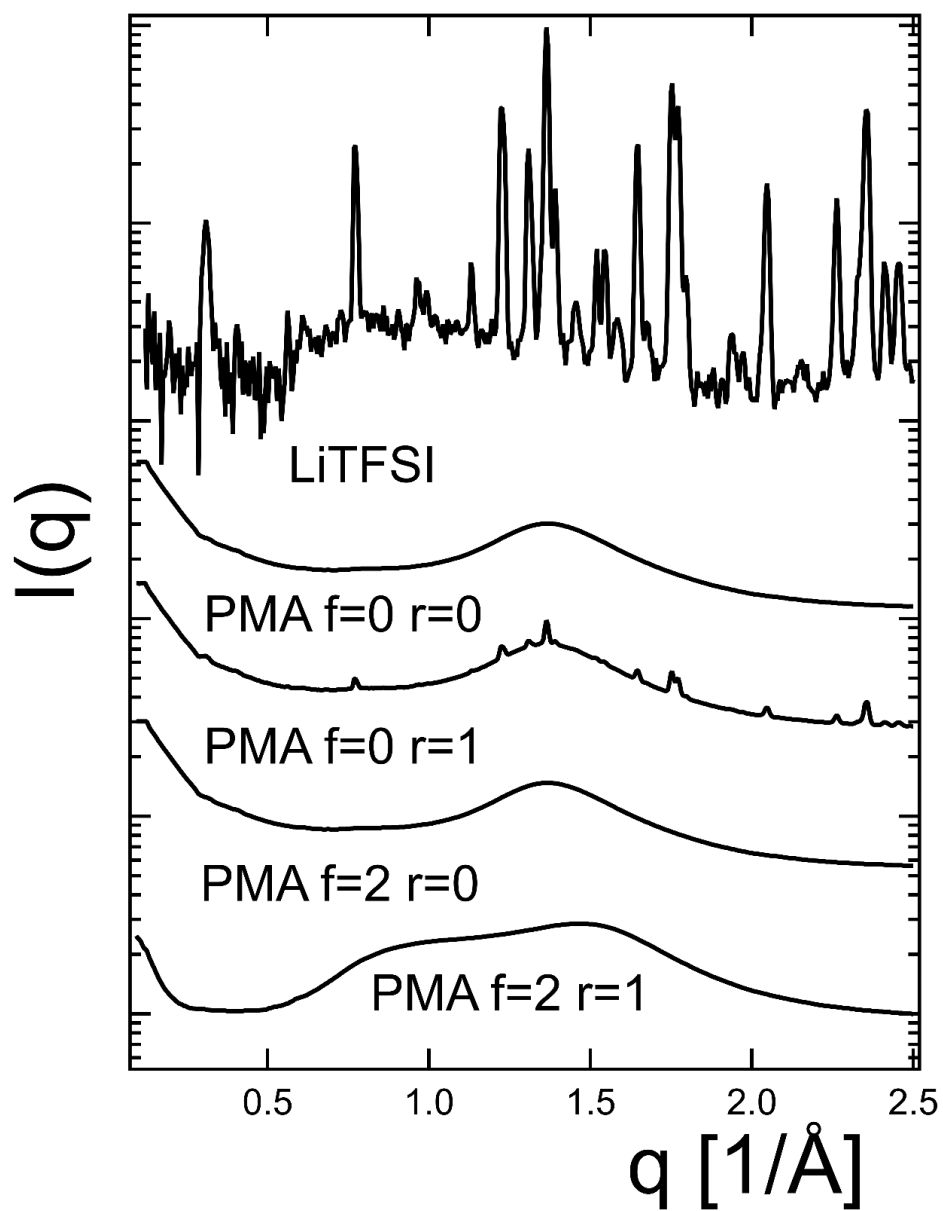


Figure 22: Representative WAXS for the lithium containing telechelic and nonfunctional polymer.

In the absence of coordinating imidazole species ($f=0$), the presence of LiTFSI in the polymer matrix results in crystalline salt peaks in addition to the broad ‘van der waals’ peak. In the presence of the imidazole species, crystalline peaks are not observed and a second broad feature emerges instead at $q \sim 0.8 \text{ 1/\AA}$. The nature of this second peak is not fully understood but it may be a consequence of ion-polymer or ion-ion spatial correlations. The value of ‘ r ’ refers to the molar ratio of salt cation to imidazole in the system.

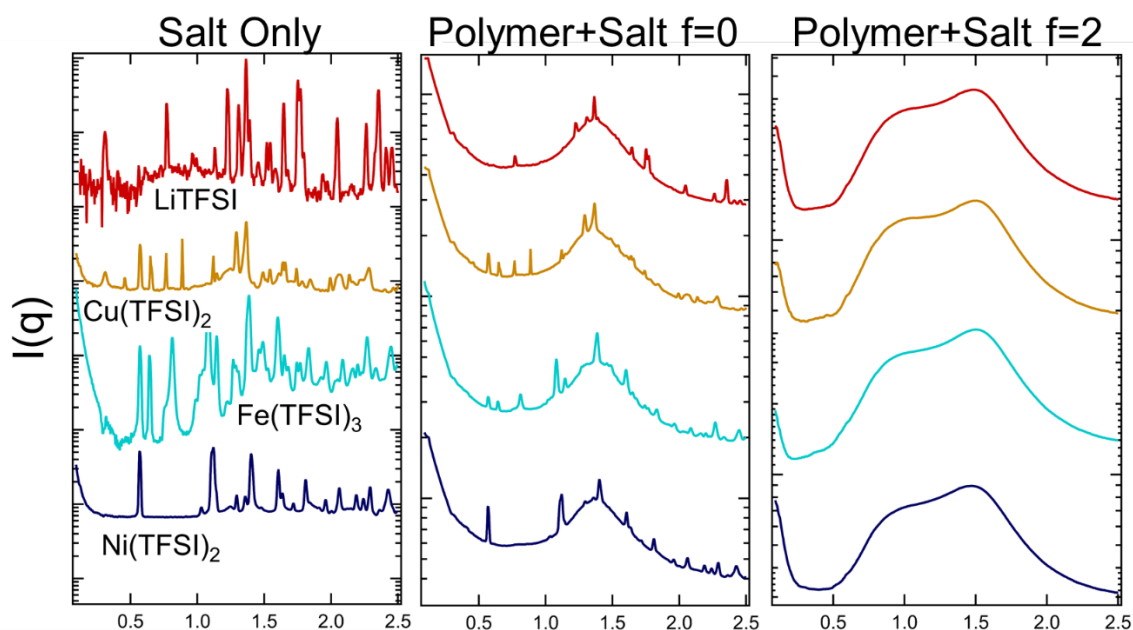


Figure 23: WAXS analysis of all salt-containing polymers.

This same trend holds for many salts tested (though Vanadium TFSI salt was not able to be tested in this way due to availability of the salt). Analysis of the crystalline scattering pattern is beyond the scope of this work. In all cases, the imidazole species plays a clear role in salt uptake, assisting to dissociate the salts from their crystalline forms.

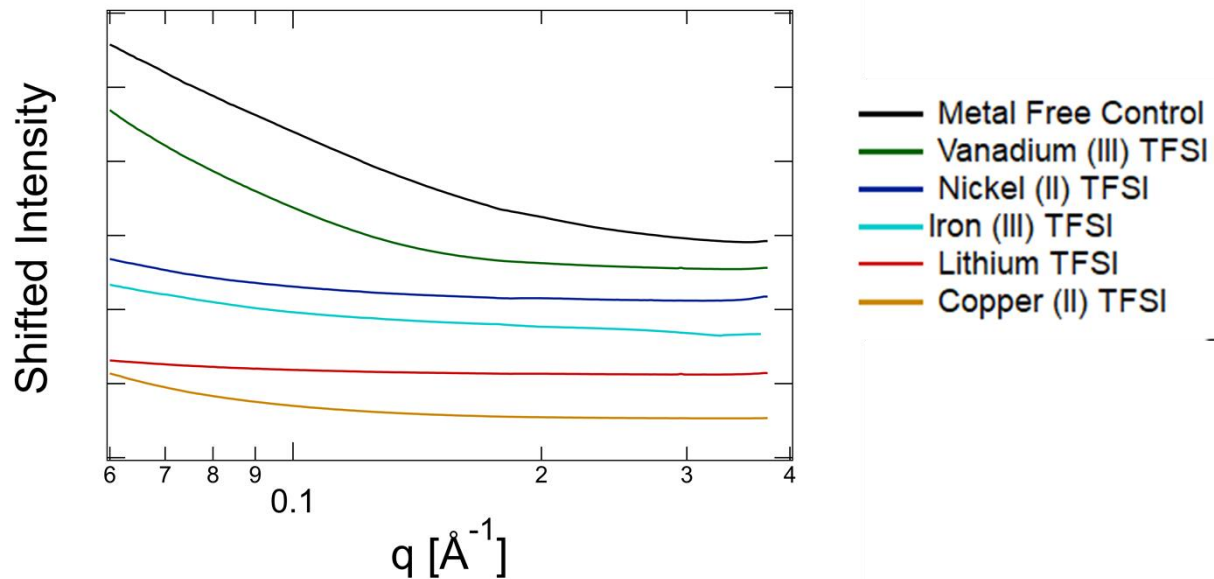


Figure 24: Small angle x-ray scattering analysis of salt-containing polymers.

SAXS is used to investigate ion-aggregates, but no clear ion-aggregate features are observed, suggesting that ions are mostly solvated and do not phase segregate into discrete aggregate clusters.

F.4 Rheology Fitting

4.1 Description of Model

I) Glassy Response

Since simple, accurate molecular expressions for the relaxation of polymeric glasses have not been developed, the glassy response of the materials was fit to a phenomenological, ‘stretched-exponential’ or Kohlrausch–Williams–Watts (KWW) form, which describes a distribution of relaxations. The KWW form shown in Equation 9 is written to express in terms of its first moment, τ_g . The breadth of this distribution is parameterized by β , which approaches unity for a perfectly uniform relaxation and indicates a broad distribution of relaxations as it approaches zero. The glassy modulus, $G_g(0)$, can be determined experimentally from the high-frequency limiting behavior of the material.

$$G(t) = G_g(0) \exp \left[- \left(\frac{t \Gamma(\beta^{-1})}{\tau_g \beta} \right)^\beta \right] \quad \text{Equation 9}$$

II) Rouse Modes

The Rouse model is an appropriate model for the relaxation of internal stresses in the polymer chain since the short chains studied here are linear and unentangled. Since stickers are placed only at the chain termini, it is assumed that all internal relaxations occur independently to the relaxations of the interchain crosslinks.

$$G_R(t) = \frac{\rho RT}{M_N} \sum_{p=1}^N \exp(-tp^2/\tau_0 N^2) \quad \text{Equation 10}$$

III) Sticky Rouse Modes

The final contribution to the stress relaxation modulus comes from the reversible crosslinks. These crosslinks have been predicted by Baxandall¹⁰⁴ to display a single relaxation mode as described by Equation 11. The prefactor to this single exponential decay mode is given by the density of elastically effective strands in the network. Assuming that each network strand is elastically effective leads to an overprediction of the elastic modulus, so a factor of ‘f’ is used to compensate for network defects.

$$G_s(t) = \frac{\rho RT}{M_N} f \exp(-t/\tau_s) \quad \text{Equation 11}$$

IV) Full model and Fitting

The full model is given by the sum of these three contributions to the elasticity.

$$G(t) = G_g(t) + G_R(t) + G_s(t) \quad \text{Equation 12}$$

Fitting of the model is performed in the frequency domain by Fourier transformation of the model functions assuming $G(t) = 0$ for $t < 0$. The Fourier transforms of the $G_R(t)$ and $G_s(t)$ are performed analytically. Since no analytical expression exists for the Fourier transform of the stretched exponential function, this transform was performed numerically via the open-source ‘libkww’ library¹¹⁰. Fitting of the corresponding frequency-domain expression was performed to minimize the least-squares residuals of the logarithms of the storage and loss moduli to ensure that the fitting is not dominated by the high-frequency points.

4.2 Additional Fitting Parameters

Table 4: Additional Fitting parameters for the rheology study

	No Salt	Lithium	Copper	Vanadium	Iron	Nickel
β	0.58	0.48	0.67	0.56	0.55	0.51
$G_g[MPa]$	2.46	2.61	2.54	2.23	1.85	2.40
f	-	0.42	0.59	0.6	0.31	0.51

F.5 Monofunctional Control Experiments:

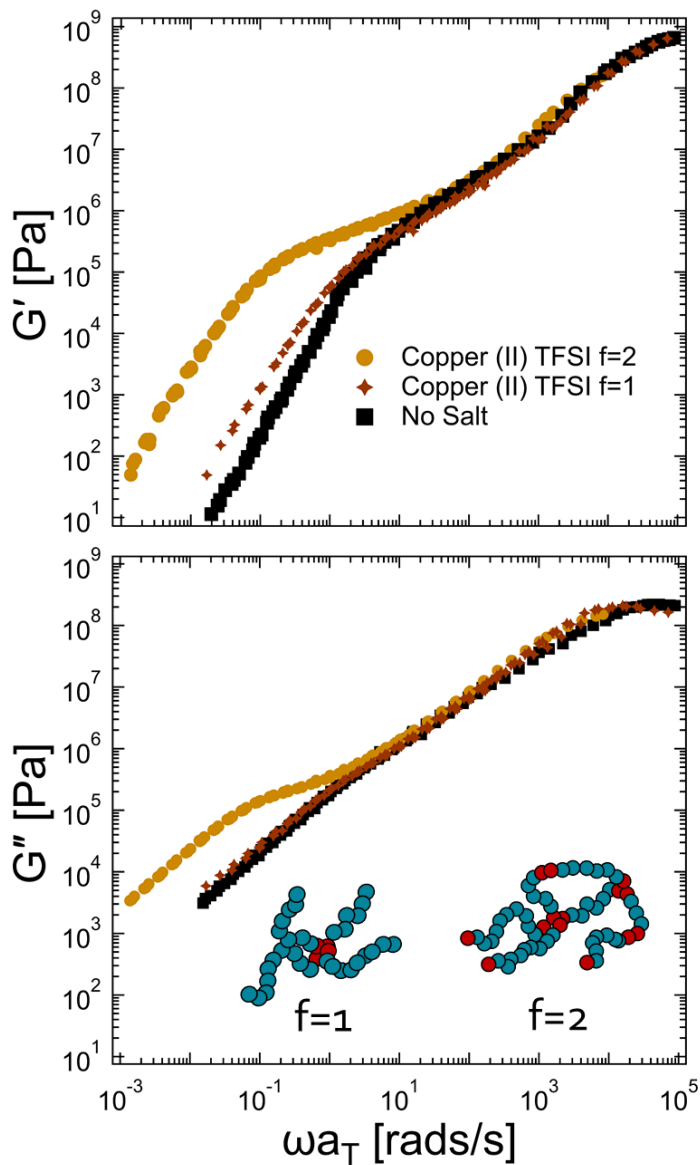


Figure 25: Control experiments of the monofunctional, nonfunctional, and telechelic polymer viscoelastic response in the presence of the copper(II) TFSI salt.

These results demonstrate that ion-ligand interactions are the sticky mode probed by these experiments. The monofunctional material is evidently below the percolation limit for gelation and consequently displays no significant delay in terminal relaxation, as is

demonstrated by the nearly identical viscoelastic response of the monofunctional material in the presence of salt and the nonfunctional material. The equivalent control experiment on the nonfunctional ($f=0$) sample in the presence of salts resulted in a gross failure of time-temperature superposition, likely due to the presence of crystalline salts in the polymer sample.

F.6 Estimation of Glassy Dynamics:

The activation energy of the alpha process, $E_{a,\alpha}$, represents the effective Arrhenius temperature dependence of the alpha relaxation timescale ($\tau_\alpha \sim \exp(E_{a,\alpha}/RT)$) and can be considered a constant within a limited temperature regime. Though I do not have access directly to the alpha relaxation time in this paper, I estimate that the temperature dependence of this quantity will be equivalent to the temperature dependence of the rheological shift factors of the salt-free material above the glass transition temperature.

$$\frac{E_{a,\alpha}(T^*)}{R} = \left. \frac{d \log(a_T)}{dT} \right|_{T=T^*} \quad \text{Equation 13}$$

F.7 Electrochemical Impedance Spectroscopy Sample Spectra

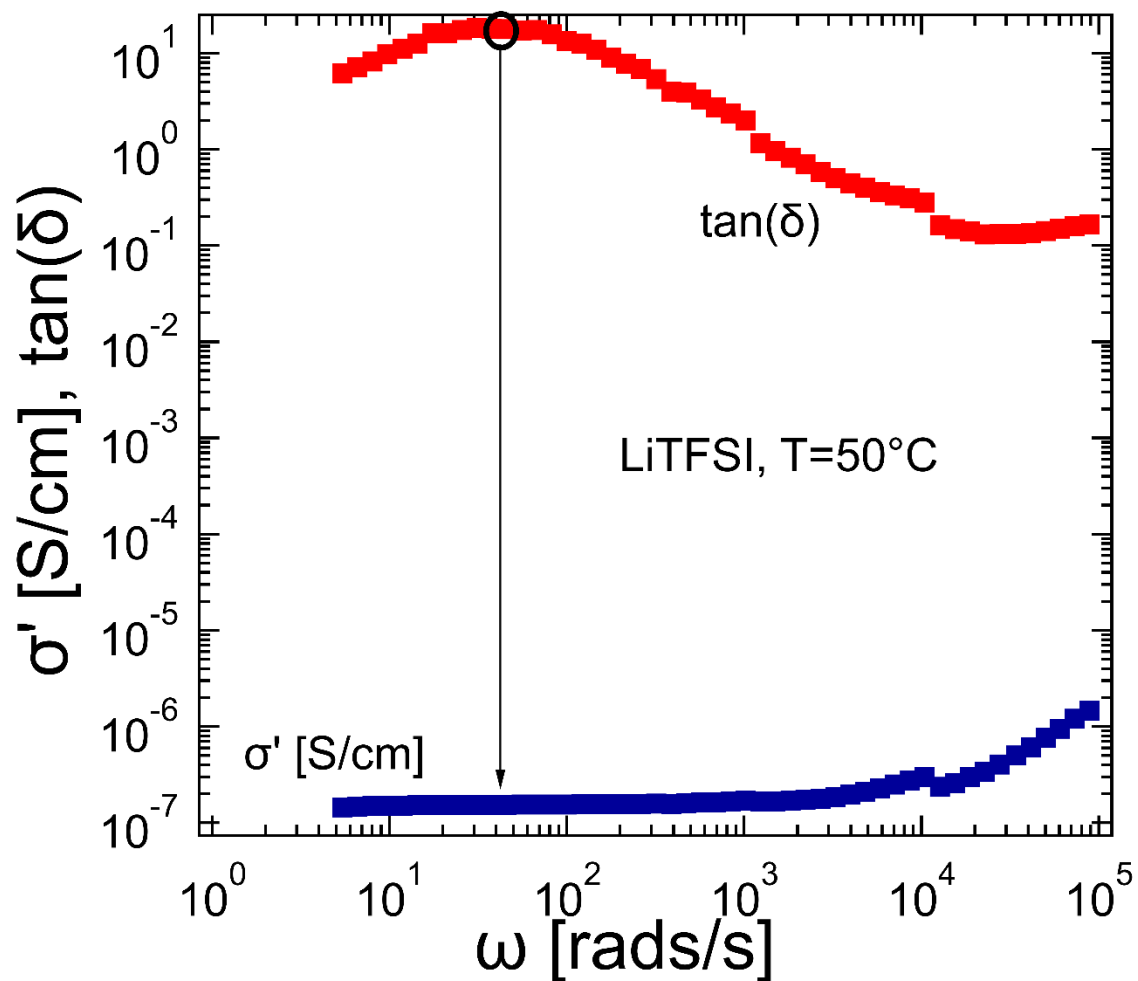


Figure 26: A representative sample spectrum for an EIS experiment.

The DC conductivity of the samples was taken to be the value of the real component of σ at the local maximum in the loss tangent.

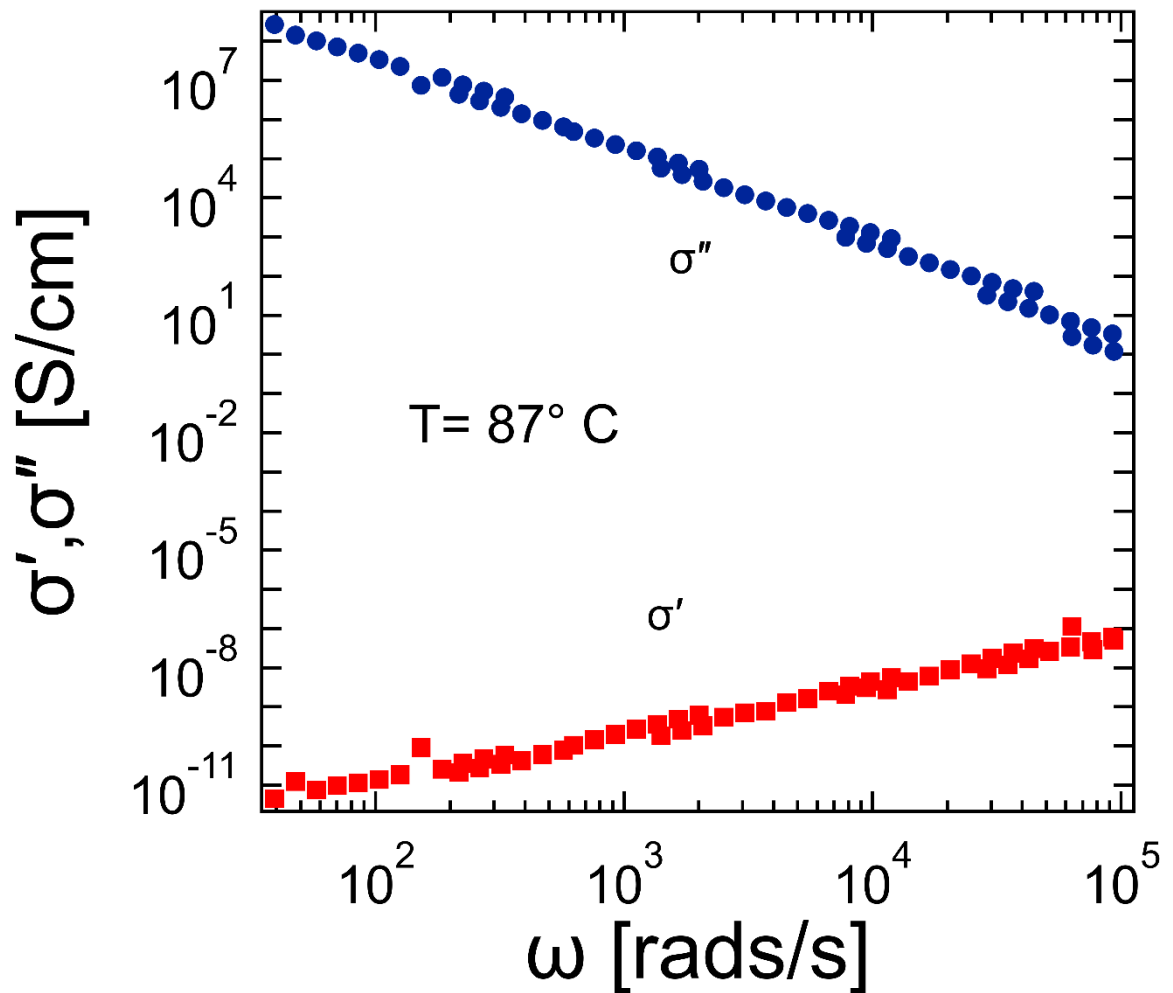


Figure 27: EIS experiments in the absence of added salts.

The weak ionic conductivity features, even at elevated temperature, suggest that the ionic conduction of these materials is almost entirely due to the added salts and there are minimal contributions from contaminants. Though no conductivity feature could be resolved, I can conclude that ion conductivity is less than 10^{-11} based on this data. The results of this experiment were verified in two different electrode geometries to rule out poor electrode contact as an explanation for the poor ion conductivity of this sample.

F.8 Differential Scanning Calorimetry

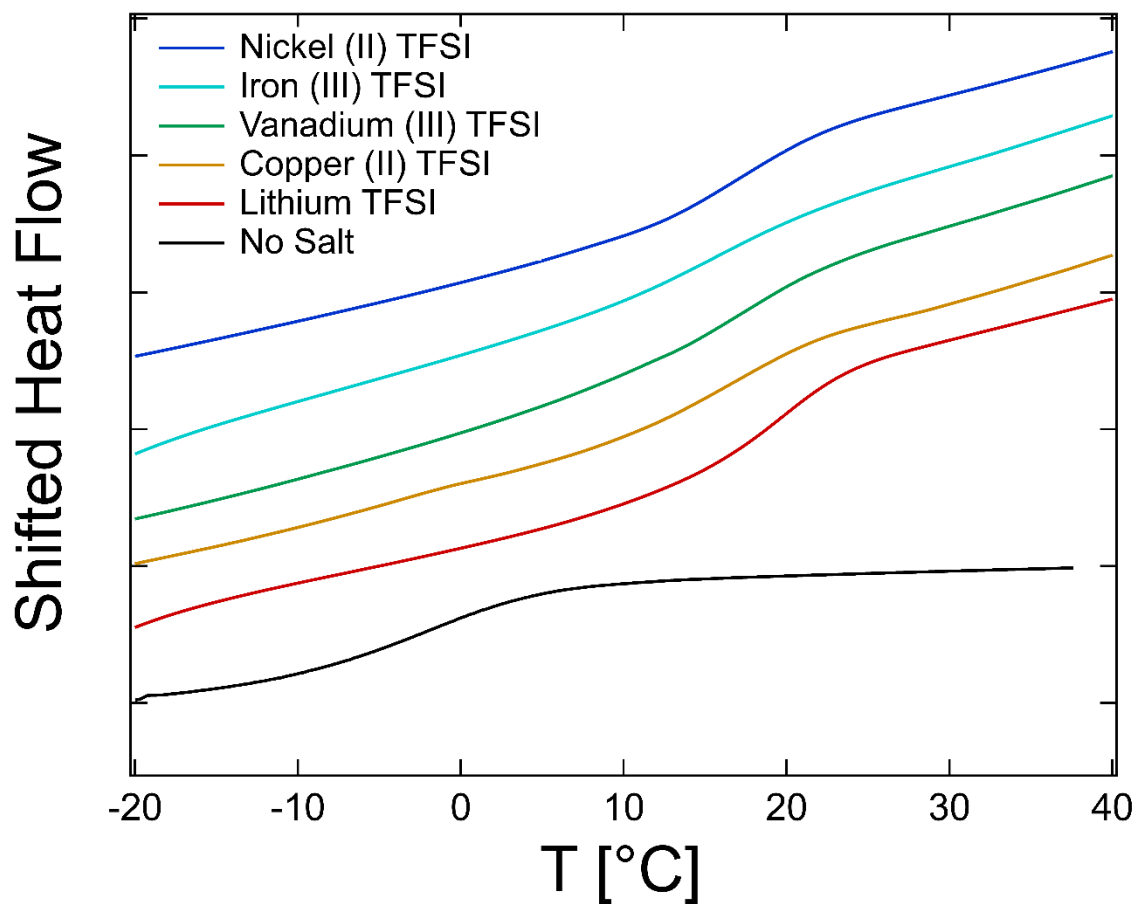


Figure 28: Differential scanning calorimetry curves for the samples tested in this study.

Table 5: T_g Values of Polymers with added salts.

	No Salt	Lithium	Copper	Vanadium	Iron	Nickel
T_g [°C]	-3	18	15	16	16	18

III. Design of Polymeric Zwitterionic Solid Electrolytes with Superionic Lithium Transport

A. Abstract

Progress toward durable, high-energy density lithium-ion batteries has been hindered by instabilities at electrolyte-electrode interfaces leading to poor cycling stability, and by safety concerns associated with energy-dense lithium metal anodes. Solid polymeric electrolytes (SPEs) can help mitigate these issues, however SPE conductivity is limited by sluggish polymer segmental dynamics. I overcome this limitation via zwitterionic SPEs that self-assemble into superionically conductive domains, permitting decoupling of ion motion and polymer segmental rearrangement. Although crystalline domains are conventionally detrimental to ion conduction in SPEs, I demonstrate that semicrystalline polymer electrolytes with labile ion-ion interactions and tailored ion sizes exhibit excellent lithium conductivity (1.6 mS/cm) and selectivity ($t_{+} \sim 0.6-0.8$). This new design paradigm for SPEs allows for simultaneous optimization of previously orthogonal properties including conductivity, Li-selectivity, mechanics, and processability.

B. Introduction

The efficient and safe storage of electrochemical energy is critical for such emerging technologies as electric vehicles and portable electronic devices^{2, 4, 111}. Practical requirements for next-generation secondary Li-ion batteries include higher energy densities and charge-discharge rates, which hinge on new high-voltage, high-capacity, and high-power cathode materials¹¹²⁻¹¹⁴ and on electrolytes with higher ionic conductivities (σ). Further, high energy densities can be reached only if Li-ion cells are operated over a wide potential range that exceeds the electrochemical stability window of current organic solvent-

based electrolytes. Next generation Li-ion cells require the development of more stable and nonflammable electrolytes. Solid polymer electrolytes (SPEs) have attracted interest due to their stability and mechanical robustness¹¹¹, but it remains challenging to attain SPEs with both high ionic conductivity and lithium selectivity¹.

Traditional SPEs, such as polyethers, exemplify vehicular ion transport (Figure 29a) where ion motion is controlled by the segmental relaxation timescale of the material (τ_g)^{22, 28, 115}. This mechanism leads to the near-universal convergence of the measured ionic conductivities of rubbery amorphous polymers as a function of temperature when the latter is referenced to the glass transition temperature ($T-T_g$). Vehicular conduction limits polymer design because only plasticized (soft) polymer electrolytes display sufficiently high ion conduction for battery applications. In fact, no solid polymers have been identified that reliably surpass the conductivity of poly(ethylene oxide) (PEO), due to its combined low T_g and moderate salt solubility^{1, 116}. Moreover, this solvation process often results in limited metal cation transport because strong cation-polymer interactions can slow down cation motion, especially for multivalent ions¹¹⁷, and thus cations frequently account for less than 20% of the total ionic current¹¹⁸.

Inorganic solid-state electrolytes (Figure 29B) offer the strongest decoupling between mechanical and conductive properties. Although their atomic rearrangements are restricted by steep energy wells, they display ionic conductivities of 0.1-12 mS/cm and excellent cation selectivities ($t_+ \approx 1$)^{57, 119-121}. These attractive features are a result of ion diffusion channels comprised of interstitial and/or lattice site vacancies that can be designed to support ion hopping/migration. In addition, the rigidity and optimized size of these ion channels often completely prevent motion of non-target ions (Figure 29B). Such materials

are clearly advantageous for their high ionic conductivity, selectivity for target ions, and high elastic modulus, but they suffer from many challenges, such as poor contact at interfaces with the electrodes¹²², brittleness and cracking¹²³⁻¹²⁴, and limited chemical and electrochemical stability against a lithium metal anode and/or high voltage cathode¹²⁵.

The design of tough, processable polymers with ion conduction properties and elastic moduli comparable to those of inorganic electrolytes could mitigate the deficiencies of both SPEs and inorganic solid-state electrolytes. However, attempts to decouple conduction from segmental mobility in ion-conductive polymers have so far met with marginal success. Composites of inorganic particles and SPEs can partially mitigate issues encountered by each material class¹²⁶⁻¹²⁷, but these composites suffer from significant drawbacks, such as particle agglomeration and high impedance at the heterogeneous interfaces. Furthermore, the conductivity, selectivity, and mechanics of these composites typically results in only modest improvements over the constitutive SPE. Another approach to overcoming the rate limitations inherent to vehicular ion conduction in traditional SPEs is to engineer disordered and dynamically heterogeneous polymers¹²⁸⁻¹²⁹ or microphase separated block copolymer architectures with SPE channels that are integrated with a higher modulus component¹³⁰. Although these SPEs do exhibit decoupling from the vehicular conduction mechanism, their conductivity values have so far been well below those of state-of-the-art SPEs. Another recent result has demonstrated crystalline ion channels in block copolymer electrolytes for proton conduction, highlighting the possibility for ion transport through organic crystalline lattices¹³¹.

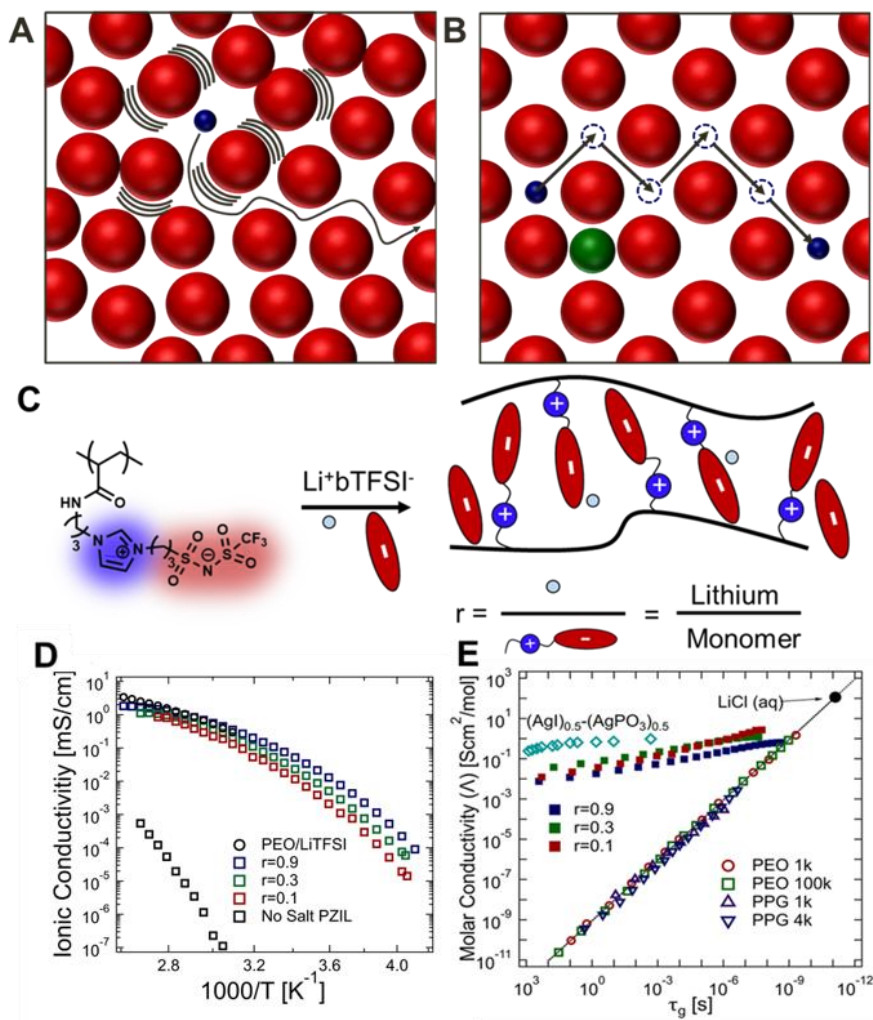


Figure 29: Transport of ions through the ZIL resembles ceramic transport.

A schematic representation of the path of an ion through (A) a typical solid polymer electrolyte, in which ion transport is coupled to the timescale of local rearrangements, and (B) an ordered solid with sufficient free volume to enable superionic transport. The atoms of a crystal are typically confined to specific lattice positions, allowing sufficiently small ions with a low charge (blue spheres) to diffuse through the matrix (red spheres) via successive discrete hops involving vacant lattice sites or interstitial sites, while the motion of larger or highly charged ions (green sphere) is excluded. (C) The zwitterionic polymer studied herein comprises IL-inspired ions tethered to the backbone. Mobile ions are doped in through the addition of a Li^+TFSI^- salt at select molar ratios. (D) The DC ionic conductivity of salt-containing PZILs shown as a function of temperature is comparable to that of PEO (a best-

in-class SPE)¹³². E) While standard SPEs have molar ionic conductivities coupled directly to the timescale of molecular rearrangements, ($\tau_g \sim 1/\Lambda$), the salt-containing ZILs demonstrate decoupling of these properties. Amorphous poly(ethylene oxide) (PEO) and poly(propylene glycol) (PPG) serve as reference SPEs, and ((Ag)0.5-(AgPO3)0.5) systems are typical superionic inorganic solids (literature data on PEO, PPG, and Ag systems from Sokolov²).

To address these challenges, semi-crystalline zwitterionic (ZI) SPEs are proposed. Key to their design is the decoupling of lithium transport from the fluidity of the matrix. This decoupling confers superionic performance resembling that of inorganic solid-state electrolytes, while the polymer matrix leads to processability and ductility akin to traditional polymeric electrolytes. I show here that facile lithium transport is enabled by bulky cationic and anionic groups tethered to the backbone and arises from the weak interactions between lithium and framework ions. I further hypothesize that the disparity in size between lithium and framework ions. I further hypothesize that the disparity in size between lithium and constituent ions of the PZIL creates sufficient free volume for superionic transport of Li⁺. The electrochemically-determined ionic conductivity of this polymer electrolyte is competitive with state-of-the-art polymeric ion conductors ($\sigma \sim 1.6$ mS/cm), despite its modest T_g (T_g~270-300 K). Significantly, ⁷Li solid-state nuclear magnetic resonance (NMR) measurements indicate the presence of multiple lithium environments associated with different mobilities, suggesting an accelerated conductivity mode through crystalline domains. From the ⁷Li and ¹⁹F NMR self-diffusion coefficients obtained via pulsed field gradient NMR (PFG NMR), I calculate a lithium transport number of 0.67, which is markedly larger than the corresponding value for PEO (t₊~0.2)¹. These results clearly illustrate the potential of polymeric zwitterionic liquids (PZILs) as a new design platform for solid polymer electrolytes with superionic conduction.

C. Results and Discussion

C.1 PZILs Display a Faster-than-Vehicular Conduction Mechanism

To leverage the superionic conduction mechanisms characteristic of inorganic solid-state electrolytes, PZILs are designed with bulky, immobilized charges, resulting in labile ion-ion interactions and significant free volume for metal cation motion (Figure 29C). The choice of a bulky, pendant imidazolium-trifluoromethanesulfonamide (Im-TFSI) zwitterion allows for weaker Coulombic interactions, and the asymmetry in cation and anion sizes promotes crystal formation with sufficient void space for Li^+ ions. The orientation of the zwitterion (with cation proximal to the backbone) is selected in accordance with calculations by Keith et al. that suggest that this orientation results in greater selectivity for lithium motion¹³³. Although zwitterionic electrolytes are not entirely unexplored¹³⁴⁻¹⁴⁰, previous reports have leveraged amorphous polymers wherein ordering of the pendant zwitterions is not possible (often due to crosslinking of the network). These disordered systems do not display the superionic mechanism that distinguishes the PZILs reported herein. Recent studies have pointed towards the promising properties of zwitterions in electrochemical applications both as an ion transport matrix¹⁴¹ and as a means to increase the dielectric constant of an electrolyte¹⁴².

The choice of salt identity and concentration is critical to maximizing salt dissolution while preventing aggregation and precipitation. Mobile lithium bis(trifluoromethanesulfonimide) ($\text{Li}^+/\text{TFSI}^-$) is a highly labile salt whose use leads to facile dissociation in the presence of ion-solvating functionalities. It should also be noted that, due to the solvation afforded by zwitterionic liquid (ZIL) groups, salt-to-monomer ratios

(parameterized by 'r') higher than the upper $r = 0.9$ value presented in Figure 29 can be obtained without salt precipitation (D.6).

Promising results were obtained from Electrochemical Impedance Spectroscopy (EIS) measurements, with high ionic conductivities being observed for the PZILs and minimal conduction for the parent, undoped polymer (Figure 29D). This dramatic conductivity difference demonstrates that the ionic current is carried by the $\text{Li}^+/\text{TFSI}^-$ dopants, suggesting that the polymer acts as a fixed charged background for the mobile ions. The ionic conductivities of the PZILs are in excess of 1 mS/cm at elevated temperature, an important metric for practical implementation. Though other polymeric electrolytes, such as PEO, have exceeded this conduction threshold, their high values have been achieved via fast segmental motion²⁸. In contrast, the doped PZILs achieve competitive ion conductivities despite sluggish segmental motion, indicated by their relatively high glass transition temperatures ($T_g \sim 270\text{-}300$ K, D.7). As a result, PZILs also maintain high ion mobilities at low temperatures below their T_g . For example, the $r=0.9$ sample has an ionic conductivity exceeding 10^{-2} mS/cm at 273 K ($1000/T = 3.6$), orders of magnitude larger than the conductivity of PEO at the same temperature ($<10^{-6}$ mS/cm)¹³² (Figure 29D).

The ionic conduction behavior of the PZIL under small potentials and across a wide range of temperatures, including temperatures near and below T_g , differs from the standard, vehicular ion-conduction mechanism. The presence of superionic conduction is best indicated by the "Walden-plot" analysis shown in Figure 29E. Traditionally, the Walden rule predicts that molar ionic conductivity ($\Lambda \equiv \sigma/c$, where c is the number density of charges in the electrolyte) is inversely proportional to the matrix viscosity¹⁴³. In viscoelastic polymers, however, it is more appropriate to consider the glassy relaxation time of the polymer, τ_g , rather

than the viscosity. Figure 29E demonstrates that the ‘polymeric Walden rule’ (dashed black line), though an excellent predictor of conduction for PEO and poly(propylene glycol) (PPG, another polyether), dramatically underestimates the conduction of PZILs, particularly as the polymer approaches its T_g ($\tau_g \rightarrow 100s$). The Walden prediction ($\Lambda \sim D_i \sim \tau_g^{-1}$) is adapted from liquid-state electrolyte theory and corresponds to a conduction mechanism enabled by local fluid rearrangements. This prediction also distinguishes ‘superionic’ from ‘subionic’ conductors, where materials with conductivities exceeding the value expected from the Walden model are designated ‘superionic.’ The conductivity behavior of the PZIL ($\tau_g(T)$, determined from rheology measurements (D.1.7)) strongly deviates from Walden predictions, with ionic conductivities at the glass transition temperature ($\tau_g(T_g) = 100$ s) exceeding SPE expectations by nearly 9 orders of magnitude. This decoupling is reminiscent of inorganic solids, such as superionic ceramics (I include $(Ag)_{0.5}-(AgPO_3)_{0.5}$) as a reference in Figure 29E), which suggests that the PZILs exhibit a solid-like structural motif that enables superionic behavior.

C.2 The PZIL Ion Conduction Mechanism Arises from Ordered Subdomains that Promote Superionic Mobility

The superionic conductivity of the PZIL arises from ordered regions within the electrolyte, which act as pathways for facile, size-selective ion motion. wide angle x-ray scattering (WAXS) measurements demonstrate the presence of both ordered and amorphous features, as shown in Figure 92A and schematically represented in Figure 92B. The amorphous fingerprint manifests as a shouldered, broad peak ranging from $q \sim 1-2.5 \text{ \AA}^{-1}$. This amorphous halo reflects polymeric segment-segment correlations¹⁴⁴⁻¹⁴⁵. The presence of sharper Bragg reflections that

are most prominent in the absence of added salt and are weak at the highest salt loading suggests a structural order arising from the zwitterionic species, likely driven by electrostatic interactions between the zwitterions. This type of side chain ordering has been reported in zwitterionic polymers¹⁴⁶⁻¹⁴⁷ and other systems¹⁴⁸. The side chain ordering in the present PZIL is confirmed by comparison of the scattering pattern of the neat polymer ($r = 0$) with that of a small molecule analog of the pendant zwitterionic groups (Figure 93B). The structural similarity between the two crystalline structures is evident from the matching of the three primary peaks. The incomplete matching of higher-order peaks is unsurprising because the constraint of backbone attachment is likely to affect fine structural features. The similarity between the crystal structure of the small molecule analog and the polymer crystallites is further supported by thermal analysis (D. 6).

This data shows that these Im-TFSI based polymer electrolytes display two distinct diffusing environments, which may correspond to the ‘ordered’ and ‘amorphous’ regions of the PZIL. Further ^7Li and ^{19}F 1D NMR, NMR relaxometry ($T_{1\rho}$), and pulsed-field gradient NMR (D.9) experiments allow atomic-scale insights into these transport environments and provide details on the supporting sub-micron diffusion processes. Significantly, in all three NMR measurements (D.7), I observe two distinct ^7Li populations with very different dynamics. These measurements consistently show that ~25% of the lithium exists in a ‘fast’ environment that relaxes and diffuses nearly an order of magnitude more quickly than the second ‘slow’ lithium population ($D_{\text{Li,fast}}=7.6\cdot 10^{-12}$ m²/s, $D_{\text{Li,slow}}=9.2\cdot 10^{-13}$ m²/s at 358 K). Although these measurements cannot spatially distinguish motion through the amorphous and crystalline domains of the material, the presence of two lithium transport environments is suggestive of an inhomogeneous transport mechanism in which the ionic mobility of lithium

is impacted by the ordered domains of the electrolyte. In contrast, ^{19}F NMR analysis reveals a single dynamic population of fluorine, suggesting that fluorine motion is not enhanced by the polymer's dynamic heterogeneity. Due to the large size of the free TFSI $^{-}$ anion, its motion may be hindered through the ordered regions of the electrolyte, as predicted by random barrier-type models of ion conduction (see D.7).

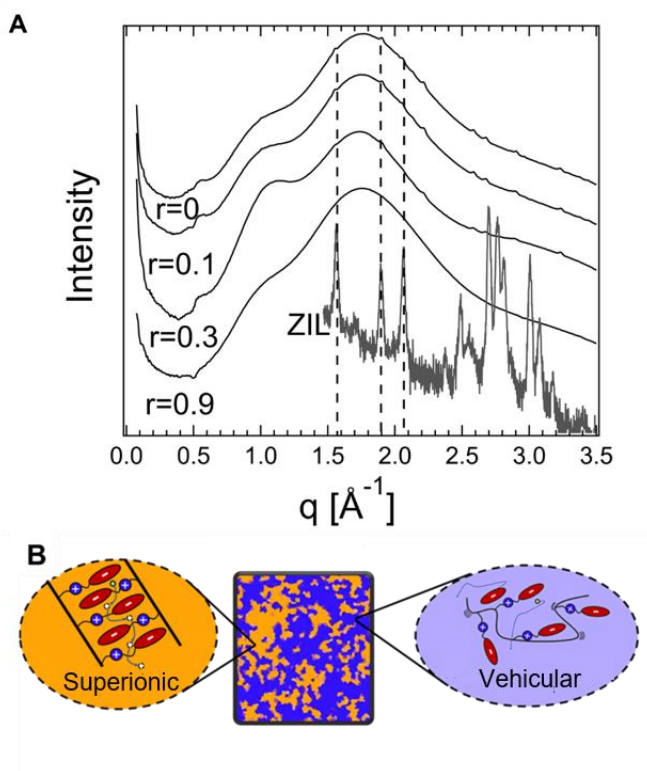


Figure 30: Structural analysis of the PZIL.

WAXS indicates the presence of two phases, one containing an ordered structure very similar to the small molecule on which the PZIL was based and another amorphous phase. A) WAXS curves demonstrate the presence of amorphous and ordered structures within the PZIL sample. The crystalline peaks of a small molecule analog for this material appear to match well with the Bragg peaks of the PZIL, suggesting a structural similarity between the structure of the small molecule crystal and the polymer. The small molecule scattering conforms to a $Pna2_1$ as detailed in section C4. B) Schematic representation of the

conduction mechanism in the polymer suggested by NMR Diffusometry. The amorphous domains are proposed to promote motion of lithium and its counterion through vehicular motion, the ordered domains are suggested to have high selectivity for lithium, transported via a superionic conduction mechanism.

C.3 Conduction Through Superionic Lattices Promotes High Cation Selectivity

The performance of Li-ion batteries is ultimately dictated by the lithium-ion flux rather than by the total ionic conductivity of the electrolyte. A more complete picture of electrolyte performance, therefore, considers the selectivity of the electrolyte as well as its conductivity, with cation transport and transference numbers being two practical metrics of electrolyte selectivity^{24, 71, 101}. The tradeoff between permeability (conductivity) and selectivity (transference) can be captured via analogy to a Robeson plot typically used to characterize separation membranes, as shown in Figure 31¹⁴⁹. A data aggregation study by Balsara and coworkers demonstrated a universal upper-bound on the Robeson plot (reproduced in the dashed line of Figure 31A) that is independent of polymer structure and backbone chemistry¹.

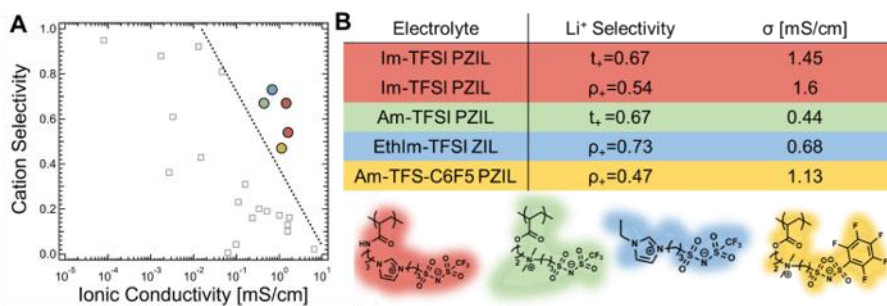


Figure 31: A) A Robeson-inspired plot of the PZIL.

The traditional tradeoff between ionic selectivity (transference or transport number) versus permeability (conductivity) is captured by the hypothetical upper-bound (dotted line). Unfilled symbols are values aggregated from a broad set of polymer electrolyte papers by Balsara and coworkers¹ demonstrating the observed upper bound for these systems based

on matrix molecular motion enabled ion transport. In comparison, the superionic PZILs studied here have comparable conductivities but much higher selectivities than the best conventional polymeric electrolytes. B) The table indicates the selectivity metrics and conductivities for PZIL electrolytes. ρ_+ indicates the electrochemically-determined limiting current fraction (D.9) and t_+ indicates the transport number determined by PFG-NMR (D.7). σ indicates the total ionic conductivity determined from EIS.

As shown in Figure 31A, the PZILs reported here surpass the universal upper bound reported by Balsara and coworkers¹ for polymer electrolytes, indicating an improvement in SPE design. Both the cation transport number (t_+ determined from PFG-NMR, see D.7) and the limiting current fraction (ρ_+ , evaluated for small potentials in D.9) indicate comparable lithium selectivities at 358 K, of 0.67 and 0.54, respectively, for the PZIL discussed thus far (Im-TFSI PZIL). Expanding on this design strategy, other PZILs (and a small-molecule ZIL, Figure 31B) with different cation/anion pairs demonstrate similar performance, and all exceed the previously observed upper bound in the Robeson-inspired plot. The simultaneously high conductivity and lithium selectivity of the PZIL suggests that engineering a solid-like and size-selective transport pathway into SPEs is a powerful strategy for outperforming the traditional ‘upper-bound’ of polymer electrolyte performance.

The grand challenge in the development of polymeric electrolytes has centered around designing electrolytes that are stiff, ionically conductive, and selective for lithium transport. Decades of work in polymer electrolyte research has suggested that ordered domains are deleterious for ion mobility within SPEs. This notion, however, is incompatible with superionic inorganic solid electrolytes, which depend on ordered lattices to enable selective ion motion. The present work demonstrates a new paradigm in which the advantageous mechanisms of inorganic electrolytes can be seamlessly integrated into organic polymers

through the molecular engineering of ordered domains, resulting in SPEs with unprecedented lithium-ion conduction and selectivity. These systems provide powerful motivation for further studies of organic crystals and polymeric zwitterionic liquids as tunable platforms for rapid and selective transport of target ions, though more studies are required to prove the in-operando stability of electrochemical cells based on these design principles.

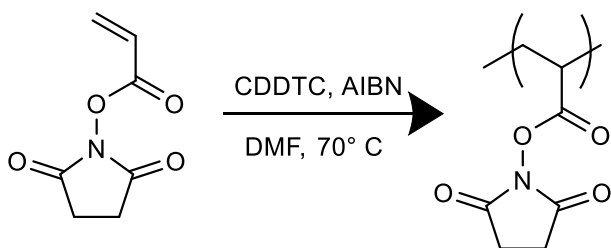
D. Appendix

D.1 Materials and Methods

1.1 Chemicals

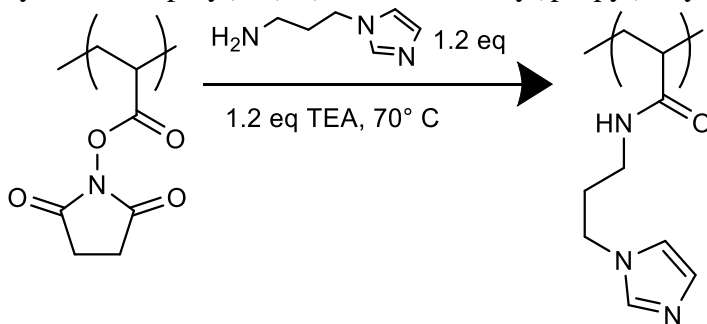
Acrylic acid N-hydroxy succinimide ester (NHS ester acrylate), trifluoromethanesulfonamide, and Sodium 3-Bromopropanesulfonate were purchased from TCI chemicals. The monomer was stored in a refrigerated compartment of a nitrogen containing glovebox until needed. Cyanomethyl dodecyl trithiocarbonate (CDDTC), aminopropyl imidazole, triethylamine (TEA), 3-Bromopropanesulfonic acid sodium salt, and 2,2'-Azobis(2-methylpropionitrile) (AIBN), and dimethylaminoethyl acrylate (DMAEA) were purchased from Sigma Aldrich. Diethyl ether (DEE), methanol (MeOH), tetrahydrofuran (THF), dichloromethane (DCM), and dimethylformamide (DMF) were purchased from Fisher chemicals. Lithium bis(trifluoromethanesulfonyl)imide (Li TFSI) was purchased from Solvonic and stored in a glove box until its use. Anhydrous casting solvents were purchased from Sigma Aldrich and placed and stored in a nitrogen containing glovebox before penetration of the sureseal container. AIBN was recrystallized 3x in methanol to yield white needle-like crystals which were stored at 0 °C.

1.2 Synthesis of poly(NHS-ester acrylate)



Controlled polymerization of poly(NHS ester acrylate) was performed via Reversible Addition Fragmentation Chain Transfer (RAFT) Polymerization as described by (Evans et al.). 5.246 g of NHS ester acrylate (31.01 mmol, 253 eq.), 39.0 mg of CDDTC (0.123 mmol 1 eq.), and 3.3 mg of AIBN (0.02 mmol, 0.16 eq.) were added to 10 mL of DMF in a 100 mL round bottom flask with a Teflon stir bar. The solution was sparged under stirring with Nitrogen gas and placed in a thermostated oil bath at 70°C for 18 hours. An aliquot for analysis was taken before the reaction began and immediately before quenching the reaction solution by placing the flask in an ice bath and opening the reactor to ambient conditions.

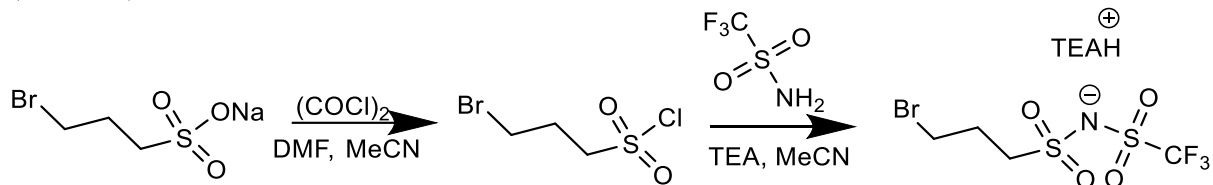
1.3 Synthesis of poly(N-(3-(1H-imidazol-1-yl)propyl)acrylamide)



After quenching the polymerization, 1.2 eq. (relative to the monomer) of Aminopropyl imidazole (4.658 g) and TEA (3.761 g) were added to the polymerization reactor. The reaction mixture was returned to the thermostated bath (70°C) for another 24 hours under stirring. Over this period a small amount of white solid (TEA salts) precipitated from solution. The solution was filtered to remove this solid and subsequently precipitated into 100 mL of DEE to yield a viscous yellow fluid. This fluid was redissolved in THF and

precipitated again in DEE. The product was collected and dried in vacuo to yield a yellow solid.

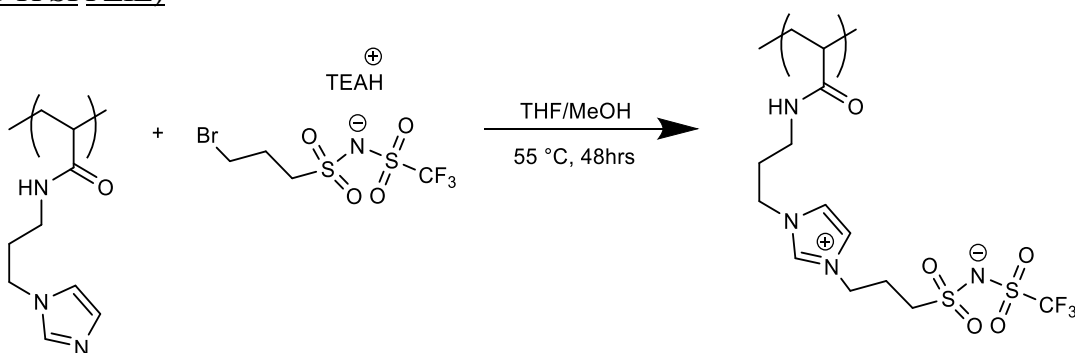
1.4 Synthesis of ((3-bromopropyl)sulfonyl)((trifluoromethyl)sulfonyl)amide triethylamine salt (TFSI-Br)



A Schlenk flask with a Teflon coated stir bar was charged with 1 g of 3-Bromopropanesulfonic acid sodium salt. Vacuum was pulled on the powder till the vacuum reached a baseline of $\sim 10^{-2}$ torr and the solution was repressurized with nitrogen. 5 mL of anhydrous acetonitrile was added to the flask and stirred rapidly to form a suspension. Meanwhile, a second flask was charged with 5mL acetonitrile and 0.68 g (1.2 eq.) oxalyl chloride and placed under an active nitrogen sparge. After a few minutes of degassing, a catalytic (several drops) quantity of dry DMF was added to the flask. This flask was stirred for 30 minutes and adopted a yellowish color. After the activation of the oxalyl chloride, the Schlenk flask containing the suspension of the sulfonic acid was chilled to 0°C and the oxalyl chloride solution was added dropwise. The solution was allowed to slowly warm to room temperature overnight leaving a yellowish solution with a white crystalline precipitate. The liquid phase was transferred via syringe to a new Schlenk flask, leaving behind the precipitate. The precipitate was washed with an additional of 3mL of dry acetonitrile to capture additional entrained product. This wash was also syringe transferred to the same Schlenk flask.

A third Schlenk flask was charged with trifluoromethanesulfonamide 0.66 g (1 eq.) and dried to baseline before adding anhydrous TEA 0.79 g (3 eq.) and 2 mL of anhydrous acetonitrile. This solution was stirred for several minutes and added dropwise via cannula to the sulfonyl chloride containing flask at 0 °C. The addition of this solution resulted in immediate formation of white precipitate. This flask was stirred and allowed to reach room temperature overnight. After the overnight rest, the quantity of precipitate increased and the solution had turned brownish-yellow color. This solution was filtered to remove the salts and concentrated by rotatory evaporation to yield a brown oil. This oil was diluted in DCM and washed with distilled water and a dilute aqueous hydrogen chloride solution (0.5 M), in a separatory column. The organic layer was dried over magnesium sulfate and further dried in vacuo to yield a viscous brown oil. Conversion was verified by ¹H and ¹⁹F NMR spectroscopy. ¹H NMR (600 MHz, Chloroform-d) 3.64 (t, J = 6.4 Hz, 1H), 3.27 – 3.21 (t, J = 7.4 Hz, 1H), 3.15 (qd, J = 7.3, 4.9 Hz, 6H on a triethylamine basis), 2.29 – 2.21 (m, 1H), 1.29 (t, J = 7.3 Hz, 9H on a triethylamine basis).

1.5 Quaternization of poly(N-(3-(1H-imidazol-1-yl)propyl)acrylamide) to Polyzwitterion (Im-TFSI PZIL)



2 g of the dried polymer was redissolved in 8 mL of a 1/1 v/v mixture of THF and MeOH along with 1.5 eq. of Br-TFSI-TEA. The solution was sealed and heated to 55 °C for

48 hours. After 48 hours the solution was concentrated by rotatory evaporation and precipitated into isopropanol to yield a brown solid. The solid was thoroughly washed with IPA, redissolved in DMF and dialyzed (8 kDa Mw cutoff) against MeOH for 5 days with a solvent exchange once per day. The bulk solution remained optically clear even after contact with dialysis solution for 24 hrs. The final product was precipitated one final time in DEE to collect a brown leathery solid. This product was dried in vacuo for 48 hours at 80 °C before salt incorporation. BigSmiles representation:

OC(=O)C(C)(C){[<]CCC(=O)NCCCn1cc[n+](CCCS(=O)(=O)[N-]
]S(=O)(=O)C(F)(F)F)c1[>]}SC(=S)SCCCCCCCCCCCC

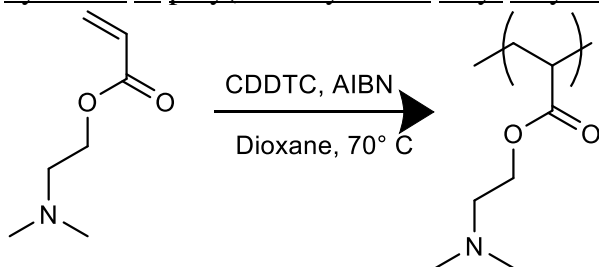
1.6 Salt Incorporation

Li⁺/TFSI⁻ salts were incorporated into the PZIL by solution casting. In a nitrogen containing glovebox, polymer was dissolved in anhydrous MeOH and a stock solution of Li⁺/TFSI⁻ salt in anhydrous MeOH was prepared via gravimetric measurements. Salt concentration was controlled by volumetric addition of stock solution via a positive displacement micropipette. The solutions were blended until all components were mutually soluble and subsequently flash frozen in liquid nitrogen and placed in vacuo to remove solvent. Polymers were dried for 24 hours at ~10⁻³ torr in a vacuum oven at room temperature, then for an additional 24 hours at 70°C. These materials were transferred to an ultra-high vacuum oven at 10⁻⁸ – 10⁻⁹ torr for 24 hours at 55 °C and finally transferred to a nitrogen-containing glovebox for all storage and sample preparation. Salt concentration is parameterized by the molar ratio, ‘r’, of salt to zwitterionic residue ($r = [\text{Li}^+/\text{TFSI}^-]/[\text{ZI}]$).

1.7 Synthesis of 3-(1-ethyl-1H-imidazol-3-ium-3-yl)propane-1-sulfonate (SO₃-Imidazole ZIL)
1.8 Synthesis of ((3-(1-ethyl-1H-imidazol-3-ium-3-yl)propyl)sulfonyl)((trifluoromethyl)sulfonyl)amide (TFSI-Imidazole ZIL)

0.4 g of 1-Ethyl-imidazole and 2.1 g of TFSI-Br were added to a vial along with 10 mL of acetonitrile and a stir bar. The solution was heated to 60°C under stirring for 96 hours. Stirring, the product was worked up first by precipitation 2x in isopropanol, resulting in a dark viscous liquid. This liquid was subsequently washed repeatedly with dichloromethane until the DCM phase appeared to absorb no color from the wash. After washing with DCM, a brown powdery product was isolated. The powder was dried in a vacuum oven at 70°C for 48 hours before transferring to a glovebox for all handling. ¹H NMR (600 MHz, DMSO-d₆) δ 9.16 (s, 1H), 7.78 (s, 2H), 4.28 (t, J = 7.1 Hz, 2H), 4.16 (q, J = 7.3 Hz, 2H), 2.99 (t, J = 7.4 Hz, 2H), 2.27 – 2.06 (p, J=7.2 Hz 2H), 1.40 (t, J = 7.3 Hz, 3H). ¹³C NMR (151 MHz, dmso) δ 136.40, 122.81, 122.69, 51.52, 47.81, 44.70, 25.30, 15.31.

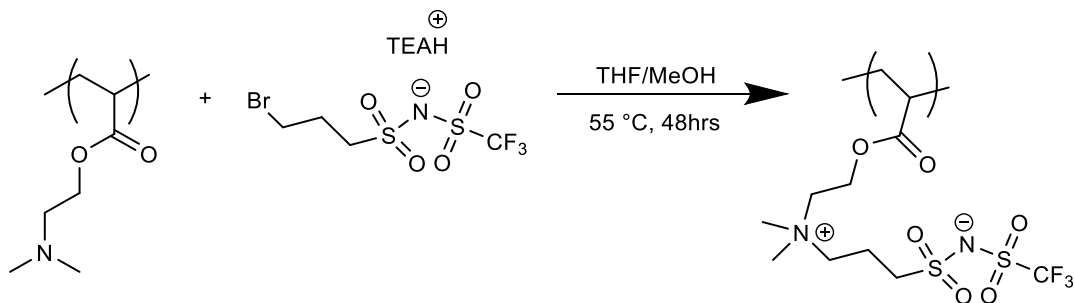
1.8 Synthesis of poly(dimethylamino ethyl acrylate) (PDMAEA)



DMAEA was polymerized using standard RAFT techniques. DMAEA monomer was passed through a basic alumina plug to remove inhibitor immediately prior to use (note: it can be difficult to remove inhibitor from this monomer and a second plug was used to attain a clear-colored monomer). The monomer (14.6 g, 0.102 mol, 250 eq.) was added to a heavy-walled and oven-dried reaction flask along with a stir bar, DDMAT (0.148 g, 0.41 mmol, 1eq.), and AIBN (7mg, 0.04 mmol, 0.1 eq.) and 30mL of 1,4 dioxane. The reaction mixture was sparged with nitrogen and submerged in a thermostated oil bath at 70°C under moderate stirring. The reaction was allowed to proceed for 18 hours before quenching by submerging

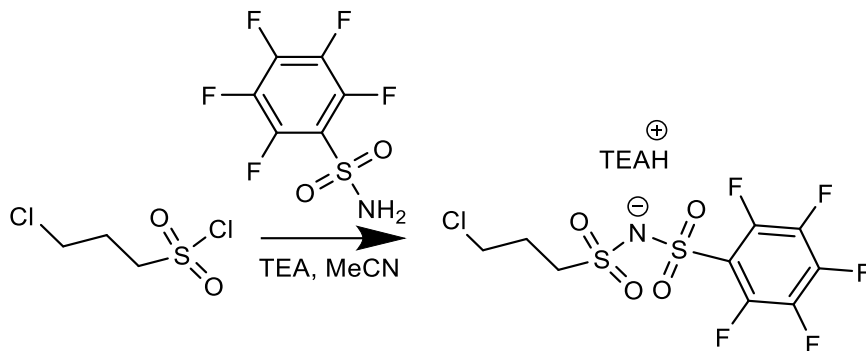
the reactor in an ice bath and exposing the reaction mixture to air. The polymer was purified by precipitation twice in cyclohexane and dried in vacuo to yield a viscoelastic liquid.

1.9 Quaternization of PDMAEA to Polyzwitterion with TFSI Anion (Am-TFSI-PZIL)



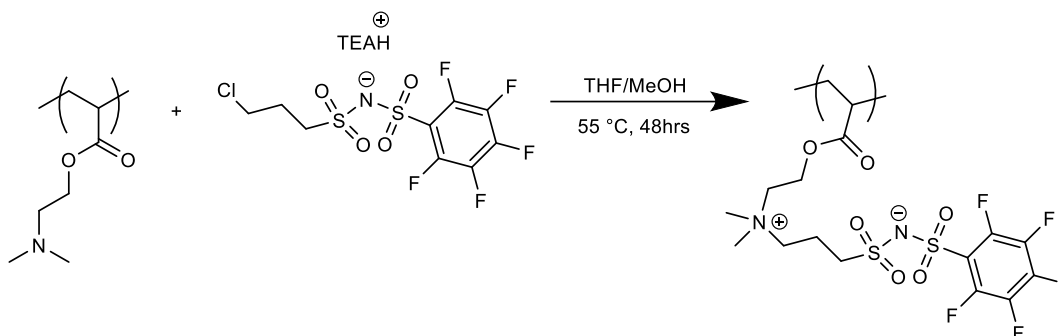
2 g of the dried polymer was redissolved in 8 mL of a 1/1 v/v mixture of THF and MeOH along with 1.5 eq. of Br-TFSI-TEA. The solution was sealed and heated to 55 °C for 48 hours. After 48 hours the solution was concentrated by rotatory evaporation and precipitated into isopropanol to yield a brown solid. The solid was thoroughly washed with IPA, redissolved in DMF and dialyzed (8 kDa Mw cutoff) against MeOH for 5 days with a solvent exchange once per day. The bulk solution remained optically clear even after contact with dialysis solution for 24 hrs. The final product was precipitated one final time in DEE to collect a brown leathery solid. This product was dried in vacuo for 48 hours at 80 °C before salt incorporation.

1.10 Synthesis of ((3-chloropropyl)sulfonyl)((perfluorophenyl)sulfonyl)amide triethylamine salt (Cl-TFS-C6F5)



A Schlenk flask was charged with pentafluorophenylsulfonamide [1.02 g, 4.1 mmol] and dried to baseline before adding anhydrous TEA [1.73 mL, 12.4 mmol] and 5 mL of anhydrous acetonitrile. Sulfonyl chloride [0.5 mL, 4.1 mmol] was added dropwise to this stirring solution at 0 °C. The addition of the sulfonyl chloride resulted in immediate formation of a white precipitate. This flask was stirred and allowed to reach room temperature overnight. After the overnight rest, the quantity of precipitate increased and the solution had turned brownish-yellow color. This solution was filtered to remove the salts and concentrated by rotatory evaporation to yield a brown oil. This oil was diluted in DCM and washed with distilled water and a dilute aqueous hydrogen chloride solution (0.5 M), in a separatory column. The organic layer was dried over magnesium sulfate, solvent removed in vacuo to yield a viscous brown oil and used in the subsequent step without further purification. Conversion was verified by ^1H and ^{19}F NMR spectroscopy. ^1H NMR (600 MHz, Chloroform- d) δ 3.70 (t, J = 6.4 Hz, 2H), 3.33 (t, J = 7.3 Hz, 2H), 3.19 (qd, J = 7.3, 4.8 Hz, 6H on TEA Basis), 2.35 (tt, J = 13.8, 13.5, 7.5, 7.2 Hz, 2H), 1.38 (t, J = 7.3 Hz, 9H on TEA Basis). ^{19}F NMR (564 MHz, cdCl_3) δ -79.05, -116.72, -117.24.

1.11 Quaternization of PDMAEA to Zwitterion with TFS Anion with Pentafluoro Group



0.277 g of the dried polymer was redissolved in 4 mL of a 1/1 v/v mixture of Acetonitrile and MeOH along with 1.5 eq. of Cl-TFS-C6F5-TEAH (1 g). The solution was sealed and heated to 55 °C for 48 hours. After 48 hours the solution was concentrated by rotatory evaporation and precipitated into isopropanol to yield a brown solid. The solid was precipitated and thoroughly washed with IPA. This product was dried in vacuo for 48 hours at 80 °C before salt incorporation.

1.12 Rheological Studies

Rheological measurements were made on an ARES-G2 strain-controlled rheometer manufactured by TA instruments. Stainless steel 8 mm parallel plates were used for all measurements. Samples were prepared for rheology by compression molding into a disc mold before loading. Rheology samples were further compressed at 70 °C and 5N of force on the rheometer instrument. During operation all samples were enclosed in a nitrogen-purged oven chamber. Final sample thicknesses were maintained within a range of 0.3-0.5 mm. All measurements were made in the ‘linear regime’ as determined via strain sweep measurements. Temperature-dependent frequency measurements were performed as a sequence of experiments with 5 minutes of soak time between steps. To investigate long-time responses of the materials a stress relaxation experiments was also performed, however the terminal region could not be located.

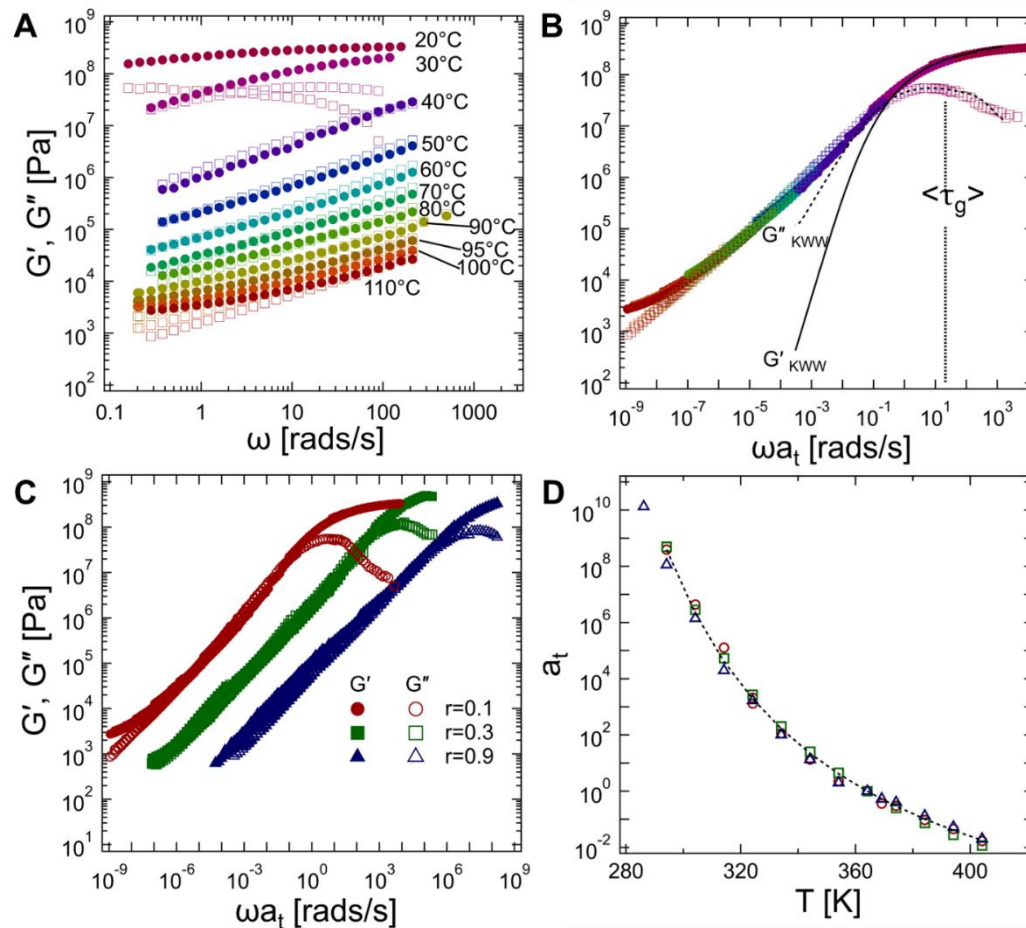


Figure 32: Rheology analysis of the PZIL.

A) Individual frequency sweep curves from the $r=0.1$ zwitterionic system with closed symbols representing the storage modulus (G') and open symbols representing the loss modulus (G''). B) The master curve for the $r=0.1$ system generated by shifting in frequency only and generated at a reference temperature of 303K. Solid and dotted fit lines correspond to the fitting of the glassy region to the KWW relation (Equation 14), which provides a phenomenological description of the glass transition. The marked τ_g curve represents the mean glassy relaxation timescale as estimated by the KWW fit. C) Master curves for all salt loaded polymers display similar behavior. The reference temperature of the $r=0.1$ curve is 303K, the $r=0.3$ and $r=0.9$ were selected at the same reference temperature and shifted by factors of 10^3 and 10^6 respectively so they can be more easily visualized in a single figure. D) The shift factor versus temperature curves for all salt loadings with a reference temperature of 90° C.

Since the structural relaxation rate generally plays a critical role in dictating the ionic conductivity of an electrolyte, it is useful to evaluate the ionic conduction performance of a material in the context of its structural relaxation rate. Frequently, the calorimetrically-determined glass transition temperature is the sole metric of polymer dynamics and ionic conductivity is classified in terms of the temperature difference from T_g i.e., ' $T-T_g$ '. This simplistic treatment of polymer dynamics is insufficient for fundamental studies of ion conduction as it cannot account for the nonlinear temperature dependence of polymer dynamics. Consequently, it is important to contextualize ion dynamics in terms of measured ion dynamic timescales.

Linear viscoelastic measurements are a robust means of assessing the temperature-dependence of polymer dynamics. Figure 32A shows individual frequency sweeps at small oscillatory strains of the $r = 0.1$ PZIL at various temperatures. Transformation of these curves by time-temperature superposition (TTS) yields the master curve shown in Figure 32B. Although TTS does not rigorously apply to thermo-rheologically complex materials, these master curves are nonetheless useful in determining dynamics over a broad range of frequencies. The master curve in Figure 32B displays typical glassy behavior at high effective frequencies (ωa_T) with a plateau in the storage modulus in the gigapascal regime and a local maximum in the loss modulus. This glassy regime was fit by the Kohlrausch-Williams-Watts (KWW) expression for the time-dependent modulus $G(t)$ (Equation 14), a common phenomenological model for the glassy relaxation of polymers, which has been expressed in terms of its first moment, τ_g , corresponding to the average timescale of segmental rearrangement (note: fitting was performed in frequency space as described in my

previous work¹⁵⁰, fitting utilized the ‘libkww’ library which provides an approximation for the Fourier transform of stretched exponential functions¹¹⁰). The ‘ β ’ parameter in this expression corresponds to the breadth of the glass transition, approaching unity in the case of a uniform relaxation and broadening as it approaches zero. The reference temperature in Equation 14 is the same as the reference temperature used to generate TTS curves (303 K). This glass transition is followed at longer effective times by a collective relaxation with scaling behavior $G' \approx G'' \sim \omega^{-0.5}$ and finally, a long-lived plateau that is confirmed by stress relaxation experiments (Section D8). This relaxation scaling behavior and plateau is consistent with a percolated network of ionic crosslinks that results in long-lived elastic behavior¹⁵¹, though detailed analysis of the viscoelastic behavior of the system is beyond the scope of this study.

$$G(t, T = T_{\text{ref}}) = G_g(0) \exp \left[- \left(\frac{t \Gamma(\beta^{-1})}{\tau_g(T_{\text{ref}}) \beta} \right)^\beta \right] \quad \text{Equation 14}$$

This construction and fitting of the master curves (Figure 32C) enables determination of the segmental relaxation timescale and its temperature dependence, $\tau_g(T)$, which is critical in understanding the overall polymer dynamics. Equation 15 illustrates the procedure used to generate the $\tau_g(T)$ function where $a_T(T)$ corresponds to the shift factor functions in Figure 32. These functions are used to generate the Walden plot (Figure 29E).

$$\tau_g(T) = \tau_g(T_{\text{ref}}) a_T(T) \quad \text{Equation 15}$$

1.13 Density Measurements

The densities of materials were estimated from weighing discs of the material that were produced by the melt pressing techniques described in 1.10. The discs of material were never exposed to air during the measurements to prevent complications from water uptake.

1.14 X-ray Scattering

Samples were placed on a Kapton film suspended across a stainless-steel washer and were dried and annealed in an inert atmosphere at 80 °C. These samples were transferred to a glovebox where they were sealed in a nitrogen atmosphere. Measurements were conducted at the National Synchrotron Light Source II (NSLS-II, beamline 11-BM, Brookhaven National Laboratory) with an X-ray energy of 13.5 keV and beam exposures of 10 seconds. Wide-angle x-ray scattering measurements were taken at two detector distances and combined to generate a single image.

1.13 Density Measurements

The densities of materials were estimated from weighing discs of the material that were produced by the melt pressing techniques described in 1.10. The discs of material were never exposed to air during the measurements to prevent complications from water uptake.

1.14 X-ray Scattering

Samples were placed on a Kapton film suspended across a stainless-steel washer and were dried and annealed in an inert atmosphere at 80 °C. These samples were transferred to a glovebox where they were sealed in a nitrogen atmosphere. Measurements were conducted at the National Synchrotron Light Source II (NSLS-II, beamline 11-BM, Brookhaven National Laboratory) with an X-ray energy of 13.5 keV and beam exposures of 10 seconds. Wide-angle x-ray scattering measurements were taken at two detector distances and combined to generate a single image.

1.15 Polymer Melt Pressing

Polymer melt pressing was accomplished using the VCM Essentials tool manufactured by MeltPrep. This melt press tool makes use of a vacuum compressive force to melt samples into well defined disc geometries in the absence of air. Polymers were melt pressed at a temperature of 50°C using the standard lid, which applies 16.5 bar of compaction pressure to the sample. Polymer samples were allowed to cool without active cooling and the geometry was disassembled in the glovebox. For the small molecule zwitterion samples, the processing temperature was set at 170°C. An ultra-low pressure lid setup was used, which applies <0.3 bar of pressure to the sample. After 3 minutes, the sample was transferred to active cooling. The ZIL samples were allowed to fully cool and rest for >48 hours before removing the separation foils. This cooling allowed the ZIL to crystallize completely to a dark solid material.

1.16 Blocking Electrode Electrochemical Impedance Spectroscopy Measurements

Electrochemical impedance spectroscopy (EIS) measurements were performed on polymer samples measured in a through-plane disc geometry with gold blocking electrodes. Electrodes were cleaned prior to use by subsequent 5-minute sonication steps in deionized water, isopropanol, and acetone followed by a 5-minute UV/ozone treatment. In a nitrogen containing glovebox, a disc of polymer was punched out from a uniform film and placed onto the clean electrodes. The polymer was sized to cover the entire electrode area so that no capacitive contribution from spacer materials could contribute to the measurement. The thickness of the electrolyte was monitored with a Mahr 1087R micrometer, which offers resolution to the nearest +/- 0.002 inches. The electrolyte was heated to 120°C and compressed with a spring. Once the thickness remained stable for 20 minutes, the electrode assembly was placed into a controlled environment sample holder (CESH) manufactured by BioLogic, sealed under nitrogen in the glovebox, and placed in an integrated temperature

stage (ITS). The temperature of the stage was monitored during measurement by a thermocouple which was placed in contact with the sample slide. EIS sweeps were performed at temperatures ranging from -30 to 115 °C with 10 minutes of isothermal hold time after the set temperature was reached. Potentiostatic EIS was performed with a frequency range of 1 MHz to 10 mHz and an amplitude of 100 mV, which was found to correspond to the linear region of behavior. A second reverse sweep (from low to high frequency) was performed to check for hysteresis, which was not found to play a significant role. Temperature was sampled from low to high temperatures, incrementing 5°C every measurement and then the experiments were repeated in a reverse Temperature ladder (stopping at room temperature). No significant hysteresis effects associated with the temperature ramp were found. The sample cell was unloaded in the glovebox and the thickness of the electrolyte was measured with a micrometer. Differences in the initial and final thicknesses were less than 1% changes in every case. The dc-ionic conductivity was taken to be the value of the real part of the conductivity (σ') at the maximum in the loss tangent (see Section D4 for raw EIS curves). I note here that, in light of the sluggish crystallization dynamics of this material as observed by DSC, there may be a time-dependent element to the ionic conductivity of these materials as the structure evolves, here I report the initial properties of the PZILs after they are annealed and leave any studies regarding their long-term performance to future works.

1.17 Differential Scanning Calorimetry

Differential scanning calorimetry (DSC) measurements were performed on a TA Instruments DSC 2500. Approximately 6 mg of each polymer sample was weighed and loaded into aluminum 'Tzero' pans with hermetically sealed lids. All samples were heated to

160° on an initial heating cycle and cooled to -80°C. Glass transition measurements were recorded on the second heating cycle at a ramp rate of 20°C/minute. The glass transition temperature was analyzed via the midpoint analysis method.

1.18 Solid State NMR:

NMR measurements were performed on a Bruker 300 MHz super wide bore ultrashield spectrometer using a Diff50 probe. NMR samples were prepared inside an Argon-containing glovebox by loading the polymer inside a 4 mm alumina rotor. The rotor is then placed in an airtight 5 mm Young's valved NMR tube. Resonant frequencies of 116.6 MHz and 282.4 MHz were used for ^7Li and ^{19}F , respectively. Chemical shift calibrations were done using 1 M NaF (Aq) (-118 ppm) and 1 M LiCl (Aq) (0 ppm). 90° pulse durations were calibrated to be 15.4 μs (16.2 kHz) at 100 W and 11.25 μs (22.2 kHz) at 50 W for ^7Li and ^{19}F , respectively. T_1 relaxation times were measured using a standard saturation recovery pulse sequence. The temperature was controlled using a N₂ flow rate of 800 L hr⁻¹. 1D spectra were measured with a standard 90° pulse and acquire sequence with a recycle delay of around $5 \cdot T_1$.

Pulse-field gradient NMR was performed using a standard Bruker diffusion pulse sequence (diffste), with stimulated echo pulses to protect the signal from shorter relaxation times in these solid-like samples. Diffusion constants could only be measured at 90°C for Li⁺ (^7Li) but was measured for 90°C to 60°C for TFSI⁻ (^{19}F), where short relaxation times were the limiting factor for measurement. The gradient strength, gradient duration, and diffusion time were varied for each measurement to acquire the full decay curve.

1.19 Size Exclusion Chromatography

Size exclusion chromatography was performed on a Waters instrument using a refractive index detector and Agilent PL gel 5 μm MiniMIX-D column. THF at 35 °C was used as the mobile phase with a flow rate of 1.0 mL/min. Polydispersity was determined against narrow polystyrene standards (Agilent).

1.20 Uniaxial Extension Experiments

Precut and premeasured strips of polymer film were loaded into a DMA 850 instrument manufactured by TA instruments with a tension clamp geometry installed. The oven was closed after loading the sample and a nitrogen purge stream was used to equilibrate the sample temperature at 25 °C for 5 minutes. The sample was prestrained to a force of 0.1N and the initial sample length was recorded at the prestrained sample length. After prestraining, the sample was deformed at a constant strain rate of 1mm/minute in accordance with a protocol defined by ASTM D1708. Due to the limited deformation range of the instrument, the samples could not be strained to break, but were strained to the maximum deformation length of the instrument before the run was terminated. The Young's modulus (E) of the materials was calculated using the slope of the initial deformation. The toughness of the materials cannot be directly estimated since the samples were not fractured during extension, but numerical integration of the experimental data using a cubic spline was used to establish a lower bound for the toughness of the materials.

1.21 ZIL X-Ray Diffraction Experiments

X-ray diffraction of the crystalline ZIL was performed on a disc of powder which had been compressed at 5 tons of ram force. This disc was placed onto a zero-background silicon plate and loaded into an Empyrean XRD Diffractometer. The x-ray energy wavelength was 1.54 Å.

1.22 Limiting Current Measurements

Lithium-lithium symmetric cells containing the polymer electrolyte were prepared to measure the PZIL's transference number. The electrolyte was first melt pressed as described in 1.10. Lithium foils were purchased from Sigma Aldrich and a punch was used to obtain circular electrodes. A cell was assembled within the CESH (controlled environment sample holder) assembly, illustrated in Figure 33, with lithium electrodes and a gold-coated steel current collector.

These cells were allowed to rest overnight before loading into the ITS temperature-controlled chamber. The cells were heated up to 83°C and allowed to equilibrate for 4 hours. After 4 hours, the open-circuit voltage of the cell was measured and was found in all cases to have a magnitude of <1mV. An unbiased EIS step was run prior to polarization with a wide frequency range (5 MHz to 10 mHz). After a 30-minute rest step the polarization was initiated. Cells were first polarized at 20 mV (this small voltage acts as a small disturbance and is not anticipated to result in any significant electrochemical reaction), and a constant potential was then applied across the cell until a steady state was reached. Every 20 minutes an EIS step was performed with a bias equal to the polarization potential of the cell. This step used a small sinus amplitude (10 mV) and a smaller frequency range (1MHz to 1Hz) to minimize the distortion of the polarization curve. Once the cell reached a constant equilibrated current, a final unbiased EIS step was taken over a larger frequency range again.

1.23 Single-crystal Structural Analysis

Large single crystals of the TFSI-Imidazolium-ZIL were prepared by 3x recrystallization of the ZIL compound in hexanes and placed in vacuo for storage until the measurement could be made. After 3 recrystallizations, the ZIL maintained the slight brown color that was

characteristic of all polymers used in the study. The persistent coloration despite the high purity inherent to large single-crystalline product is evidence that any discolored impurity is scant in these materials. The single crystals were analyzed using a Kappa Apex II Diffractometer with active nitrogen flow to prevent uptake of water by the ZIL.

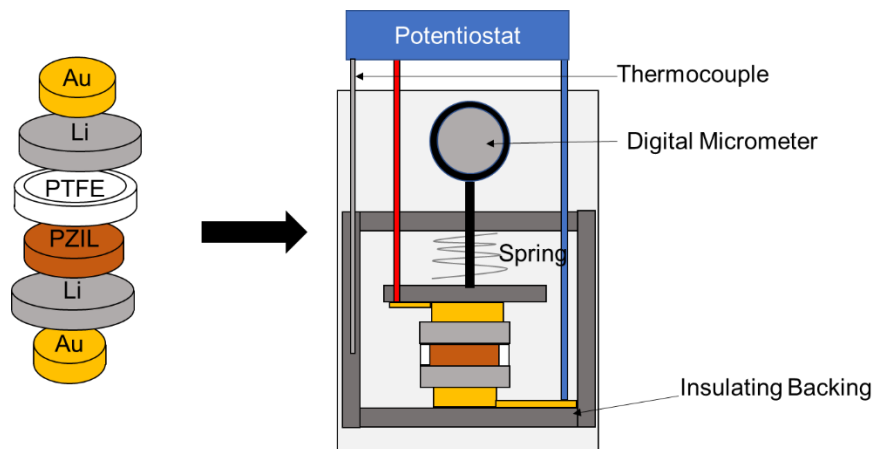


Figure 33: Limiting current measurement setup.

These measurements are performed using gold-plated steel current collectors and lithium electrodes. A PTFE spacer is used to set the thickness of the cell stack during testing, as well as to contain the PZIL sample. During measurement, the cell assembly is loaded into an inert-gas environment with temperature control.

1.24 Thermogravimetric Analysis

Thermogravimetric analysis (TGA) was performed on the materials to monitor their thermal stability and to confirm removal of volatiles. TGA was performed using a TA instruments Discovery TGA with an aluminum hangdown pan and an Aluminum oxide crucible. Sample masses of ~2mg were loaded into pre-tared crucibles in an air environment. The samples were exposed to a thermal ramp of 10°C/minute from room temperature to 600°C under an inert nitrogen atmosphere.

1.25 Electrochemical Stability Testing

The electrochemical stability of the PZIL electrolyte was tested through galvanostatic cycling of a lithium half-cell composed of a composite PZIL cathode and a lithium metal anode. The composite PZIL cathode was prepared by hand mixing the PZIL with carbon additives and PTFE binder in a 72:18:10 ratio by mass. Cathodes were punched out with loadings between 5.5 mg cm^{-1} and 8.0 mg cm^{-1} . Electrochemical tests were carried out using a Swagelok cell, a Whatman GF/D glass fiber separator, a 1 M LiPF_6 in ethylene carbonate and dimethylcarbonate (50/50 by volume, Sigma Aldrich) electrolyte, and a lithium foil anode (Sigma Aldrich). Two cells were prepared to gauge stability at high and low voltages separately, and cycled at a rate of 2.5 mA per gram of PZIL.

1.26 Safety

Oxalyl chloride or $(\text{COCl})_2$ is a compound which can present hazards to unaware users. Though it is well known that this compound can react violently with water, it is not as well known that the same effect may be produced in nonaqueous environments if steps are not taken to contain the reaction. The reaction steps for Swern-Oxidation should be followed as described above with the formation of the catalytically active $(\text{COCl})_2$ prepared in a separate flask from the reactor containing the sulfonate. DMSO should be used in catalytic quantities during this reaction to prevent any violent reaction. Further the addition of the active oxalyl chloride to the sulfonate should take place at low temperature, high dilution, and slow addition rates since the reaction is highly spontaneous.

D.2 Limiting Current Fraction Analysis Using Symmetric Li/Li Cells

Although limitations such as electrode polarization limit the lengthscales that are probed by MHz electrochemical impedance spectroscopy to lengthscales comparable to the size of the electrical double-layer of the electrode, truly long-range ion transport must be accomplished in order to extract usable ionic current from an electrolyte. The Balsara-Bruce-Vincent type electrochemical measurements presented in this section are used as a simultaneous demonstration of DC ionic conduction in the presence of lithium plating and stripping reactions as well as a measure of the portion of current in the electrochemical cell which can be attributed to lithium motion. I note that, despite modern critiques¹⁵², these experiments represent the state-of-the-art method to understand the selectivity of polymer electrolytes. Although advanced electrophoretic NMR techniques may be able to give a more complete picture of transport in electrolytes, these methods have not been well validated in polymer electrolytes.

2.1 Analysis of EIS Data obtained on Li/Li symmetric cells containing the Im-TFSI PZIL r=0.9 electrolyte

The EIS scan collected on the Li/Li symmetric cell contains contributions from interfacial resistance as well as the bulk resistance of the Im-TFSI PZIL r=0.9 electrolyte. Consequently, an appropriate equivalent circuit contains two R/Q elements, as shown in Figure 34.

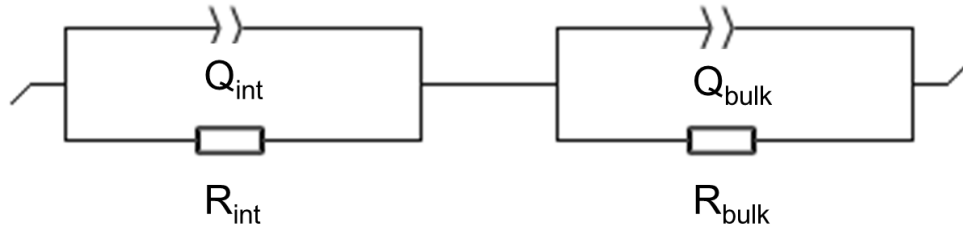


Figure 34: The Equivalent circuit model used to fit the EIS data in the Bruce-Vincent cell.

The above model is used to fit the EIS data collected prior to the start of the polarization experiments, and at 20-minute intervals during the experiment. Figure 35 shows a Cole-Cole representation of the data prior to polarization and after a steady current was reached. The parameters used to generate the fitting functions are given in Table 6.

Table 6: Values of Equivalent Circuit Fitting Parameters Before and After

Polarization

	Q_{int} [nF $\cdot s^{a_{int}-1}$]	R_{int} [k Ω]	a_{int} [-]	Q_{bulk} [pF $\cdot s^{a_{bulk}-1}$]	R_{bulk} [k Ω]	a_{bulk} [-]
Before Polarization	2.8 ₀₅	1.3 ₀₁₆	0.78 ₁₅	18.6 ₁	1.0 ₄₄₂	0.91 ₂₄
After Polarization	5.5 ₉₈	2.2 ₂₅₇	0.60 ₆₃	9.5 ₅	1.0 ₇₆₅	1.0

Henceforth, the values of these EIS fitting parameters are denoted with a subscript '0' when they refer to values measured prior to polarization, and with a subscript 'ss' when they refer to post-polarization values. A rise in the interfacial resistance is observed during the polarization process, but the bulk resistance remains largely unchanged. Although large changes in the impedance spectra are not observed, these small changes may be suggestive of some slight instability of the Li|PZIL interface. The electrochemical stability of the electrolyte is further discussed in C5.

For this cell, the cell area was 6.283 mm^2 and the cell thickness was 0.492 mm . This corresponds to a bulk ionic conductivity before polarization of 0.75 mS/cm , a value which is in relatively good agreement with the blocking electrode conductivity at this temperature of 0.89 mS/cm . These values are in good agreement and do not differ by greater than the experimental uncertainty of fitting.

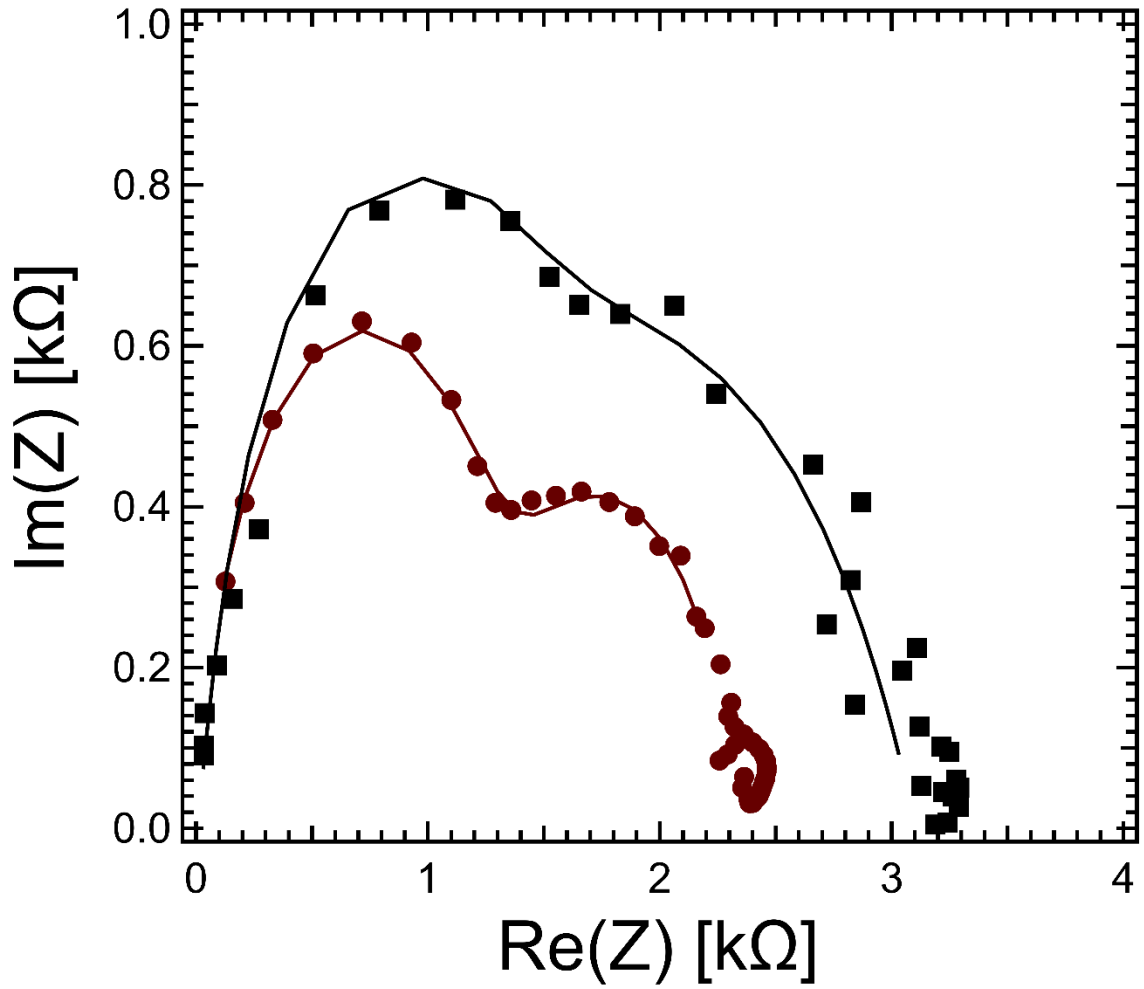


Figure 35: The EIS spectrum of the polymers before (red circle) and after (black square) polarization of the cell.

The markers indicate the measured points, and the solid lines indicate the fits to the equivalent circuit using the model depicted in Figure 34: The Equivalent circuit model used to fit the EIS data in the Bruce-Vincent cell. and the parameters in data Table 6.

2.2 Analysis of Polarization Current for Im-TFSI PZIL of $r=0.9$

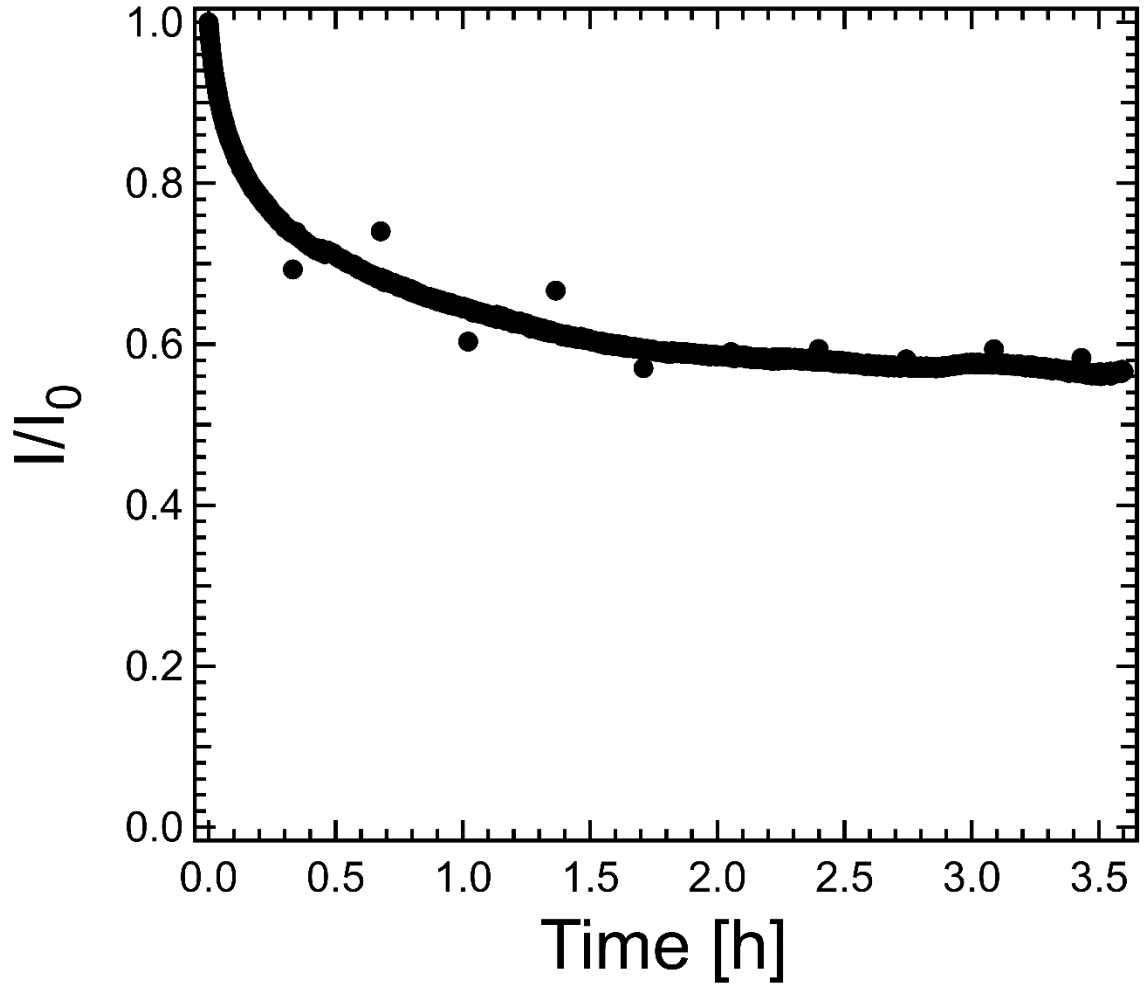


Figure 36: Normalized current versus time graph of the cell undergoing polarization.

In this case, the initial current I_0 ($8.33 \mu\text{Amperes}$) observed experimentally, and the calculated value of I_Ω ($8.53 \mu\text{Amperes}$), differ somewhat due to the delay between sampling the current and applying the polarization.

The normalized current of the cell is shown above. Equilibration of the cell takes 1-2 hours, which is consistent with other reports, though this equilibration time may vary based on factors such as the cell geometry and conductivity of the electrolyte. Outlier points can be

observed after each EIS step due to small disturbances in the voltage of the cell from the oscillating voltage applied during EIS.

The limiting current fraction is computed using Equation 16:

$$\rho_{+,0} = \frac{I_{ss}(\Delta V - I_0 R_{int,0})}{I_0(\Delta V - I_{ss} R_{int,ss})} \quad \text{Equation 16}$$

Where, in accordance with Balsara and coworkers, ρ_+ is used to define the limiting current fraction of the cell. The additional subscript of $\rho_{+,0}$ is used to clarify that this limiting current measure is based on the initial current measurement before polarization, I_0 . Since the current may rapidly decay in the first several seconds of measurement, a slightly more accurate measure of the limiting current can be determined using Equation 17:

$$\rho_{+,\Omega} = \frac{I_{ss}(\Delta V - I_\Omega R_{int,0})}{I_\Omega(\Delta V - I_{ss} R_{int,ss})} \quad \text{Equation 17}$$

Where I_Ω is defined in Equation 18:

$$I_\Omega \equiv \frac{\Delta V}{R_{int,0} + R_{bulk,0}} \quad \text{Equation 18}$$

I compute both estimates of the limiting current fraction, and I see a moderate difference using the two methods, due to the rapid decay of current and the finite amount of time required to sample the current. I report both metrics here but consider $\rho_{+,\Omega}$ to be a superior indicator of the limiting current fraction. This current fraction is sometimes reported as the

‘transference number’ in some literature but is reported here as the current fraction as this definition helps to distinguish it from the transference number, which has a strict definition relevant to electrochemistry.

Table 7: The two selectivity metrics determined from analysis of the symmetric Li/Li cell.

ΔV Cell [mV]	$\rho_{+,0}$	$\rho_{+,\Omega}$
20	0.56 ₉	0.53 ₈

Table 8: Some relevant information about the cell used in this experiment including the electrolyte area and thickness, the initial current, the initial current density (J_0), and the initial area specific interfacial resistance.

Area [mm ²]	Thickness [mm]	I_0 [μ A]	J_0 [μ A/mm ²]	$R_{int}/Area$ [k Ω /mm ²]
6.28 ₃	0.49 ₂	8.33	1.33	0.20 ₇

2.3 Analysis of EIS and Polarization data obtained on Li/Li symmetric cells containing the EthIm-TFSI ZIL $r=0.1$ Electrolyte

In the EIS data for the EthIm-TFSI ZIL $r=0.1$, it was found that a slightly altered equivalent circuit gave better and more consistent fitting. This alternative equivalent circuit is given in Figure 37. No significant interfacial resistance is detected in the EIS spectrum. This may be a result of the superior electrode-electrolyte contact present in the small molecule electrolyte, since this material can be cast as a liquid and was allowed to crystallize in contact with the lithium electrode or a consequence of the superior stability of the ZIL to the PZIL in the presence of lithium.

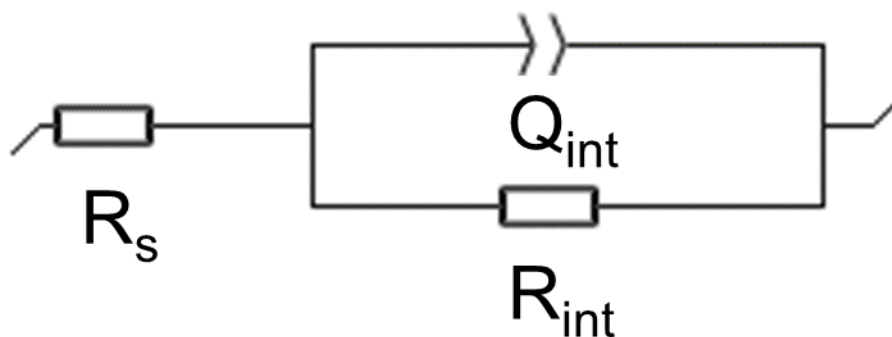


Figure 37: The Equivalent circuit model used to fit the EIS data in the Bruce-Vincent cell.

Table 9: Best-fit values for the equivalent circuit (Figure 37) used to generate fits in Figure 38.

	R_s [pΩ]	Q_{bulk} [nF · s ^{a_{bulk}-1}]	R_{bulk} [kΩ]	a_{bulk} [-]
Before Polarization	6.905	0.637	3.453	0.804
After Polarization	3.263	0.630	3.939	0.804

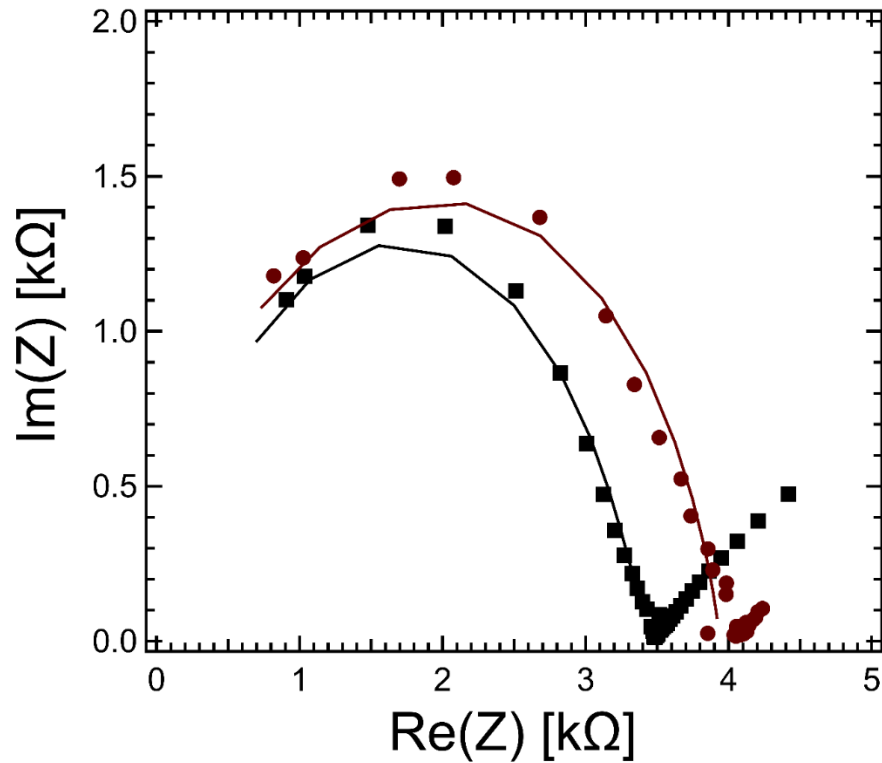


Figure 38: The EIS spectrum of the polymers before (red circle) and after (black square) polarization of the cell.

The markers indicate the measured points, and the solid lines indicate the fits to the equivalent circuit using the model depicted in Figure 37.

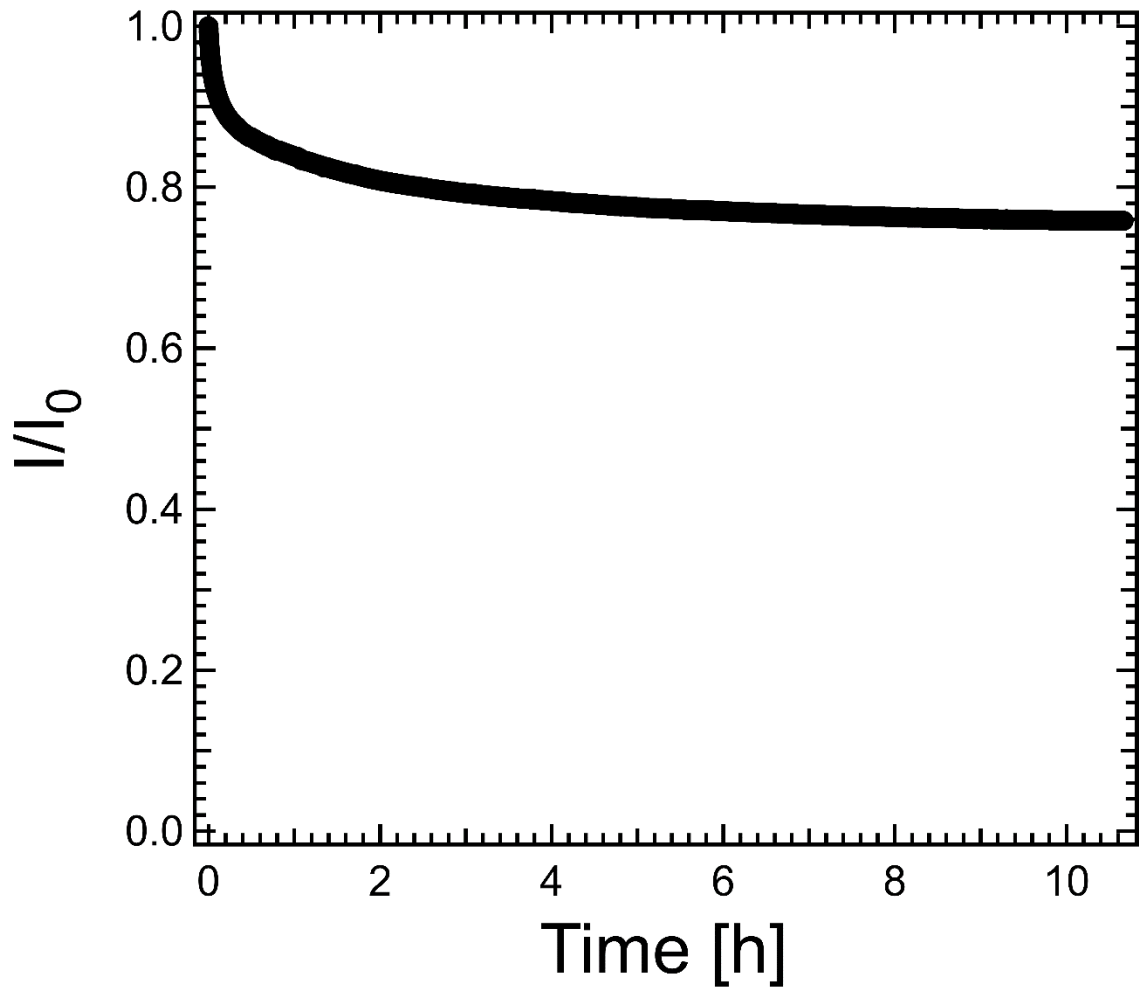


Figure 39: Normalized current versus time graph of the cell undergoing polarization.

In this case, the initial current I_0 ($5.53 \mu\text{Amperes}$) observed experimentally, and the calculated value of I_Ω ($5.79 \mu\text{Amperes}$), differ somewhat due to the delay between sampling the current and applying the polarization.

The analysis from section D2.2 was again applied to determine the values of the limiting current using the two metrics described. Notably, interfacial resistance plays a significantly reduced role in this system.

Table 10: The two selectivity metrics determined from analysis of the symmetric Li/Li cell.

ΔV Cell [mV]	$\rho_{+,0}$	$\rho_{+,\Omega}$
20	0.76	0.73

Table 11: Some relevant information about the cell used in this experiment including the electrolyte area and thickness, the initial current, and the initial current density (J_0).

Area [mm ²]	Thickness [mm]	I_0 [μA]	J_0 [$\mu A/mm^2$]
50.27	0.8	5.53	0.110

2.4 Analysis of EIS and Polarization data obtained on Li/Li symmetric cells containing the Am-TFS-C6F5 ZIL $r=0.9$ Electrolyte

Analysis of the symmetric cell for the Am-TFS-C6F5 electrolyte follows the same procedure as outlined above for the other systems.

Table 12: Values of Equivalent Circuit Fitting Parameters Before and After

Polarization

	Q_{int} [μF $\cdot s^{a_{\text{int}}-1}$]	R_{int} [$\text{k}\Omega$]	a_{int} [$-$]	Q_{bulk} [nF $\cdot s^{a_{\text{bulk}}-1}$]	R_{bulk} [$\text{k}\Omega$]	a_{bulk} [$-$]
Before Polarization	0.20 ₀₇	6.445	5.9 ₁₆	1.07	5.557	0.79 ₂₇
After Polarization	0.34 ₇₀	7.940	0.55 ₈₂	1.304	5.778	0.79 ₁₉

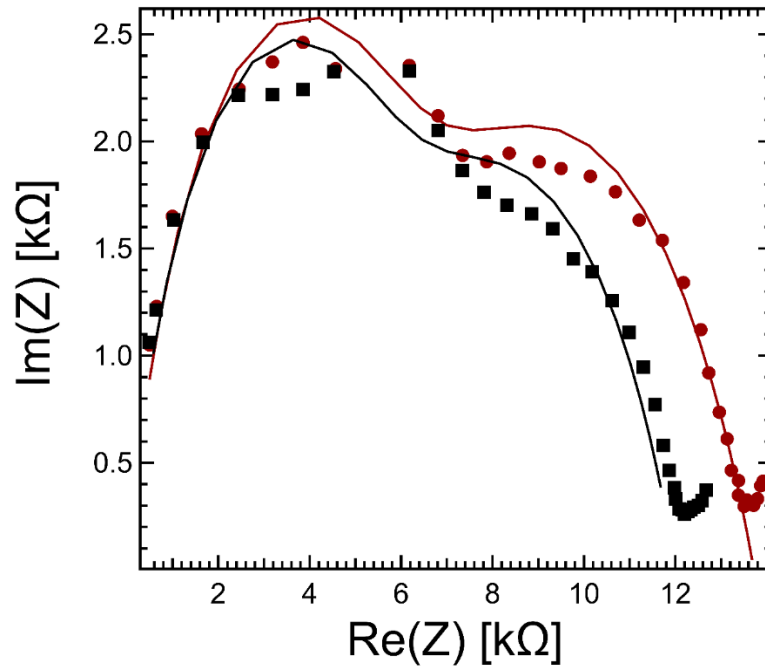


Figure 40: The EIS spectrum of the polymers before (red circle) and after (black square) polarization of the cell.

The markers indicate the measured points, and the solid lines indicate the fits to the equivalent circuit using the model depicted in Figure 37 and the parameters in Table 12.

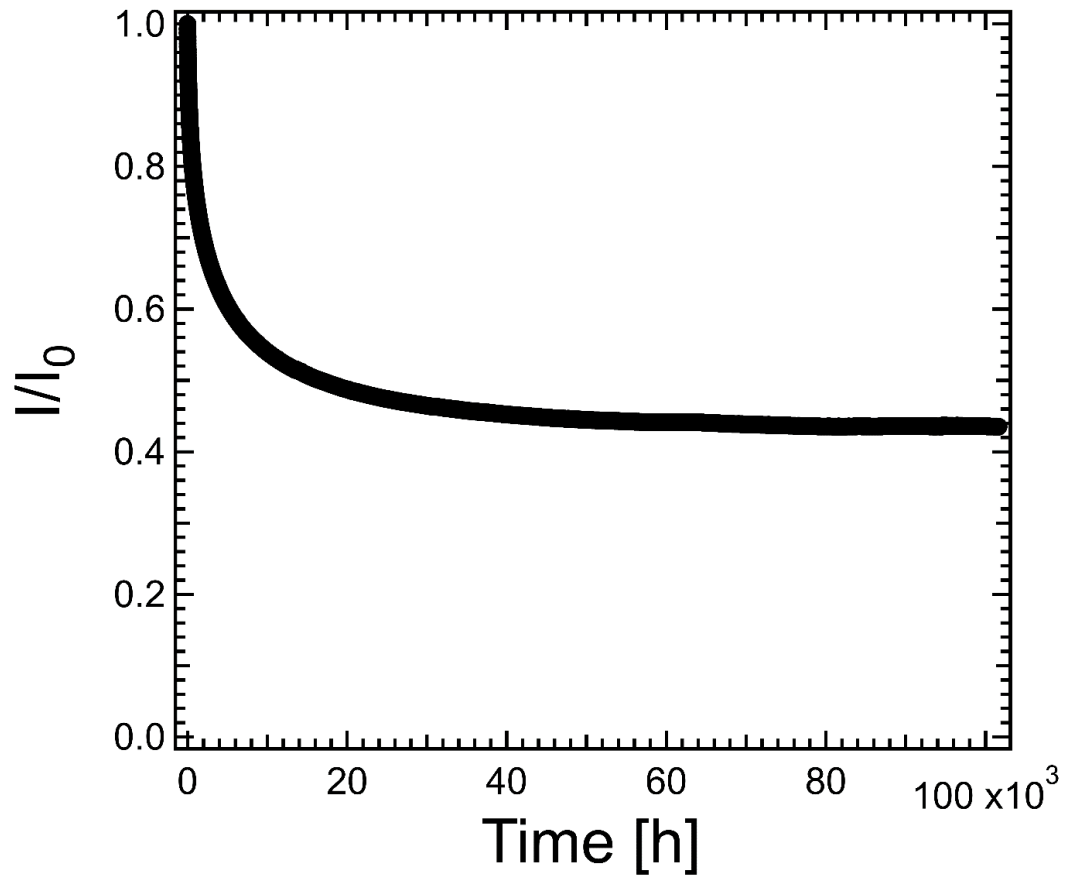


Figure 41: Normalized current versus time graph of the cell undergoing polarization.

In this case, the initial current I_0 ($2.30 \mu\text{Amperes}$) observed experimentally, and the calculated value of I_Ω ($1.66 \mu\text{Amperes}$) differ somewhat.

Table 13: The two selectivity metrics determined from analysis of the symmetric Li/Li cell.

ΔV Cell [mV]	$\rho_{+,0}$	$\rho_{+,\Omega}$
20	0.19	0.47

Table 14: Some relevant information about the cell used in this experiment including the electrolyte area and thickness, the initial current, the initial current density (J_0), and the initial area specific interfacial resistance.

Area [mm ²]	Thickness [mm]	I_0 [μ A]	J_0 [μ A/mm ²]	$R_{\text{int}}/\text{Area}$ [k Ω /mm ²]
28.3	0.39	2.30	0.081 ₂₇	0.19 ₆₃

D.3 Solid-State NMR

3.1 Discussion of Solid-State NMR for Im-TFSI PZIL

The 1D ^7Li NMR data collected on the salt-containing PZILs indicate that lithium exists in multiple environments. A fit of the ^7Li spectrum (Figure 42A) reveals two Gaussian line-shapes centered at similar overlapping chemical shifts (1.08 and 1.32 (calibrated using a 1.0 M LiCl (aq) sample)) but with different linewidths. The narrow component accounts for 24% of the total integrated intensity, while the broad component accounts for 76%. The similar chemical shifts of two signals suggest that all the Li^+ ions, which are solely introduced by the $\text{Li}^+/\text{bTFSI}^-$ salt, exist in rather similar bonding environments. The NMR linewidths are inversely proportional to the molecular relaxation timescales (T_2) of the Li^+ and suggest that ~24% of Li ions exist in an environment with faster dynamics, and ~76% of the Li ions in environments associated with slower dynamics. In contrast, the 1D ^{19}F NMR spectrum (Figure 42D) reveals two fluorine populations with clear differences in chemical shift and yet a less dramatic difference in line-width as compared to the ^7Li data. These ^{19}F environments are attributed to polymer-bound TFSI $^-$ and free fluorine coming from the bTFSI $^-$ counterion.

^7Li $T_{1\rho}$ relaxometry measurements were performed and corroborate the observation from 1D NMR that Li^+ exists in two dynamic environments. $T_{1\rho}$ measurements use a spin-lock radiofrequency pulse (here, of 10 kHz), which serves to probe ion dynamics on the order of milliseconds and are more selective to typical diffusion timescales of interest than standard T_1 or T_2 relaxation measurements. Figure 42C shows a fit of the $T_{1\rho}$ signal decay curve when a single dynamic mode is considered and when two dynamic environments are considered. For all temperatures measured, the data require two dynamic timescales to obtain an accurate fit, consistent with the two lithium environments identified with 1D

NMR. Additionally, the relative populations of the two lithium environments are in good agreement with the two fractions identified from 1D NMR, with ~74% of the lithium showing a $T_{1\rho}$ of 240 microseconds and ~26% displaying a relaxation at 1.2 milliseconds.

The multiple dynamic environments detected for lithium were further verified by pulsed-field gradient (PFG) NMR methods, which revealed multiple ${}^7\text{Li}$ diffusion coefficients and only a single ${}^{19}\text{F}$ diffusion environment. PFG-NMR measurements were carried out using a standard variable magnetic field gradient Bruker diffusion pulse sequence (diffste) which includes a stimulated echo, serving to protect the signal from shorter relaxation times observed in these solid-like samples. The PFG measurements used herein probe diffusion across lengthscales roughly in the 0.1-1 μm characteristic diffusion lengthscale, making this a much larger lengthscale probe of the ion dynamics than the relaxometry or lineshape analyses. A reasonable fit of the curve representing the evolution of the ${}^7\text{Li}$ signal intensity versus magnetic field gradient strength at a fixed diffusion time (Figure 42B) requires two exponential decay functions describing two distinct lithium dynamic environments. The relative populations of the two environments are consistent with relaxometry and 1D NMR results with ~26% of the lithium exhibiting a diffusion coefficient of $7.59 \cdot 10^{-12} \text{ m}^2\text{s}^{-1}$ and ~74% exhibiting a lower diffusivity of $9.16 \cdot 10^{-13} \text{ m}^2\text{s}^{-1}$ (Figure 42F). The ${}^{19}\text{F}$ diffusion curve can be reasonably fit with one exponential decay function corresponding to a self-diffusion coefficient of $1.28 \cdot 10^{-12} \text{ m}^2\text{s}^{-1}$, as shown in Figure 42E, even though 1D experiments indicated two chemical environments for fluorine. The presence of a single observable diffusion ${}^{19}\text{F}$ timescale is most likely due to the low mobility of polymer-bound Im-TFSI units leading to very slow decay of the corresponding ${}^{19}\text{F}$ NMR signal that is essentially filtered out in the PFG-NMR measurements.

Overall, analyses of the scattering data and microscopic diffusion information altogether suggest that the fast mode of Li^+ conduction occurs within crystalline domains of the electrolyte. The Walden plot analysis qualitatively demonstrates the presence of a solid-like mechanism of conduction in this polymer material. While solid-like conduction can occur in amorphous super- T_g polymers when the dynamics of strand rearrangement is much slower than ion rearrangement, it is more likely to occur in a ‘frozen structure,’ such as the crystalline domains detected by WAXS. Consequently, these results suggest that Li^+ diffusion occurs via two mechanisms: a fast ballistic or hopping-type transport mechanism within the crystalline domains of the polymer, and a slower, liquid-like diffusion process within amorphous regions. The presence of two lithium environments validated by 1D NMR line-shape analysis, $T_{1\rho}$ relaxometry, and PFG-NMR measurements is consistent with this hypothesis. In contrast, TFSI⁻ ions probed by ^{19}F NMR exhibit significant motion in only the amorphous regions of the electrolyte. This observation is consistent with the Andersen-Stuart¹⁵³ and related barrier-type models¹⁵⁴⁻¹⁵⁶, which predict that larger ions will experience a larger barrier for diffusion in dense domains such as crystallites. Here, dense crystalline regions lead to selective Li transport due to the large size difference between the TFSI⁻ and Li^+ ions, which could account for the complete filtering-out of PFG-NMR signal decay due to ^{19}F nuclei in the crystalline regions of the electrolyte.

This understanding leads to a consistent picture of ionic motion through the bulk PZIL material, with crystalline domains acting as highly Li^+ -selective transport regions and dual-ion conducting amorphous domains exhibiting slightly preferential diffusion of TFSI⁻ ions. The single diffusion coefficient measured by ^{19}F PFG-NMR is attributed to the amorphous-phase conduction of the TFSI⁻ ion, the lack of a second coefficient being consistent with the

notion that TFSI ion is highly hindered within the crystallites (and polymer-bound Im-TFSI units are immobile). The ‘slow mode’ diffusion coefficient of lithium is also likely to correspond to the amorphous-phase conductivity of this species, as this phase is likely to have a reduced strand density resulting in a ‘Coulombically-dominated’ energy barrier for diffusion, which favors TFSI motion over Li^+ . Consequently, the ‘fast mode’ of lithium conduction corresponds to a ballistic/hopping transport within crystalline regions of the material.

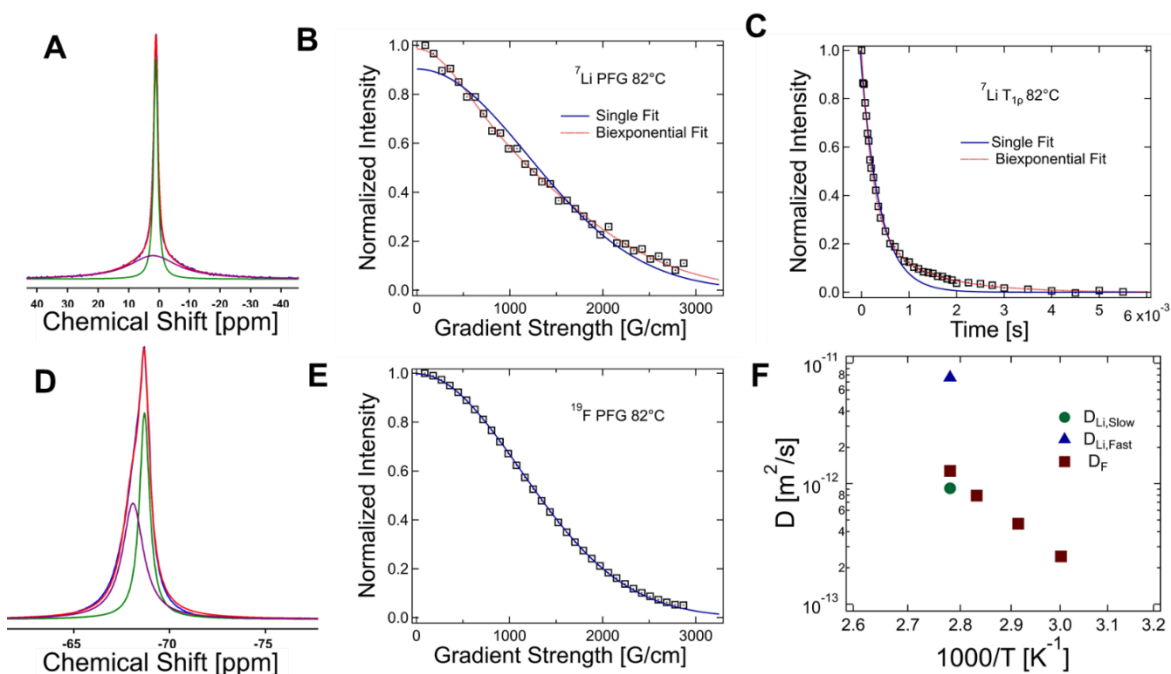


Figure 42: Solid State NMR Data for the PZILs.

A) Line shape analysis of the 1D ^7Li NMR spectrum. The blue curve is the experimental data, the pink curve is the broad Gaussian component and the green curve is the narrow gaussian component with the red curve representing the sum of these components. The fit using two Gaussian lines centered at very similar resonant frequencies demonstrates that lithium exists in two environments that are chemically similar but display different dynamics. B) The Li^7 pulsed field gradient profile with fits based on one and two components. The diffusion profile requires two signal components to fit the decay, with

relative weights in line with the populations of the two lithium environments determined from the fit of the 1D ^7Li NMR line shape in A). C) The ^7Li $T_{1\rho}$ relaxometry curve with one- and two-component fits reveals once again that two lithium populations are necessary to fit the decay curve. The size of these populations again agrees with the 1D and PFG-NMR results. D) The ^{19}F line shape analysis with the same curve labels as in panel A. In this case, the widths of the curves are similar, but the chemical shifts differ more significantly, suggesting the presence of two chemical environments, tentatively assigned to polymer-bound and free fluorine-containing species. E) The ^{19}F diffusion curve can be fit assuming a single diffusion mode, suggesting that all mobile fluorine exists in a similar diffusing environment. F) The diffusion coefficients obtained from PFG-NMR experiments as a function of inverse temperature demonstrate that the amorphous conductivities of the lithium and fluorine are similar, suggesting that the high conductivity of these electrolytes is derived from the motion of lithium through the crystalline domains of the material.

3.2 A Note on Spectrum Fitting

Several expressions are used to fit the diffusion and relaxometry data herein. These expressions contain an exponential decay function such as Equation 19. Typically, when a single exponential decay function does not provide an adequate fit the poor fitting can be remedied by either modifying the exponential by adding a ‘stretch’ to the exponential as in equation or by adding a second exponential decay function which represents another distinct dynamic population.

It is frequently the case that both approaches may improve the data fit, however the interpretation of these two fitting modes differs significantly. While a stretched exponential indicates broadening of dynamics within a single population, multiple exponentials indicate multiple populations with different dynamics. To resolve this issue of ambiguous fitting, fitting was performed via the following procedure: 1) Begin from a stretched exponential fit, if the fit collapses to the single-exponent limit use the single-exponential fit, otherwise maintain this stretched exponential fit 2) if the stretched-exponential fit fails, add a second exponential mode. In this manner, a second exponential mode is only added if the stretched exponential fit fails to describe the data, this approach will only accept the hypothesis of multiple dynamic populations when dynamic broadening fails to account for the dynamics.

When fitting the lineshapes of NMR spectra both Gaussian and Lorentzian fits were considered. Regardless of this choice, two components are required to fit the lineshape of both the 1D lithium and fluorine spectra

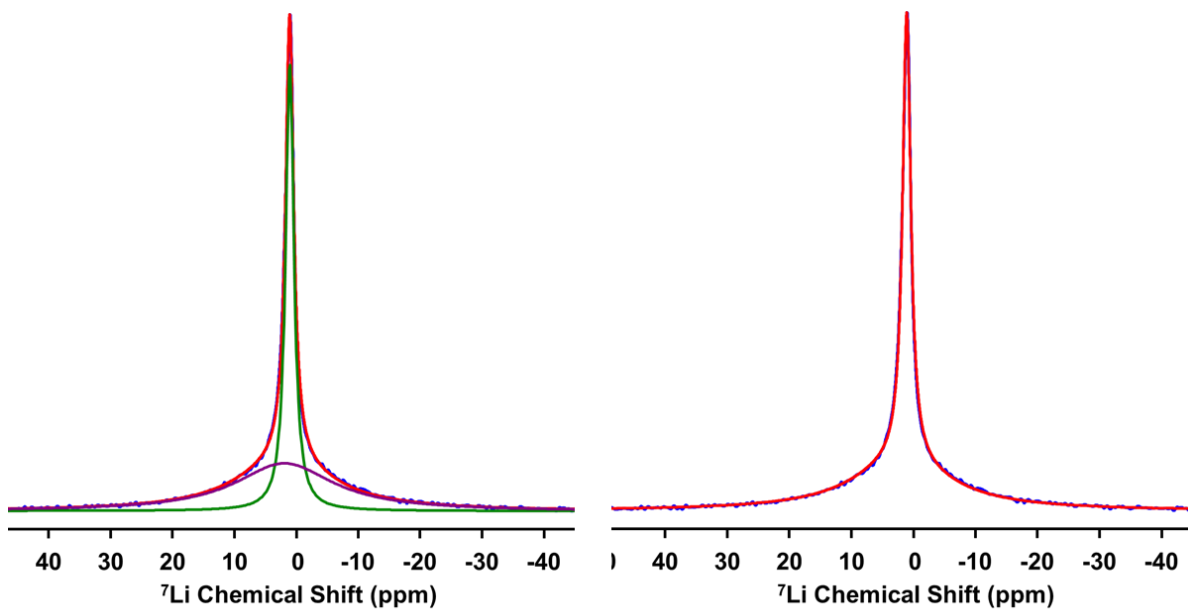


Figure 43: Lineshape fitting example.

The image from Figure 42 is expanded so that the agreement between experimental lineshape and the fitted shape. The green and purple components represent individual Gaussian components to the fit and the red shape is the sum of these components. The blue curve is the experimental lineshape. The right panel reproduces the figure on the left, but the individual components have been removed from this panel for clarity.

3.3 ^{19}F T_1 Measurements of Im-TFSI PZIL

T_1 decay curves presented in this section have been fit using a single exponential decay function of the form:

$$I = I_0 \exp\left(-\frac{t}{T_1}\right) \quad \text{Equation 19}$$

where I is the observed NMR signal intensity, T_1 is the NMR spin-lattice relaxation time, t is the experimental signal decay time, and I_0 is the initial signal intensity at time $t=0$.

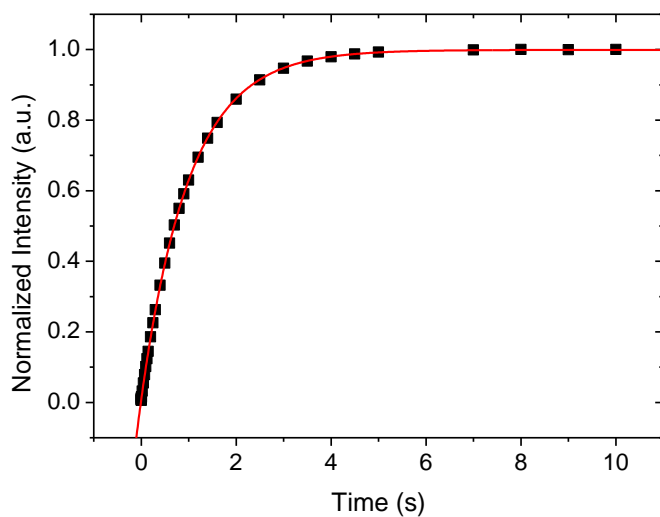


Figure 44: The normalized intensity versus time curve for a ^{19}F T_1 experiment on the Im-TFSI PZIL with $r=0.9$ at a temperature of 355 K. The black squares correspond to measured data and the red curve is a single exponential fit (Equation 19).

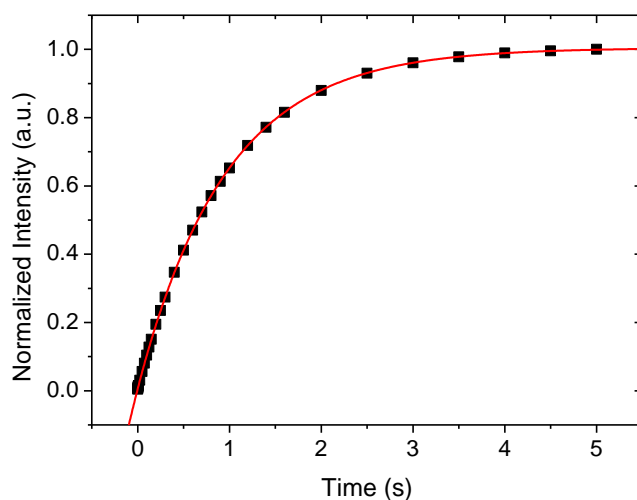


Figure 45: The normalized intensity versus time curve for a ^{19}F T_1 experiment on the Im-TFSI PZIL with $r=0.9$ at a temperature of 346 K. The black squares

correspond to measured data and the red curve is a single exponential fit (Equation 19).

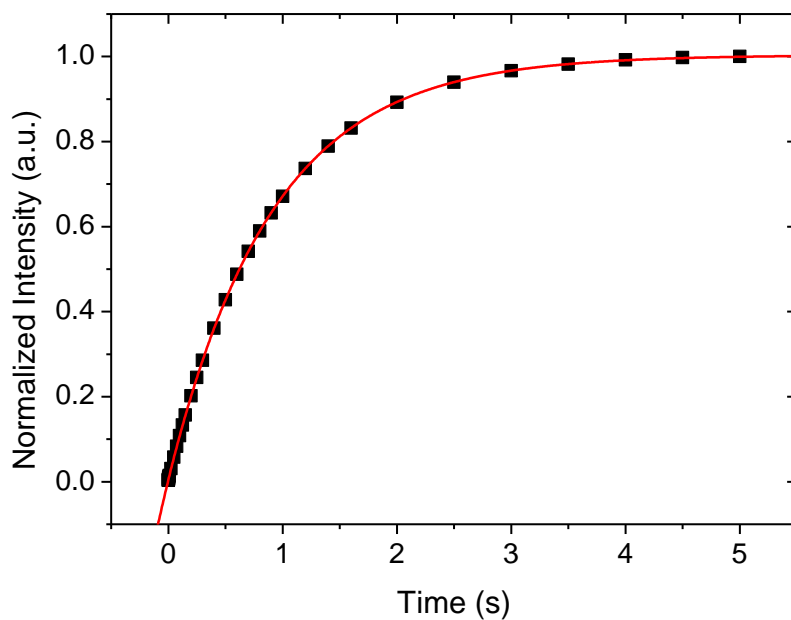


Figure 46: The normalized intensity versus time curve for a ^{19}F T_1 experiment on the Im-TFSI PZIL with $r=0.9$ at a temperature of 337 K. The black squares correspond to measured data and the red curve is a single exponential fit (Equation 19).

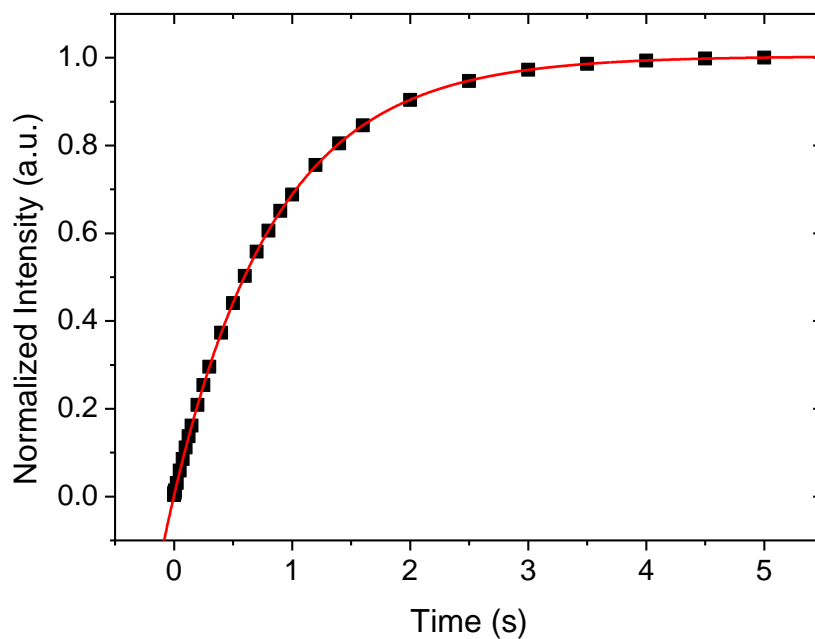


Figure 47: The normalized intensity versus time curve for a ^{19}F T_1 experiment on the Im-TFSI PZIL with $r=0.9$ at a temperature of 328 K. The black squares correspond to measured data and the red curve is a single exponential fit (Equation 19).

Table 15: Parameters obtained from single-component fits of the ^{19}F T_1 relaxation decay curves in Figure 44 to Figure 47.

Temperature [C]	I_0	A	T_1 [ms]
355	1.013 ± 0.001	0.992 ± 0.001	1013 ± 1
346	$1.0043 \pm$	$0.9948 \pm$	$958.3 \pm$
	0.0003	0.0002	0.8

337	1.0035	0.9961 ±	907.5 ±
	±0.0002	0.0001	0.6
328	1.0036 ±	0.9974 ±	865.5 ±
	0.0003	0.0002	0.7

7.4 ${}^7\text{Li}$ $T_{1\rho}$ Experiments of Im-TFSI PZIL

$T_{1\rho}$ decay curves presented in this section have been fit using the single exponential decay function presented previously (Equation 19, and using a double exponential decay function of the form:

$$I = I_1 \exp\left(-\frac{t}{T_{1\rho,1}}\right) + I_2 \exp\left(-\frac{t}{T_{1\rho,2}}\right) \quad \text{Equation 20}$$

where I is the observed NMR signal intensity, $T_{1\rho,i}$ is the NMR spin-lattice relaxation time in the rotating frame of reference for component i , t is the experimental signal decay time, and I_i is the initial signal intensity at time $t=0$ for component i .

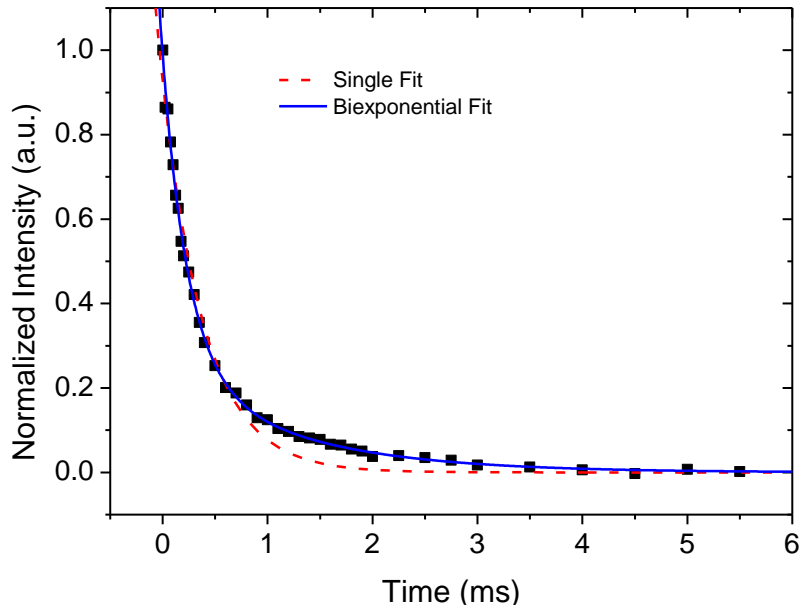


Figure 48: The normalized intensity versus time curve for a ${}^7\text{Li}$ $T_{1\rho}$ experiment on the Im-TFSI PZIL with $r=0.9$ at a temperature of 355 K.

The black squares correspond to measured data and the red and blue curves are fits using single (Equation 19) and biexponential functions (Equation 20), respectively.

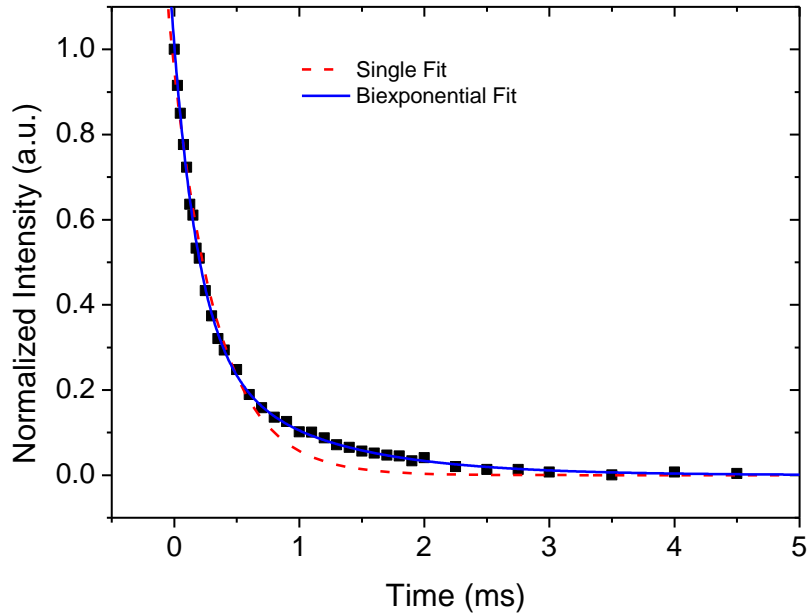


Figure 49: The normalized intensity versus time curve for a ${}^7\text{Li}$ $T_{1\rho}$ experiment on the Im-TFSI PZIL with $r=0.9$ at a temperature of 346 K.

The black squares correspond to measured data and the red and blue curves are fits using single (Equation 19) and biexponential functions (Equation 20), respectively.

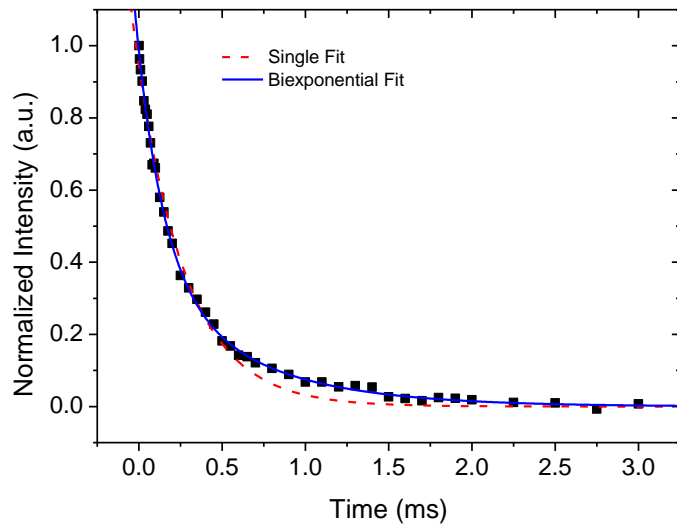


Figure 50: The normalized intensity versus time curve for a ${}^7\text{Li}$ $T_{1\rho}$ experiment on the Im-TFSI PZIL with $r=0.9$ at a Temperature of 337 K.

The black squares correspond to measured data and the red and blue curves are fits using single (Equation 19) and biexponential functions (Equation 20), respectively.

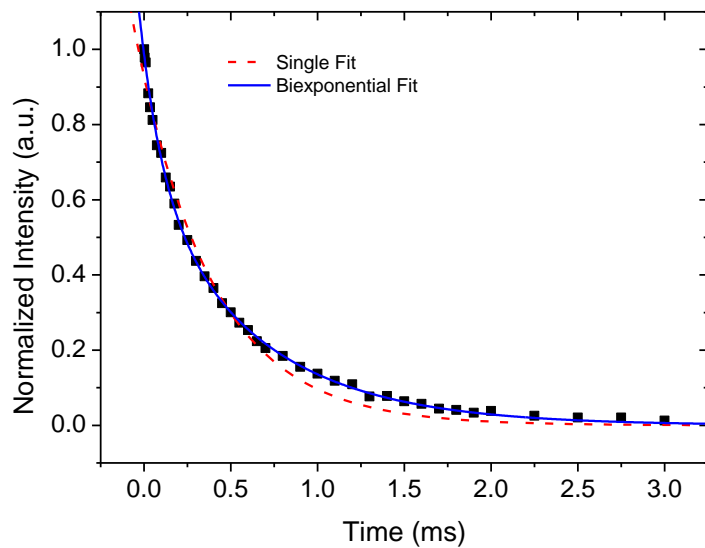


Figure 51: The normalized intensity versus time curve for a ${}^7\text{Li}$ $T_{1\rho}$ experiment on the Im-TFSI PZIL with $r=0.9$ at a temperature of 328 K.

The black squares correspond to measured data and the red and blue curves are fits using single (Equation 19) and biexponential functions (Equation 20), respectively.

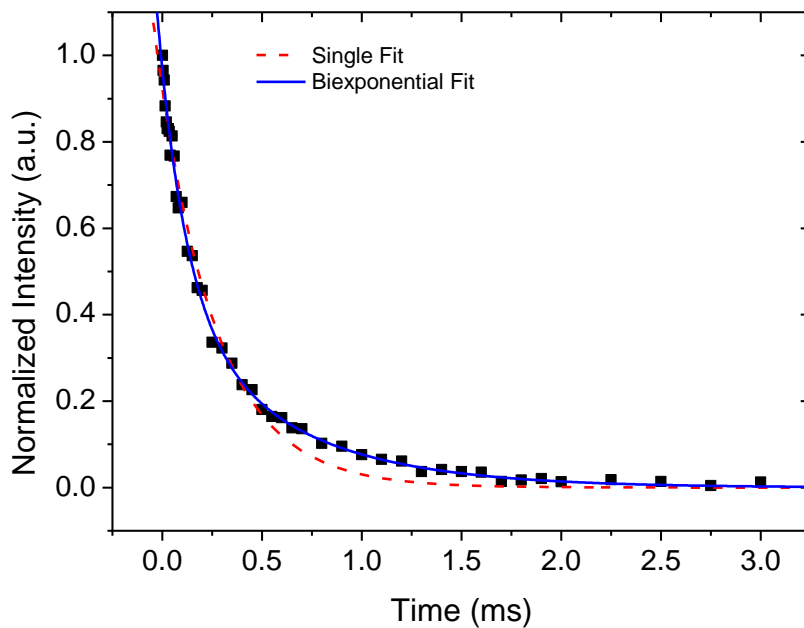


Figure 52: The normalized intensity versus time curve for a ${}^7\text{Li}$ $T_{1\rho}$ experiment on the Im-TFSI PZIL with $r=0.9$ at a temperature of 320 K.

The black squares correspond to measured data and the red and blue curves are fits using single (Equation 19) and biexponential functions (Equation 20), respectively.

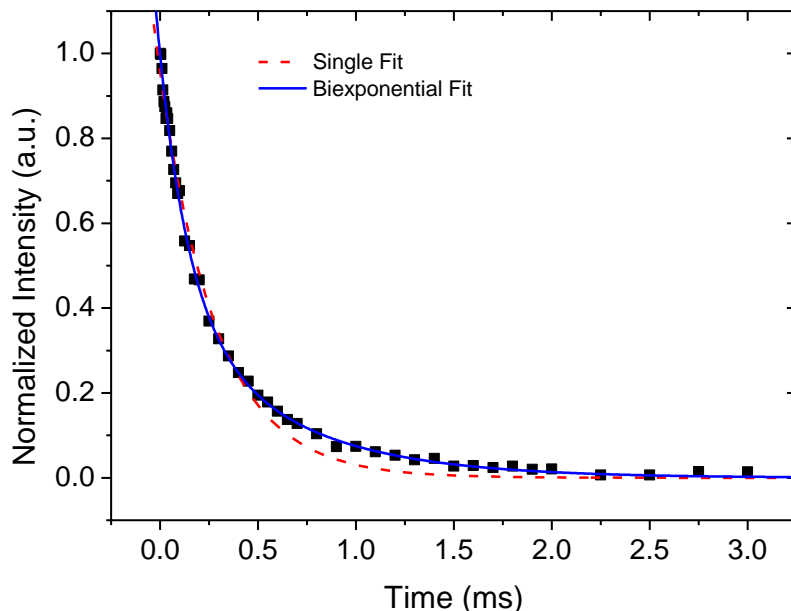


Figure 53: The normalized intensity versus time curve for a ${}^7\text{Li}$ $T_{1\rho}$ experiment on the Im-TFSI PZIL with $r=0.9$ at a temperature of 311 K.

The black squares correspond to measured data and the red and blue curves are fits using single (Equation 19) and biexponential functions (Equation 20), respectively.

All $T_{1\rho}$ decay curves presented in Figure 48-Figure 53 are not accurately described using a single exponential function (Equation 19) and instead require a biexponential function shown in Equation 20. ${}^7\text{Li}$ $T_{1\rho}$ parameters obtained from these biexponential fits are presented in Table 16. As mentioned previously, there is good agreement between the intensities of the two ${}^7\text{Li}$ $T_{1\rho}$ components and the two lithium diffusion modes at a temperature of 355 K. Additionally, the first mode (with shorter $T_{1\rho}$) decreases in prominence compared to the second mode as temperature is reduced. This observation is consistent with a pattern where motion through the superionic mode becomes the dominant mode of lithium transport in the electrolyte as temperature is reduced.

Table 16: Parameters obtained from two-component fits of the ^7Li $T_{1\rho}$ decay curves.

Temperature [K]	I_1	$T_{1\rho,1}$ [μs]	I_2	$T_{1\rho,2}$ [ms]
355	0.736 ± 0.03	238 ± 17	0.252 ± 0.03	1190 ± 50
346	0.715 ± 0.03	205 ± 9	0.297 ± 0.03	916 ± 20
337	0.633 ± 0.03	132 ± 10	0.353 ± 0.03	649 ± 26
328	0.622 ± 0.05	163 ± 11	0.364 ± 0.05	626 ± 55
320	0.5922 ± 0.05	151 ± 12	0.405 ± 0.06	588 ± 55
311	0.556 ± 0.07	142 ± 17	0.413 ± 0.07	593 ± 77

3.5 ^7Li Pulsed Field Gradient Diffusion Profile of Im-TFSI PZIL

Single and double exponential functions used to fit the PFG NMR decay curves presented in sections 3.4 and 3.5.

$$I = I_0 \exp\left(-D\gamma^2 G^2 \delta^2 \left(\Delta - \frac{\delta}{3}\right)\right) \quad \text{Equation 21}$$

$$I = I_1 \exp\left(-D_1 \gamma^2 G^2 \delta^2 \left(\Delta - \frac{\delta}{3}\right)\right) + I_2 \exp\left(-D_2 \gamma^2 G^2 \delta^2 \left(\Delta - \frac{\delta}{3}\right)\right) \quad \text{Equation 22}$$

Where D is the self-diffusion constant, γ is the gyromagnetic ratio, G is the gradient field strength, δ is the gradient pulse duration, and Δ is the time between gradient pulses.

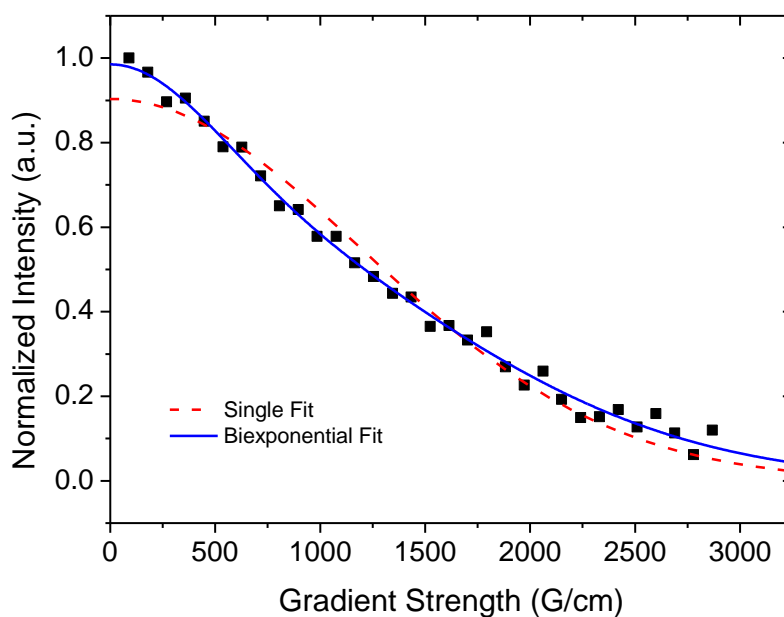


Figure 54: The normalized intensity versus gradient strength curve obtained from a ^7Li PFG NMR measurement on the Im-TFSI PZIL with $r=0.9$ at a temperature of 355 K.

The black squares correspond to measured data and the red and blue curves are fits using single (Equation 21) and biexponential functions (Equation 22), respectively.

Pulsed field gradient NMR measurements at a temperature of 355 K indicate two transport modes for lithium. This claim is supported by the significant improvement in the fit of the PFG NMR signal decay curve when using two diffusing components as compared to when using a single component. This analysis is further supported by the remarkable consistency between the relative intensities of the two lithium diffusion modes determined across NMR relaxometry, PFG NMR, and NMR lineshape analysis.

Table 17: Parameters obtained from a biexponential fit of the ^7Li PFG NMR data in Figure 54.

Temperature	D1 [m ² /s]	D2 [m ² /s]	I1	I2	Δ [ms]	δ [ms]
355 K	$(9.16 \pm 0.5) \cdot 10^{-13}$	$(7.59 \pm 0.5) \cdot 10^{-12}$	0.73	0.26	10	1.6
	10^{-13}	10^{-12}	8	2	0	5

3.6 ^{19}F Pulsed Field Gradient Diffusion Profiles of Im-TFSI PZIL

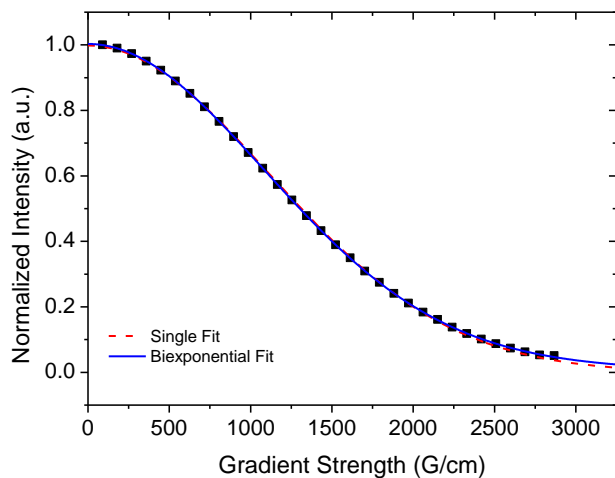


Figure 55: The normalized intensity versus gradient strength obtained from a ^{19}F PFG NMR measurement on the Im-TFSI PZIL with $r=0.9$ at a temperature of 355 K.

The black squares correspond to measured data and the red and blue curves are fits using single (Equation 21) and biexponential functions (Equation 22), respectively. The single exponential fit appears to fully capture the behavior of the curve, suggesting that a single diffusive mode is sufficient to describe the motion of fluorine in this polymer.

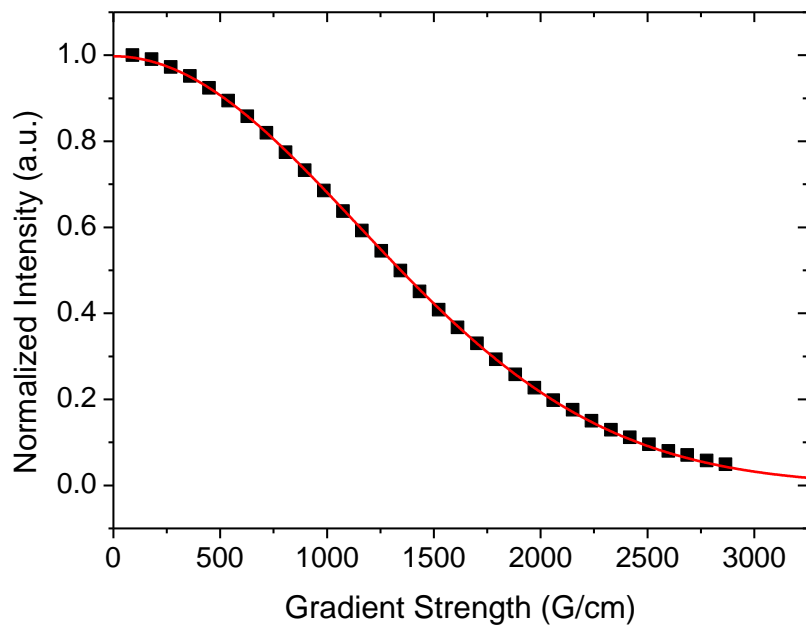


Figure 56: The normalized intensity versus gradient strength obtained from a ^{19}F PFG NMR measurement on the Im-TFSI PZIL with $r=0.9$ at a temperature of 346 K.

The black squares correspond to measured data and the red curve is fit using a single exponential function (Equation 21). The single exponential fit appears to fully capture the behavior of the curve, suggesting that a single diffusive mode is sufficient to describe the motion of fluorine in this polymer.

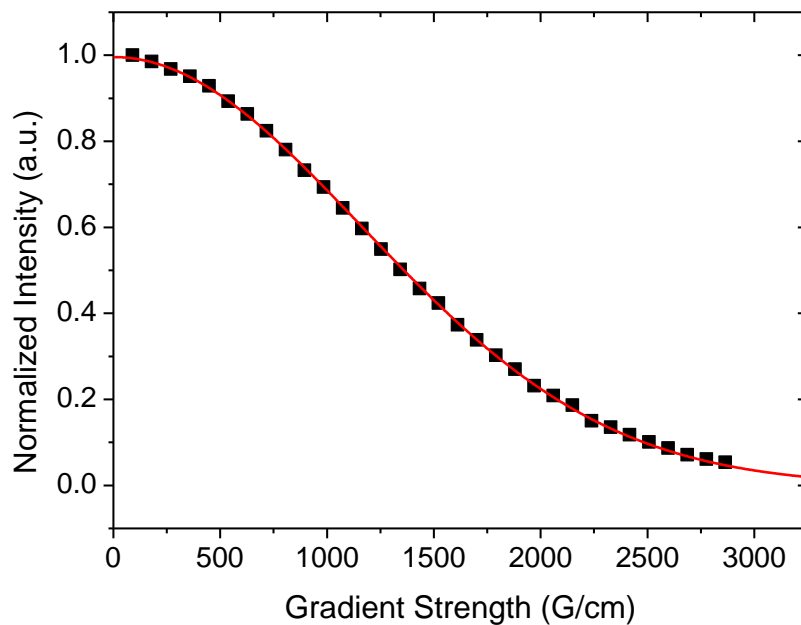


Figure 57: The normalized intensity versus gradient strength obtained from a ^{19}F PFG NMR measurement on the Im-TFSI PZIL with $r=0.9$ at a temperature of 337 K.

The black squares correspond to measured data and the red curve is fit using a single exponential function (Equation 21). The single exponential fit appears to fully capture the behavior of the curve, suggesting that a single diffusive mode is sufficient to describe the motion of fluorine in this polymer.

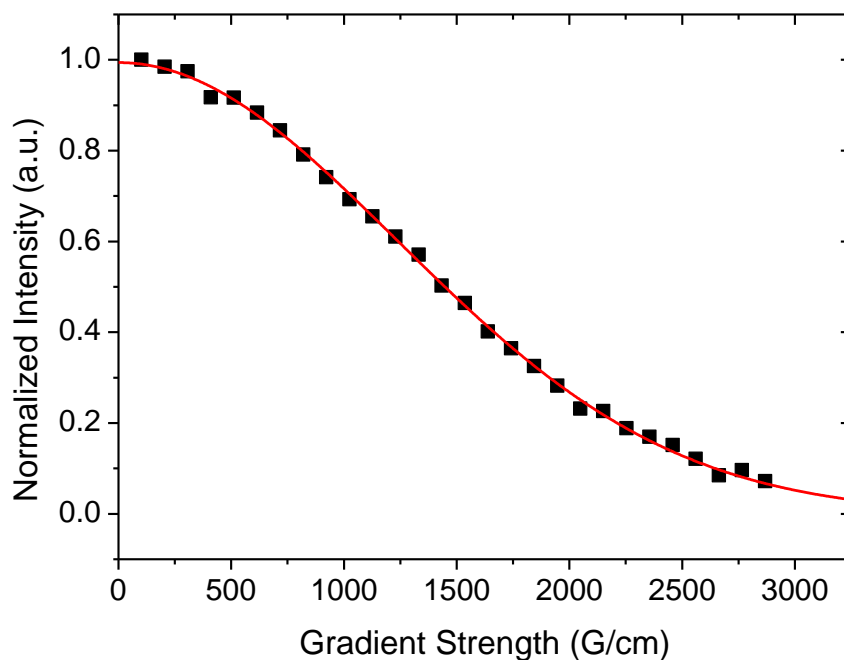


Figure 58: The normalized intensity versus gradient strength obtained from a ^{19}F PFG NMR measurement on the Im-TFSI PZIL with $r=0.9$ at a temperature of 328 K.

The black squares correspond to measured data and the red curve is fit using a single exponential function (Equation 21). The single exponential fit appears to fully capture the behavior of the curve, suggesting that a single diffusive mode is sufficient to describe the motion of fluorine in this polymer.

Table 18: Parameters obtained from single-component fits of the ^{19}F PFG NMR data in Figure 54-Figure 58.

Temperature	D [m ² /s]	I0	Δ [ms]	δ [ms]
355	$(1.275 \pm 0.006) \cdot 10^{-12}$	0.998	50	1.0
346	$(7.96 \pm 0.006) \cdot 10^{-13}$	0.998	53	1.2
337	$(4.65 \pm 0.02) \cdot 10^{-13}$	0.996	65	1.4
328	$(2.49 \pm 0.02) \cdot 10^{-13}$	0.994	77	1.65

3.7 Lithium-Ion transport number of Im-TFSI PZIL

The lithium-ion transport number of the Im-TFSI PZIL is defined as the product of the concentration of lithium and the average diffusivity of lithium divided by the product of concentration (c) and diffusivity (D) for all other mobile ionic species as shown in Equation 23.

$$t_{\text{Li}} = \frac{\langle D_{\text{Li}} \rangle c_{\text{Li}}}{\sum \langle D_i \rangle c_i} \quad \text{Equation 23}$$

Where the index ‘i’ corresponds to any ionic species in the system and the brackets correspond to a number-average. In this case, I have demonstrated that the total ionic conductivity of the system is reduced by orders of magnitude in the absence of the Li⁺/TFSI⁻ salt – suggesting that this dopant provides the majority of the mobile ionic species in the system. Consequently, it is approximated that the only relevant mobile ionic species are the Li⁺ and TFSI⁻. Importantly, the neutral pair of Li/TFSI may contribute to the observed diffusion of Lithium and TFSI. The motion of neutral pairs is a component of the distinction between t_+ and ρ_+ (further discussed in the manuscript). An additional simplification of Equation 23 is made by substituting the fact that $c_{\text{Li}} = c_{\text{TFSI}}$, which is universal for 1:1 salts. Equation 24 gives a relation which is used to practically evaluate the lithium transport number of this system. Where the average diffusion coefficient is calculated from the biexponential fit

$$t_{\text{Li}} = \frac{D_{\text{Li},1} I_{\text{Li},1} + D_{\text{Li},2} I_{\text{Li},2}}{D_{\text{Li},1} I_{\text{Li},1} + D_{\text{Li},2} I_{\text{Li},2} + D_{\text{TFSI}}} \quad \text{Equation 24}$$

Equation 25 demonstrates the evaluation of this expression to obtain a lithium transport number.

$$t_{\text{Li}} = \frac{9.16 \cdot 10^{-13} \cdot 0.738 + 7.59 \cdot 10^{-12} \cdot 0.262}{9.16 \cdot 10^{-13} \cdot 0.738 + 7.59 \cdot 10^{-12} \cdot 0.262 + 1.275 \cdot 10^{-12}} = 0.676$$

Equation
25

3.8 ^7Li Pulsed Field Gradient Diffusion Profile of Am-TFSI PZIL

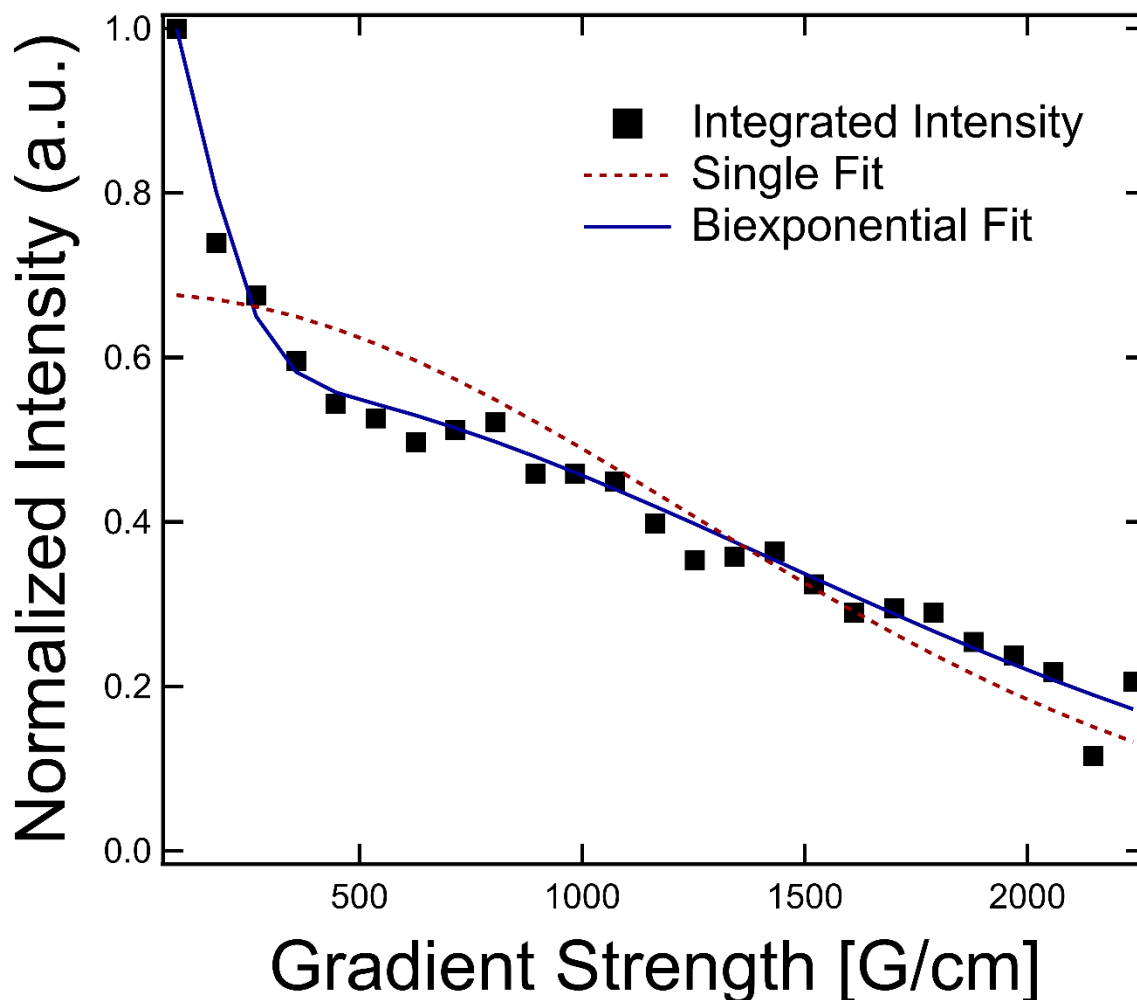


Figure 59: The normalized intensity versus gradient strength curve for a ^7Li PFG NMR experiment of the Im-TFSI PZIL with $r=0.9$ at a Temperature of 355 K.

The black points correspond to measured data and the red and blue curves are fits to single (Equation 21) and biexponential functions (Equation 22), respectively.

The ^7Li PFG NMR decay curve clearly contains two components with widely different diffusion behaviors, as evidenced by the poor fit obtained using a single exponential function. Diffusion parameters for the two lithium environments obtained from biexponential fits of the data using Equation 21 are shown in Table 19.

Table 19: Parameters obtained from a biexponential fit of the ^7Li PFG NMR data in Figure 59.

Temperature	D1 [m ² /s]	D2 [m ² /s]	I1	I2	Δ [ms]	δ [ms]
355 K	$(7.84 \pm 0.07) \cdot 10^{-13}$	$(8.48 \pm 0.2) \cdot 10^{-11}$	0.530	0.471	42	1

3.9 ^{19}F Pulsed Field Gradient Diffusion Profile of Am-TFSI PZIL

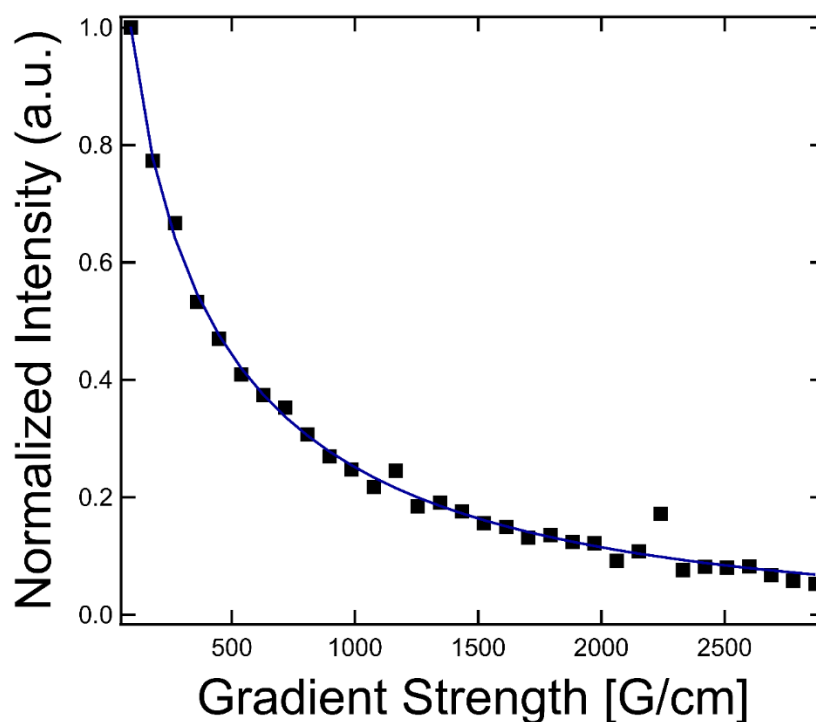


Figure 60: The normalized intensity versus gradient strength curve for a ^{19}F PFG NMR experiment of the Im-TFSI PZIL with $r=0.9$ at a Temperature of 355 K.

The black points correspond to measured data and the blue curve is a fit to single stretched exponential function (Equation 26).

The best fit of the ^{19}F PFG NMR decay curve in Figure 60 was obtained using a single-component, stretched exponential (β is the stretch factor):

$$I = I_0 \exp\left(-\left[D\gamma^2 G^2 \delta^2 \left(\Delta - \frac{\delta}{3}\right)\right]^\beta\right) \quad \text{Equation 26}$$

Table 20: Parameters obtained from a single-component, stretched exponential fit of the ^{19}F PFG NMR data in Figure 60.

Temperature	D [m ² /s]	β	I_0	Δ [ms]	δ [ms]
355 K	$(1.96 \pm 0.7) \cdot 10^{-11}$	0.248 ± 0.0 2	1.95 ± 0.2	42	1

3.10 Lithium-Ion transport number of Am-TFSI PZIL

Evaluation of the transport number uses the procedure described in C7.6 as shown in Equation 27.

$$t_{\text{Li}} = \frac{7.84 \cdot 10^{-13} \cdot 0.53 + 8.48 \cdot 10^{-11} \cdot 0.471}{7.84 \cdot 10^{-13} \cdot 0.53 + 8.48 \cdot 10^{-11} \cdot 0.471 + 1.96 \cdot 10^{-11}} = 0.673 \quad \text{Equation 27}$$

Notably, the diffusivities from NMR are nearly an order of magnitude faster for the Am-TFSI PZIL than the Im-TFSI PZIL, however these is not a correspondent increase in the

ionic conductivity of the Am-TFSI PZIL as measured by EIS. Accordingly, the NMR measurements in this case greatly overpredict the ionic conductivity, presumably due to significant ion pairing in the Am-TFSI PZIL.

D.4 Additional Structural Analysis of the Zwitterion

The structure of the ZIL was further characterized. In Figure 61, optical microscopy images of the ZIL (A) and the cast ZIL electrolyte (B) are shown. These microscopy images demonstrate the crystalline nature of the compound. Figure 61C shows a snapshot of the crystallographic structure of the ZIL in the absence of lithium salt. This ZIL assembles into a Pna21 spacegroup and has a site of crystallographic disorder. Complete crystallographic information for this compound can be accessed using at the Cambridge Crystallography Data Centre (Deposition Number 2122282).

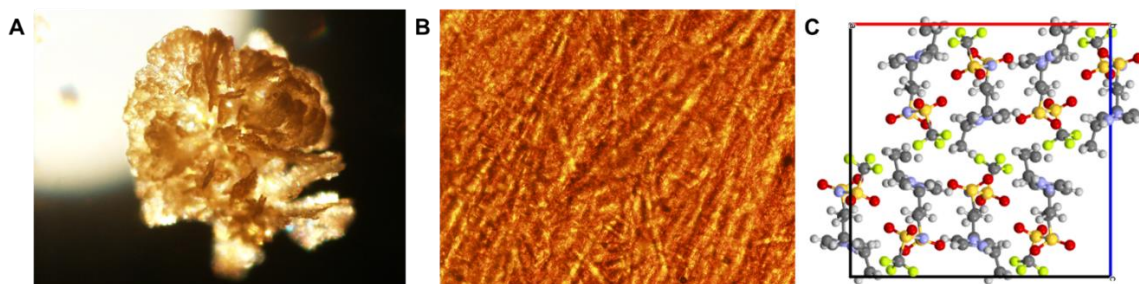


Figure 61: Microscopy and scattering analysis of the single crystal.

A) An optical microscopy image of the ZIL molecule after 3x recrystallization. B) An optical microscopy image of the ZIL electrolyte which was solvent cast from acetonitrile along with ~5% by mass LiTFSI salt (estimated to range between 4-6%). C) The structure of the ZIL crystal (without salt) viewed along the 'b' direction. The unit cell is belongs to a $Pna2_1$ spacegroup and there is a site of crystallographic disorder at the terminal carbon of the ethyl pendant chain (attached to the 1-position of the imidazolium ring). The crystallographic information file for this crystal has been deposited with the Cambridge Crystallographic Data Centre.

D.5 Room temperature stability of Im-TFSI PZIL $r=0.9$ versus Lithium

A composite cathode made of the PZIL mixed with carbon additives and PTFE was charged and discharged against a lithium foil anode using a standard organic liquid electrolyte (1 M LiPF_6 in ethylene carbonate and dimethylcarbonate) to assess the voltage stability of the PZIL at room temperature. All testing was performed galvanostatically with a current of 2.5 mA/g. This method is preferred over cyclic voltammetry experiments, which overestimate the electrochemical stability of solid-state electrolytes¹⁵⁷ The presence of carbon additives (typically missing in Cyclic Voltammetry experiments) can catalyze degradation of the solid-electrolyte and is needed to accurately gauge electrochemical stability. Additionally, the fast sweep rates in CV experiments and poor electronic

conductivity of solid-electrolytes limit the degradation current that can be detected.

Galvanostatic cycling overcomes this limitation by cycling at a slow constant current, which provides sufficient time for the electrolyte to equilibrate and fully react at the set potential.

The stability (voltage) window of the electrolyte is comprised between the potentials at which capacity starts to increase significantly (e.g., past 10 mAh g⁻¹) as measured in the (dis)charge curves. Here, the stability window lies between 3.8V and 1.16 V vs. Li for Im-TFSI PZIL. This room temperature stability window makes Im-TFSI PZIL suitable for industrially relevant lithium-ion cathode materials such as LiFePO₄, which operates around 3.5 V vs. Li.

I do note that there is significant capacity outside of this voltage window that may be the result of electrochemically catalyzed reactions of the electrolyte. Several possible reactions may occur including breaking of the amide bond or reactions of the RAFT end groups. I believe that additional efforts to engineer a more voltage-stable PZIL may be necessary for practical implementation of this class of electrolyte.

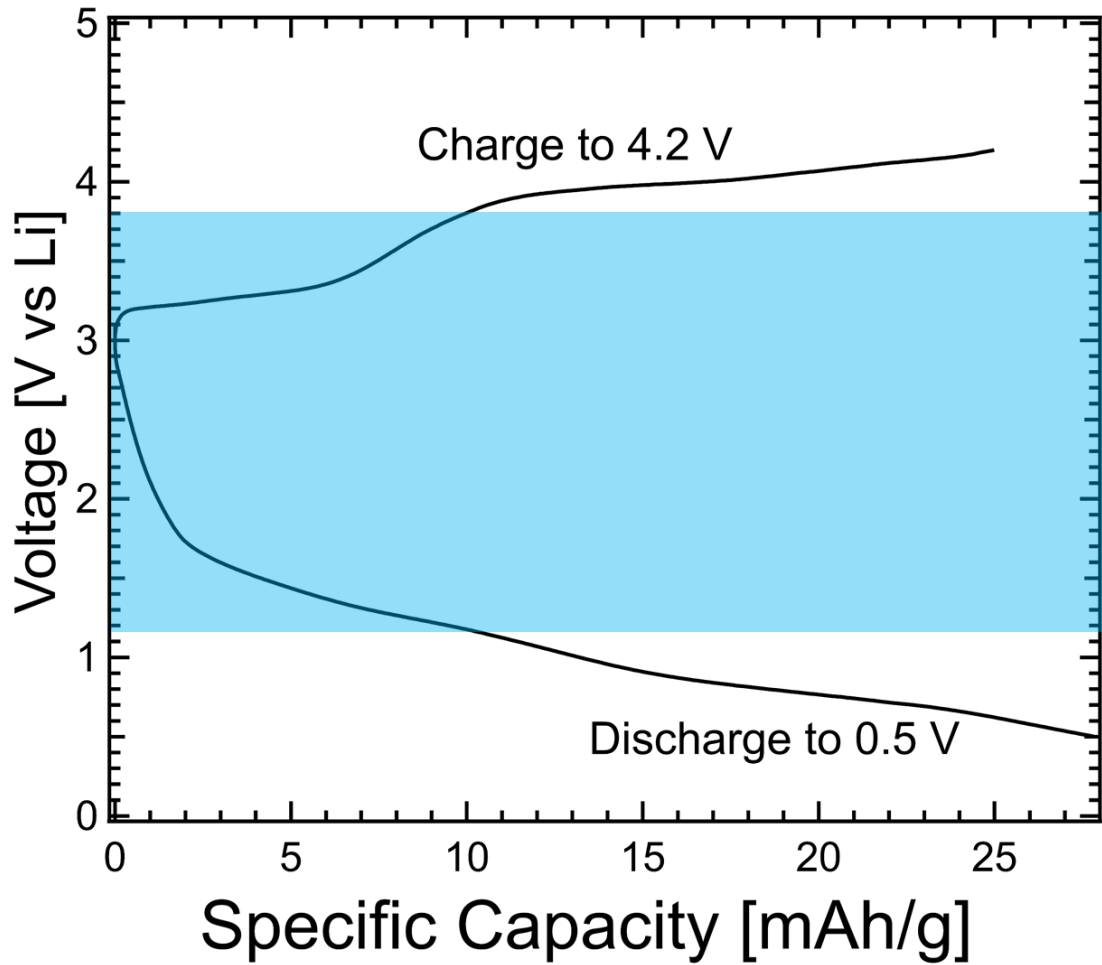


Figure 62: The Voltage against lithium versus the capacity for the cell described above.

A stability window is defined with the blue square as the voltage range where the cell exhibits minimal capacity (capacity < 10mAh/g).

D.6 Evaluating the High-Salt Limit

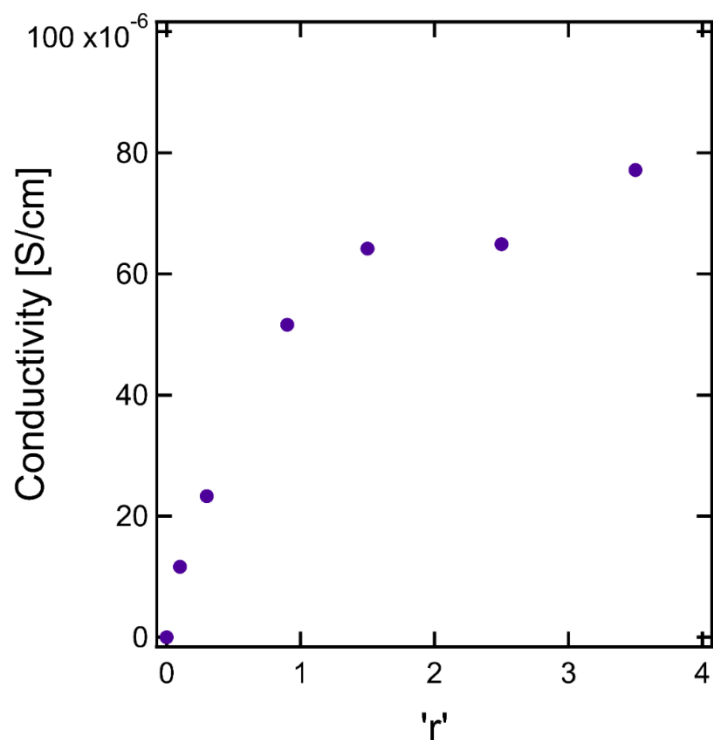


Figure 63: Conductivity versus 'r' for the PZILs over a larger range of salt concentrations.

Higher monomer/salt ratios have been evaluated (without full characterization) to determine the optimal formulation range for these PZILs. Although the conductivity monotonically increases throughout this composition range, the lower salt formulations are the primary subject of investigation in the current report since these offered the best tradeoff of mechanical properties and ion conduction.

Table 21: This table demonstrates the precipitous drop in the calorimetric glass transition temperature as large quantities of salt are added to the electrolyte.

Salt Loading (r-ratio)	T_g [°C]
0	25
0.1	11
0.3	2
0.9	-5
1.5	-12
2.5	-35
3.5	-42

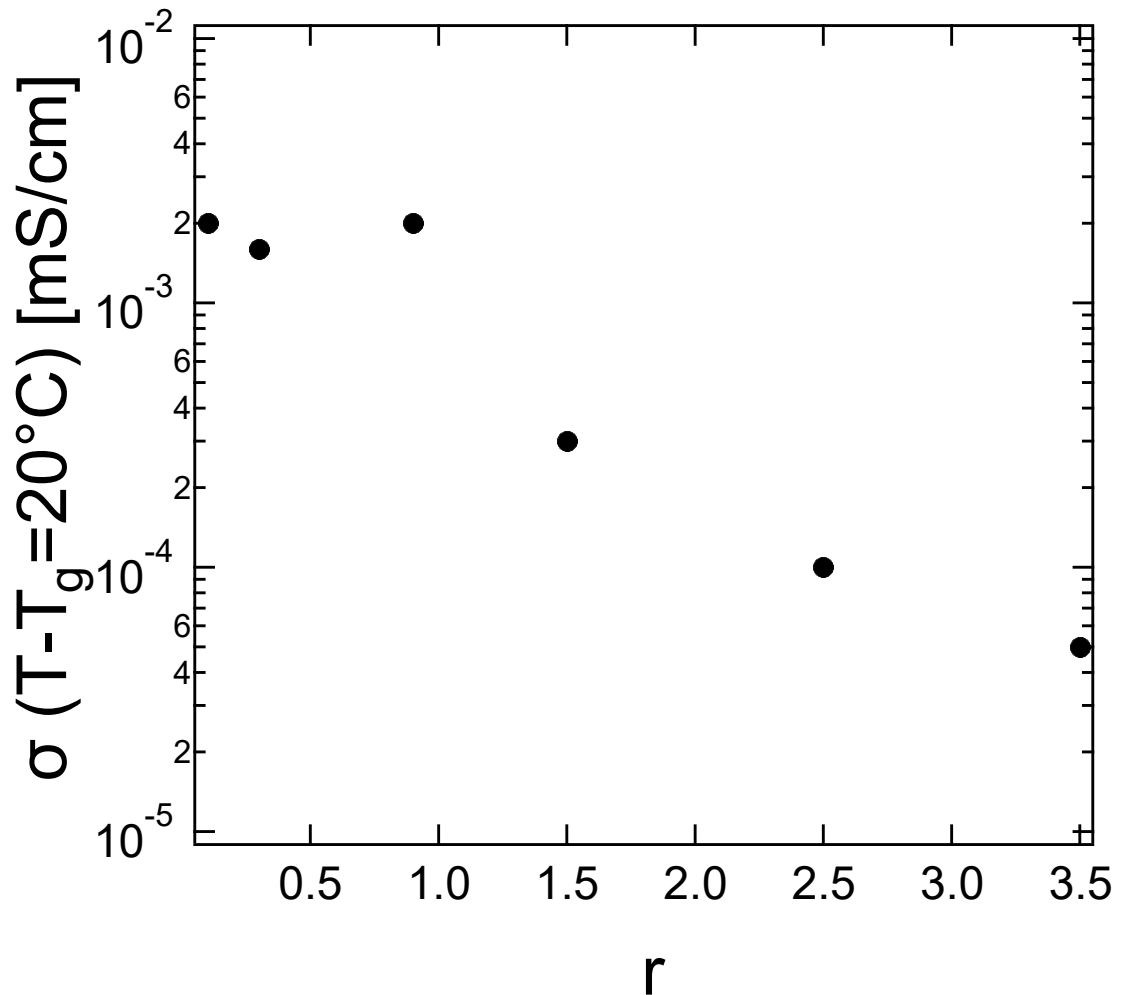


Figure 64: Ionic conductivity (normalized by glass transition temperature) plotted against the salt concentration as parameterized by r.

A precipitous drop in normalized conductivity is observed at the same concentration at which Bragg peaks disappear. There is indeed a precipitous drop in conduction through this transition. This suggests that as the crystalline structure melts, a more conventional vehicular transport mechanism dominates. This difference is even more pronounced when the number of charge carriers is considered since the number-density of mobile charges is proportional to salt concentration.

D.7 Thermal Analysis

7.1 Thermogravimetric Analysis of Materials

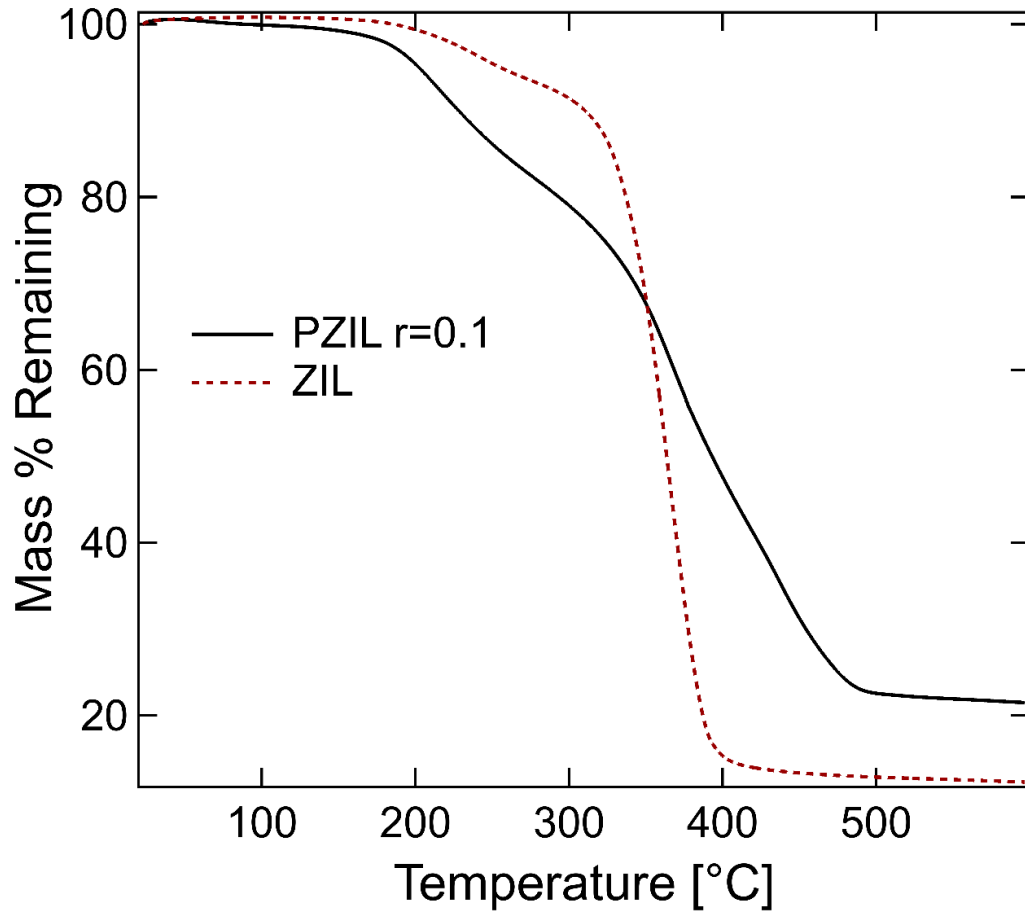


Figure 65: The decomposition profiles of the ZIL and PZILs.

The onset of mass loss for the PZILs, indicated by the temperature at which 1% of mass has been lost, is found to be 180°C, so this temperature was utilized as a maximum temperature for further thermal analysis. Evidently there are two reaction stages for degradation of both the PZILs and the ZIL indicated by the presence of an initial drop in the mass % remaining at ~200°C and a second more severe drop at ~350°C.

7.2 Lithium bTFSI Melting Curve

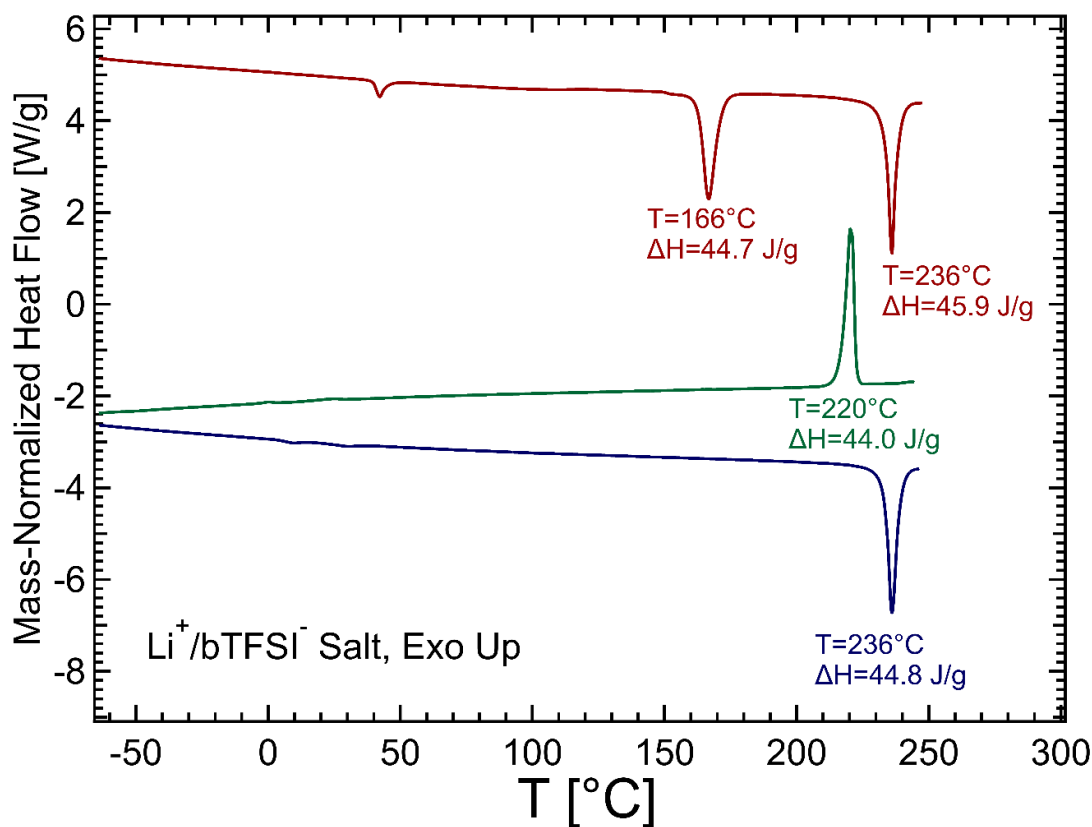


Figure 66: Calorimetric studies of Li⁺/bTFSI⁻.

Understanding the melting behavior of the Li⁺/TFSI salt is important in distinguishing the features seen in the polymer from the salt. The curves are shifted so that the order of scans is chronological when descending. Upon the first heating major endothermic peaks are observed at 166 and 236 °C. According to the literature, these endothermic features can be attributed to a solid-solid transition (reported at 152 °C in the literature) and a melting temperature (reported at 234 °C), respectively. An additional peak at 50 °C may be an artifact or a feature of some adsorbed species coming off the salt. Upon cooling, a single crystallization feature is observed with an enthalpy that approximately matches the melting enthalpy of the crystals upon heating. A solid-solid transition peak is not observed, likely due to the fast cooling rate of the sample. Upon reheating the sample, the melting feature is observed again, with similar enthalpy to the observed 1st melting enthalpy and

crystallization enthalpies. Note that the enthalpies associated with these transitions are approximate ($\pm 20\%$) due to limited resolution in the mass of the sample.

7.3 Melting Behavior of the ZIL

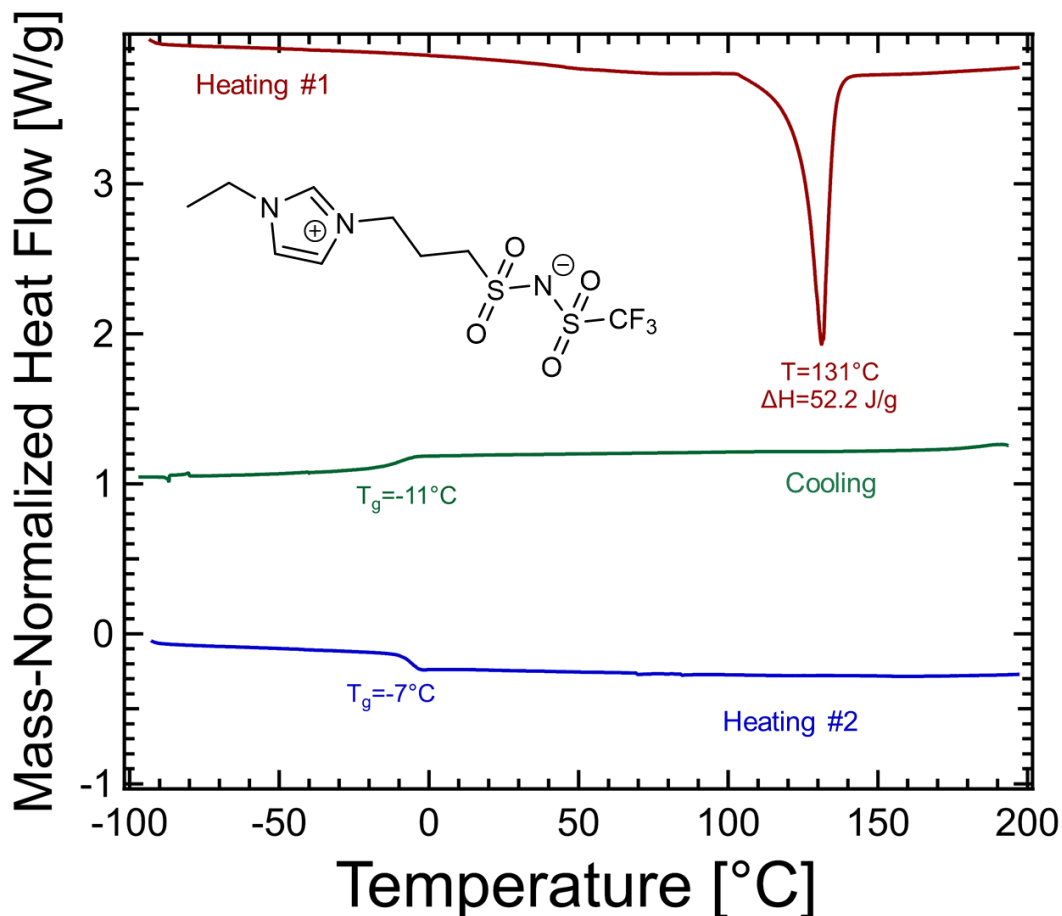


Figure 67: Calorimetric studies of the ZIL.

Another useful reference system to consider is the zwitterionic liquid (inset). This above figure shows a heat-cool-heat cycle of this zwitterion small molecule where the curves are formatted so that they are sequential in time as read from top to bottom and the curves have been shifted for clear viewing. The first heating results in a sharp melting transition as may be expected of a crystalline material. However, upon cooling no crystallization peak is observed and the material instead undergoes a glass transition around -11°C . I observe that this amorphous liquid state is maintained within this ZIL for >24 hours but the material eventually converts back to a crystalline solid. The sluggish crystallization kinetics of this molecule are consistent with observations by Ohno et al. that many organic zwitterionic

compounds comprised of IL-type salts gradually crystallize, but sometimes take weeks¹⁵⁸ to return to the crystalline state. The sluggish crystallization kinetics of the small molecule ZIL are worth considering in the following analysis of the polymers, which may exhibit even more sluggish crystallization due to the polymer-bound nature of the ZILs. Note that the enthalpy of the crystallization is an approximate value ($\pm 20\%$) due to limited resolution of the sample mass.

7.4 Calorimetric Analysis of PZILs

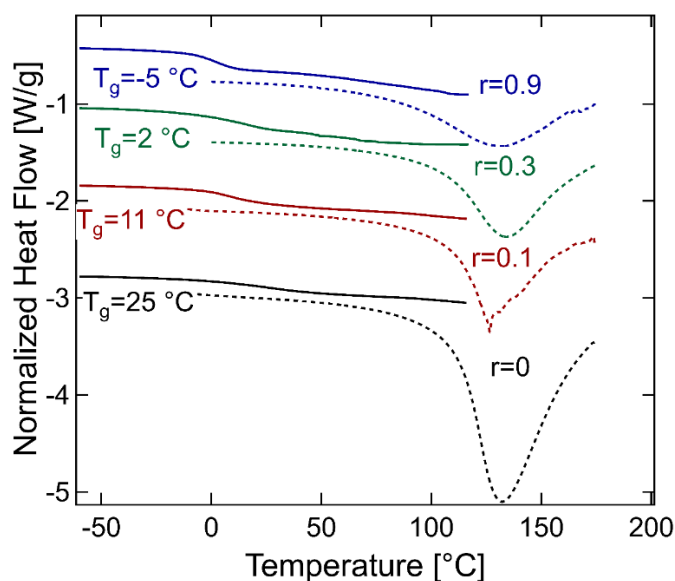


Figure 68: Calorimetric studies of the PZI.

The first pass of the calorimetric cycle is indicated by the dotted line; the second heating is indicated by the solid line. In the first pass, an endotherm is evident for all samples, typically an endotherm in DSC is typical of either 1) a melting temperature or 2) an enthalpy of vaporization of a volatile component. Since there is no removal of any volatile component evident in TGA analysis of the sample and since the samples were thoroughly dried and packed in a glovebox, I conclude that this peak is evidence of crystalline melting. The melting temperatures in all cases are relatively constant at $\sim 130^\circ\text{C}$. This is remarkably consistent with the melting temperature of the small molecule crystallite. I note again that agreement between the small molecule crystal and the polymer crystal is fortuitous in this case since tethering the molecule to the polymer backbone can change many of its properties. Upon a second heating cycle, only a glass transition is observed. This is

consistent with the small molecule ZIL, in which the slow crystallization dynamics prevent the observation of a second melting.

The glass transition temperature observed in the second melting scan may differ significantly from the actual T_g observed in the electrolyte due to the interplay of crystallinity with T_g . Therefore the calorimetric T_g is unlikely to be the T_g experienced within the working polymer electrolyte. Consequently, it is the rheometric T_g which is preferred for all measures of dynamics and is used in the Walden plot of the main paper. Although it is not a central theme of this work, it does bear noting that the trend of salt concentration versus T_g shows that these variables are inversely related for the PZIL. I hypothesize that adding mobile salt charges reduces monomer-monomer interactions and results in faster dynamics, however this trend may bear additional study.

D.8 Stress Relaxation Experiment

An evident feature of the TTS curves presented in Figure 32 is the appearance of a low-frequency plateau at observed timescales, rather than terminal relaxation behavior. Evidently this inability to fully relax stress at long times is a consequence of the zwitterionic functionalities of the polymer since the linear, ZI-free chain would relax at these timescales. Although this long-time rheological behavior is beyond the scope of the current work, it was

briefly probed in the $r=0.9$ sample via a stress relaxation experiment.

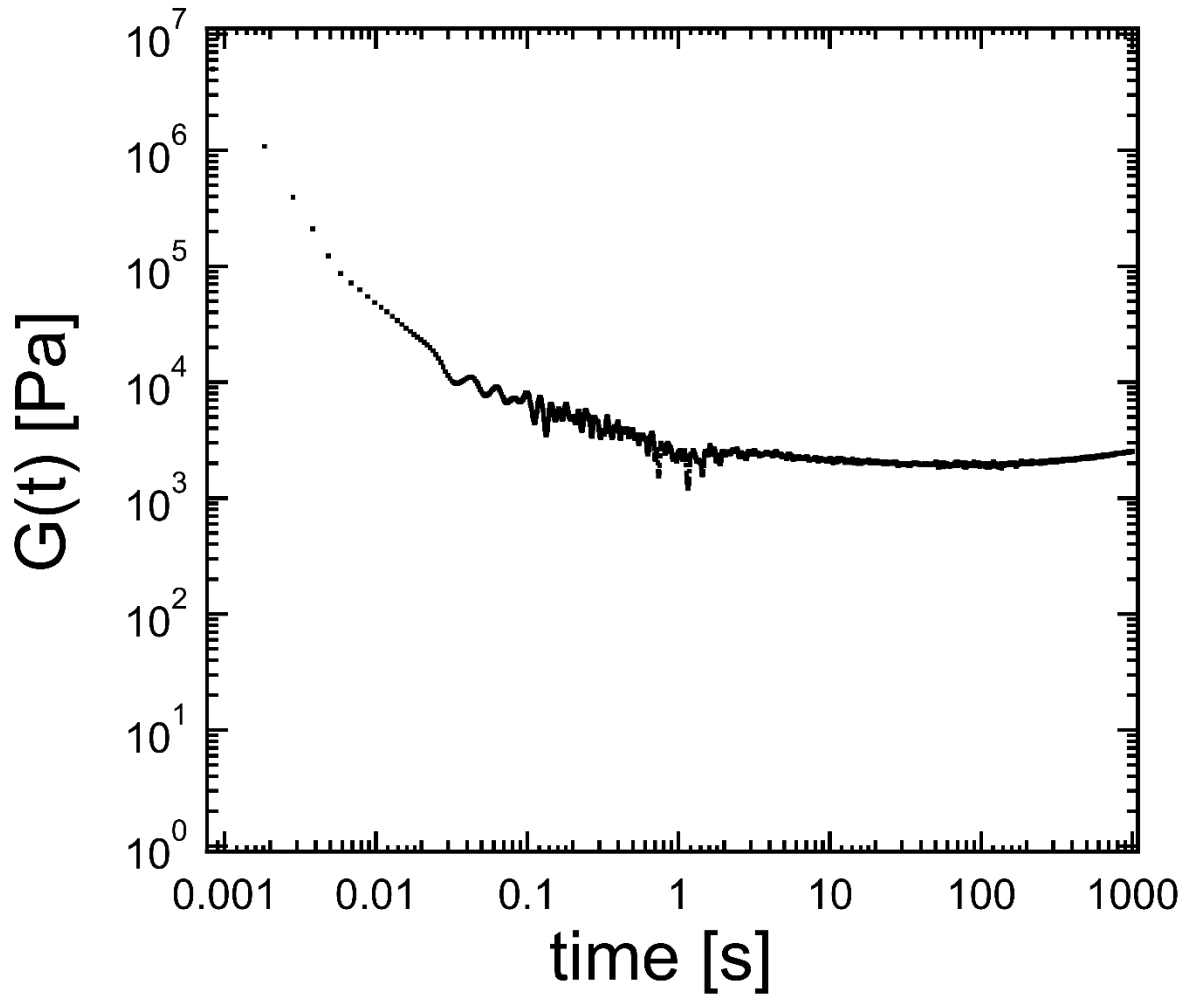


Figure 69: Stress relaxation of the PZI.

Stress relaxation reveals no terminal behavior over a 1000 second window at 70°C. This delay in terminal relaxation could occur from interactions between zwitterions between chains, which are known to transiently crosslink the material. Evidently this crosslinking mechanism is not a permanent one since the polymer could be dissolved into polar organic solvents.

D.9 Raw Dielectric Spectroscopy Data

Dielectric spectroscopy measurements are used to evaluate the ionic conductivity of the electrolyte. I note that these AC-type measurements only probe the small-lengthscale and are taken in the range of small potentials ($<100\text{mV}$). High performance in these dielectric spectroscopy tests represents a necessary but not sufficient demonstration of the merits of the materials as battery electrolytes in real cells where transport much occur over macroscopic lengthscales ($\sim\text{cm}$) and at larger potentials ($\sim 3\text{-}6\text{ V}$).

9.1 Salt-Free Polymer ($r=0$)

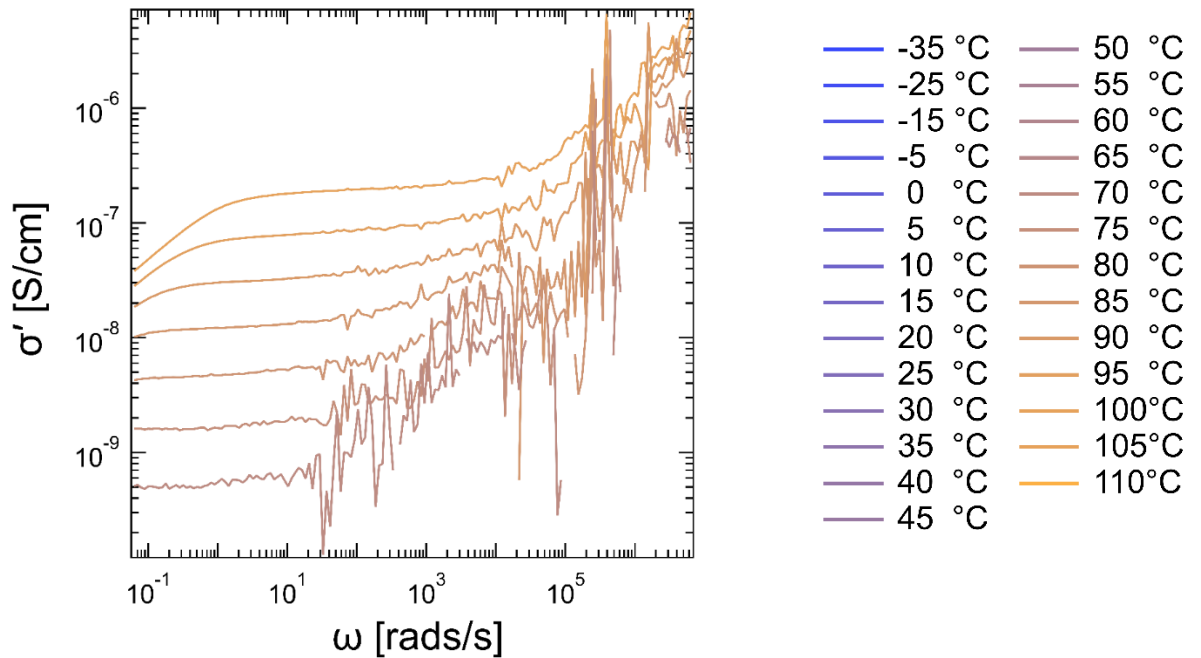


Figure 70: The real part of the conductivity is plotted against frequency for the salt-free polymer.

The high frequency data is noisy, but a clear plateau at low frequencies can be observed corresponding to the DC conductivity of the samples. For the salt-free polymer, the loss tangent is not provided as this data is too noisy to be useful. The temperature legend correlates the colors and temperatures of all plots in this section.

9.2 Salt-Free Polymer (r=0.1)

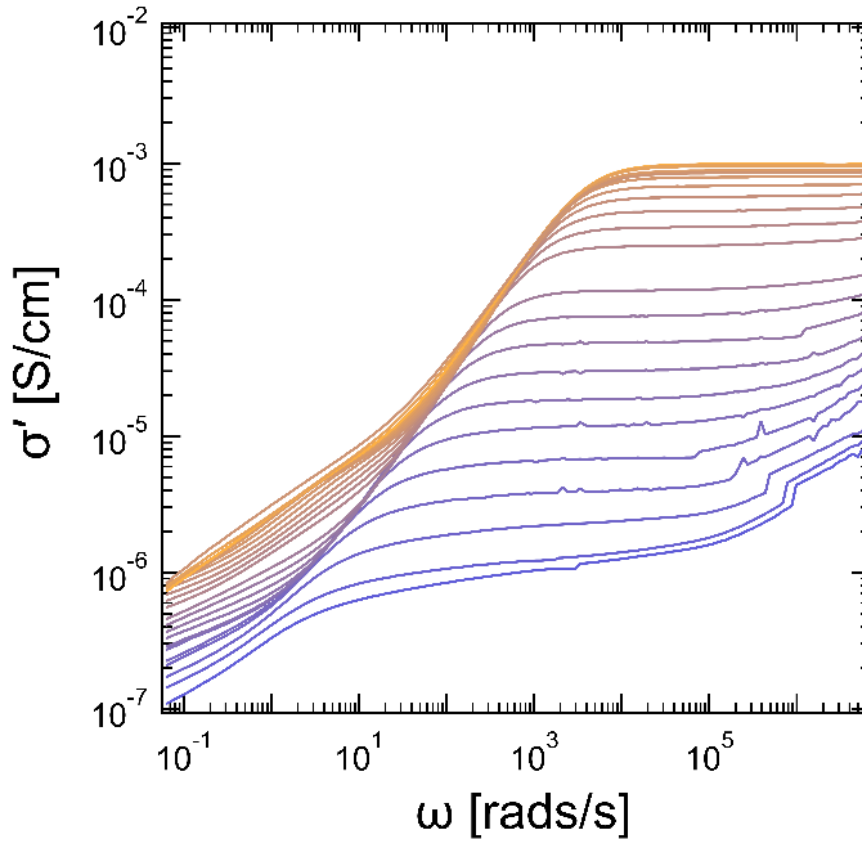


Figure 71: The real component of the conductivity is provided for the r=0.1 sample at temperatures ranging from -30 to 110 °C.

A plateau corresponding to the DC conductivity occurs at high frequencies followed by electrode polarization at lower frequencies.

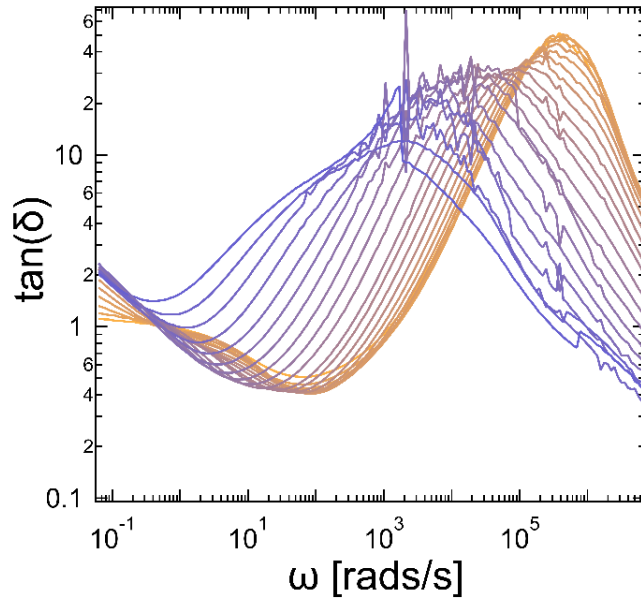


Figure 72: The loss tangent is provided as a function of frequency for the $r=0.1$ sample at temperatures ranging from -35 to 110 °C.

The peak of this loss tangent at values much greater than unity indicates approximate DC behavior.

9.3 Salt Loading $r=0.3$

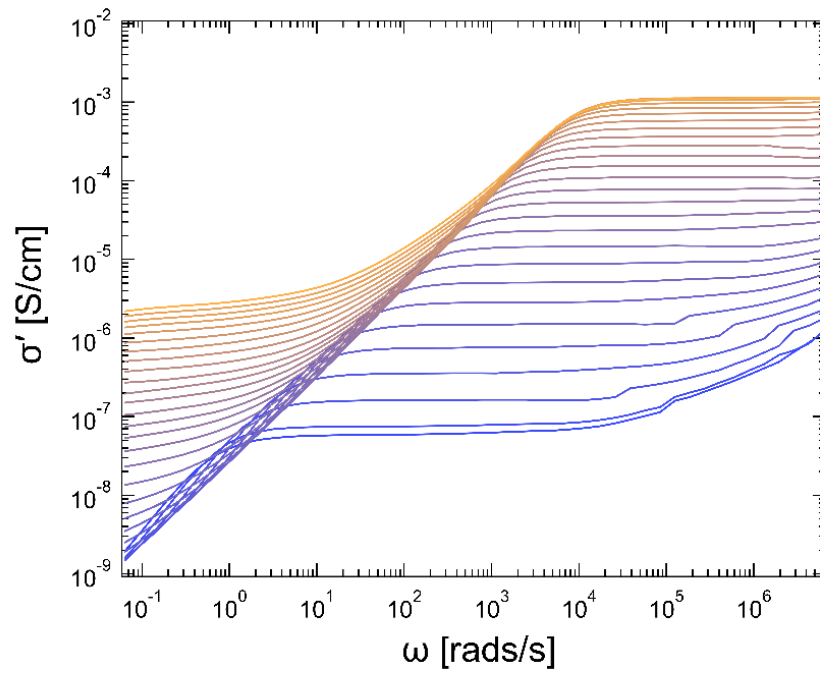


Figure 73: The real component of the conductivity is provided for the $r=0.3$ sample at temperatures ranging from -35 to 110 °C.

A plateau corresponding to the DC conductivity occurs at high frequencies followed by electrode polarization at lower frequencies.

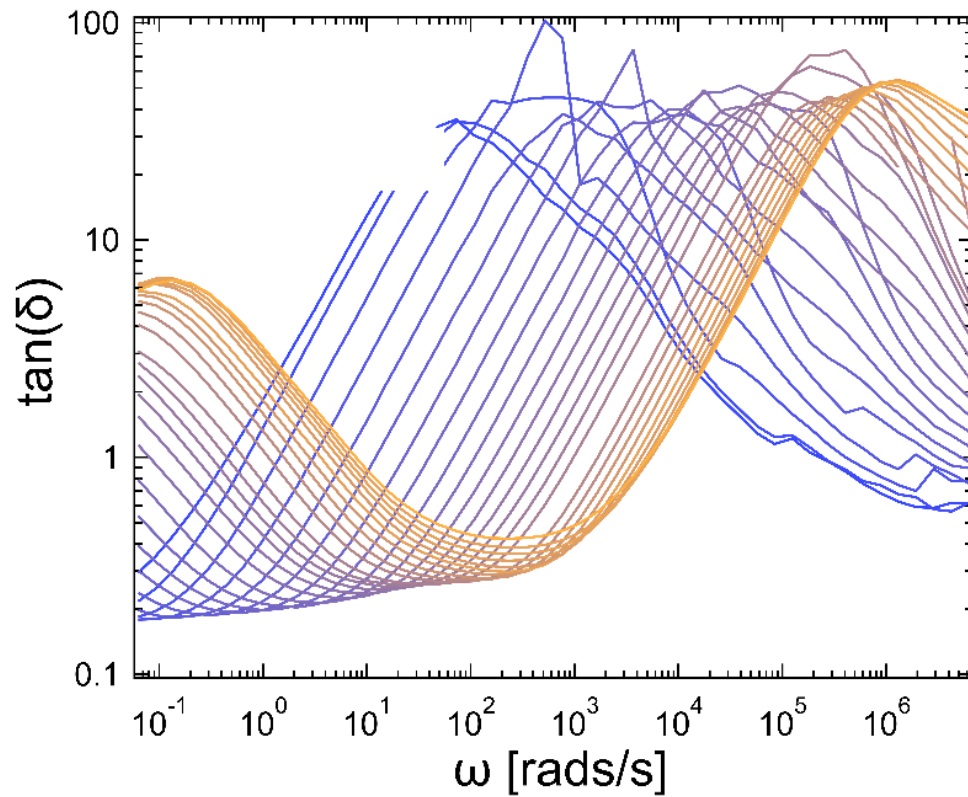


Figure 74: The loss tangent is provided as a function of frequency for the $r=0.3$ sample at temperatures ranging from -35 to 110 °C.

The peak of this loss tangent at values much greater than unity indicates approximate DC behavior.

9.4 Salt Loading $r = 0.9$

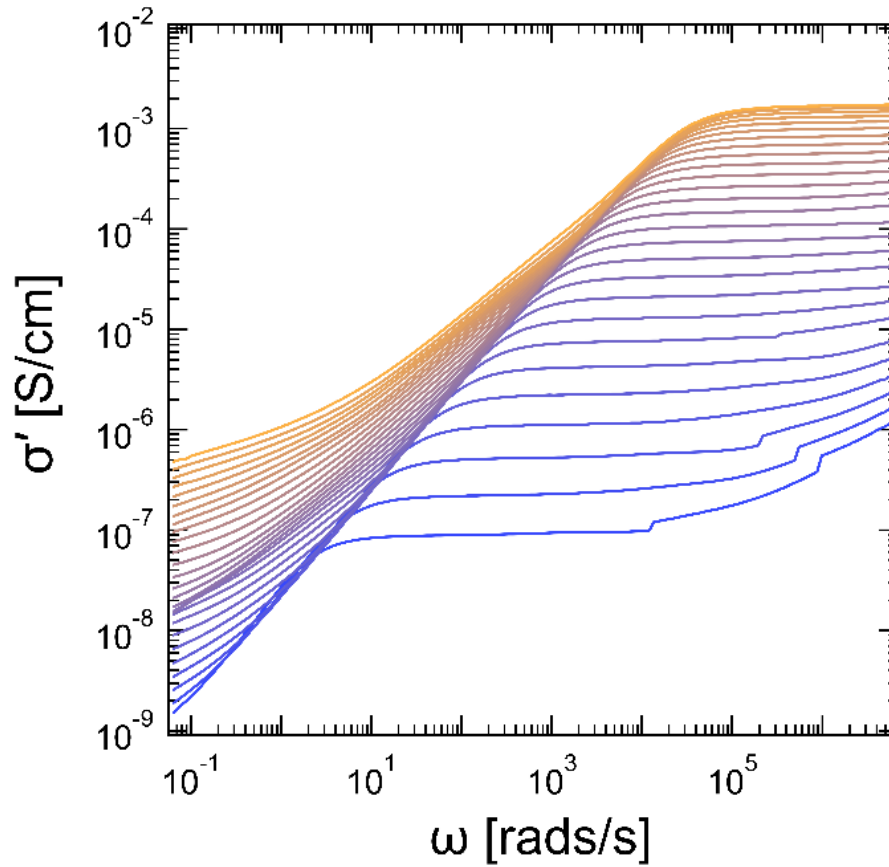


Figure 75: The real component of the conductivity is provided for the $r=0.9$ sample at temperatures ranging from -35 to 110 °C.

A plateau corresponding to the DC conductivity occurs at high frequencies followed by electrode polarization at lower frequencies.

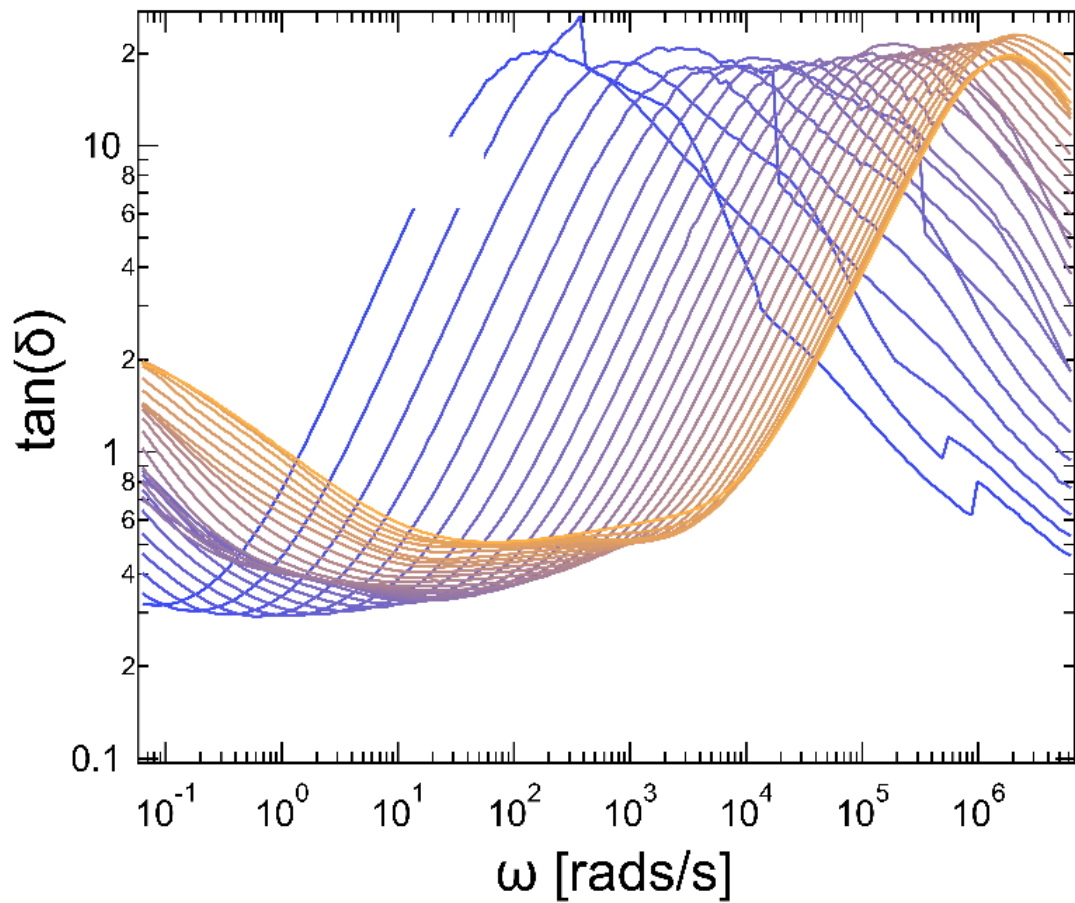


Figure 76: The loss tangent is provided as a function of frequency for the $r=0.3$ sample at temperatures ranging from -35 to 110 °C.

The peak of this loss tangent at values much greater than unity indicates approximate DC behavior.

D.10 NMR Spectra

The NMR spectra in this section are cropped to focus on the relevant chemical shift regimes, no peaks were cropped from the spectra even when a limited chemical shift regime is shown. Solvation of the zwitterions by a single deuterated solvent was not always practical due to the unfavorable solvation of the zwitterions, consequently a secondary solvent was sometimes added to improve the solubility for analytical purposes only.

10.1 ^1H NMR Spectrum of Crude NHS Acrylate Polymer

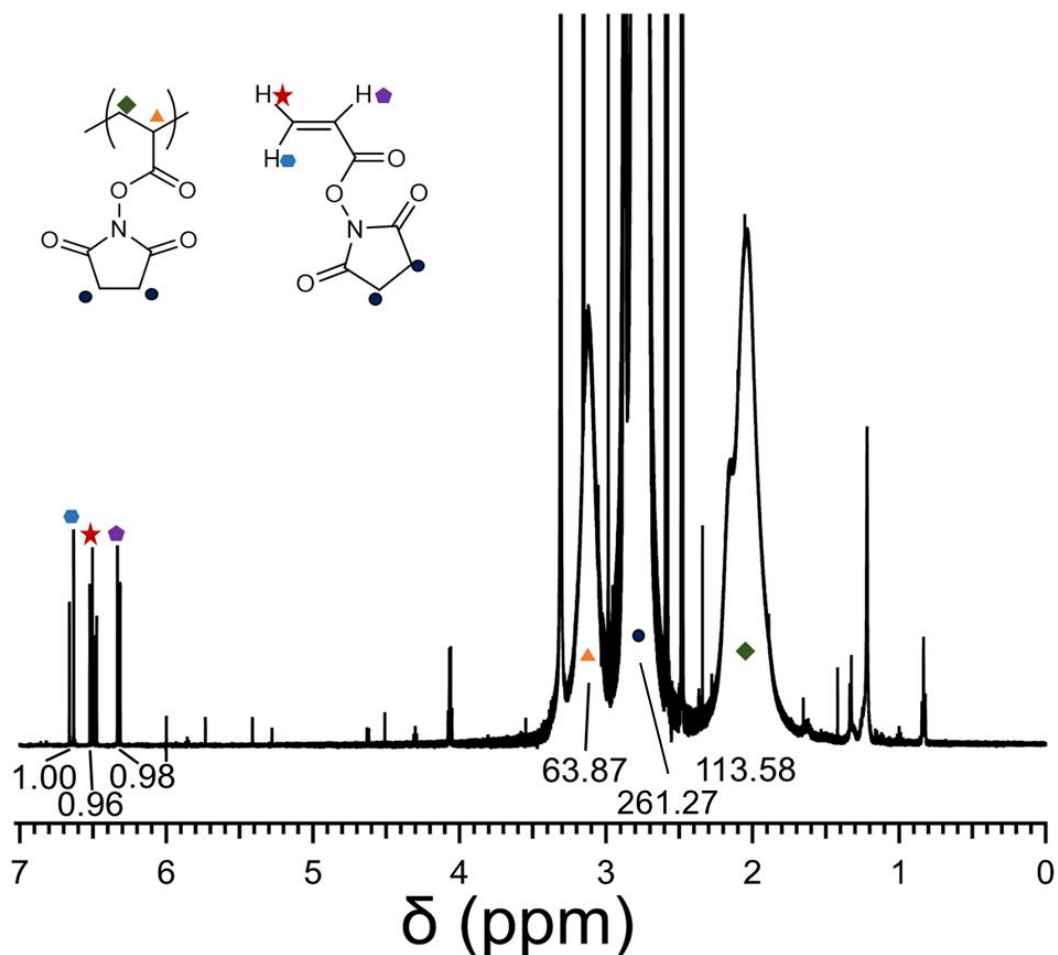


Figure 77: Crude ^1H NMR of the NHS ester acrylate after polymerization.

The conversion of the polymerization is evaluated by comparison of the vinyl monomer peaks with the backbone peaks of the polymer (◆) to be 0.991. The corresponding number average degree of polymerization 248 and a molar mass of 42 kg/mol.

10.2 ^1H NMR of Purified NHS Acrylate Polymer

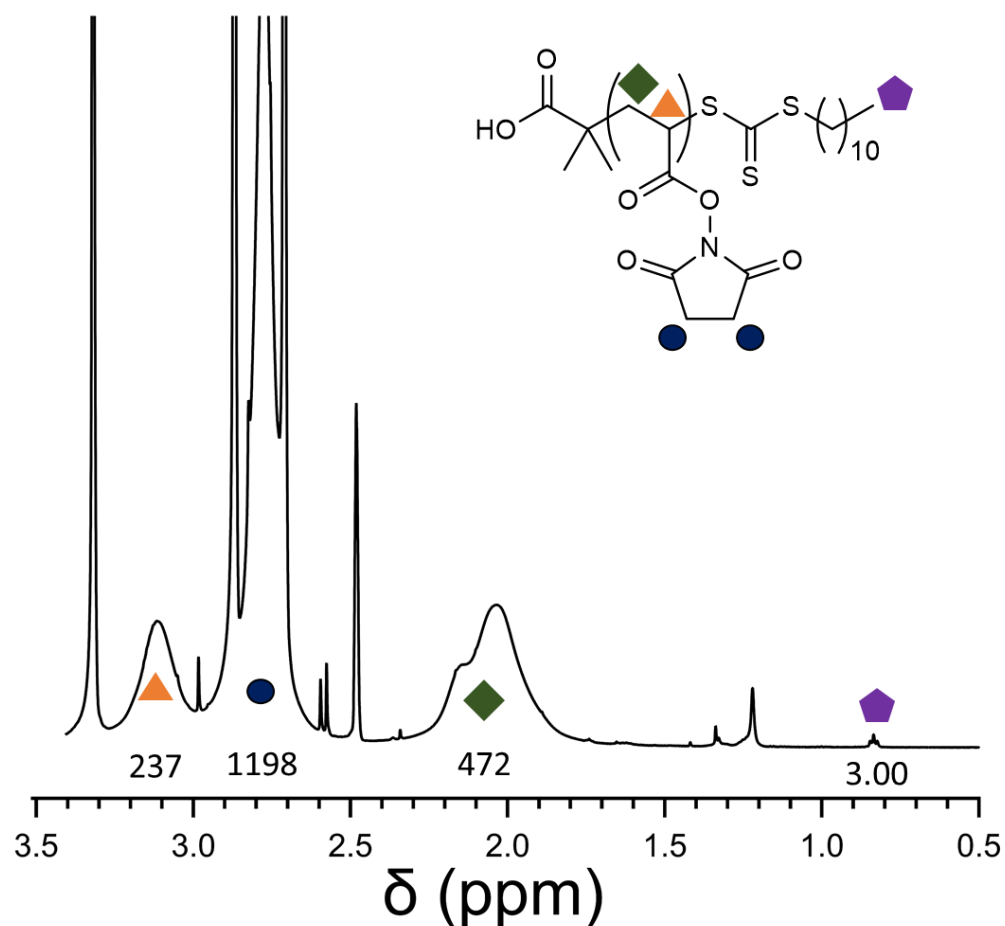


Figure 78: ^1H NMR of Purified NHS Acrylate Polymer.

End group analysis based on the anticipated chain end of this polymer from idealized RAFT polymerization gives a number average degree of polymerization of 236.5, which corresponds to a number averaged molar mass of 40 kg/mol.

10.3 ^1H and ^{19}F NMR of TFSI Br

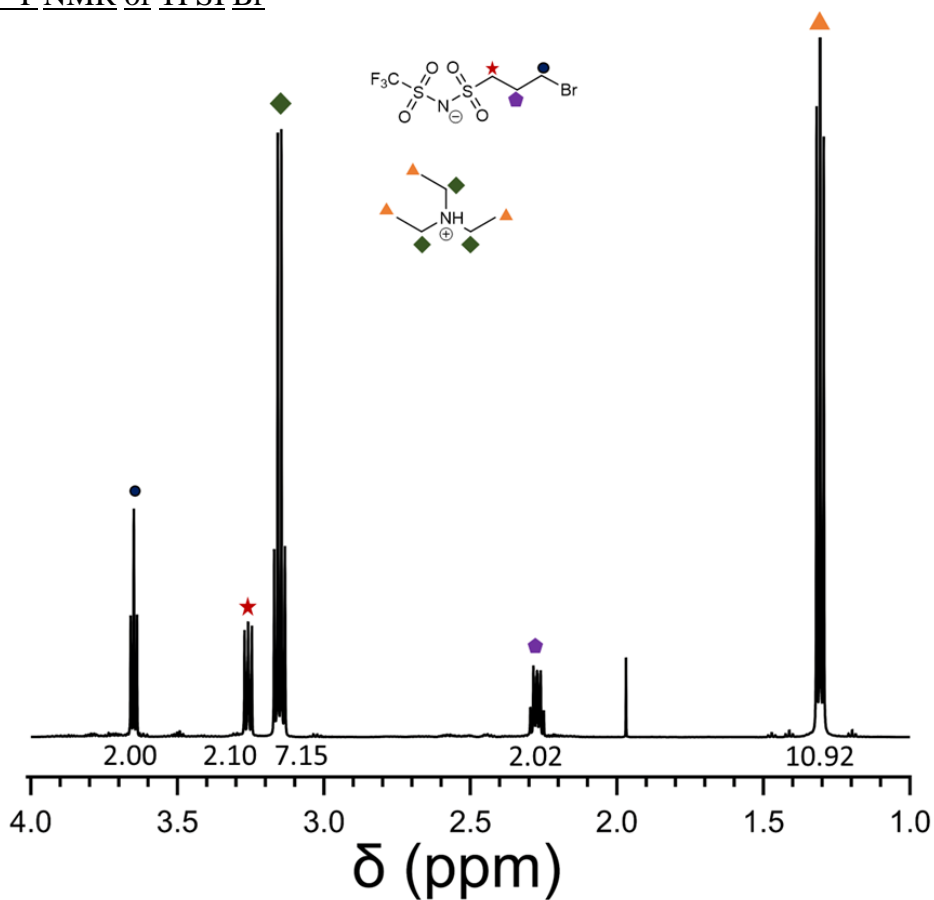


Figure 79: ^1H NMR of TFSI-Bromide compound after washes.

Some excess triethylamine remains. Though the compound could be isolated more carefully by recrystallization of a version with an alternative counterion such as lithium or potassium, the triethylamine counterion is preferred in this case because counterion removal can be easily monitored by ^1H NMR.

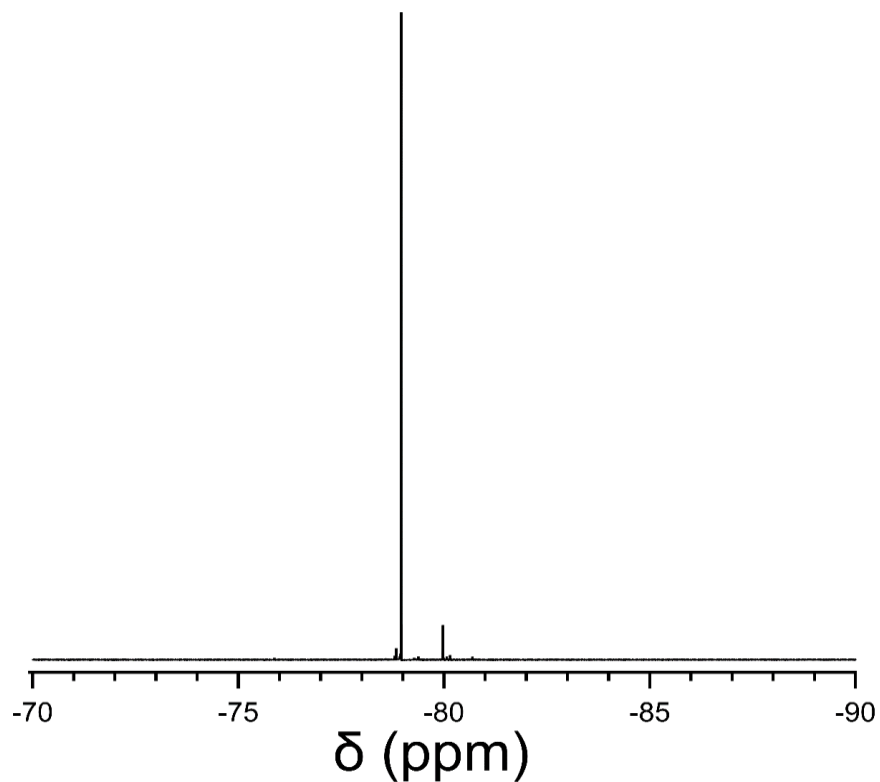


Figure 80: ^{19}F NMR of TFSI Br.

The preparation of the fluorine compound cannot be confirmed by ^1H NMR since no protons undergo a significant chemical shift upon conversion from the acid chloride to the TFSI product. The above spectrum is the ^{19}F 1D NMR of the small molecule. The presence of a fluorine peak at a chemical shift consistent with previous reports¹⁵⁹ is used instead to confirm the preparation of the correct product.

10.4 ^1H NMR of Imidazole Functionalized Polymer

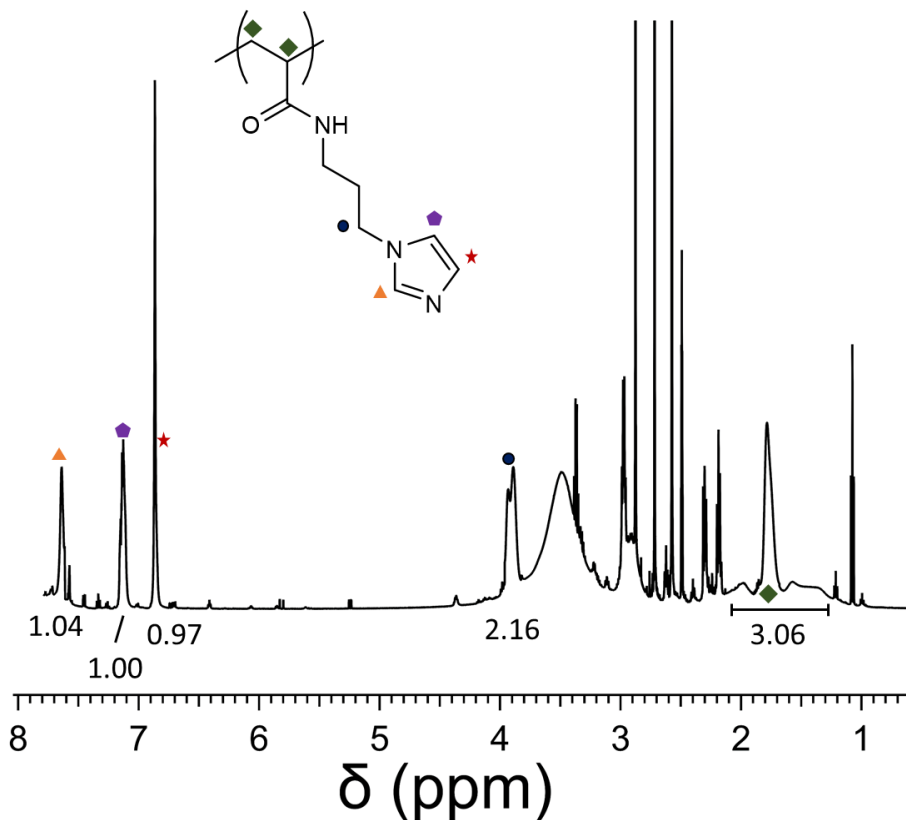


Figure 81: ^1H of imidazole functionalized polymer poly(Im).

This ^1H NMR spectrum was taken of an aliquot of the polymer after the imidazole addition reaction had been allowed to proceed for 18 hrs. Polymer was isolated from this sample by reverse precipitation in diethyl ether. The presence of imidazole peaks in good agreement with the integration for backbone peaks suggests that this crude sample has successfully undergone replacement of the NHS-acrylate group with aminopropyl imidazole. The crude peaks in this sample will be removed in subsequent dialysis steps after the conversion of the polymer to the zwitterionic form. The presence of a peak

corresponding to the amide group is not present on this spectrum, presumably this is because this proton can exchange with the deuteriums from the deuterated methanol solvent.

10.5 ^1H NMR of Washed Product Polymer

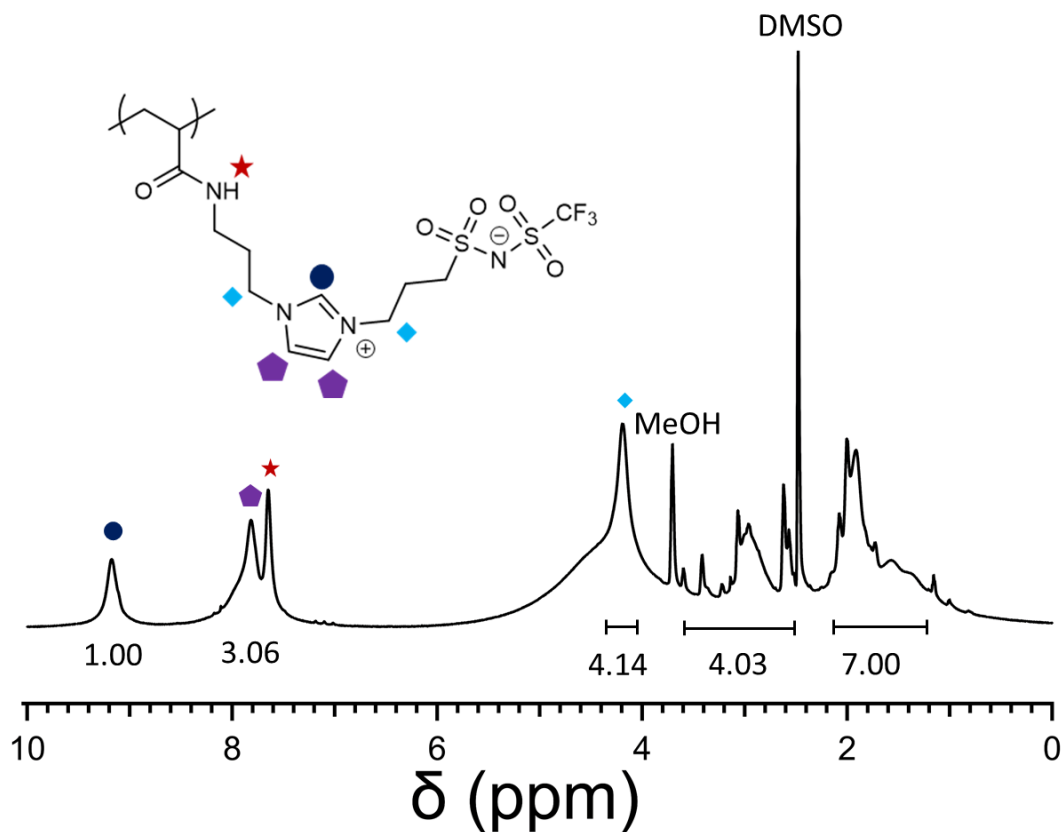


Figure 82: ^1H NMR of poly(Im-c3-TFSI).

The ^1H NMR spectrum of the polymer indicates quantitative conversion of the imidazole polymer to the PZIL as suggested by the downfield shift of the proton at the 2-position of the ring consistent with deshielding as a result of aromatizing imidazole to imidazolium. Simultaneously, the protons at the 4 and 5 positions merge and shift

downfield. The presence of an additional peak at 7.8 ppm is attributed to the amide peak, which was previously silenced in the d-MeOH, but is not silenced in this NMR, which was collected using d-DMSO as a solvent, which will not undergo much proton exchange. The lack of TEA peaks in this spectrum suggests quantitative removal of excess salts. Though the peaks upfield are broad and difficult to assign individually, their total integration suggests agreement with the anticipated structure. The presence of end group peaks at ~1ppm is still evident in this spectrum indicating that side-reaction of the end group has not occurred.

10.6 ^1H , ^{13}C , and ^{19}F NMR of EthIm-c3-TFSI

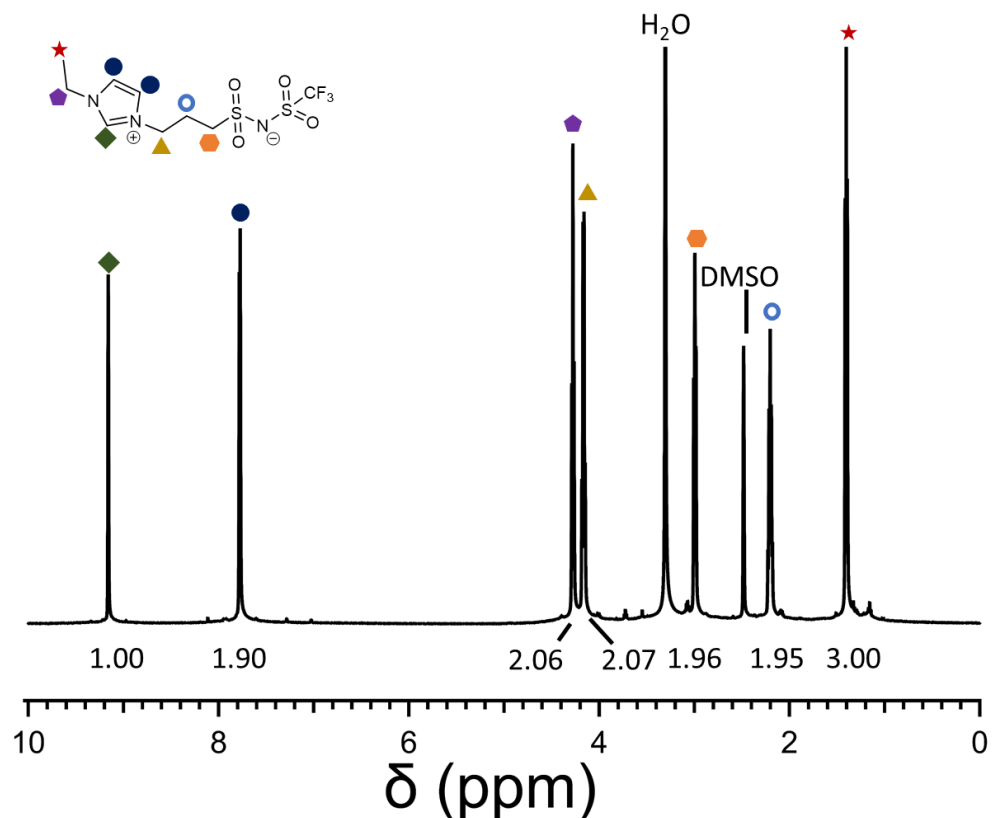


Figure 83: ^1H NMR of EthIm-c3-TFSI .

The ^1H NMR of this compound follows splitting patterns consistent with the proposed structure. NMR is taken on the sample prior to final drying. Residual water in the sample is

consistent with the observed hydroscopic nature of the zwitterion, though no water is used in the purification steps.

10.6 ^1H NMR of EthIm-c3-TFSI

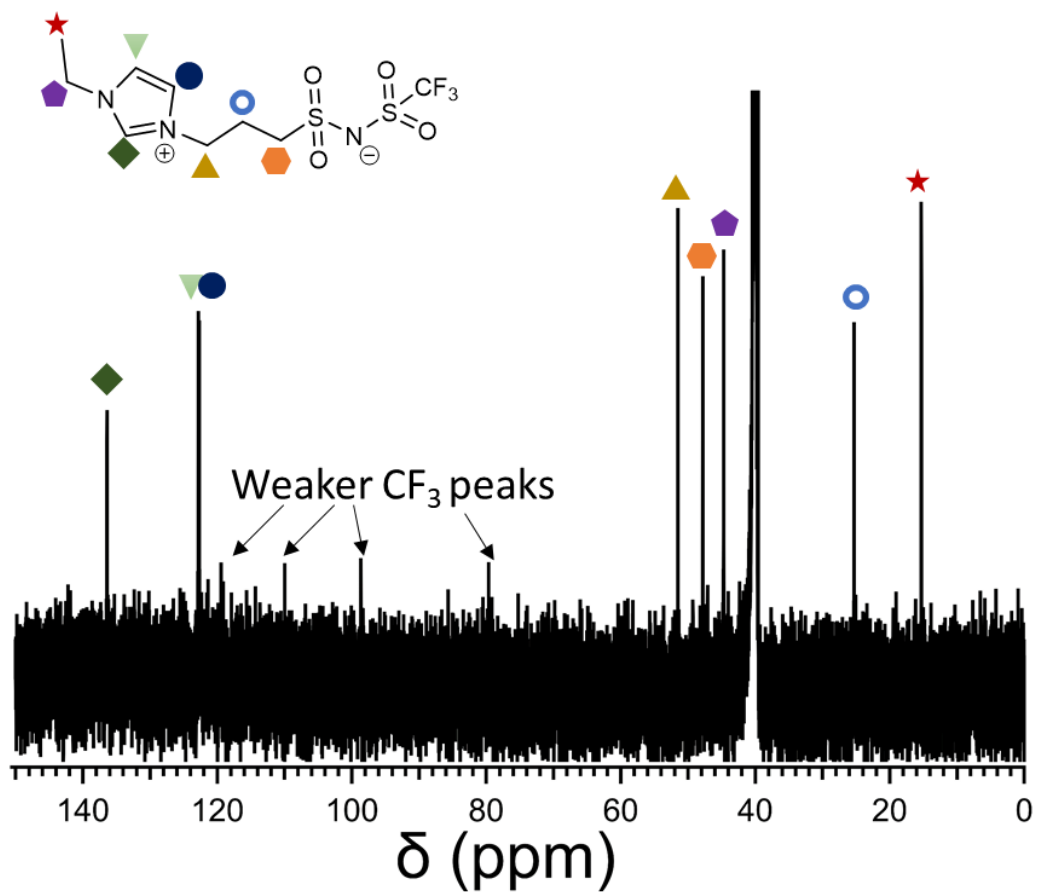


Figure 84: ^{13}C NMR of EthIm-c3-TFSI.

^{13}C NMR shows peaks correspondent with the ZIL molecule. The CF_3 signal is triply split by the presence of fluorines, resulting in four evident signals corresponding to this carbon. The large peak at 40ppm corresponds to d-DMSO.

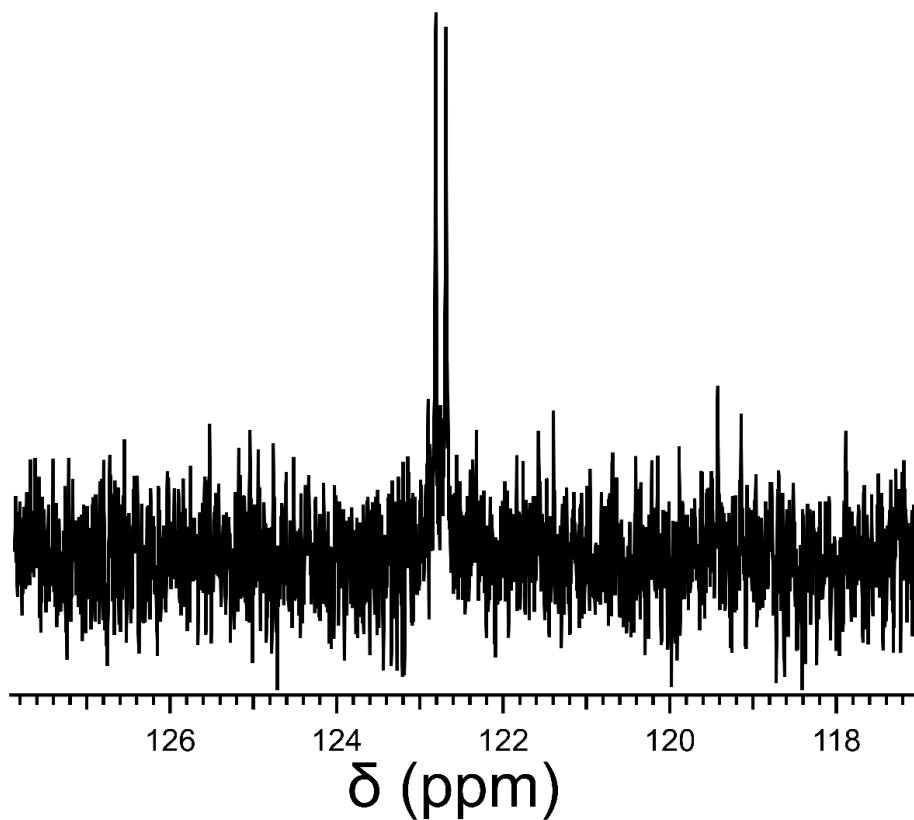


Figure 85: ^{19}F NMR of EthIm-c3-TFSI .

This figure shows a zoomed in region of the NMR spectrum above, it is presented here to demonstrate that there are two distinct signals near 123 ppm, a feature that is difficult to decipher in the zoomed-out spectrum.

10.7 ^1H NMR of Crude PDMAEA

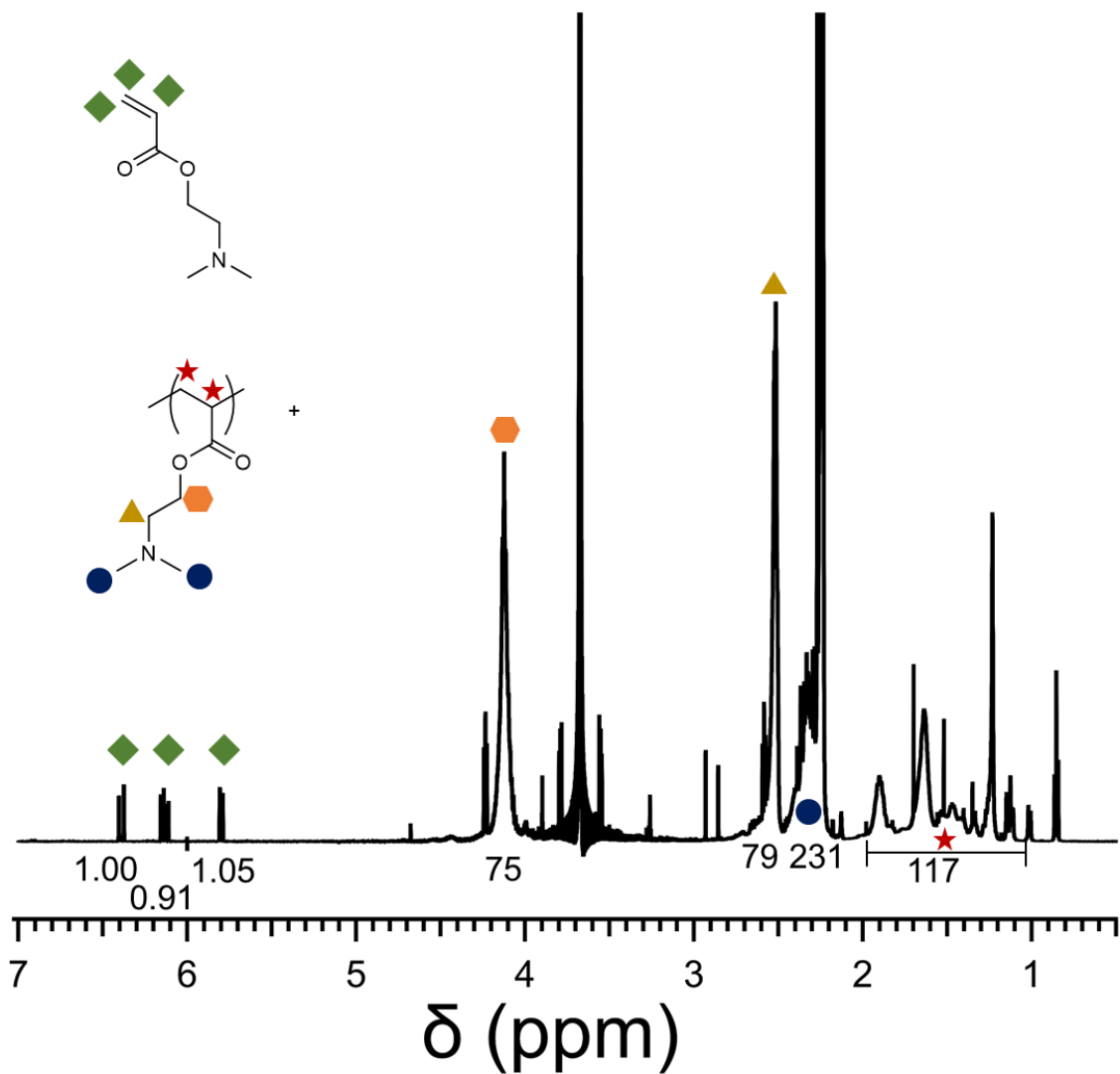


Figure 86: ^1H NMR of Crude PDMAEA.

The conversion of the reaction is evaluated from analysis of the crude reaction product using the comparison of monomer vinyl peaks to the hydrogen signals from the carbon adjacent to the ester (orange hexagon). The conversion after 18hrs was nearly complete at

97.5%. Based on this conversion, a molar mass can be estimated assuming that each chain is initiated from a RAFT initiator. This estimate yields: $N_N = 243$, $M_N = 34.8$ kg/mol.

10.8 ^1H NMR of Purified PDMAEA

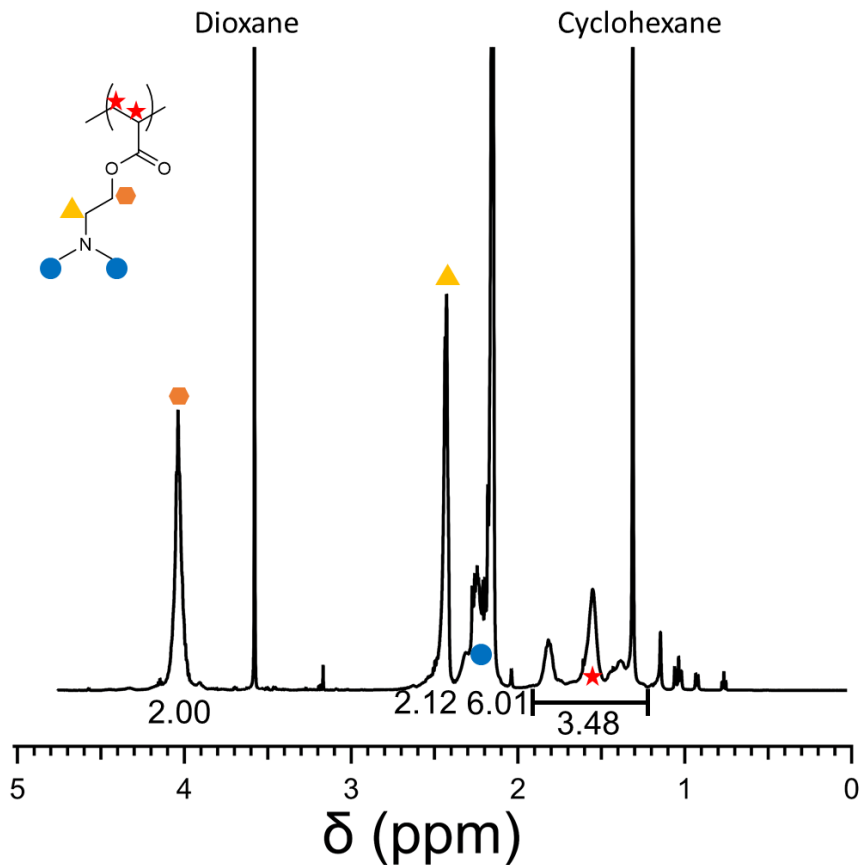


Figure 87: ^1H NMR of Purified PDMAEA.

The precipitated polymer after drying for 24 hours at room temperature shows some residual solvent. This solvent is rigorously removed in the final steps but is not rigorously removed here since the polymer needs to be redissolved for post-polymerization functionalization reactions. The peaks characteristic of the polymer are observed in expected peak positions and in expected ratios. The backbone peaks integrate to a slightly higher intensity than anticipated (3.48 vs 3.00) due to the presence of the cyclohexane peak in this integral region.

The end group signal corresponding to the methyl chain end of the dodecyl group (t, $\delta=0.77$ ppm) has an intensity ratio with the protons alpha to the ester of the repeat unit (b, $\delta=0.404$ ppm) of 3/449, which corresponds to: $N_N = 224.5$, $M_N = 32.1$ kg/mol. This is in good agreement with estimates of polymer size from the crude NMR.

10.9 ^1H NMR of Purified Am-TFSI PZIL

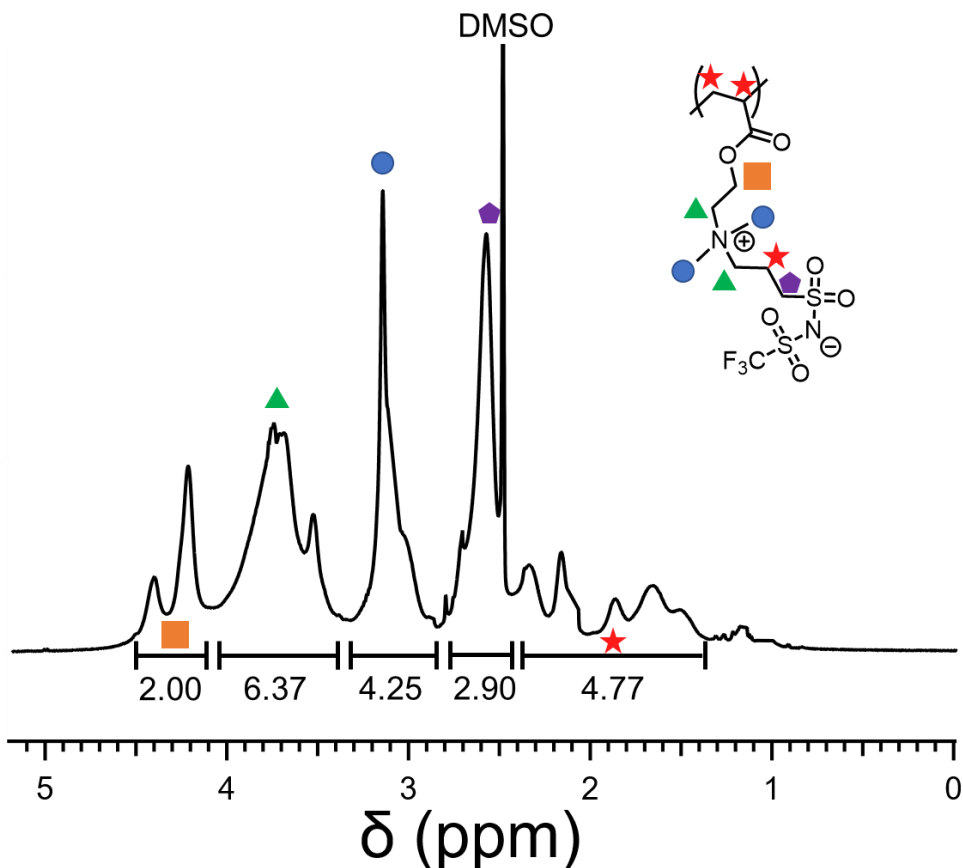


Figure 88: ^1H NMR of Purified Am-TFSI PZIL.

Upon quaternization of the neutral PDMAEA to the zwitterionic polymer, the most prominent proton signal at $\delta=2.2$ ppm shifts downfield, suggesting quantitative conversion of the tertiary nitrogen to a quaternary form. This NMR was taken after drying the sample. The integration value of the peak corresponding to the purple hexagon is likely due to the convolution of DMSO and polymer peaks.

10.10 ^1H and ^{19}F NMR of Cl-c3-SI-C6F5

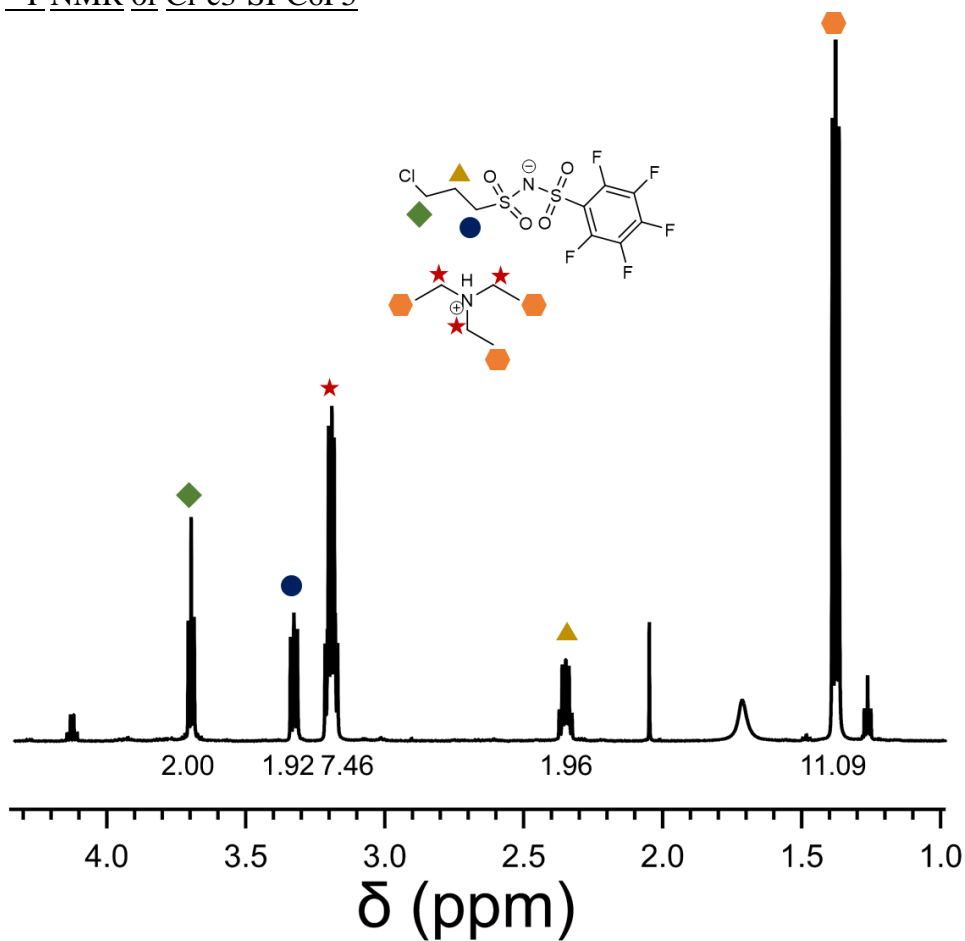


Figure 89: ^1H NMR of Cl-c3-SI-C6F5.

^1H NMR shows the presence of the three peaks corresponding to the alkyl tail with expected splitting. Triethylamine is in slight excess, but this ion is removed in purification of the PZIL in a subsequent step.

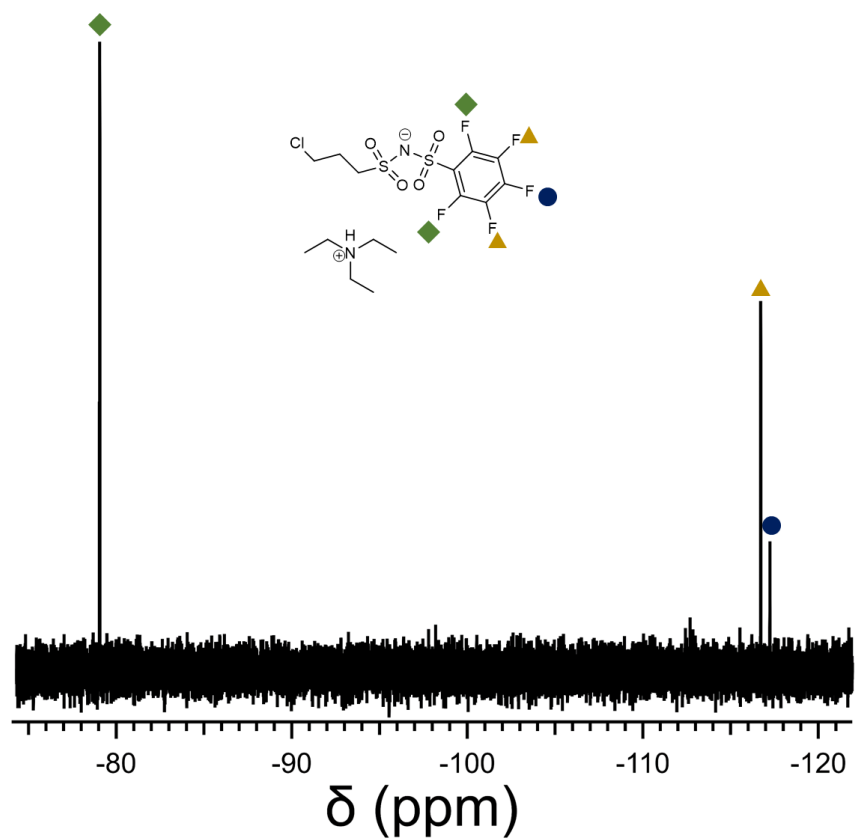


Figure 90: ^{19}F NMR of Cl-c3-SI-C6F5.

^{19}F NMR demonstrates the presence of the three signal expected for the pentafluorophenyl group. The presence of the pentafluorophenyl group in the organic phase suggests that these fluorine signal come from the intended product.

D.11 Size Exclusion Chromatography

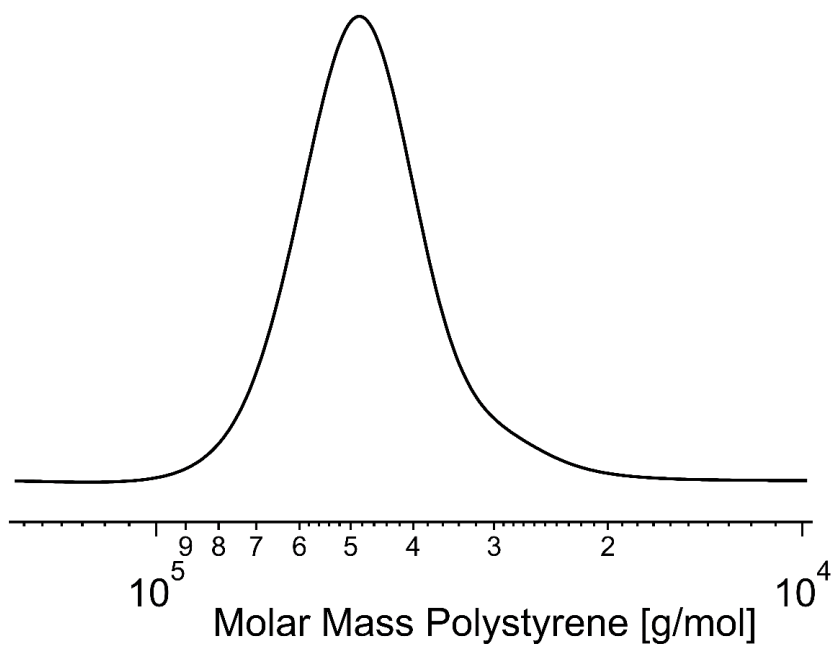


Figure 91: The normalized intensity is plotted against the calibrated equivalent mass of a narrow polystyrene standard.

Size exclusion chromatography (SEC) was performed on poly(N-(3-(1H-imidazol-1-yl)propyl)acrylamide) to determine the breadth of the molar mass distribution. The curve above shows the refractive index signal versus the calibrated molar mass of narrow polystyrene standards. The molecular mass data may be summarized in Table 22.

Table 22: The molecular weight of the polymer prior to conversion to the zwitterionic form estimated by NMR and SEC.

$M_{N,NMR}^a$	$M_{N,SEC}^b$	\mathcal{D}^b
[kDa]	[kDa]	
42.4	44.1	1.13

^aCalculated by end-group analysis, assuming complete conversion of the NHS ester functionality

^bCalculated assuming polystyrene standards, deviation from true molecular weight is anticipated since polystyrene may not be representative of the hydrodynamic volume occupied by this polymer.

IV. Design of Polymeric Zwitterionic Solid Electrolytes with Superionic Lithium Transport

A. Abstract

Solid polymeric electrolytes (SPEs) can help mitigate many issues limiting the performance of Li-ion batteries such as instabilities at electrolyte–electrode interfaces and safety concerns associated with energy-dense lithium metal anodes; however, SPE conductivity is limited by sluggish polymer segmental dynamics. I have previously proposed polymeric zwitterionic (PZI) electrolytes which permit decoupling of ion motion and polymer segmental rearrangement. Herein, I refine design rules for these PZIs with respect to roles of the tethered ion chemistry and architecture on the conductivity and Li-ion selectivity. Bulky, ionic-liquid inspired tethered-cations and anions are crucial to attaining highly ionically conductive PZIs, where the bulky tethered-sulfonamide is particularly influential, though I do not find a similar effect of ion chemistry on the lithium selectivity. Further, conductivity is strongly enhanced by the addition of electron withdrawing groups to the tethered-anion, varying by nearly two orders of magnitude depending on electron withdrawing strength.

B. Introduction

Solid polymer electrolytes (SPEs) confer advantages over traditional liquid electrolytes for high power and high energy density applications as they can be engineered to have superior electrochemical stability and mechanical robustness to traditional liquid electrolytes¹⁻³. However, it remains challenging to obtain SPEs with high flux of reactive lithium species⁴. This shortfall is mostly due to the insufficient polarity and sluggish dynamics of most polymer electrolytes compared to traditional fluids. In most amorphous

polymer electrolytes such as polyethers, ions are transported through the dynamic rearrangement of free volume sites that allow for ion motion between solvation sites⁵⁻⁶. This mechanism inexorably links the local rearrangement of polymer segments (segmental dynamics) of these electrolytes to their ionic transport. This limits polymer design as only high-plasticized or soft polymer electrolytes display sufficient segmental dynamics for applications. In addition, this mechanism does not provide a reliable means to impart cation selectivity, which is normally less than 20% for lithium⁷⁻⁹ due to the large coulombic energy barrier for the hopping of small compact ions¹⁰.

The limitations of this conductivity mechanism have inspired efforts to engineer solid electrolyte scaffolds that decouple mechanical and conductive properties. Block copolymer electrolytes contain soft and hard domains that separately provide transport pathways and mechanical reinforcement resulting in decoupling of some mechanical properties from conduction¹¹⁻¹⁵. Within the soft segments of block copolymer electrolytes, however, transport is still limited by the constraints of the vehicular transport and often is additionally constrained by factors such as grain-boundary resistances¹⁶ and reduced dynamics near soft-hard interfaces¹⁷. Polymer gel-type electrolytes can boast conductivities $>10^{-3}$ S/cm and can display significant elasticity, however these electrolytes utilize a fast-relaxing fluid to impart ion transport¹⁸⁻¹⁹. This strategy can result in materials which are less leak-proof and electrochemically stable compared to fully solid electrolytes. In contrast, inorganic, solid-state electrolytes offer dramatic decoupling of conductivity from structural relaxations with ionic conductivities of 0.1-12 mS/cm being reported despite the rigidity of the inorganic matrices²⁰⁻²³. The fast transport of these materials is enabled through a percolated pathway of solvation sites that enable opportunistic hopping of the ionic species in the absence of

rearrangement of the ceramic²⁴⁻²⁵. While these materials offer a promising route towards solid electrolytes; however, they suffer from additional challenges such as limited chemical and electrochemical stability²⁶, brittleness²⁷⁻²⁸, and high interfacial resistances when placed in contact with electrodes²⁹.

Decoupling of ion conductivity from segmental dynamics is a promising route towards combining the robustness and processability of polymer electrolytes with the improved conductivity of ceramics. Sokolov and coworkers have demonstrated that packing frustration of polymers with large fragility indices leads to free volume spaces that allow for ion motion even as the temperature approaches the polymer glass transition (T_g , i.e. arrest of the relaxation modes)³⁰⁻³¹. While this approach demonstrates important physics in decoupling ion transport from polymer relaxation rates, a promising route towards materials with the favorable properties of ceramics without many of the downsides, the transport rates in these materials are still too low for most applications. Similarly, electrolytes with ion channels³²⁻³⁵, molecular confinement³⁶⁻⁴¹, and even properly designed crystalline materials⁴²⁻⁴⁷ have been shown to exhibit similar decoupling from polymer chain dynamics, in some cases with reported conductivities approaching application-relevant transport rates. However, more research is needed to develop robust design rules for these systems and to demonstrate their applicability in electrochemical cells.

Zwitterionic materials have emerged as fast, selective ion transporting materials due to their unprecedented dielectric constants, despite having no net charge. These materials, which consist of a covalently tethered cationic and anionic groups, have some of the highest reported dielectric constants for organic materials (up to 270 ~5x the dielectric constant of water)⁴⁸. This results in high solubility for added salts, even beyond equimolar addition of

salt⁴⁹, leading to high carrier densities. The high dielectric constants of these materials can also contribute to high selectivities for lithium as high permittivities lower the coulombic energy barrier for transport of compact ions such as lithium, resulting in a more size-selective electrolyte. An additional attractive feature of ZIs compared to other highly charged systems such as polyelectrolytes and ILs is their net charge neutral nature. While the ion migration of polyelectrolytes and ILs presents a significant issue to imparting selectivity, ZIs do not display appreciable-long range transport as the cations and anions are not able to separately migrate in an electric field.

While amorphous zwitterions demonstrate potential as fast ion transporters⁴⁹ or as dielectricizers to lower the coulombic energy barrier for ion transport^{48, 50}, conduction from segmental relaxation can also be achieved through the formation of ordered structures. I recently demonstrated superionic conductivity (partial decoupling of ion transport from chain dynamics) in a semicrystalline PZIL where selective Li⁺ transport is hypothesized to occur through zwitterionic crystals⁵¹. This leads to both high conductivity and high Li⁺ selectivity as the counterion is not similarly favored in this form of transport. Similar high conductivity that hints at superionicity has been observed in small molecule zwitterions by Forsythe and coworkers, who found significant ion conductivity of crystalline ZIs.

Despite their promise, ZI electrolytes are poorly understood, and their chemical design has not been systematically studied. Although it is known that changes in ion chemistry result in immense property changes for ionic materials, most studies of small molecule and polymeric ZI electrolytes use only the sulfonate anion chemistry. Although the sulfonate anion is a strongly acidic group, it is known from studies of polymers with ionic liquid functionalities that the sulfonate groups often result in strong binding of ionic dopants with

polymer functionalities resulting in low counterion mobilities. Similarly, ionic salts comprised of sulfonate ions are typically higher melting than IL anion chemistries, indicating that ion-ion interactions in these materials are less diffuse and labile than typical IL chemistries. These results hint towards the importance of exploring a larger chemical design space in the development of ZI electrolytes.

Herein I develop design rules for dry PZIs where transport appears to occur through the crystalline regions of a polymer with crystallizable zwitterionic sidechains. NMR diffusometry and relaxometry indicate clearly that the lithium exists in multiple different dynamic environments, displaying both a fast and slow mode associated with the crystalline and amorphous regions. In contrast, the counterion exists in only one, relatively slowly relaxing environment leading to a high transference number. I find that more diffuse tethered anions and cations, inspired by ionic liquid designs, display faster ion dynamics, where differences in ion dynamics are not well explained by differences in polymer segmental relaxation rates. Instead, I find that the melting temperature is a more robust explanatory variable for ion dynamics – consistent with my understanding of the ion transport mechanism in these electrolytes. The ion dynamics can be further tuned by altering the strength of interaction between Li^+ and the tethered anion. By adding electron withdrawing groups to the tethered anion, the interaction becomes weaker and conductivity increases. Although I observe differences in net transport rates due to modifications of tethered-ion size and chemistry, no similar trend is seen in selectivity.

C. Results and Discussion

Tethered Ion Size Plays a Crucial Role in PZIL Conduction

The design of zwitterionic polymers (PZIs) is intimately connected to the design of the pendant zwitterion (ZI) functionality. In prior work I investigated zwitterionic polymers that crystallize into structurally similar unit cells to the small molecule crystalline analogues. I anticipate that transport through the crystalline regions of the PZI will resemble the transport through these ZI crystals, which are more facile to study due to their complete crystallization and simpler dynamics. In accordance with this observation, I begin the discussion with the design of small molecule zwitterions and build on this knowledge to design PZI electrolyte materials.

Even prior to doping by charge carriers, the melting and physical behavior of ZIs polymeric zwitterions (PZIs) is determined by the ion size and degree of delocalization of the tethered anion and cation. I find that many design rules of ZIs and ILs are in parallel, however distinct differences arise in ZIs due to the tethered nature of these ions. For instance, while imidazolium and sulfonamide ions constitute some of the most common room temperature IL's such as 1-Ethyl-3-methylimidazolium bis(trifluoromethylsulfonyl) imide ($T_m = -16\text{ }^\circ\text{C}$), when they are joined together by a relatively short tether, they form a ZI with a relatively high melting point ($T_m = 131^\circ\text{C}$).

In ZIs as in small molecule ILs, more diffuse ion structure leads to lower T_m 's, which is also indicative of more diffuse ion-ion interactions and faster dynamics within the ZI, even below its melting point. In Figure 92 I demonstrate the design of ZIs containing 'bulky' and 'compact' anions (An) and cations (Cat). These ZIs are named with by introducing a

subscript ‘bulky’ to indicate a bulky cation (imidazolium) or anion (sulfonamide) and a subscript ‘compact’ to indicate a compact cation (ammonium) or anion (sulfonate). I investigate the melting temperature (T_m) of these ILs as T_m is inversely related to ion-ion interaction strength, which is related to the barrier for activated transport of ions through the matrix. I find that melting point trends follow expectations from IL design where bulkier ions result in lower melting points i.e. the melting point trend follows the order $\text{Cat}_{\text{bulky}}\text{-An}_{\text{bulky}} < \text{Cat}_{\text{compact}}\text{-An}_{\text{bulky}} \approx \text{Cat}_{\text{bulky}}\text{-An}_{\text{compact}} < \text{Cat}_{\text{compact}}\text{-An}_{\text{compact}}$. Furthermore, I find that the anion design change is more influential than the cation design change ($\text{Cat}_{\text{bulky}}\text{-An}_{\text{compact}} > \text{Cat}_{\text{compact}}\text{-An}_{\text{bulky}}$), this is consistent with the observations of Ohno et al. that “it is difficult to improve the properties of pure zwitterions through the modification of the cation sites.”⁴⁹ I proceed to apply these simple design rules from the small molecule ZIs to PZI electrolytes, investigating polymer-tethered versions of these same ZIs.

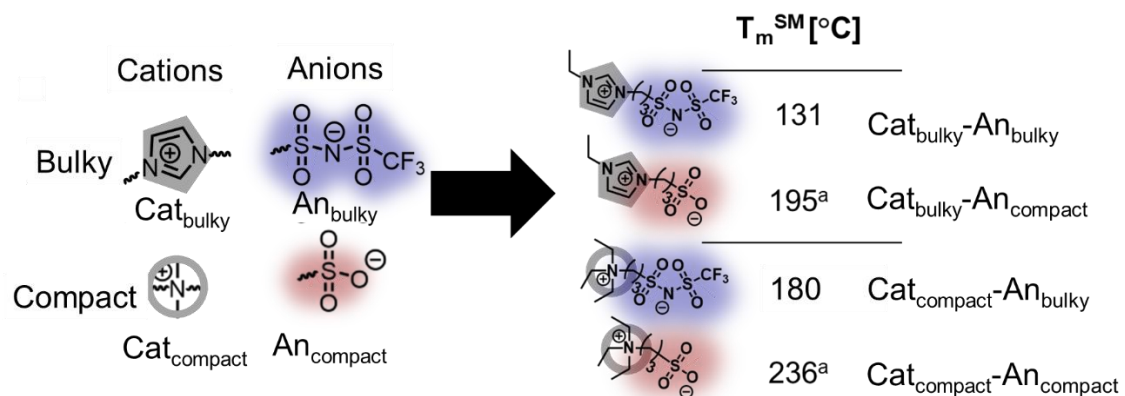


Figure 92: ZIs synthesized with bulky and nonbulky ions.

ZIs are prepared with a mix of bulky and compact anions and cations. The trend in melting temperatures of the small molecules (T_m^{SM}) is consistent with the design rule that bulkier ions lead to lower melting temperatures.

Upon doping the PZI with a Lithium salt, I anticipate that changes to the zwitterion chemistry impact conductivity by altering both the physical properties of the crystalline regions and the strength of interaction with Li⁺ (coordination and solvation). PZIs are highly polar, so regardless of specific chemistry, lithium bis(trifluoromethanesulfonimide) (Li⁺/TFSI⁻ – a salt commonly used in battery applications due to high electrochemical stability) is well solvated. In Chapter 3 I showed that a typical PZIs could solvate up to $r=3.5$ where $r \equiv \frac{\text{moles of salt}}{\text{mole of ZI}}$, leading to very high carrier densities. In this work, I use only a relatively modest $r=0.9$ to ensure a minimal amount of ion pairing and to retain crystallinity within the electrolyte. I show that Li⁺/TFSI⁻ accounts for the bulk of the ionic conductivity in these electrolytes as the parent PZI displays minimal conductivity signal until it is doped with salt. This suggests that the polymer mainly acts as a fixed charged background that enables the motion of the Li⁺/TFSI⁻ dopant. Though in some cases the rearrangement of ZI moieties can generate an ‘apparent conductivity’ due to local alignment of the ZIs. This effect is minimal for PZIs as full-chain rearrangement in the electric field would be sluggish and would require larger potentials.

In this system, ion motion is dependent upon having low barrier for activated transport between solvation sites, this is anticipated to be strongly related to both on the strength of its interaction between mobile and tethered ions. I find that bulkier tethered ions lead to higher ionic conductivity as measured by EIS, (Figure 93A) with poly(Cat_{bulky}-An_{bulky}) displaying the highest ionic conductivity and poly(Cat_{compact}-An_{compact}) the lowest. Indeed, as in the trends in T_m , the structure of the tethered anion appears to play a stronger role (factor of 100) than the tethered cation (a factor of 5 difference). Further, it appears that conductivity differences cannot be explained by trends in segmental dynamics. The failure of the ionic

conductivities to collapse when normalized against their temperature difference from the glass transition temperature (renormalized by $T-T_g$), indicates a lack of dependence on segmental dynamics (Figure 93B). The improved conductivity is attributed to a reduction in the strength of interaction between the Li^+ and TFSI^- free ions with the ZI matrix (more dynamic coordination), which could lead to faster activated transport rates in both the crystalline and amorphous regions of the electrolyte.

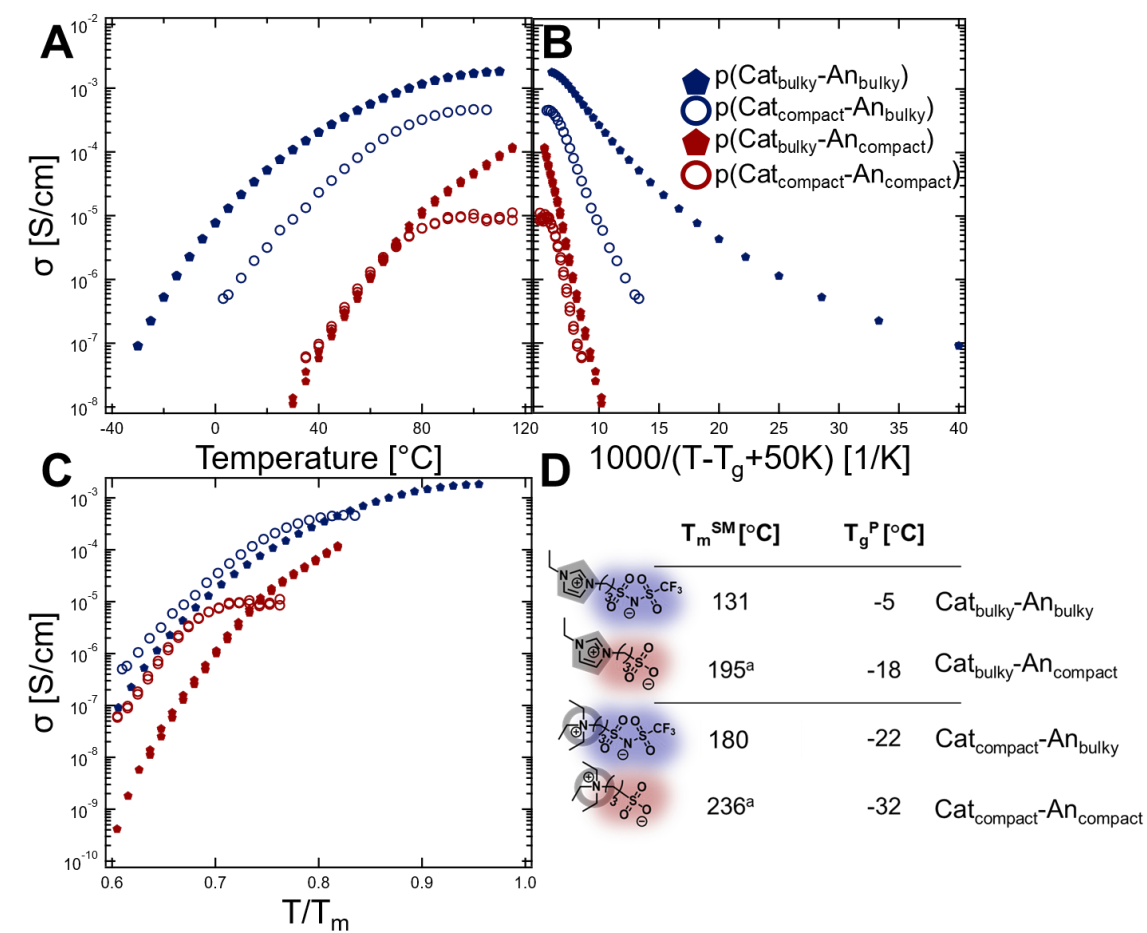


Figure 93: Ionic conductivity studies of bulky and compact PZIs.

A) The ionic conductivity of the polymers with variation in ion identity shows significant differences dependent upon the identity of the ion. The anion appears to play a critical role and both An_{bulky} PZIs have higher ionic conductivities. B) Normalization of the conductivity

data by $T-T_g$ does not collapse conductivity data, indicating that the segmental dynamics of the system are not responsible for the majority of the differences in ion mobility. C) Normalization against T_m provides a more successful collapse of the data, suggesting that this thermodynamic parameter is a better explanation of the dynamics. D) The T_g 's of the polymers and the T_m 's of the small molecules herein. Bulkier ions lead to lower melting temperatures for the small molecules, however there is no similar trend in the glass transition temperatures. ^aIndicates values that are comparable to those found by Ohno et al.⁴⁹

In crystalline solids, it is known that local motions below the melting temperature of the crystallite may be crucial in promoting ion mobility through the system and that the onset of these motions often phenomenologically arises at $T=2/3T_m$ ⁵². This universal behavior suggests that the melting temperature can be a thermodynamic scaling factor for ion mobility in crystalline ion conductors. I evaluate the role of crystalline dynamics by rescaling the temperature by the melting temperature of the crystallite (Figure 93C), however, since melting transitions in the polymer can be broad and thermal-history dependent, I use the melting temperature of small-molecule ZI analogues (Figure 93D). This rescaling results in significantly improved collapse of the observed ion conductivity of these polymer electrolytes, suggesting reduction in T/T_m leads to better conductivity.

Ion selectivity structured electrolytes depends on a pathway of vacancies through which ions can opportunistically hop. Via NMR diffusometry, it is clear that in both TFSI-containing PZI's, the Li^+ exists in indistinct transport environments, evident from the failure of a one-component fit to explain the data (Figure 94A). These inhomogeneous dynamics reflect the vastly different transport rates through the crystalline and amorphous components of the electrolyte where the Li^+ moves through the amorphous regions via a comparatively slow vehicular mechanism and through the crystalline regions via a faster superionic mode.

In contrast, ^{19}F PFG experiments reveal only one single component of fluorine transport – consistent with homogeneous fluorine dynamics (Figure 94B). This single mode of fluorine transport may suggest limited TFSI⁻ mobility in the crystalline regimes due to its large size. As a result, TFSI may be limited to conduction through the comparatively slow amorphous regions via a vehicular mechanism. Alternatively, it is possible given the high anticipated dielectric constant (polarity) of the PZI, that the TFSI is primarily excluded from the crystalline regions and is segregated to the amorphous areas.

Both poly(Cat_{bulky}-An_{bulky}) and poly(Cat_{compact}-An_{bulky}) polymers demonstrate high transport numbers (selectivity) reflecting the high relative mobility of Li⁺ as opposed to its counterion ($t_+ \equiv \frac{D_{\text{Li}}}{D_{\text{Li}}+D_{\text{F}}}$, where D_{Li} and D_{F} are the measured diffusion coefficients of Lithium and Fluorine, respectively). The fact that both systems (with a bulky and a compact tethered cation) have identical high transport numbers indicates that the difference in interaction strength has a minimal impact on the overall selectivity. This is reflective of the complex transport environment in these systems, where overall electrolyte selectivity is a function of the amorphous and crystalline transport rates as well as the amount of lithium contained within the polymer crystallites. Since this change of cation identity is likely to simultaneously impact the polymer crystallinity, the segmental dynamics of the amorphous regions, and the polymer-ion interaction strength – it cannot yet be determined whether the use of less bulky cations in the tethered ZI could be a robust strategy to improve t_+ ,

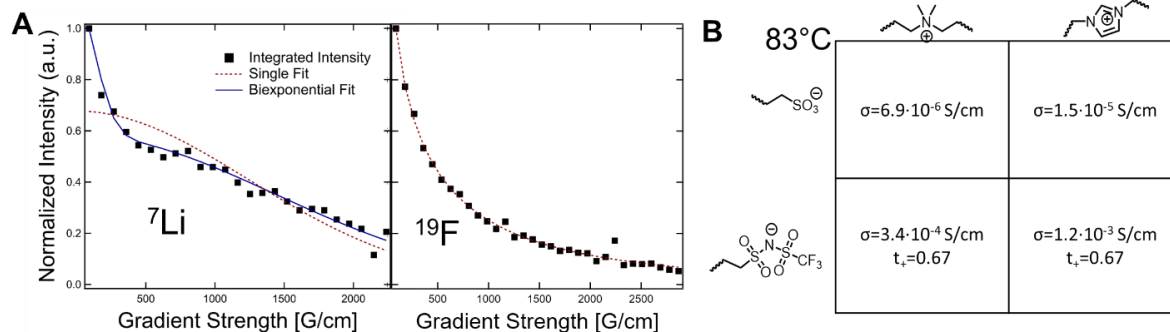


Figure 94: NMR and selectivity studies of bulky and compact PZIs.

A) Pulsed-field gradient NMR of the Am-C3-TFSI PZI is used as a direct means to measure the diffusion coefficients of these polymers. Notably, ^7Li curve requires a biexponential fit, suggesting the presence of two transport environments for lithium. In contrast, the ^{19}F curve is well fit by a single exponential, suggesting only one transport environment for fluorine. B) The table summarizes the properties of the PZIs with various ion identities at a fixed temperature of 83°C. Increasing the bulkiness of the ions resulted in higher ionic conductivity, with a strong dependence on the anion bulkiness. The impact of ion bulk on the transport number was less pronounced, with selectivity being constant as cation identity was altered.

Electron Withdrawing Nature of TFSI is Key to the Anion Design

I have shown above that increasing the diffuse nature of the tethered ions and the anion in particular was critical to the high conductivity of the electrolyte. Accordingly, I sought to further enhance the diffuseness of this ion through by incorporating 'R' groups as pictured in Figure 95. Installing functionalities at the 'R' position can withdraw electron density from the ion, increasing the effective bulkiness of the ion, this may lead to more diffuse ion-ion interactions and lower energies for activated transport of Li^+ . Figure 95 depicts the functionalities installed onto the PZIL - these groups range from nonwithdrawing functionalities such as methyl and tert-butyl functionalities to moderately withdrawing

functionalities containing fluorines. The electron withdrawing nature of these groups is quantified according to the Molecular Electrostatic potential analysis of Remya and Suresh⁵³, which employs density functional theory to probe the effect of these functionalities on the electron density of a standard aromatic ring. Table 23 shows tabulated values of ΔV_c for the functionalities in Figure 95, where higher values of ΔV_c indicate more withdrawing functionalities.

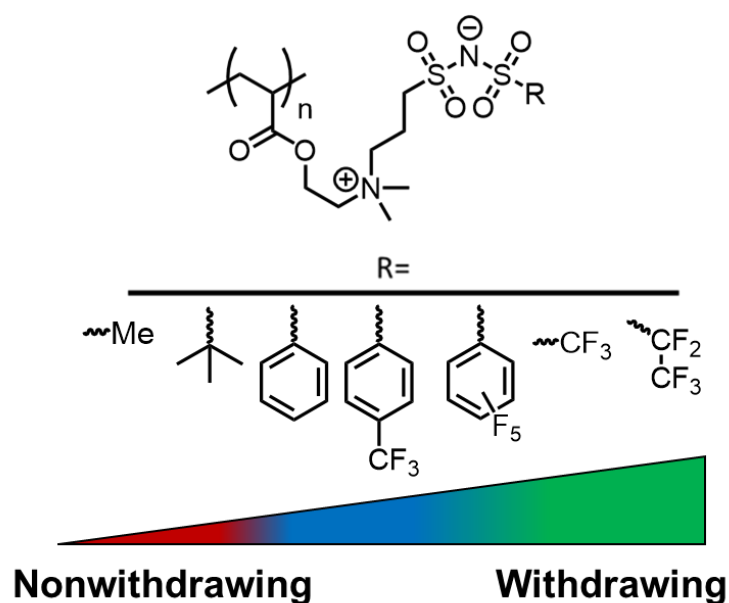


Figure 95: Electron withdrawing groups ranked by their withdrawing strength.

The material systems for this study consists of the ammonium cation and the sulfonamide anion with variation in the 'R' group of this polymer. The 'R' groups display a range of electron withdrawing character ranging from moderately withdrawing to non-withdrawing.

Table 23: Electron withdrawing strength of ‘R’ groups studied herein.

Group	ΔV_c (kcal mol ⁻¹) ^a	Classification
Me	NA	Non-withdrawing
t-Bu	NA	Non-withdrawing
C6H4-CF3	2.5 ^b	Weakly Withdrawing
C6H5	0.2	Weakly Withdrawing
CF3	13.7	Moderately Withdrawing
CF2CF3	14.7	Moderately Withdrawing
C6F5	9.8	Moderately Withdrawing

^aBased on the calculations of Remya and Suesh⁵³.

^bWithdrawing group is computed from a highly similar chemical functionality

Incorporation of electron withdrawing groups had a profound effect on the conductivity of the salt-doped PZILs, with a nearly 100x difference in the ionic conductivity between the worst and best performing polymers. Figure 96A shows the temperature-dependent conductivity behavior of these salt-doped polymers. Polymer conductivity is measured on a forward and reverse temperature sweep to ensure that no significant hysteresis is observed. The incorporation of the electron withdrawing functionalities impacted both the maximum conductivity of the polymers as well as their dependencies on temperature. Most polymers displayed relatively Arrhenius conductivities over this temperature range, however the slight deviation from Arrhenius behavior suggests partial coupling of conductivity to polymer segmental motion. Notably, the CF₃ polymer displays more significant deviation from

Arrhenius behavior than the others. Although this is not fully understood, it may be a consequence of greater incorporation of the salt into the crystalline domains of this electrolyte due to the similar nature of the tethered anion and the TFSI⁻ ion, resulting in dynamics that differ from the other PZILs.

The high-temperature conductivity performance of these PZILs correlates strongly with the electron withdrawing strength of the functionality, suggesting an effective strategy to further promote activated transport of ionic dopants. To further clarify the influence of the electron withdrawing groups on the conduction of the ZILs, their ionic conductivity at an application-relevant temperature of 100°C is plotted for the various R groups in Figure 96B. The moderately withdrawing functionalities (CF₃, CF₂CF₃, C₆F₅) display the highest conductivities and the non-withdrawing groups (CH₃, t-Bu) have the lowest. Based on this result I conclude that the electron withdrawing group on the anion can further increase the effective bulkiness of the ion, leading to more labile lithium-anion interactions and faster transport. This suggests that further improvements may be possible by synthesizing PZILs containing even stronger withdrawing groups. Although many of the strongest withdrawing groups are either charged functionalities or reactive groups, some suitable candidates such as C(CN)₃ ($\Delta V_c=23$ kcal/mol) or SF₃ ($\Delta V_c=22.5$ kcal/mol) may result in further improvements to ion dynamics.

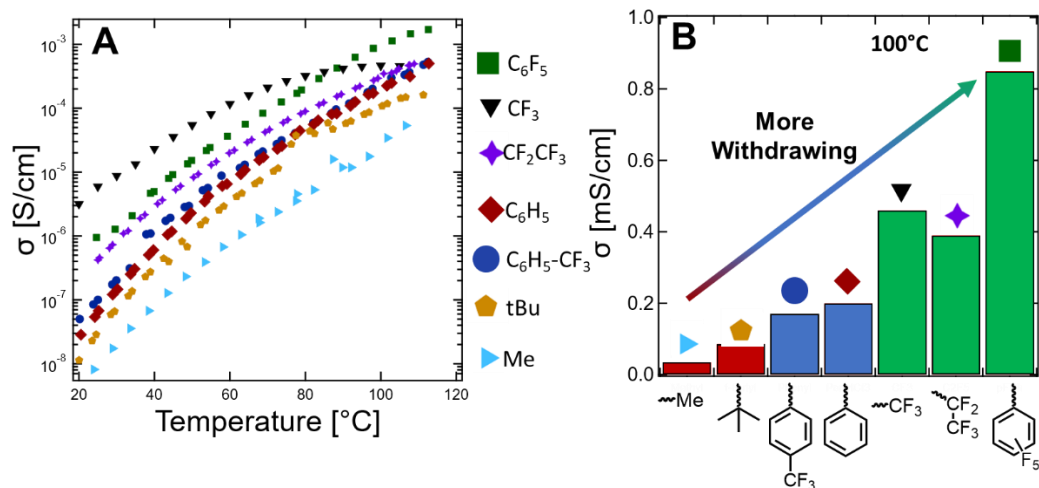


Figure 96: Conductivity studies of PZIs with electron withdrawing groups.

A) The ionic conductivity of these polymer electrolytes is plotted against temperature. For many compounds, an up and down sweep in temperature is pictured. A strong influence of 'R' groups on both the maximum conductivity and the conductivity trend is observed. B) The conductivity at 100°C shows a strong trend with the strength of electron withdrawing groups, with conductivity varying nearly two orders of magnitude between the pentafluorophenyl group and the methyl group. The bars colors correspond to the degrees of electron withdrawal as classified in Table 23 with green, blue, and red boxes corresponding to moderately withdrawing, weakly withdrawing, and non-withdrawing groups, respectively.

In this study I refined design rules for solid-state PZI electrolytes, which are promising hosts for ion transport of lithium in electrochemical applications but have not been systematically studied in their design. Firstly, I found that the diffuseness of the polymer-tethered cation and anion correlated to the mobility of lithium salts through the resulting PZI, with a greater influence of tethered anion than tethered cation. In contrast to standard design principles for SPEs, this trend could not be well explained by the glass transition temperatures of the polymers – suggesting that the diffuse interactions between bound and

tethered ions are key in enabling activated transport of dopant species in both the crystalline and amorphous phases of the electrolyte. I further investigated these systems by NMR, finding evidence of an inhomogeneous transport mechanism and high (0.67) selectivities for lithium-ion transport in these electrolytes. Finally, I found that modification of the functional group proximal to the anion is an effective way to modulate the electronic properties of this ion. I demonstrated a remarkable influence of these modifications on conductivity of the resulting PZIL, where these small chemical changes resulted in nearly two orders of magnitude of conductivity variation at 100°C. The conductivity correlated well with the estimated withdrawing strength of the functionality, further suggesting that diffuse ion-ion interactions are crucial to the performance of PZILs as conduits for lithium transport.

D. Appendix

D.1 Materials and Methods

Chemicals

Acrylic acid N-hydroxy succinimide ester (NHS ester acrylate), trifluoromethanesulfonamide, and Sodium 3-Bromopropanesulfonate were purchased from TCI chemicals. The monomer was stored in a refrigerated compartment of a nitrogen containing glovebox until needed. Diethyl ether (DEE), methanol (MeOH), tetrahydrofuran (THF), dichloromethane (DCM), and dimethylformamide (DMF) were purchased from Fisher chemicals. Lithium bis(trifluoromethanesulfonyl)imide (Li TFSI) was purchased from Solvonic and stored in a glove box until its use. All other chemicals were purchased from Sigma Aldrich. AIBN was recrystallized 3x in methanol to yield white needle-like crystals which were stored at 0 °C.

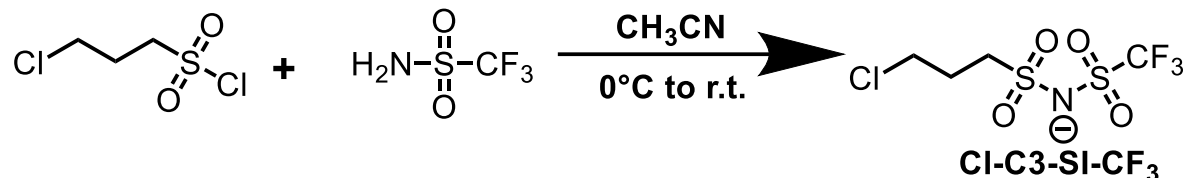
Synthesis of poly(dimethylamino ethyl acrylate) (PDMAEA)

The synthesis of this polymer is detailed in prior work.

Synthesis of Imidazole-Acrylamide Polymer poly(Im-Am)

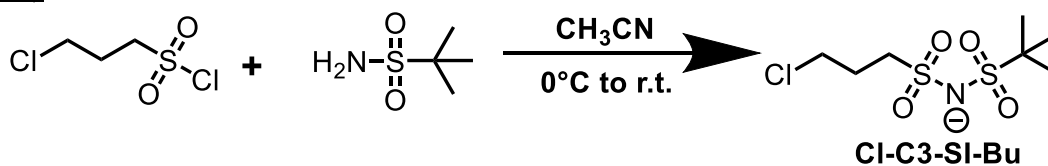
The synthesis of this polymer is detailed in previous work.

Synthesis of ((3-chloropropyl)sulfonyl)((trifluoromethyl)sulfonyl)amide (Cl-C₃-SI-CF₃)



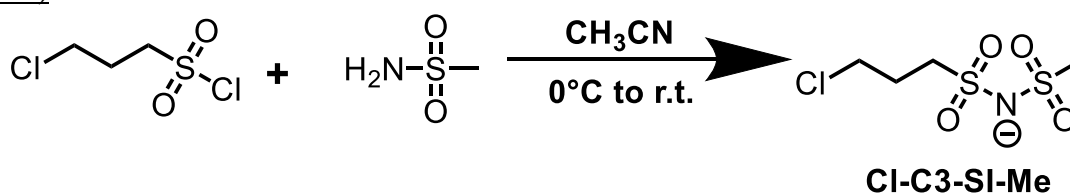
A round bottom flask was charged with 1 equivalent of trifluoromethanesulfonamide at a concentration of 0.2g/mL in acetonitrile and 3 equivalents of triethylamine. The solution was degassed with nitrogen while stirring on ice. After the solution had degassed and the reactor had chilled the degassing needle was removed from the liquid to leave a blanket of nitrogen in the reactor. A syringe was used to slowly transfer 1 equivalent of 3-chloropropane sulfonyl chloride to the reactor. This solution was stirred overnight and the temperature of the reactor was allowed to reach room temperature. A slightly brownish color developed during reaction. The reaction crude was concentrated and redissolved in DCM. The DCM was washed via 3 aqueous and a 1M HCl washes. The organic layer was dried and concentrated to yield a brownish viscous product. The compound was verified by NMR.

Synthesis of ((3-chloropropyl)sulfonyl)((tert-butyl)sulfonyl)amide triethylamine salt (Cl-C₃-SI-Bu)



A round bottom flask was charged with 1 equivalent of 2-methylpropane-2-sulfonamide at a concentration of 0.2g/mL in acetonitrile and 3 equivalents of triethylamine. The solution was degassed with nitrogen while stirring on ice. After the solution had degassed and the reactor had chilled the degassing needle was removed from the liquid to leave a blanket of nitrogen in the reactor. A syringe was used to slowly transfer 1 equivalent of 3-chloropropane sulfonyl chloride to the reactor. This solution was stirred overnight and the temperature of the reactor was allowed to reach room temperature. A slightly brownish color developed during reaction. The reaction crude was concentrated and redissolved in DCM. The DCM was washed via 3 aqueous and a 1M HCl washes, however starting material remained after washing. The product was finally isolated by column chromatography. The organic layer was dried and concentrated to yield a brownish viscous product. The compound was verified by NMR.

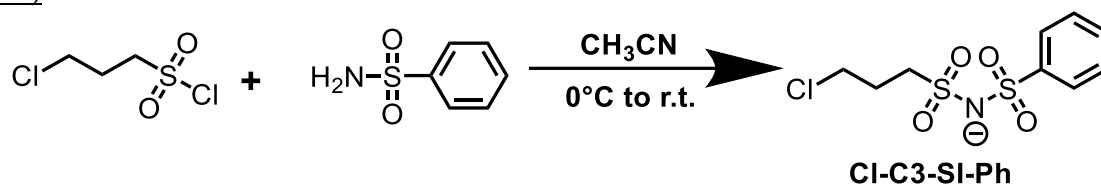
Synthesis of ((3-chloropropyl)sulfonyl)((methyl)sulfonyl)amide triethylamine salt (Cl-C3-SI-Me)



A round bottom flask was charged with 1 equivalent of methanesulfonamide at a concentration of 0.2g/mL in acetonitrile and 3 equivalents of triethylamine. The solution was degassed with nitrogen while stirring on ice. After the solution had degassed and the reactor had chilled the degassing needle was removed from the liquid to leave a blanket of nitrogen in the reactor. A syringe was used to slowly transfer 1 equivalent of 3-chloropropane sulfonyl chloride to the reactor. This solution was stirred overnight and

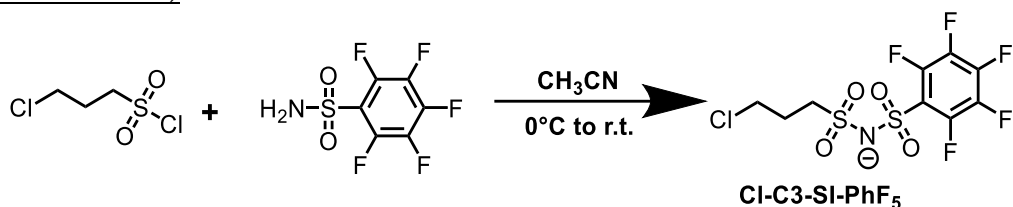
the temperature of the reactor was allowed to reach room temperature. A slightly brownish color developed during reaction. The reaction crude was concentrated and redissolved in DCM. The DCM was washed via 3 aqueous and a 1M HCl washes, however starting material remained after washing. The product was finally isolated by column chromatography. The organic layer was dried and concentrated to yield a brownish viscous product. The compound was verified by NMR.

Synthesis of ((3-chloropropyl)sulfonyl)((phenyl)sulfonyl)amide triethylamine salt (Cl-C3-SI-Ph)



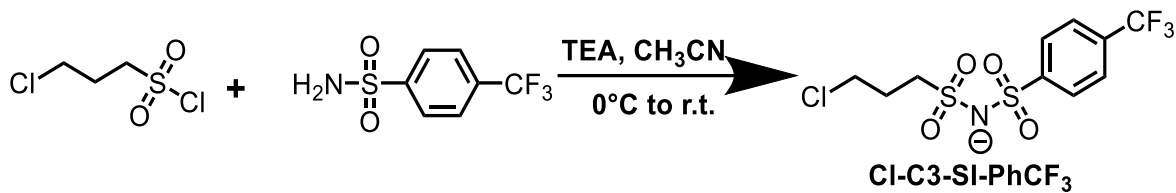
A round bottom flask was charged with 1 equivalent of benzenesulfonamide at a concentration of 0.2g/mL in acetonitrile and 3 equivalents of triethylamine. The solution was degassed with nitrogen while stirring on ice. After the solution had degassed and the reactor had chilled the degassing needle was removed from the liquid to leave a blanket of nitrogen in the reactor. A syringe was used to slowly transfer 1 equivalent of 3-chloropropane sulfonyl chloride to the reactor. This solution was stirred overnight and the temperature of the reactor was allowed to reach room temperature. A slightly brownish color developed during reaction. The reaction crude was concentrated and redissolved in DCM. The DCM was washed via 3 aqueous and a 1M HCl washes, however starting material remained after washing. The product was finally isolated by column chromatography. The organic layer was dried and concentrated to yield a brownish viscous product. The compound was verified by NMR.

Synthesis of ((3-chloropropyl)sulfonyl)((pentafluorophenyl)sulfonyl)amide triethylamine salt (Cl-C3-SI-PhF5)



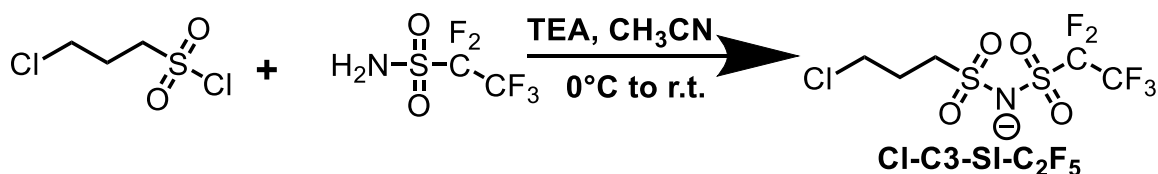
A round bottom flask was charged with 1 equivalent of pentafluorobenzenesulfonamide at a concentration of 0.2g/mL in acetonitrile and 3 equivalents of triethylamine. The solution was degassed with nitrogen while stirring on ice. After the solution had degassed and the reactor had chilled the degassing needle was removed from the liquid to leave a blanket of nitrogen in the reactor. A syringe was used to slowly transfer 1 equivalent of 3-chloropropane sulfonyl chloride to the reactor. This solution was stirred overnight and the temperature of the reactor was allowed to reach room temperature. A slightly brownish color developed during reaction. The reaction crude was concentrated and redissolved in DCM. The DCM was washed via 3 aqueous and a 1M HCl washes, however starting material remained after washing. The organic layer was dried and concentrated to yield a brownish viscous product. The compound was verified by NMR.

Synthesis of ((3-chloropropyl)sulfonyl)((4-(trifluoromethyl)phenyl)sulfonyl)amide triethylamine salt (Cl-C3-SI-PhCF3)



A round bottom flask was charged with 1 equivalent of 4-(trifluoromethyl)benzenesulfonamide at a concentration of 0.2g/mL in acetonitrile and 3 equivalents of triethylamine. The solution was degassed with nitrogen while stirring on ice. After the solution had degassed and the reactor had chilled the degassing needle was removed from the liquid to leave a blanket of nitrogen in the reactor. A syringe was used to slowly transfer 1 equivalent of 3-chloropropyl sulfonyl chloride to the reactor. This solution was stirred overnight and the temperature of the reactor was allowed to reach room temperature. A slightly brownish color developed during reaction. The reaction crude was concentrated and redissolved in DCM. The DCM was washed via 3 aqueous and a 1M HCl washes, however starting material remained after washing. The organic layer was dried and concentrated to yield a brownish viscous product. The compound was verified by NMR.

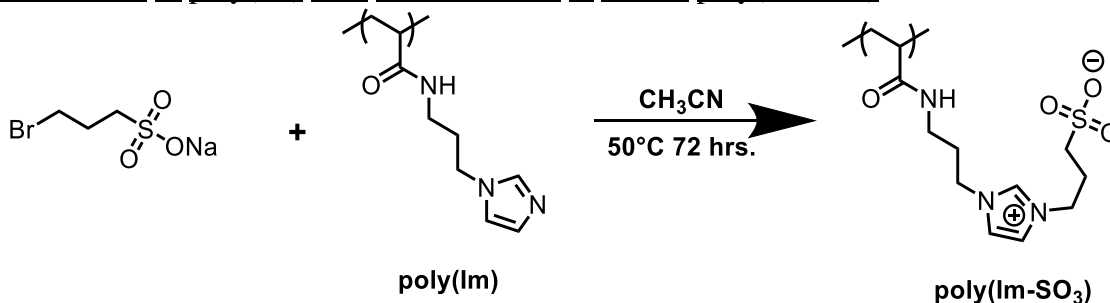
Synthesis of ((3-chloropropyl)sulfonyl)(perfluoroethane)amide triethylamine salt (Cl-C3-SI-C₂F₅)



A round bottom flask was charged with 1 equivalent of perfluoroethylsulfonamide at a concentration of 0.2g/mL in acetonitrile and 3 equivalents of triethylamine. The solution was degassed with nitrogen while stirring on ice. After the solution had degassed and the reactor had chilled the degassing needle was removed from the liquid to leave a blanket of

nitrogen in the reactor. A syringe was used to slowly transfer 1 equivalent of 3-chloropropane sulfonyl chloride to the reactor. This solution was stirred overnight and the temperature of the reactor was allowed to reach room temperature. A slightly brownish color developed during reaction. The reaction crude was concentrated and redissolved in DCM. The DCM was washed via 3 aqueous and a 1M HCl washes, however starting material remained after washing. The organic layer was dried and concentrated to yield a brownish viscous product. The compound was verified by NMR.

Quaternization of poly(Im) with Br-C3-SO₃Na to Obtain poly(Im-SO₃)



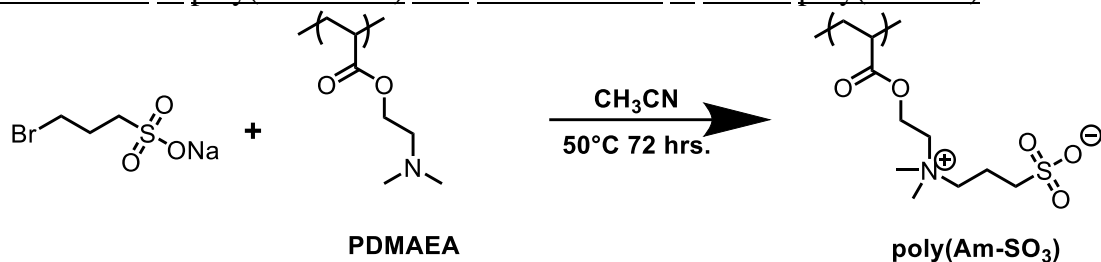
The polymer (poly(Im)) was dissolved in acetonitrile at a concentration of 0.5g/mL along with 3 equivalents of sodium 3-bromopropylsulfonate in a scintillation vial. The product was stirred at an elevated temperature of 50°C for 72 hours and a crude NMR was taken to confirm the conversion of the imidazole to the imidazolium. The product was subsequently purified by precipitation into cold 50/50 vol/vol THF/IPA blends 3x and extensively washed with water to remove any residual ions. Although the removal of NMR-inactive sodium could not be verified by NMR, this extensive washing has previously yielded complete counterion removal, which is confirmed by the low conductivity of the polymer in the absence of dopant salt. The polymer was subsequently dried for 48 hours in a

standard vacuum oven at 80° C and in an ultra-high vacuum environment at 10⁻⁸ torr for an additional 24 hours prior to salt doping.

Quaternization of poly(Im-Am) with Cl-C3-TFS-CF3 to Obtain poly(Im-TFS-CF3)

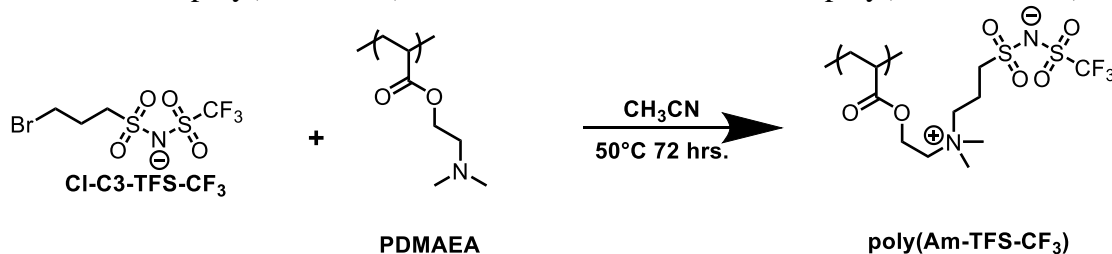
The synthesis of this polymer is detailed in Chapter 3.

Quaternization of poly(PDMAEA) with Br-C3-SO₃Na to Obtain poly(Im-SO₃)



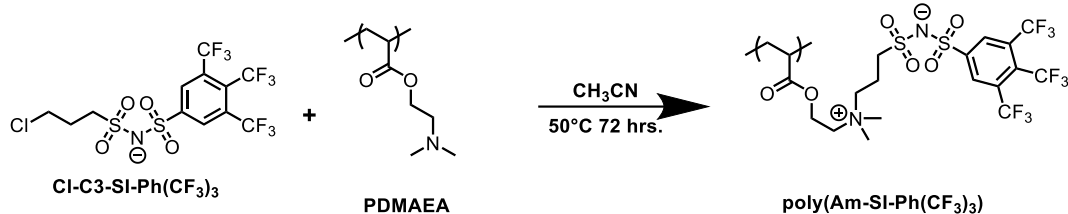
The polymer (PDMAEA) was dissolved in acetonitrile at a concentration of 0.5g/mL along with 3 equivalents of sodium 3-bromopropyl-1-sulfonate in a scintillation vial. The product was stirred at an elevated temperature of 50°C for 72 hours and a crude NMR was taken to confirm the conversion of the amine to an ammonium. The product was subsequently purified by precipitation into cold 50/50 vol/vol THF/IPA blends 3x and extensively washed with water to remove any residual ions. Although the removal of NMR-inactive sodium could not be verified by NMR, this extensive washing has previously yielded complete counterion removal, which is confirmed by the low conductivity of the polymer in the absence of dopant salt. The polymer was subsequently dried for 48 hours in a standard vacuum oven at 80° C and in an ultra-high vacuum environment at 10⁻⁸ torr for an additional 24 hours prior to salt doping.

Quaternization of poly(PDMAEA) with Br-C3-TFS-CF₃ to Obtain poly(Am-TFS-CF₃)



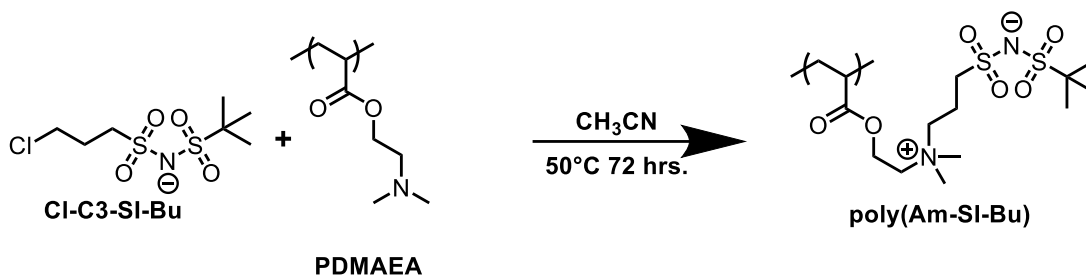
This synthesis was reported previously in chapter 3.

Quaternization of poly(PDMAEA) with Cl-C3-TFS-(CF₃)₃ to Obtain poly(Am-SI-C(F₃)₃)



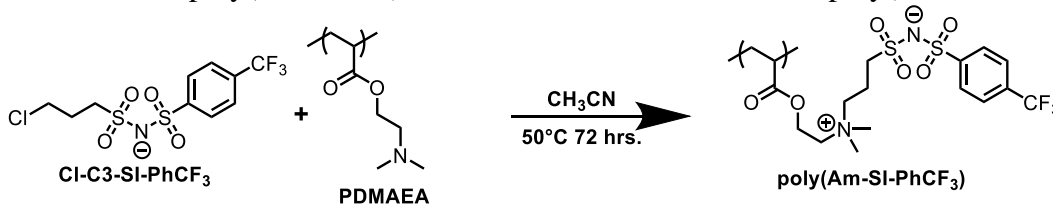
The polymer (PDMAEA) was dissolved in acetonitrile at a concentration of 0.5g/mL along with 3 equivalents of Cl-C3-SI-Ph(CF₃)₃ in a scintillation vial. The product was stirred at an elevated temperature of 50°C for 72 hours and a crude NMR was taken to confirm the conversion of the amine to an ammonium. The product was subsequently purified by precipitation into cold 50/50 vol/vol THF/IPA blends 3x and extensively washed with water to remove any residual ions. Although the removal of NMR-inactive sodium could not be verified by NMR, this extensive washing has previously yielded complete counterion removal, which is confirmed by the low conductivity of the polymer in the absence of dopant salt. The polymer was subsequently dried for 48 hours in a standard vacuum oven at 80° C and in an ultra-high vacuum environment at 10⁻⁸ torr for an additional 24 hours. Unfortunately, this polymer was mostly lost during processing so it was not characterized further, however its synthesis is reported here for interested parties.

Quaternization of poly(PDMAEA) with Cl-C3-TFS-t-Bu to Obtain poly(Am-TFS-t-Bu)



The polymer (PDMAEA) was dissolved in acetonitrile at a concentration of 0.5g/mL along with 3 equivalents of Cl-C3-SI-Bu in a scintillation vial. The product was stirred at an elevated temperature of 50°C for 72 hours and a crude NMR was taken to confirm the conversion of the amine to an ammonium. The product was subsequently purified by precipitation into cold 50/50 vol/vol THF/IPA blends 3x and extensively washed with water to remove any residual ions. Although the removal of NMR-inactive sodium could not be verified by NMR, this extensive washing has previously yielded complete counterion removal, which is confirmed by the low conductivity of the polymer in the absence of dopant salt. The polymer was subsequently dried for 48 hours in a standard vacuum oven at 80° C and in an ultra-high vacuum environment at 10⁻⁸ torr for an additional 24 hours prior to salt doping.

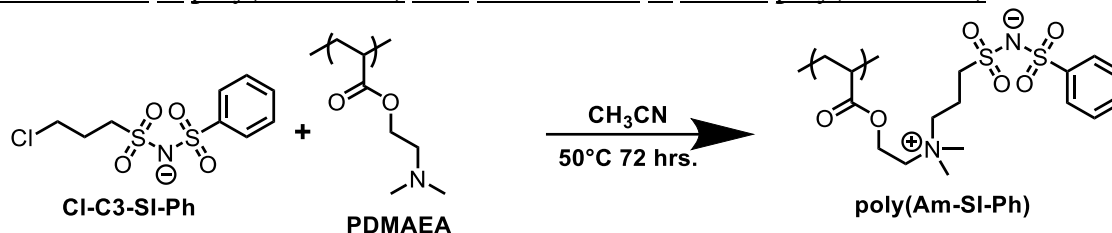
Quaternization of poly(PDMAEA) with Cl-C3-SI-PhCF₃ to Obtain poly(Am-SI-PhCF₃)



The polymer (PDMAEA) was dissolved in acetonitrile at a concentration of 0.5g/mL along with 3 equivalents of Cl-C3-SI-PhCF₃ in a scintillation vial. The product was stirred at an elevated temperature of 50°C for 72 hours and a crude NMR was taken to confirm the

conversion of the amine to an ammonium. The product was subsequently purified by precipitation into cold 50/50 vol/vol THF/IPA blends 3x and extensively washed with water to remove any residual ions. Although the removal of NMR-inactive sodium could not be verified by NMR, this extensive washing has previously yielded complete counterion removal, which is confirmed by the low conductivity of the polymer in the absence of dopant salt. The polymer was subsequently dried for 48 hours in a standard vacuum oven at 80° C and in an ultra-high vacuum environment at 10⁻⁸ torr for an additional 24 hours prior to salt doping.

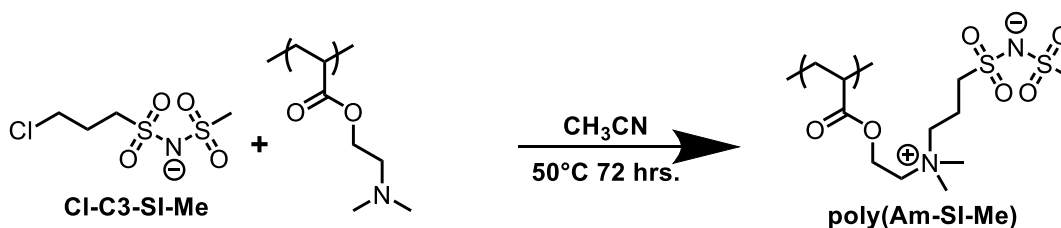
Quaternization of poly(PDMAEA) with Cl-C3-SI-Ph to Obtain poly(Am-SI-Ph)



The polymer (PDMAEA) was dissolved in acetonitrile at a concentration of 0.5g/mL along with 3 equivalents of Cl-C3-SI-Ph in a scintillation vial. The product was stirred at an elevated temperature of 50°C for 72 hours and a crude NMR was taken to confirm the conversion of the amine to an ammonium. The product was subsequently purified by precipitation into cold 50/50 vol/vol THF/IPA blends 3x and extensively washed with water to remove any residual ions. Although the removal of NMR-inactive sodium could not be verified by NMR, this extensive washing has previously yielded complete counterion removal, which is confirmed by the low conductivity of the polymer in the absence of dopant salt. The polymer was subsequently dried for 48 hours in a standard vacuum oven at

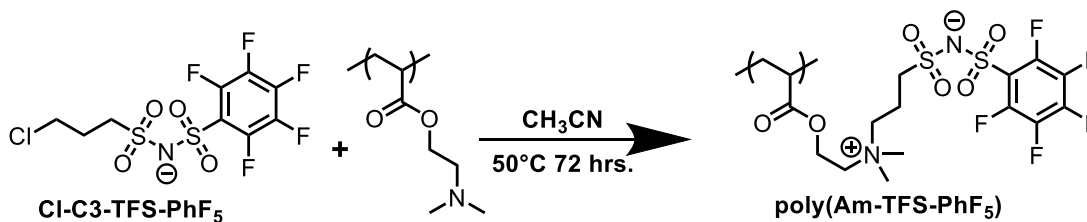
80° C and in an ultra-high vacuum environment at 10⁻⁸ torr for an additional 24 hours prior to salt doping.

Quaternization of poly(PDMAEA) with Cl-C3-SI-Me to Obtain poly(Am-SI-Me)



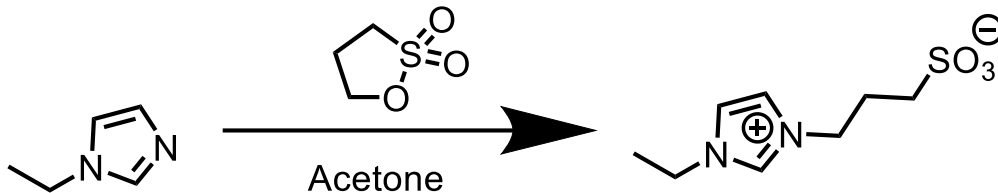
The polymer (PDMAEA) was dissolved in acetonitrile at a concentration of 0.5g/mL along with 3 equivalents of Cl-C3-SI-Me in a scintillation vial. The product was stirred at an elevated temperature of 50°C for 72 hours and a crude NMR was taken to confirm the conversion of the amine to an ammonium. The product was subsequently purified by precipitation into cold 50/50 vol/vol THF/IPA blends 3x and extensively washed with water to remove any residual ions. Although the removal of NMR-inactive sodium could not be verified by NMR, this extensive washing has previously yielded complete counterion removal, which is confirmed by the low conductivity of the polymer in the absence of dopant salt. The polymer was subsequently dried for 48 hours in a standard vacuum oven at 80° C and in an ultra-high vacuum environment at 10⁻⁸ torr for an additional 24 hours prior to salt doping.

Quaternization of poly(PDMAEA) with Cl-C3-SI-PhF5 to Obtain poly(Am-SI-PhF5)



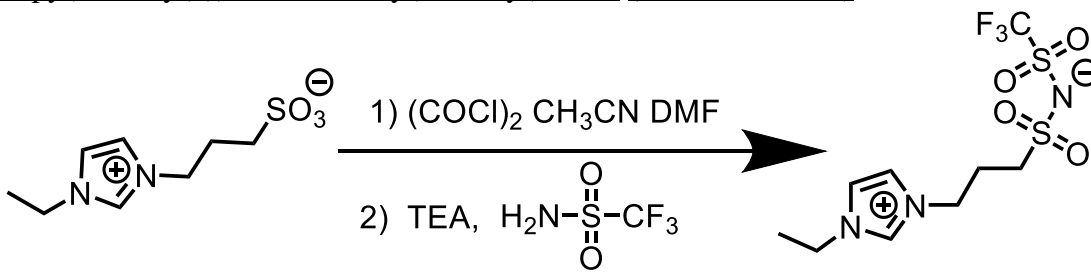
This synthesis was reported previously in Chapter 3.

Synthesis of 3-(1-ethyl-1H-imidazol-3-ium-3-yl)propane-1-sulfonate (EthIm-C3-SO₃)



In a glove box, 7.32 g (76 mmol, 1 eq) of 1-ethyl imidazole was placed into a Schlenk flask. In a second Schlenk flask 70 mL of anhydrous acetone and 9.3 g (76 mmol, 1 eq) of propane sulfone were mixed along with a stir bar. Outside the box, the second reactor was placed on ice and the ethyl imidazole was slowly added to the reactor while stirring. The reaction was stirred overnight, allowing the reaction temperature to equilibrate to room temperature. After ~18 hours a significant quantity of white precipitate had formed. The precipitate was removed by filtration and was washed with excess acetone and ether. Later, a second crop of crystals was collected from the filtrate in the same fashion. Both crops were analyzed by NMR and found to both correspond the product compound. ¹H NMR (600 MHz, Deuterium Oxide) δ 8.71 (s, 1H), 7.42 (s, 2H), 4.26 (t, J = 7.1 Hz, 2H), 4.13 (q, J = 7.3 Hz, 2H), 2.81 (t, J = 7.46 Hz, 2H), 2.21 (p, J = 7.2 Hz, 2H), 1.39 (t, J = 7.38 Hz, 3H). ¹³C NMR (151 MHz, d₂O) δ 135.09, 122.23, 122.19, 47.73, 47.22, 44.86, 25.05, 14.30

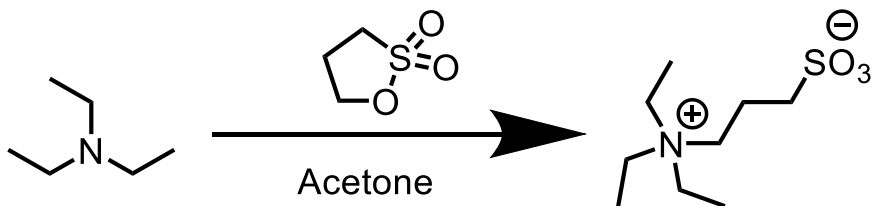
Synthesis of ((3-(1-ethyl-1H-imidazol-3-ium-3-yl)propyl)sulfonyl)((trifluoromethyl)sulfonyl)amide (EthIm-C3-TFSI)



A Schlenk flask was charged with 5.12 g of EthIm-c3-SO₃ (23.4 mmol, 1eq) and dried on a vacuum line overnight until the vacuum reached its baseline level of ~20militorr. The reactor was repressurized with nitrogen and dissolved in 40 mL of anhydrous CH₃CN added by syringe transfer. In a second round bottom flask 20mL of anhydrous CH₃CN was added under a blanked of nitrogen and a nitrogen flow was used to actively sparge the solution. 3.56 g of (COCl)₂ (28mmol, 1.2 eq) was added to this reactor along with a catalytic quantity of DMF ~0.2 mL (added slowly). This catalytic solution developed a yellowish color over the next ~20 minutes under active sparging. The flask containing the zwitterion was then cooled to 0°C and the catalytic solution was added to it dropwise. The reaction mixture was allowed to warm overnight and a significant quantity of precipitate formed. Stirring was ceased and the precipitate was allowed to settle. The liquid phase was removed from the Schlenk flask and transferred to a new dried flask under a nitrogen blanket. The precipitate was a washed with ~10 mL to capture product entrained in the liquid phase and this liquid was combined with the first syringe transfer in the new dry Schelenk flask. A new round bottom flask was charged with 3 equivalents of triethylamine, 1.2 equivalents of trifloromethane sulfonamide and 20 mL of anhydrous acetonitrile. This mixture was sparged with nitrogen and added dropwise to the chilled Schlenk flask via syringe transfer under active stirring. Immediately upon addition the formation of a white precipitate occurred. This mixture was stirred overnight and allowed to warm to room temperature. The precipitate was filtered off and removed. The supernatant was concentrated to yield an off-white solid. The solid was redissolved in DCM and washed 5x in a separatory funnel with distilled water. The organic layer was dried with MgSO₄ and concentrated to yield solid off-white crystals. These crystals were recrystallized in IPA to purify the final product. Purified

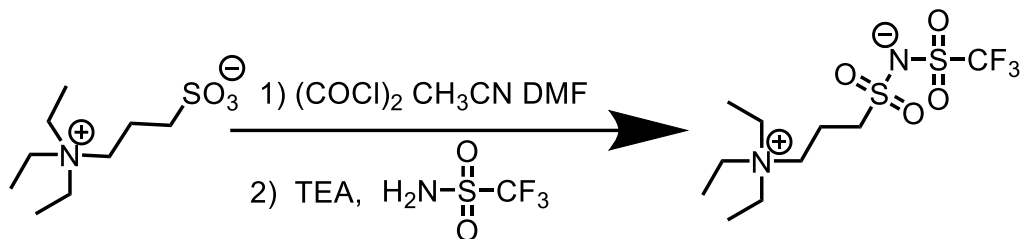
crystals were dried in a vacuum oven at 80°C and further dried in an ultra-high vacuum system at 10⁻⁸ millitorr. Crystals was stored in an Argon-containing glovebox before using. Product was characterized by NMR, melting point analysis, and IR. ¹H NMR (600 MHz, DMSO-d₆) δ 9.16 (s, 1H), 7.78 (s, 1H), 7.77 (s, 1H), 4.28 (t, J = 7.0 Hz, 2H), 4.17 (q, J = 7.3 Hz, 2H), 3.00 (t, J = 7.7 Hz, 2H), 2.20 (p, J = 7.2 Hz, 2H), 1.40 (t, J = 7.3 Hz, 3H).

Synthesis of 3-(triethylammonio)propane-1-sulfonate (Am-C3-SO₃)



In a glove box, 13.1 g (129 mmol, 1 eq) of anhydrous triethylamine was placed into a Schlenk flask. In a second Schlenk flask 70 mL of anhydrous acetone and 15.3 g (129 mmol, 1 eq) of propane sultone were mixed along with a stir bar. Outside the box, the second reactor was placed on ice and the triethylamine was slowly added to the reactor while stirring. The reaction was stirred overnight, allowing the reaction temperature to equilibrate to room temperature. After ~18 hours a significant quantity of white precipitate had formed. The precipitate was removed by filtration and was washed with excess acetone and ether. Later, a second crop of crystals was collected from the filtrate in the same fashion. Both crops were analyzed by NMR and found to both correspond the product compound. ¹H NMR (600 MHz, Deuterium Oxide) δ 3.29 – 3.15 (m, 8H), 2.87 (t, J = 7.1 Hz, 1H), 2.03 (dd, J = 17.0, 7.5 Hz, 1H), 1.17 (t, J = 7.4 Hz, 9H). ¹³C NMR (151 MHz, Deuterium Oxide) δ 185.46 , 54.71 , 52.64 , 47.19 , 17.20 , 6.55 .

Synthesis of ((3-(triethylammonio)propyl)sulfonyl)((trifluoromethyl)sulfonyl)amide (Am-C3-TFSI)



A Schlenk flask was charged with 5.12 g of Am-c3-SO₃ (23.4 mmol, 1eq) and dried on a vacuum line overnight until the vacuum reached its baseline level of ~20militorr. The reactor was repressurized with nitrogen and dissolved in 40 mL of anhydrous CH₃CN added by syringe transfer. In a second round bottom flask 20mL of anhydrous CH₃CN was added under a blanked of nitrogen and a nitrogen flow was used to actively sparge the solution. 3.56 g of (COCl)₂ (28mmol, 1.2 eq) was added to this reactor along with a catalytic quantity of DMF ~0.2 mL (added slowly). This catalytic solution developed a yellowish color over the next ~20 minutes under active sparging. The flask containing the zwitterion was then cooled to 0°C and the catalytic solution was added to it dropwise. The reaction mixture was allowed to warm overnight and a significant quantity of precipitate formed. Stirring was ceased and the precipitate was allowed to settle. The liquid phase was removed from the Schlenk flask and transferred to a new dried flask under a nitrogen blanket. The precipitate was a washed with ~10 mL to capture product entrained in the liquid phase and this liquid was combined with the first syringe transfer in the new dry Schelenk flask. A new round bottom flask was charged with 3 equivalents of triethylamine, 1.2 equivalents of trifloromethane sulfonamide and 20 mL of anhydrous acetonitrile. This mixture was sparged with nitrogen and added dropwise to the chilled Schlenk flask via syringe transfer under active stirring. Immediately upon addition the formation of a white precipitate occurred. This mixture was stirred overnight and allowed to warm to room temperature. The

precipitate was filtered off and removed. The supernatant was concentrated to yield an off-white solid. The solid was redissolved in DCM and washed 5x in a separatory funnel with distilled water. The organic layer was dried with MgSO_4 and concentrated to yield solid off-white crystals. These crystals were recrystallized in IPA to purify the final product. Purified crystals were dried in a vacuum oven at 80°C and further dried in an ultra-high vacuum system at 10^{-8} millitorr. Crystals was stored in an Argon-containing glovebox before using. ^1H NMR (600 MHz, DMSO-d_6) δ 3.31 – 3.25 (m, 2H), 3.23 (q, $J = 7.3$ Hz, 6H), 3.09 (t, $J = 6.9$ Hz, 2H), 2.09 – 1.92 (m, 2H), 1.16 (t, $J = 7.1$ Hz, 9H).

D.2 NMRs

^1H NMR of Cl-C3-SI-CF₃

This NMR spectrum has been published in Chapter 3.

^{13}C NMR of Cl-C3-SI-CF₃

This NMR spectrum has been published in Chapter 3.

^{19}C NMR of Cl-C3-SI-CF₃

This NMR spectrum has been published in Chapter 3.

¹H NMR of Cl-C3-SI-Me

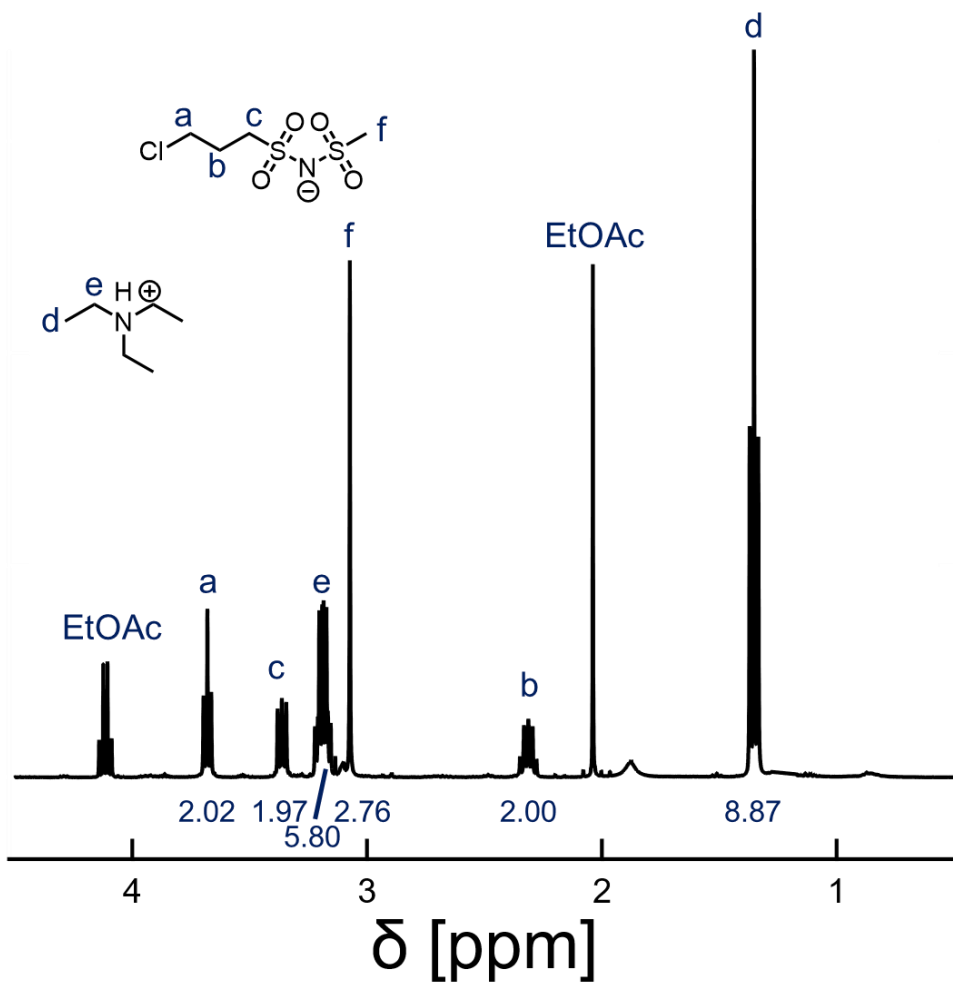


Figure 97: ¹H NMR of Cl-C3-SI-Me.

Chemical shifts and integrations of the compound are consistent with expectations. NMR is taken after column chromatography using ethyl acetate as the eluent. Starting material peaks are eliminated by this chromatography.

¹H NMR of Cl-C3-SI-Bu

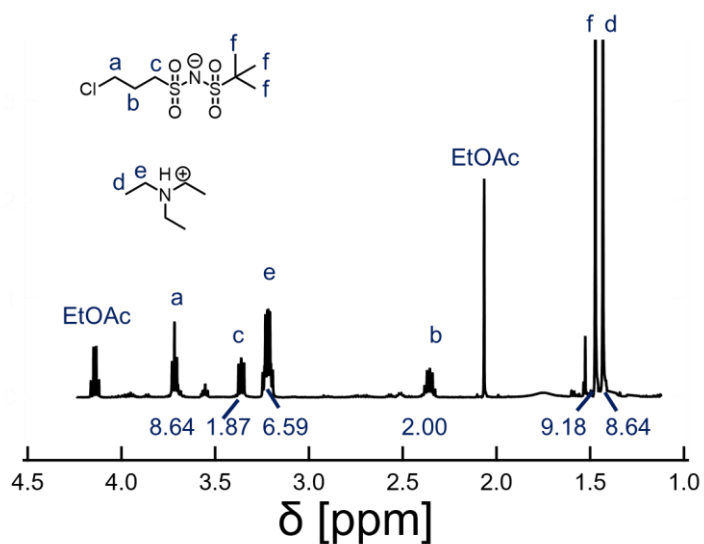


Figure 98: ¹H NMR of Cl-C3-SI-Bu. ¹H NMR of Cl-C3-SI-C2F5

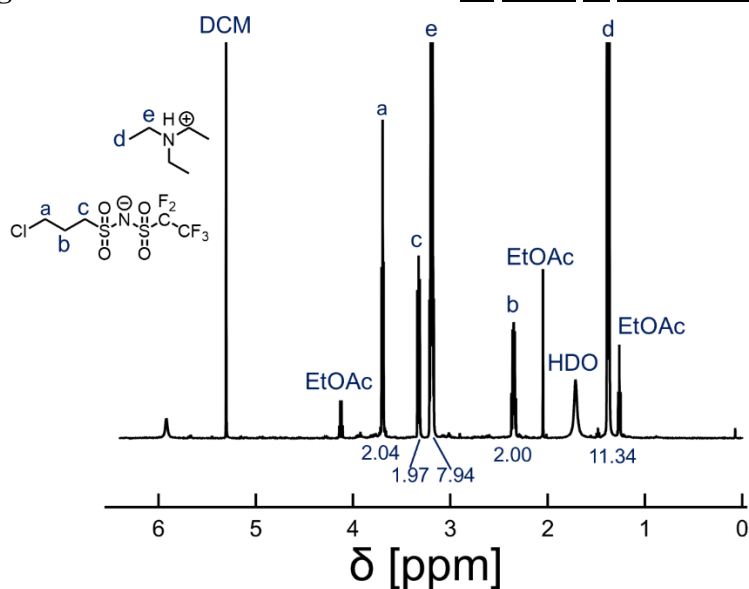


Figure 99: ¹H NMR of Cl-C3-SI-C2F5.

Peak positions and integrations are in agreement with expectations. The presence of excess triethylamine is evident after purification. The triethylamine will be removed in later steps and the product was used without further purification.

^{19}F NMR of Cl-C3-TFS-C2F5

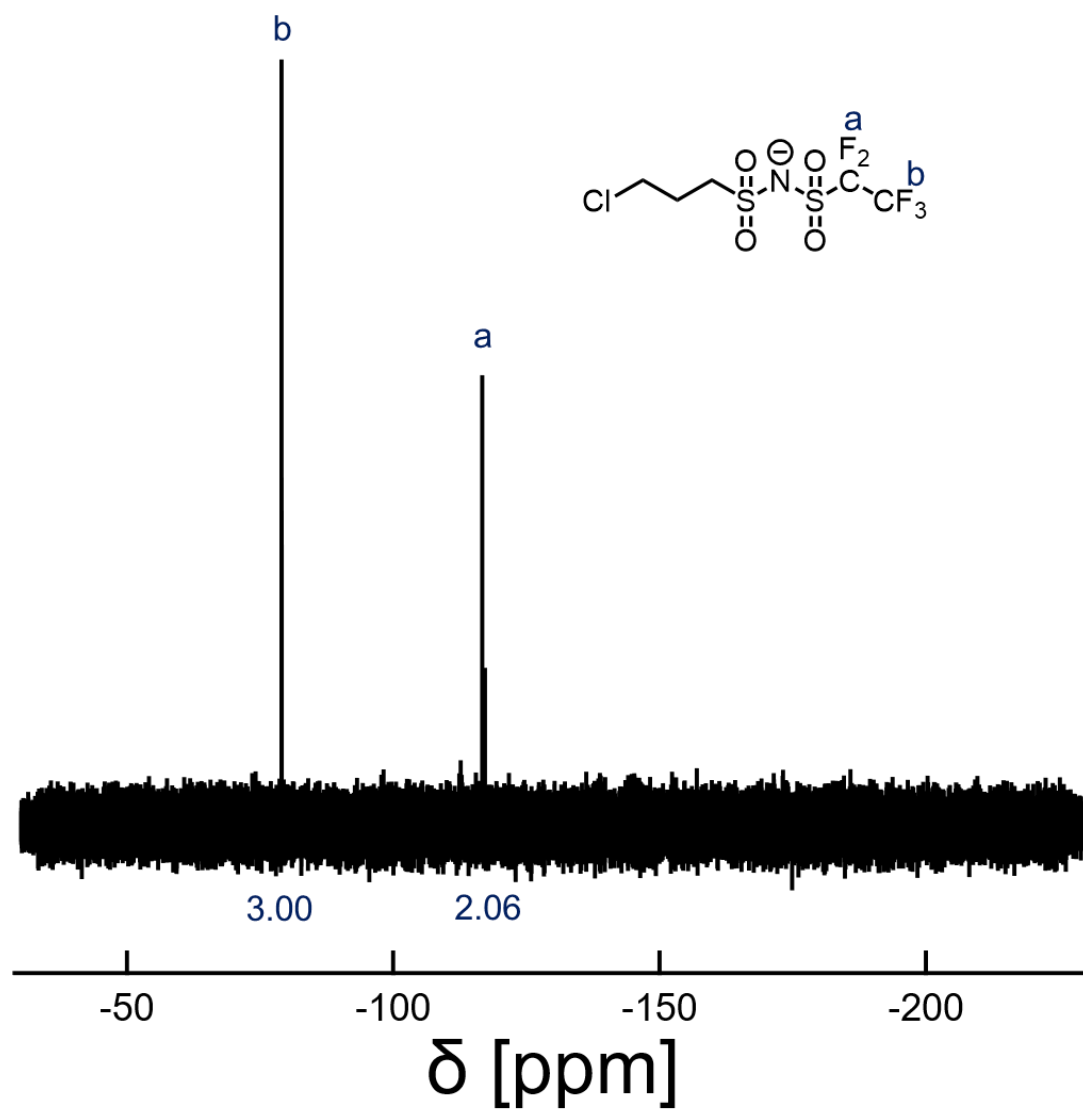


Figure 100: ^{19}F NMR of Cl-C3-TFS-C2F5.

The fluorine signals corresponding to perfluoroethyl group are present in the ^{19}F spectrum.

¹H NMR of Cl-C3-TFS-Ph(CF₃)₃

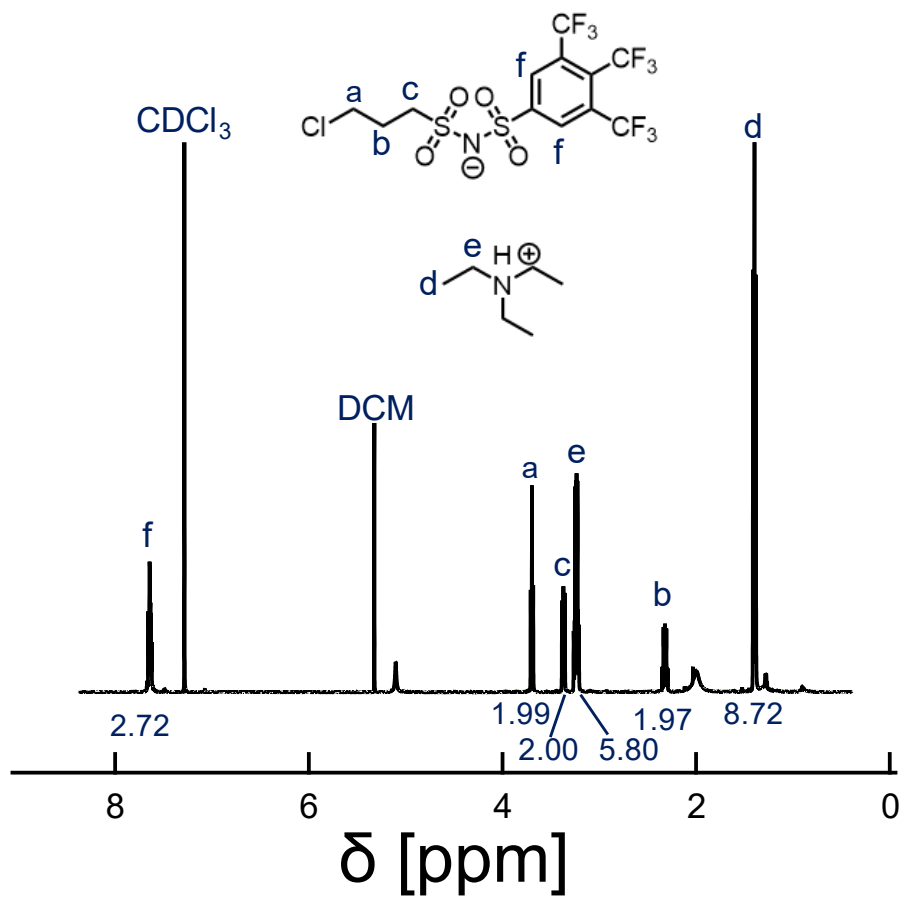


Figure 101: NMR spectrum of Cl-C3-TFS-Ph(CF₃)₃.

¹H NMR of Cl-C3-TFS-Ph

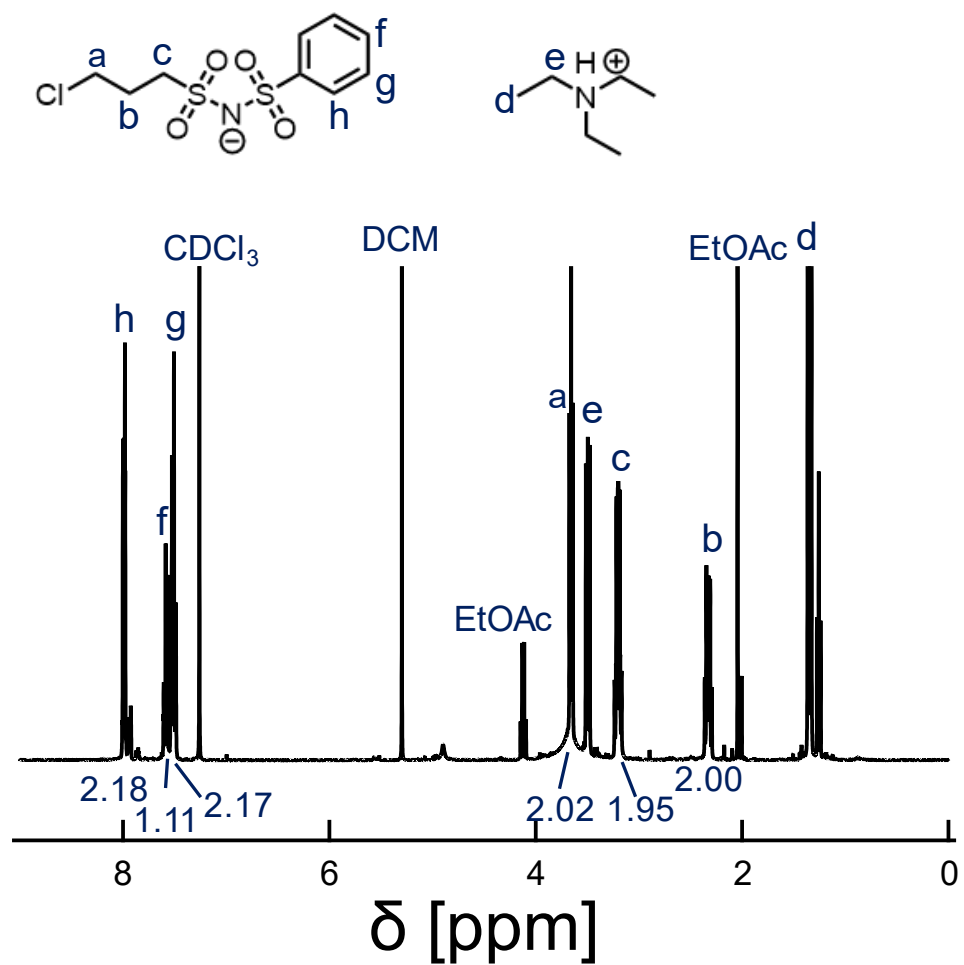


Figure 102: NMR Spectrum of Cl-C3-TFS-Ph.

¹H NMR of EthIm-C3-SO3

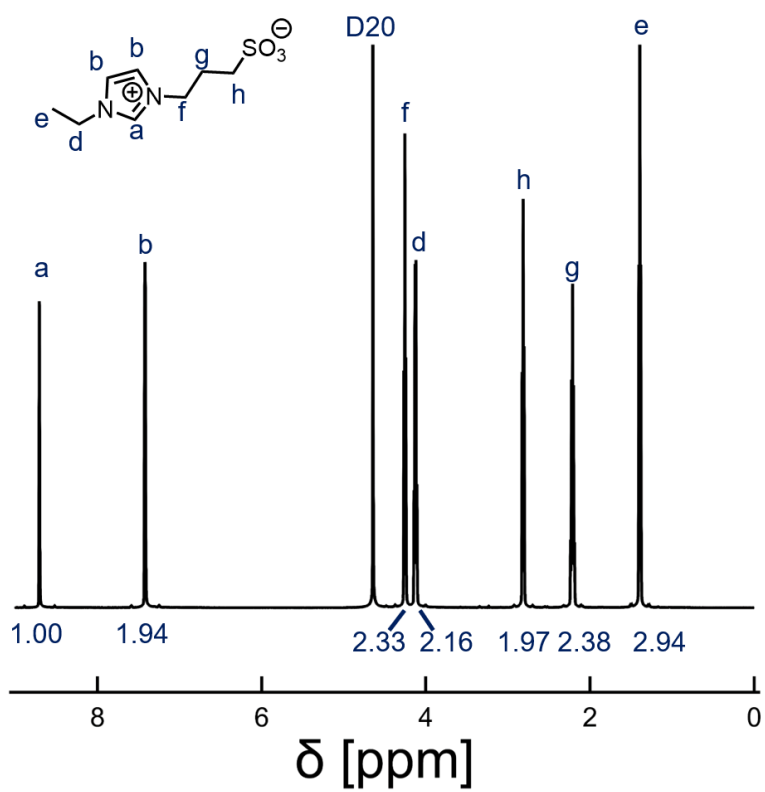


Figure 103: NMR spectrum of of EthIm-C3-SO3.

¹H NMR of EthIm-C3-SO₃

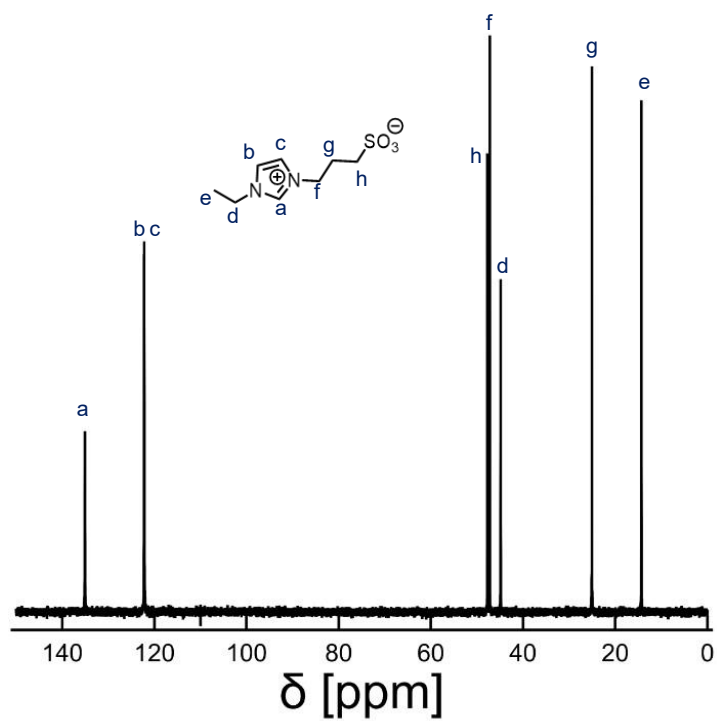


Figure 104: NMR Spectrum of EthIm-C3-SO₃.

¹³H NMR of TEA-C3-SO3

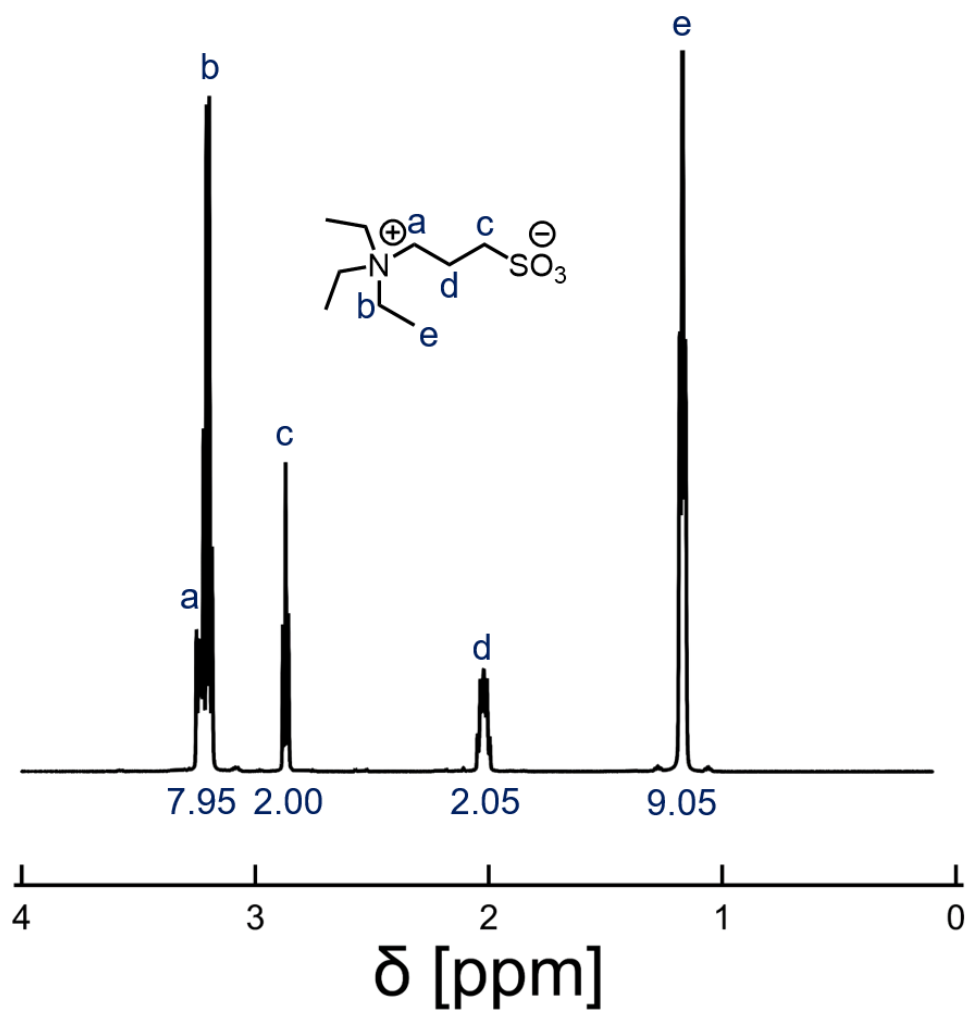


Figure 105: NMR Spectrum of TEA-C3-SO3.

^{13}C NMR of TEA-C3-SO₃

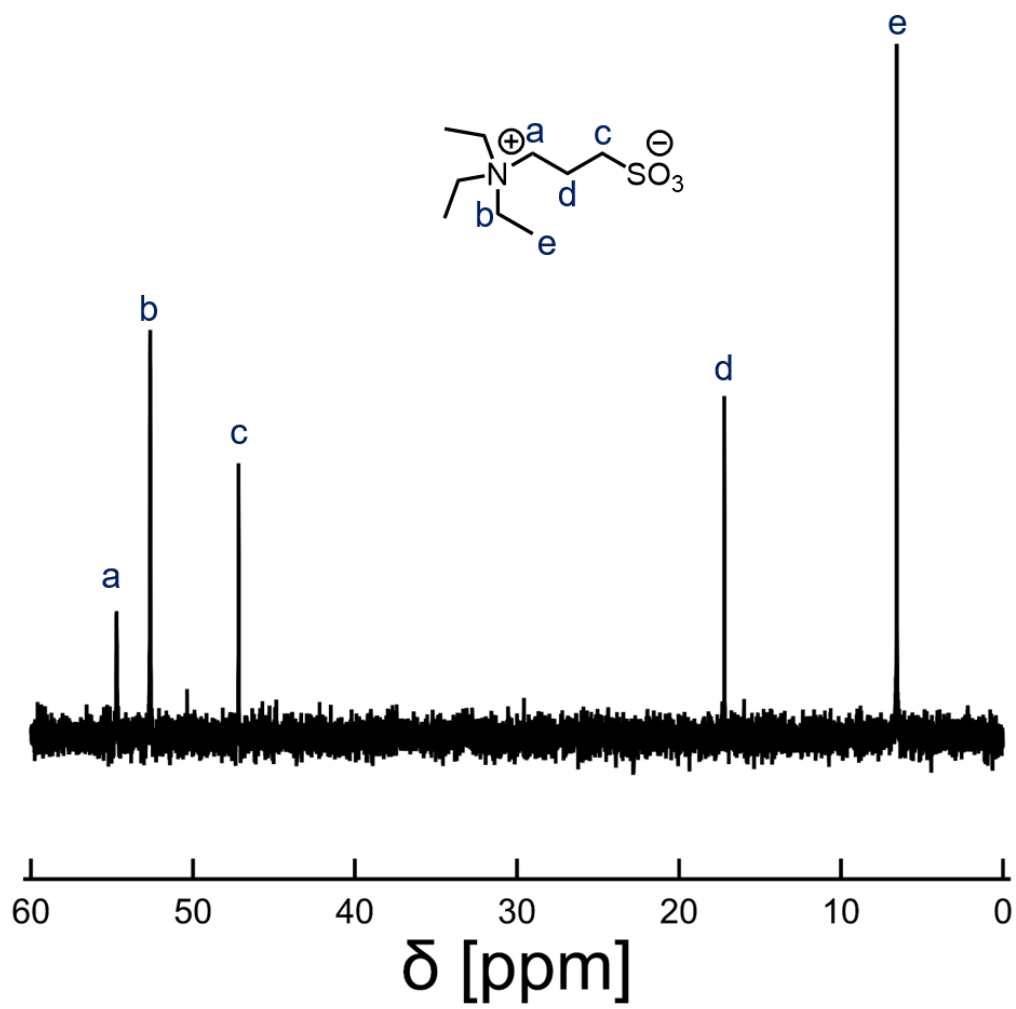


Figure 106: NMR Spectrum of TEA-C3-SO₃.

¹H NMR of EthIm-C3-TFSI

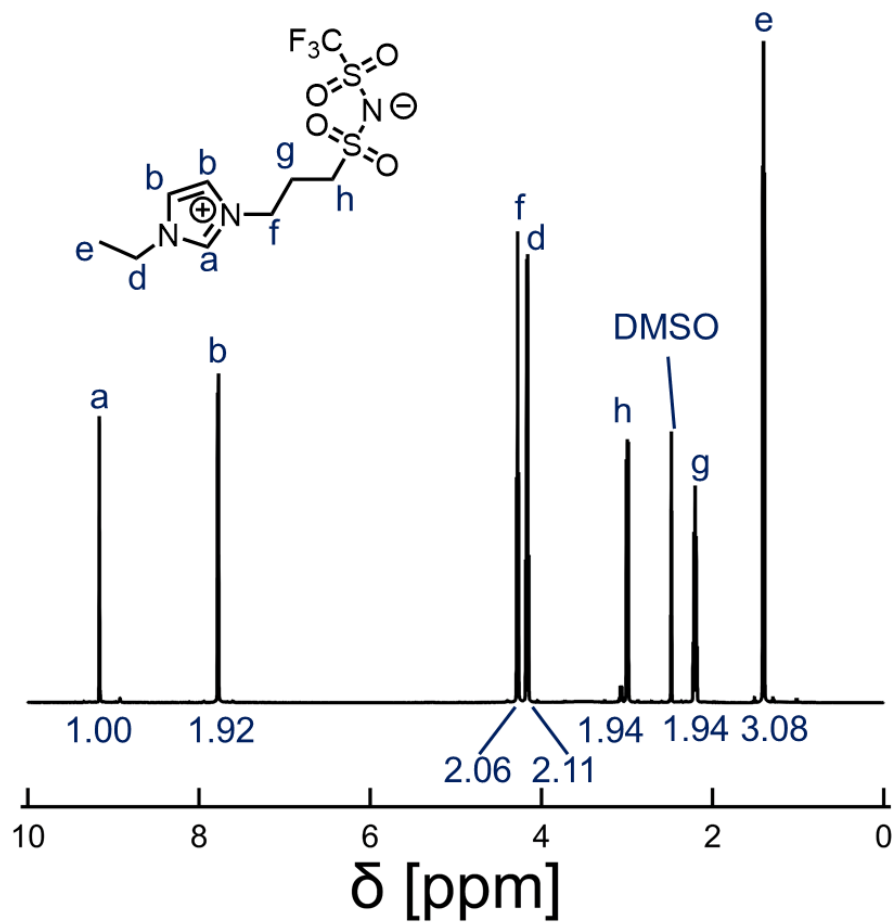


Figure 107: NMR Spectrum of EthIm-C3-TFSI.

¹H NMR of EthIm-C3-SO3

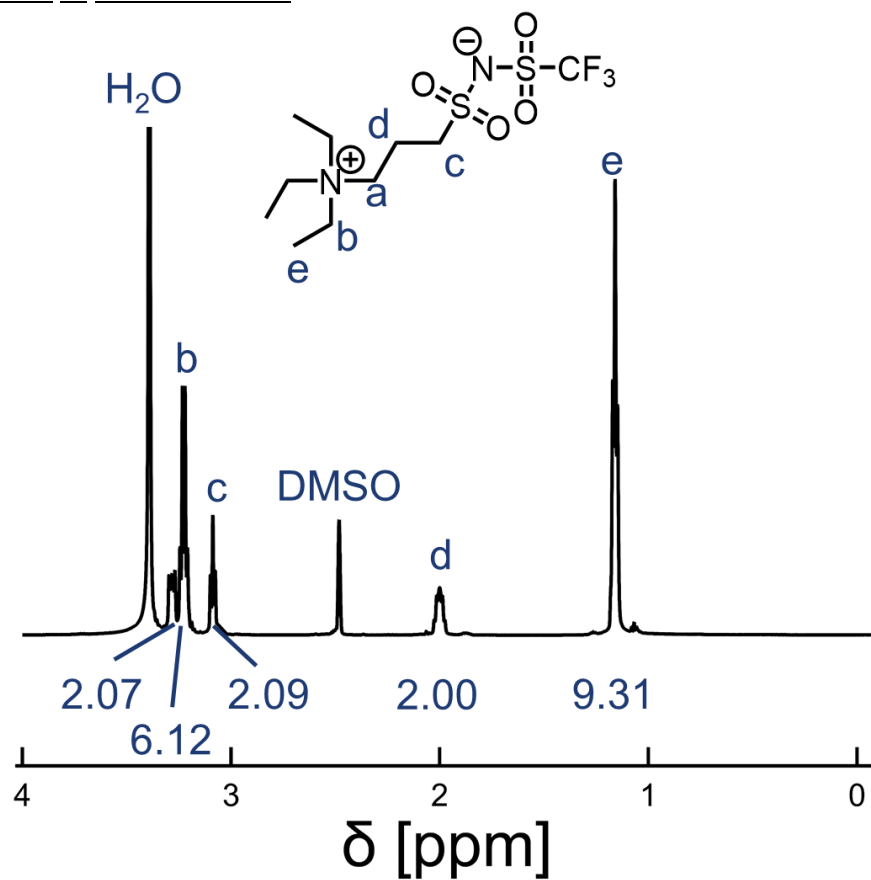


Figure 108: NMR Spectrum of EthIm-C3-SO3.

¹H NMR of EthIm-C3-SO₃

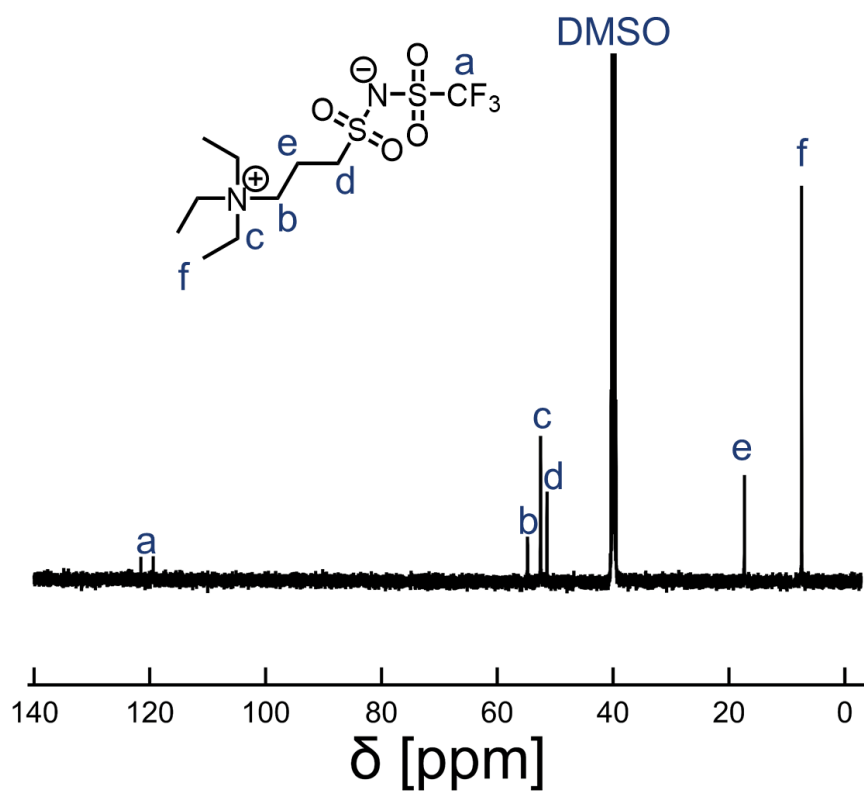


Figure 109: NMR Spectrum of EthIm-C3-SO₃.

^{19}F NMR of EthIm-C3-SO3

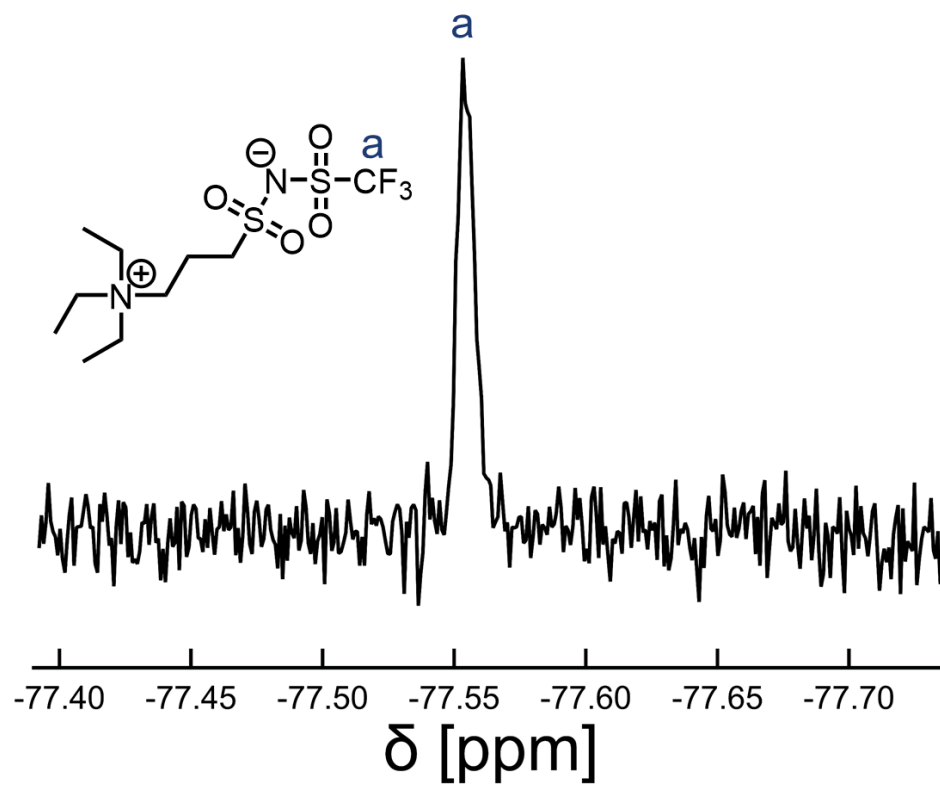


Figure 110: ^{19}F NMR spectrum of EthIm-C3-SO3.

D.3 Chromatography Analysis of Polymers

Gel Permeation Chromatography Analysis of poly(Pyr-MA)

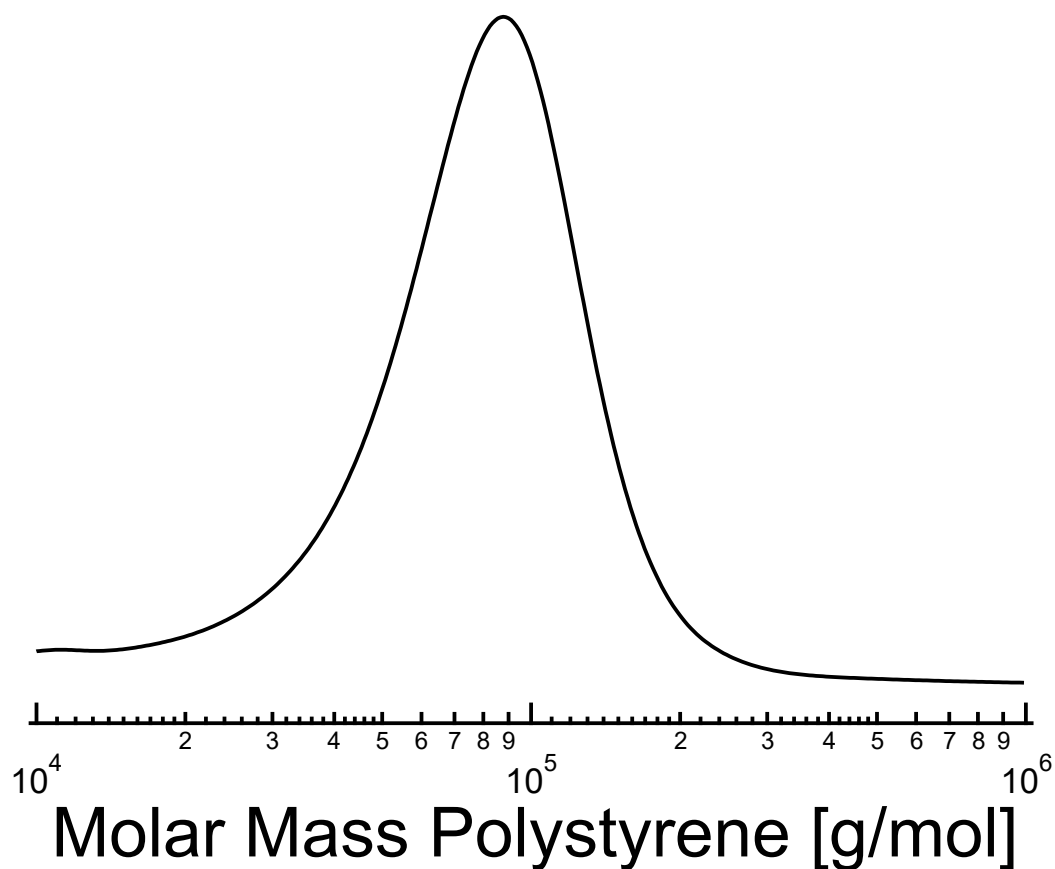


Figure 111:SEC of Pyr(MA).

The normalized intensity is plotted against the equivalent molecular weight of a polystyrene standard for the Pyr(MA) polymer after removal of the dodecyl end group from the RAFT polymer. The roughly Gaussian shape of the molecular weight distribution is consistent with a controlled polymerization. Analysis was carried using DMF as the mobile eluent.

Table 24: The molecular weight of the polymer prior to conversion to the zwitterionic form estimated by NMR and SEC.

$M_{N,NMR}^a$ [kDa]	$M_{N,SEC}^b$ [kDa]	D^b
17.4	19.5	1.37

^aCalculated by end-group analysis

^bCalculated assuming polystyrene standards, deviation from true molecular weight is anticipated since polystyrene may not be representative of the hydrodynamic volume occupied by this polymer.

Gel Permeation Chromatography Analysis of poly(Im) Prepolymer

This GPC curve is published in Chapter 3.

Gel Permeation Chromatography Analysis of PDMAEA

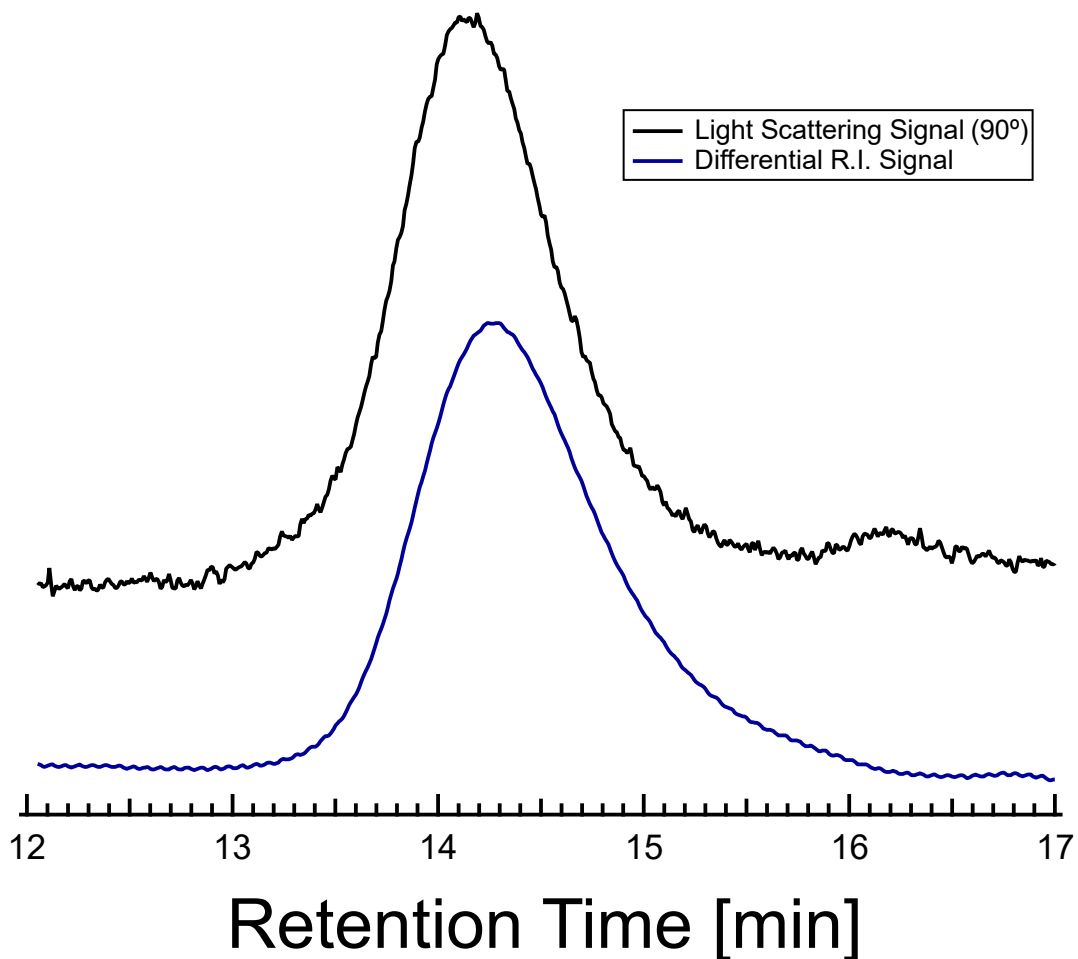


Figure 112: SEC analysis of PDMAEA.

The molecular weight distribution of PDMAEA was investigated using GPC MALS with chloroform as the mobile phase. The figure above shows the RI detector signal and the signal for a representative light scattering signal.

Table 25: The absolute molecular mass was determined using standard Zimm plot methodologies to obtain the absolute molar mass of this material.

$M_{N,NMR}^a$ [kDa]	$M_{N,SEC}^b$ [kDa]	D^b
32.1	37.1	1.11

^aCalculated by end-group analysis

^bCalculated using standard MALS analysis. Using a computed dilute-limit dn/dc of 0.1443 mL/g.

D.4 IR Spectrum of Im-c3-TFSI

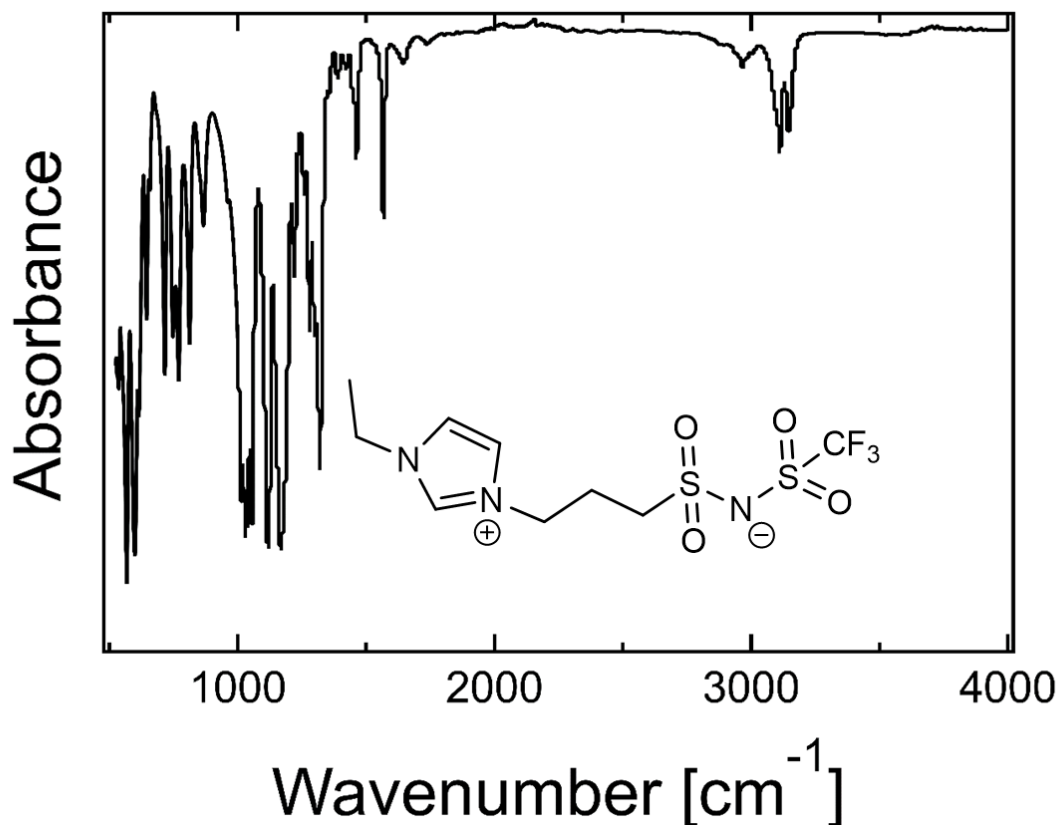


Figure 113: IR Spectrum of Im-c3-TFSI.

The IR spectrum of the solid state of the crystal is shown above. Notably the IR was not performed under a nitrogen flow, so absorption of water into the crystal is possible.

V: Conclusions and Outlook

The need for solid state energy storage solutions is more pressing than ever as electrification of the grid requires greater storage requirements and the demand for high-power electric vehicles continues to rise. The key challenge for these devices continues to be the electrolyte despite extensive research on this subject over the last several decades.

Continued research in this area must address the entire range of properties required of a solid

electrolyte, including ion transport rates, selectivity, electrochemical stability and mechanical robustness. This dissertation covers both applied and fundamental aspects of electrolyte design. I begin by discussing polymer electrolytes that interact with ions via metal-ligand interactions (Chapter 2). I find that these materials display ion transport rates that are inextricably linked to the solvation site dynamics of these materials. This results in a coupling between ion transport and polymer relaxation dynamics that is inherent to unstructured electrolytes that can limit the performance of all but extensively plasticized polymer electrolytes. In order to overcome this limitation, I designed zwitterionic polymers that display semicrystalline domains that promote selective ion transport (Chapter 3). These materials display an excellent balance of the selectivity, conductivity and mechanical properties that are typically orthogonal to each other. I further refine the design of these materials in Chapter 4, finding that tethered ion size is coupled to ion transport rates in these electrolytes. As my career in this research group will continue beyond this thesis, there are several aspects that are not covered in complete detail, especially a significant effort to characterize the structural and dynamical phases of transport in ZI/salt blends. This work will be briefly discussed in this section. Although many remaining avenues for future work exist within the area of polymer electrolytes generally, I will refine this outlook to discuss the future ZI design, especially as electrolytes but also in other areas.

This thesis has extensively demonstrated the usefulness of ZI moieties as components of polymers to promote fast ion transport, however the fundamentals of ZI self-assembly and transport are yet unknown. Ongoing studies characterize the phase diagram of ZI/salt blends to understand the phase behavior of the system. As discussed in Chapter 1, the few studies

on this system demonstrate eutectic-like behavior of these blends, however this behavior is now well or fully characterized. Figure 114 shows the first fully-developed state diagram for a blend of ZI/salt. This figure represents the state that the material is anticipated to reach if it cooled from the liquid state with corresponding regions: I) ZI crystallite, II liquid-like/pseudosolid blend, and III) salt crystallite. The remarkable aspect of this phase diagram is the pocket of pure phase I on the far left hand side of the diagram. The presence of this pocket proves that lithium salt is indeed incorporated into the zwitterionic crystal as I have hypothesized in chapters 3 and 4. This crucially indicates that lithium enters standard zwitterionic crystals, presumably through defective sites – enabling the rapid and selective transport of this species. In the coming year I look forward to seeing more results from computational collaborators that will elucidate this property and may give further insights into this transport mechanism. The potential for novel molecular characterization within this phase diagram is great, especially as the salt identity and the separate identities of the bound cation and anion are also critical in dictating the phase space of this electrolyte. I also believe that great potential exists to characterize the transport behavior and relate this behavior to the local ordering of the electrolyte.

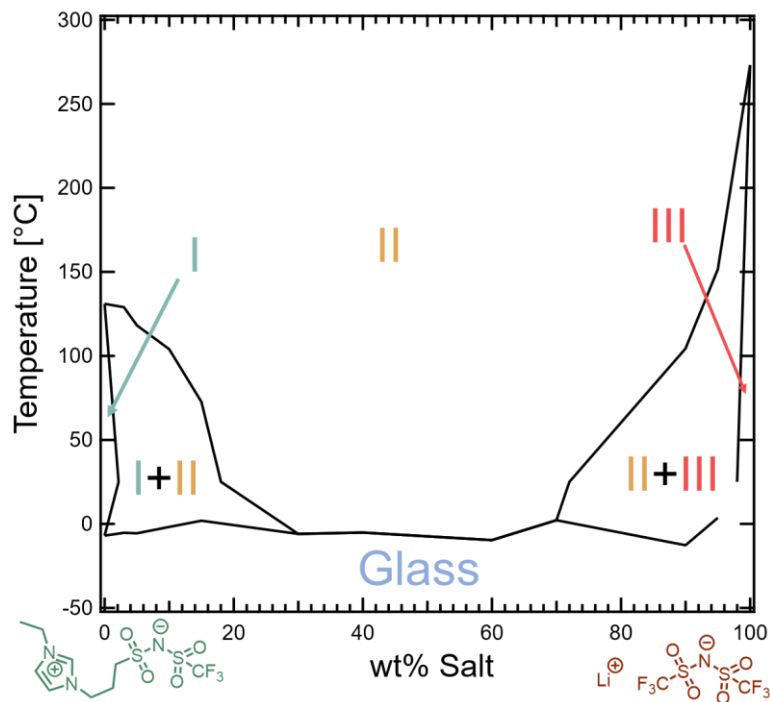


Figure 114: State diagram of a blend of EthIm-c3-TFSI and LiTFSI.

The state diagram of a zwitterion/salt blend represents the behavior of this blend when cooled to the temperature of interest from the liquid state. A glassy region where dynamics are greatly slowed is found at low temperatures – this state impedes the formation of the equilibrium structures.

Although zwitterionic polymers were heavily used in the above work, the small molecules also display promising behavior as hosts for ionic transport. I previously showed (Figure 31) that ZI small molecule electrolytes display competitive ion conductivity and ultra-high selectivity for lithium-ion transport. Work to characterize the ion transport in these systems has utilized a relatively sparse number of ion identities and has not considered salt concentration as an important variable to tune the structure and dynamics of these systems, instead typically doping with a large amount of salt to achieve liquidlike properties. Ongoing work inspired by this thesis will consider the transport mechanism of these small

molecule electrolytes as a function of the salt concentration and develop relationships between the structure of the electrolyte and its ion transport properties. This will require multiscale characterization of transport by electrochemical and NMR methods. The use of modern electrophoretic NMR techniques may also be crucial in elucidating the transport properties and mechanisms at play in these electrolytes. However, it remains to see if these fully crystalline materials may suffer the same disadvantages of ceramic electrolytes such as brittleness and poor interfacial adhesion.

Another possibility is to leverage the excellent dielectric properties of these ZI materials along with the favorable mechanics of polymers to attain highly conductive electrolytes that have polymer-like properties. In such an electrolyte the polymer will provide ‘soft’ mechanical properties that enable processability and adhesion of the electrolyte while the zwitterion can assist in dissociation and transport of the salt, which acts to carry the ionic species. In this application the polymer will likely need to be a high molecular weight, low- T_g polymer such as a long PDMS chain, however it will need to be considered whether a homogeneous blend of PDMS/ZI/salt can be attained, however I believe it is a likely prospect that a kinetically stabilized blend can be formed, even if this blending is thermodynamically unfavorable. In the case that this blend cannot be attained, it may be favorable to incorporate ionic groups onto the backbone, thermodynamically stabilizing the ternary blend. I have already demonstrate marked improvement to salt solvation ability of PDMS when functionalities are clicked to this backbone.

Although I have shown that PZIs and ZIs can support high ionic conductivity and cation selectivity, a real electrolyte must support high cell current by promoting high fluxes of

redox active ions and allowing for interfacial reactions with the electrode to occur. As such, high ionic conductivity is insufficient to ensure satisfactory performance of a battery or electrochemical device. Future work should consider the resilience of these electrolytes to the electrochemical environment in a real cell and limitations at the electrode-electrolyte interface.

For the ionic conductivity to be representative of the flux of a resistor, the resistor must be Ohmic in the range of interest. Ohm's law will typically fail when an electrolyte experiences a chemical degradation as a function of the applied voltage that impacts the transport properties of the electrolyte. As such, potential electrolytes should be studied for their voltage stability in tandem with their ionic conductivity. Standard electrochemical stability techniques, although useful, are not sufficient in fully understanding the practical voltage stability of an electrolyte. This is a consequence of interfacial reactions that can be catalyzed by the electrodes. Consequently, both bulk and interfacial investigations of stability should be conducted. Future work to consider zwitterionic electrolytes should carefully consider the behavior of these molecules in real electrochemical cells as high voltages are applied.

Although ion transport is essential to the performance of electrochemical cells, the redox-active species must also undergo electrochemical reactions for the cell to function. In liquid electrolytes, the solvated material is generally electrochemically available for reactions that lead to current within the cell. However, issues at the interface are common, especially in rigid superionic ceramics that may experience poor interfacial contact or hindered electroactivity at the interface due to the strong binding of lithium to the interface. This issue can also arise in block copolymer electrolytes where the redox active species is

concentrated within the conducting block domains of the electrolyte, leading to reduced utilization of the electrode interface for reactions. As such, fundamental transport measurements, bulk and interfacial stability investigations, and extended testing in full electrochemical cells will all be required to implement emerging SPEs into real devices.

Although lithium is currently the most widely used component of battery electrolytes, the future of electrochemical energy storage will require the use of a multitude of battery chemistries due to the limited abundance of lithium. As such, the development of alternative battery chemistries such as those based on Mg^{2+} , Zn^{2+} , and Al^{3+} emerge as possible sustainable, low-cost, and safe alternatives to lithium-ion battery cells. One challenge for such battery chemistries is the low mobility of multivalent ions in traditional electrolytes¹³⁵; even liquid electrolytes generally have low mobilities for such cations. In typical liquid electrolytes the hydration shells of multivalent ions are so large that the mobility of the multivalent ion is lowered by the large size of the shell, resulting in poor selectivity of these electrolytes for the multivalent species. However, zwitterions in the liquid phase may solve this problem since the ultra-high dielectric constant of these materials can mitigate these hydration effects and result in increased selectivity without introducing additional mobile ionic species. Therefore, I suggest that the liquid phase of zwitterion/multivalent salts may be an improvement upon the current state of the art for transport of multivalent ions. Although future studies may investigate whether a solid transport mode is possible in a similar fashion to ZI/Lithium blends, however the prospects for this transport are not as favorable due to the large size of multivalent ions.

I further suggest that the fundamental understanding of these zwitterionic molecules developed herein may be useful in applications beyond electrochemistry due to their

excellent dielectric properties and high affinities for salt solvation. One obvious application is the use of these materials as soft supercapacitors. Since these materials generally boast some of the highest reported dielectric constants of any soft material, they may outperform currently existing hosts in this application. These dielectric properties of these materials may also be useful in electrosynthesis applications. In electrosynthesis, a charge-neutral electrolyte is required to solvate starting materials and enable their transport and conversion in electrochemical reactions. Although water is a commonly employed host for this, the limited solubility of organic compounds in water and the limited stability window of water can reduce the efficacy of these techniques, this understanding of the liquid ZI phase may prove invaluable in promoting electrochemical reactions that require larger potentials. Finally I suggest that this liquid zwitterion phase could prove invaluable in desalination of water. Due to the incredible salt solvation ability of ZIs, these compounds may be able to interact with salts to create dense ionic phases that can be easily separated from the bulk phase to remove ions, possibly enabling low cost and portable desalination of water when non-water soluble zwitterions are employed.

Overall this dissertation has achieved several new fundamental understandings for ion transport in soft materials. Firstly, I showed that ion transport in unstructured electrolytes follows a hierarchical mechanism where the segmental relaxation timescale plays a crucial role in initiating the migration of an ion from a solvation site. This coupling is inherently limiting for glassy electrolyte designs for such unstructured electrolytes. Based upon this insight I developed structured electrolytes based on zwitterion chemistry. These molecules self-assemble into ordered domains that promote rapid ion transport through crystalline regions of the electrolyte, allowing for fast, selective ion transport even below the glass

transition temperature of the polymer. I have further developed design rules for these systems by altering the identity of the tethered ion species. These alterations suggest that ion transport is strongly related to the bulkiness of the tethered ion, suggesting that the ion/zwitterion interaction strength is crucial in controlling the rates for activated transport within these electrolytes. Finally in this section I point towards the positive outlook for these zwitterionic compounds. Although these materials already represent a new and promising class of polymer electrolyte, additional design rules and validation of properties such as electrochemical and interfacial stability are required. Finally, I suggest that the unique properties of these molecules may enable innovation in previously unexplored areas beyond electrochemical applications. Future research should seek to explore the possibilities of these underutilized zwitterionic compounds, focusing especially on their interesting self-assembly behavior and the unique interactions with ions.

References

1. Galluzzo, M. D.; Maslyn, J. A.; Shah, D. B.; Balsara, N. P., Ohm's law for ion conduction in lithium and beyond-lithium battery electrolytes. *The Journal of Chemical Physics* **2019**, *151* (2), 020901.
2. Bocharova, V.; Sokolov, A. P., Perspectives for Polymer Electrolytes: A View from Fundamentals of Ionic Conductivity. *Macromolecules* **2020**, *53* (11), 4141-4157.
3. Hallinan, D. T.; Balsara, N. P., Polymer Electrolytes. *Annual Review of Materials Research* **2013**, *43* (1), 503-525.
4. Bruce, P. G.; Vincent, C. A., Polymer electrolytes. *Journal of the Chemical Society, Faraday Transactions* **1993**, *89* (17), 3187-3203.
5. Evans, J.; Vincent, C. A.; Bruce, P. G., Electrochemical measurement of transference numbers in polymer electrolytes. *Polymer* **1987**, *28* (13), 2324-2328.
6. Marcus, Y.; Hefter, G., Ion Pairing. *Chemical Reviews* **2006**, *106* (11), 4585-4621.
7. Nordness, O.; Brennecke, J. F., Ion Dissociation in Ionic Liquids and Ionic Liquid Solutions. *Chemical Reviews* **2020**, *120* (23), 12873-12902.
8. Kirchner, B.; Malberg, F.; Firaha, D. S.; Hollóczki, O., Ion pairing in ionic liquids. *Journal of Physics: Condensed Matter* **2015**, *27* (46), 463002.
9. Hollóczki, O.; Malberg, F.; Welton, T.; Kirchner, B., On the origin of ionicity in ionic liquids. Ion pairing versus charge transfer. *Physical Chemistry Chemical Physics* **2014**, *16* (32), 16880-16890.
10. Harris, K. R., Can the Transport Properties of Molten Salts and Ionic Liquids Be Used To Determine Ion Association? *The Journal of Physical Chemistry B* **2016**, *120* (47), 12135-12147.

11. Ueno, K.; Tokuda, H.; Watanabe, M., Ionicity in ionic liquids: correlation with ionic structure and physicochemical properties. *Physical Chemistry Chemical Physics* **2010**, *12* (8), 1649-1658.
12. Stassen, H. K.; Ludwig, R.; Wulf, A.; Dupont, J., Imidazolium Salt Ion Pairs in Solution. *Chemistry – A European Journal* **2015**, *21* (23), 8324-8335.
13. MacFarlane, D. R.; Forsyth, M.; Izgorodina, E. I.; Abbott, A. P.; Annat, G.; Fraser, K., On the concept of ionicity in ionic liquids. *Physical Chemistry Chemical Physics* **2009**, *11* (25), 4962-4967.
14. Schreiner, C.; Zugmann, S.; Hartl, R.; Gores, H. J., Fractional Walden Rule for Ionic Liquids: Examples from Recent Measurements and a Critique of the So-Called Ideal KCl Line for the Walden Plot. *Journal of Chemical & Engineering Data* **2010**, *55* (5), 1784-1788.
15. Schauser, N. S.; Grzetic, D. J.; Tabassum, T.; Kliegle, G. A.; Le, M. L.; Susca, E. M.; Antoine, S.; Keller, T. J.; Delaney, K. T.; Han, S.; Seshadri, R.; Fredrickson, G. H.; Segalman, R. A., The Role of Backbone Polarity on Aggregation and Conduction of Ions in Polymer Electrolytes. *Journal of the American Chemical Society* **2020**, *142* (15), 7055-7065.
16. Jones, S. D.; Schauser, N. S.; Fredrickson, G. H.; Segalman, R. A., The Role of Polymer–Ion Interaction Strength on the Viscoelasticity and Conductivity of Solvent-Free Polymer Electrolytes. *Macromolecules* **2020**, *53* (23), 10574-10581.
17. Grindy, S. C.; Learsch, R.; Mozhdghi, D.; Cheng, J.; Barrett, D. G.; Guan, Z.; Messersmith, P. B.; Holten-Andersen, N., Control of hierarchical polymer mechanics with bioinspired metal-coordination dynamics. *Nature Materials* **2015**, *14* (12), 1210-1216.

18. Shen, K.-H.; Hall, L. M., Effects of Ion Size and Dielectric Constant on Ion Transport and Transference Number in Polymer Electrolytes. *Macromolecules* **2020**, *53* (22), 10086-10096.
19. Savoie, B. M.; Webb, M. A.; Miller, T. F., Enhancing Cation Diffusion and Suppressing Anion Diffusion via Lewis-Acidic Polymer Electrolytes. *The Journal of Physical Chemistry Letters* **2017**, *8* (3), 641-646.
20. Fan, F.; Wang, Y.; Hong, T.; Heres, M. F.; Saito, T.; Sokolov, A. P., Ion Conduction in Polymerized Ionic Liquids with Different Pendant Groups. *Macromolecules* **2015**, *48* (13), 4461-4470.
21. Zhao, Y.; Bai, Y.; Li, W.; An, M.; Bai, Y.; Chen, G., Design Strategies for Polymer Electrolytes with Ether and Carbonate Groups for Solid-State Lithium Metal Batteries. *Chemistry of Materials* **2020**, *32* (16), 6811-6830.
22. Wang, Y.; Fan, F.; Agapov, A. L.; Yu, X.; Hong, K.; Mays, J.; Sokolov, A. P., Design of superionic polymers—New insights from Walden plot analysis. *Solid State Ionics* **2014**, *262*, 782-784.
23. Voronel, A.; Veliyulin, E.; Machavariani, V. S.; Kisliuk, A.; Quitmann, D., Fractional Stokes-Einstein Law for Ionic Transport in Liquids. *Physical Review Letters* **1998**, *80* (12), 2630-2633.
24. Mindemark, J.; Lacey, M. J.; Bowden, T.; Brandell, D., Beyond PEO—Alternative host materials for Li⁺-conducting solid polymer electrolytes. *Progress in Polymer Science* **2018**, *81*, 114-143.

25. Berthier, C.; Gorecki, W.; Minier, M.; Armand, M. B.; Chabagno, J. M.; Rigaud, P., Microscopic investigation of ionic conductivity in alkali metal salts-poly(ethylene oxide) adducts. *Solid State Ionics* **1983**, *11* (1), 91-95.
26. Armand, M., Polymer solid electrolytes - an overview. *Solid State Ionics* **1983**, *9-10*, 745-754.
27. Gadjourova, Z.; Andreev, Y. G.; Tunstall, D. P.; Bruce, P. G., Ionic conductivity in crystalline polymer electrolytes. *Nature* **2001**, *412* (6846), 520-523.
28. Mongcopa, K. I. S.; Tyagi, M.; Mailoa, J. P.; Samsonidze, G.; Kozinsky, B.; Mullin, S. A.; Gribble, D. A.; Watanabe, H.; Balsara, N. P., Relationship between Segmental Dynamics Measured by Quasi-Elastic Neutron Scattering and Conductivity in Polymer Electrolytes. *ACS Macro Letters* **2018**, *7* (4), 504-508.
29. Bruce, P. G.; Vincent, C., Polymer electrolytes. *Journal of the Chemical Society, Faraday Transactions* **1993**, *89* (17), 3187-3203.
30. Borodin, O.; Smith, G. D., Mechanism of ion transport in amorphous poly (ethylene oxide)/LiTFSI from molecular dynamics simulations. *Macromolecules* **2006**, *39* (4), 1620-1629.
31. Geng, Z.; Schausser, N. S.; Lee, J.; Schmeller, R. P.; Barbon, S. M.; Segalman, R. A.; Lynd, N. A.; Hawker, C. J., Role of Side-Chain Architecture in Poly(ethylene oxide)-Based Copolymers. *Macromolecules* **2020**, *53* (12), 4960-4967.
32. Deng, C.; Webb, M. A.; Bennington, P.; Sharon, D.; Nealey, P. F.; Patel, S. N.; de Pablo, J. J., Role of Molecular Architecture on Ion Transport in Ethylene oxide-Based Polymer Electrolytes. *Macromolecules* **2021**, *54* (5), 2266-2276.

33. Bennington, P.; Deng, C.; Sharon, D.; Webb, M. A.; de Pablo, J. J.; Nealey, P. F.; Patel, S. N., Role of solvation site segmental dynamics on ion transport in ethylene-oxide based side-chain polymer electrolytes. *Journal of Materials Chemistry A* **2021**, *9* (15), 9937-9951.
34. Lee, B. F.; Kade, M. J.; Chute, J. A.; Gupta, N.; Campos, L. M.; Fredrickson, G. H.; Kramer, E. J.; Lynd, N. A.; Hawker, C. J., Poly(allyl glycidyl ether)-A versatile and functional polyether platform. *J Polym Sci A Polym Chem* **2011**, *49* (20), 4498-4504.
35. Strawhecker, K. E.; Manias, E., Crystallization Behavior of Poly(ethylene oxide) in the Presence of Na⁺ Montmorillonite Fillers. *Chemistry of Materials* **2003**, *15* (4), 844-849.
36. Ni'mah, Y. L.; Cheng, M.-Y.; Cheng, J. H.; Rick, J.; Hwang, B.-J., Solid-state polymer nanocomposite electrolyte of TiO₂/PEO/NaClO₄ for sodium ion batteries. *Journal of Power Sources* **2015**, *278*, 375-381.
37. Feng, J.; Wang, L.; Chen, Y.; Wang, P.; Zhang, H.; He, X., PEO based polymer-ceramic hybrid solid electrolytes: a review. *Nano Convergence* **2021**, *8* (1), 2.
38. Lehmann, M. L.; Yang, G.; Nanda, J.; Saito, T., Well-designed Crosslinked Polymer Electrolyte Enables High Ionic Conductivity and Enhanced Salt Solvation. *Journal of The Electrochemical Society* **2020**, *167* (7), 070539.
39. Li, W.; Pang, Y.; Liu, J.; Liu, G.; Wang, Y.; Xia, Y., A PEO-based gel polymer electrolyte for lithium ion batteries. *RSC Advances* **2017**, *7* (38), 23494-23501.
40. Gregorio, V.; García, N.; Tiemblo, P., Ionic Conductivity Enhancement in UHMW PEO Gel Electrolytes Based on Room-Temperature Ionic Liquids and Deep Eutectic Solvents. *ACS Applied Polymer Materials* **2022**, *4* (4), 2860-2870.

41. Snyder, R. L.; Choo, Y.; Gao, K. W.; Halat, D. M.; Abel, B. A.; Sundararaman, S.; Prendergast, D.; Reimer, J. A.; Balsara, N. P.; Coates, G. W., Improved Li⁺ Transport in Polyacetal Electrolytes: Conductivity and Current Fraction in a Series of Polymers. *ACS Energy Letters* **2021**, *6* (5), 1886-1891.
42. Goulart, G.; Sanchez, J.-Y.; Armand, M., Synthesis and electrochemical characterization of new polymer electrolytes based on dioxolane homo and co-polymers. *Electrochimica acta* **1992**, *37* (9), 1589-1592.
43. Kumar, Y.; Hashmi, S. A.; Pandey, G. P., Lithium ion transport and ion–polymer interaction in PEO based polymer electrolyte plasticized with ionic liquid. *Solid State Ionics* **2011**, *201* (1), 73-80.
44. Suthanthiraraj, S. A.; Vadivel, M. K., Effect of propylene carbonate as a plasticizer on (PEO)₅₀AgCF₃SO₃:SnO₂ nanocomposite polymer electrolyte. *Applied Nanoscience* **2012**, *2* (3), 239-246.
45. Shin, J.-H.; Henderson, W. A.; Passerini, S., PEO-Based Polymer Electrolytes with Ionic Liquids and Their Use in Lithium Metal-Polymer Electrolyte Batteries. *Journal of The Electrochemical Society* **2005**, *152* (5), A978.
46. Sharma, J. P.; Singh, V., Influence of high and low dielectric constant plasticizers on the ion transport properties of PEO: NH₄HF₂ polymer electrolytes. *High Performance Polymers* **2020**, *32* (2), 142-150.
47. Polu, A. R.; Singh, P. K., Improved ion dissociation and amorphous region of PEO based solid polymer electrolyte by incorporating tetracyanoethylene. *Materials Today: Proceedings* **2022**, *49*, 3093-3097.

48. Li, Y.; Zhang, L.; Sun, Z.; Gao, G.; Lu, S.; Zhu, M.; Zhang, Y.; Jia, Z.; Xiao, C.; Bu, H.; Xi, K.; Ding, S., Hexagonal boron nitride induces anion trapping in a polyethylene oxide based solid polymer electrolyte for lithium dendrite inhibition. *Journal of Materials Chemistry A* **2020**, *8* (19), 9579-9589.
49. Vishwakarma, V.; Jain, A., Enhancement of thermal transport in Gel Polymer Electrolytes with embedded BN/Al₂O₃ nano- and micro-particles. *Journal of Power Sources* **2017**, *362*, 219-227.
50. Cai, Y.; Zeng, L.; Zhang, Y.; Xu, X., Multiporous sp²-hybridized boron nitride (d-BN): stability, mechanical properties, lattice thermal conductivity and promising application in energy storage. *Physical Chemistry Chemical Physics* **2018**, *20* (31), 20726-20731.
51. Tian, H.; Seh, Z. W.; Yan, K.; Fu, Z.; Tang, P.; Lu, Y.; Zhang, R.; Legut, D.; Cui, Y.; Zhang, Q., Theoretical Investigation of 2D Layered Materials as Protective Films for Lithium and Sodium Metal Anodes. *Advanced Energy Materials* **2017**, *7* (13), 1602528.
52. Wang, J.; Zhang, C.; Zhang, Y.; Xue, Z., Advances in host selection and interface regulation of polymer electrolytes. *Journal of Polymer Science* **2022**, *60* (5), 743-765.
53. Heitjans, P.; Indris, S., Diffusion and ionic conduction in nanocrystalline ceramics. *Journal of Physics: Condensed Matter* **2003**, *15* (30), R1257.
54. Sun, J.; Clark, B. K.; Torquato, S.; Car, R., The phase diagram of high-pressure superionic ice. *Nature communications* **2015**, *6* (1), 1-8.
55. Millot, M.; Hamel, S.; Rygg, J. R.; Celliers, P. M.; Collins, G. W.; Coppari, F.; Fratanduono, D. E.; Jeanloz, R.; Swift, D. C.; Eggert, J. H., Experimental evidence for superionic water ice using shock compression. *Nature Physics* **2018**, *14* (3), 297-302.

56. Kamaya, N.; Homma, K.; Yamakawa, Y.; Hirayama, M.; Kanno, R.; Yonemura, M.; Kamiyama, T.; Kato, Y.; Hama, S.; Kawamoto, K., A lithium superionic conductor. *Nature materials* **2011**, *10* (9), 682-686.
57. Bron, P.; Johansson, S.; Zick, K.; Schmedt auf der Günne, J.; Dehnen, S.; Roling, B., Li₁₀SnP₂S₁₂: An Affordable Lithium Superionic Conductor. *Journal of the American Chemical Society* **2013**, *135* (42), 15694-15697.
58. Zhang, Z.; Shao, Y.; Lotsch, B.; Hu, Y.-S.; Li, H.; Janek, J.; Nazar, L. F.; Nan, C.-W.; Maier, J.; Armand, M.; Chen, L., New horizons for inorganic solid state ion conductors. *Energy & Environmental Science* **2018**, *11* (8), 1945-1976.
59. Zhang, H.; Wang, X.; Chremos, A.; Douglas, J. F., Superionic UO₂: A model anharmonic crystalline material. *The Journal of Chemical Physics* **2019**, *150* (17), 174506.
60. Stramare, S.; Thangadurai, V.; Weppner, W., Lithium Lanthanum Titanates: A Review. *Chemistry of Materials* **2003**, *15* (21), 3974-3990.
61. Knauth, P., Inorganic solid Li ion conductors: An overview. *Solid State Ionics* **2009**, *180* (14), 911-916.
62. Thangadurai, V.; Narayanan, S.; Pinzaru, D., Garnet-type solid-state fast Li ion conductors for Li batteries: critical review. *Chemical Society Reviews* **2014**, *43* (13), 4714-4727.
63. Bachman, J. C.; Muy, S.; Grimaud, A.; Chang, H.-H.; Pour, N.; Lux, S. F.; Paschos, O.; Maglia, F.; Lupart, S.; Lamp, P.; Giordano, L.; Shao-Horn, Y., Inorganic Solid-State Electrolytes for Lithium Batteries: Mechanisms and Properties Governing Ion Conduction. *Chemical Reviews* **2016**, *116* (1), 140-162.

64. Chen, R.; Qu, W.; Guo, X.; Li, L.; Wu, F., The pursuit of solid-state electrolytes for lithium batteries: from comprehensive insight to emerging horizons. *Materials Horizons* **2016**, *3* (6), 487-516.
65. He, X.; Zhu, Y.; Mo, Y., Origin of fast ion diffusion in super-ionic conductors. *Nature Communications* **2017**, *8* (1), 15893.
66. Smith, J. G.; Siegel, D. J., Low-temperature paddlewheel effect in glassy solid electrolytes. *Nature Communications* **2020**, *11* (1), 1483.
67. Wu, E. A.; Banerjee, S.; Tang, H.; Richardson, P. M.; Doux, J.-M.; Qi, J.; Zhu, Z.; Grenier, A.; Li, Y.; Zhao, E.; Deysheer, G.; Sebti, E.; Nguyen, H.; Stephens, R.; Verbist, G.; Chapman, K. W.; Clément, R. J.; Banerjee, A.; Meng, Y. S.; Ong, S. P., A stable cathode-solid electrolyte composite for high-voltage, long-cycle-life solid-state sodium-ion batteries. *Nature Communications* **2021**, *12* (1), 1256.
68. Armand, M., The history of polymer electrolytes. *Solid State Ionics* **1994**, *69* (3), 309-319.
69. Austen Angell, C.; Ansari, Y.; Zhao, Z., Ionic Liquids: Past, present and future. *Faraday Discussions* **2012**, *154* (0), 9-27.
70. Wang, Y.; Sun, C.-N.; Fan, F.; Sangoro, J. R.; Berman, M. B.; Greenbaum, S. G.; Zawodzinski, T. A.; Sokolov, A. P., Examination of methods to determine free-ion diffusivity and number density from analysis of electrode polarization. *Physical Review E* **2013**, *87* (4), 042308.
71. Chintapalli, M.; Timachova, K.; Olson, K. R.; Mecham, S. J.; Devaux, D.; DeSimone, J. M.; Balsara, N. P., Relationship between Conductivity, Ion Diffusion, and

Transference Number in Perfluoropolyether Electrolytes. *Macromolecules* **2016**, *49* (9), 3508-3515.

72. Wang, Y.; Fan, F.; Agapov, A. L.; Saito, T.; Yang, J.; Yu, X.; Hong, K.; Mays, J.; Sokolov, A. P., Examination of the fundamental relation between ionic transport and segmental relaxation in polymer electrolytes. *Polymer* **2014**, *55* (16), 4067-4076.

73. Douglas, J. F., A dynamic measure of order in structural glasses. *Computational Materials Science* **1995**, *4* (4), 292-308.

74. Zhang, H.; Wang, X.; Yu, H.-B.; Douglas, J. F., Fast dynamics in a model metallic glass-forming material. *The Journal of Chemical Physics* **2021**, *154* (8), 084505.

75. Xing, K.; Tress, M.; Cao, P.; Cheng, S.; Saito, T.; Novikov, V. N.; Sokolov, A. P., Hydrogen-bond strength changes network dynamics in associating telechelic PDMS. *Soft Matter* **2018**, *14* (7), 1235-1246.

76. Sijbesma, R. P.; Beijer, F. H.; Brunsveld, L.; Folmer, B. J. B.; Hirschberg, J. H. K. K.; Lange, R. F. M.; Lowe, J. K. L.; Meijer, E. W., Reversible Polymers Formed from Self-Complementary Monomers Using Quadruple Hydrogen Bonding. *Science* **1997**, *278* (5343), 1601-1604.

77. Cordier, P.; Tournilhac, F.; Soulié-Ziakovic, C.; Leibler, L., Self-healing and thermoreversible rubber from supramolecular assembly. *Nature* **2008**, *451* (7181), 977-980.

78. Yount, W. C.; Loveless, D. M.; Craig, S. L., Small-Molecule Dynamics and Mechanisms Underlying the Macroscopic Mechanical Properties of Coordinatively Cross-Linked Polymer Networks. *Journal of the American Chemical Society* **2005**, *127* (41), 14488-14496.

79. Holten-Andersen, N.; Harrington, M. J.; Birkedal, H.; Lee, B. P.; Messersmith, P. B.; Lee, K. Y. C.; Waite, J. H., pH-induced metal-ligand cross-links inspired by mussel yield self-healing polymer networks with near-covalent elastic moduli. *Proceedings of the National Academy of Sciences* **2011**, *108* (7), 2651-2655.

80. Sanoja, G. E.; Schausser, N. S.; Bartels, J. M.; Evans, C. M.; Helgeson, M. E.; Seshadri, R.; Segalman, R. A., Ion Transport in Dynamic Polymer Networks Based on Metal–Ligand Coordination: Effect of Cross-Linker Concentration. *Macromolecules* **2018**, *51* (5), 2017-2026.

81. Hunt, J. N.; Feldman, K. E.; Lynd, N. A.; Deek, J.; Campos, L. M.; Spruell, J. M.; Hernandez, B. M.; Kramer, E. J.; Hawker, C. J., Tunable, High Modulus Hydrogels Driven by Ionic Coacervation. *Advanced Materials* **2011**, *23* (20), 2327-2331.

82. Lemmers, M.; Sprakel, J.; Voets, I. K.; van der Gucht, J.; Cohen Stuart, M. A., Multiresponsive Reversible Gels Based on Charge-Driven Assembly. *Angewandte Chemie International Edition* **2010**, *49* (4), 708-711.

83. Rowan, S. J.; Cantrill, S. J.; Cousins, G. R. L.; Sanders, J. K. M.; Stoddart, J. F., Dynamic Covalent Chemistry. *Angewandte Chemie International Edition* **2002**, *41* (6), 898-952.

84. Fortman, D. J.; Brutman, J. P.; Cramer, C. J.; Hillmyer, M. A.; Dichtel, W. R., Mechanically Activated, Catalyst-Free Polyhydroxyurethane Vitrimers. *Journal of the American Chemical Society* **2015**, *137* (44), 14019-14022.

85. Rotello, V. M.; Thayumanavan, S., Molecular recognition and polymers : control of polymer structure and self-assembly. **2010**.

86. Hoy, R. S.; Fredrickson, G. H., Thermoreversible associating polymer networks. I. Interplay of thermodynamics, chemical kinetics, and polymer physics. *The Journal of Chemical Physics* **2009**, *131* (22), 224902.
87. Ahmadi, M.; Hawke, L. G. D.; Goldansaz, H.; van Ruymbeke, E., Dynamics of Entangled Linear Supramolecular Chains with Sticky Side Groups: Influence of Hindered Fluctuations. *Macromolecules* **2015**, *48* (19), 7300-7310.
88. Polymers in Drug Delivery: Chemistry and Applications. *Molecular Pharmaceutics* **2017**, *14* (8), 2459-2459.
89. Xue, Z.; He, D.; Xie, X., Poly(ethylene oxide)-based electrolytes for lithium-ion batteries. *Journal of Materials Chemistry A* **2015**, *3* (38), 19218-19253.
90. Shi, J.; Vincent, C. A., The effect of molecular weight on cation mobility in polymer electrolytes. *Solid State Ionics* **1993**, *60* (1), 11-17.
91. Chen, Q.; Tudryn, G. J.; Colby, R. H., Ionomer dynamics and the sticky Rouse model. *Journal of Rheology* **2013**, *57* (5), 1441-1462.
92. Mordvinkin, A.; Suckow, M.; Böhme, F.; Colby, R. H.; Creton, C.; Saalwächter, K., Hierarchical Sticker and Sticky Chain Dynamics in Self-Healing Butyl Rubber Ionomers. *Macromolecules* **2019**, *52* (11), 4169-4184.
93. Ma, B.; Nguyen, T. D.; Olvera de la Cruz, M., Control of Ionic Mobility via Charge Size Asymmetry in Random Ionomers. *Nano Letters* **2020**, *20* (1), 43-49.
94. Yan, Q.; de Pablo, J. J., Phase Equilibria of Size-Asymmetric Primitive Model Electrolytes. *Physical Review Letters* **2001**, *86* (10), 2054-2057.

95. Barteau, K. P.; Wolffs, M.; Lynd, N. A.; Fredrickson, G. H.; Kramer, E. J.; Hawker, C. J., Allyl Glycidyl Ether-Based Polymer Electrolytes for Room Temperature Lithium Batteries. *Macromolecules* **2013**, *46* (22), 8988-8994.
96. Schauer, N. S. Mono- and Multivalent Ion Conduction in Solid Polymer Electrolytes. University of California, Santa Barbara, 2020.
97. Anastasaki, A.; Willenbacher, J.; Fleischmann, C.; Gutekunst, W. R.; Hawker, C. J., End group modification of poly(acrylates) obtained via ATRP: a user guide. *Polymer Chemistry* **2017**, *8* (4), 689-697.
98. Stukalin, E. B.; Cai, L.-H.; Kumar, N. A.; Leibler, L.; Rubinstein, M., Self-Healing of Unentangled Polymer Networks with Reversible Bonds. *Macromolecules* **2013**, *46* (18), 7525-7541.
99. Kapinos, L. E.; Song, B.; Sigel, H., Metal ion-coordinating properties of imidazole and derivatives in aqueous solution: interrelation between complex stability and ligand basicity. *Inorganica Chimica Acta* **1998**, *280* (1), 50-56.
100. Bauman, J. E.; Wang, J. C., Imidazole Complexes of Nickel(II), Copper(II), Zinc(II), and Silver(I). *Inorganic Chemistry* **1964**, *3* (3), 368-373.
101. Schauer, N. S.; Sanoja, G. E.; Bartels, J. M.; Jain, S. K.; Hu, J. G.; Han, S.; Walker, L. M.; Helgeson, M. E.; Seshadri, R.; Segalman, R. A., Decoupling Bulk Mechanics and Mono- and Multivalent Ion Transport in Polymers Based on Metal–Ligand Coordination. *Chemistry of Materials* **2018**, *30* (16), 5759-5769.
102. Andersson Trojer, M.; Movahedi, A.; Blanck, H.; Nydén, M., Imidazole and Triazole Coordination Chemistry for Antifouling Coatings. *Journal of Chemistry* **2013**, *2013*, 946739.

103. Mark, J. E., Physical properties of polymers handbook. **2010**.
104. Baxandall, L. G., Dynamics of reversibly crosslinked chains. *Macromolecules* **1989**, 22 (4), 1982-1988.
105. Lodge, T.; Hiemenz, P. C., *Polymer chemistry*. 2021.
106. Chakravorty, A.; Cotton, F. A., STABILITY CONSTANTS AND STRUCTURES OF SOME METAL COMPLEXES WITH IMIDAZOLE DERIVATIVES1a. *The Journal of Physical Chemistry* **1963**, 67 (12), 2878-2879.
107. Murmann, R. K., Mechanisms of inorganic reactions - A study of metal complexes in solution (Basolo, Fred; Pearson, Ralph G.). *Journal of Chemical Education* **1968**, 45 (2), A146.
108. McAuley, A.; Hill, J., Kinetics and mechanism of metal-ion complex formation in solution. *Quarterly Reviews, Chemical Society* **1969**, 23 (1), 18-36.
109. Hall, L. M.; Seitz, M. E.; Winey, K. I.; Opper, K. L.; Wagener, K. B.; Stevens, M. J.; Frischknecht, A. L., Ionic Aggregate Structure in Ionomer Melts: Effect of Molecular Architecture on Aggregates and the Ionomer Peak. *Journal of the American Chemical Society* **2012**, 134 (1), 574-587.
110. Wuttke, J., Laplace–Fourier Transform of the Stretched Exponential Function: Analytic Error Bounds, Double Exponential Transform, and Open-Source Implementation “libkww”. *Algorithms* **2012**, 5 (4), 604-628.
111. Jr., D. T. H.; Balsara, N. P., Polymer Electrolytes. *Annual Review of Materials Research* **2013**, 43 (1), 503-525.

112. Ling, J.; Karuppiah, C.; Krishnan, S. G.; Reddy, M. V.; Misnon, I. I.; Ab Rahim, M. H.; Yang, C.-C.; Jose, R., Phosphate Polyanion Materials as High-Voltage Lithium-Ion Battery Cathode: A Review. *Energy & Fuels* **2021**, *35* (13), 10428-10450.
113. Li, W.; Erickson, E. M.; Manthiram, A., High-nickel layered oxide cathodes for lithium-based automotive batteries. *Nature Energy* **2020**, *5* (1), 26-34.
114. Liang, G.; Peterson, V. K.; See, K. W.; Guo, Z.; Pang, W. K., Developing high-voltage spinel $\text{LiNi}_{0.5}\text{Mn}_{1.5}\text{O}_4$ cathodes for high-energy-density lithium-ion batteries: current achievements and future prospects. *Journal of Materials Chemistry A* **2020**, *8* (31), 15373-15398.
115. Sun, J.; Stone, G. M.; Balsara, N. P.; Zuckermann, R. N., Structure–Conductivity Relationship for Peptoid-Based PEO–Mimetic Polymer Electrolytes. *Macromolecules* **2012**, *45* (12), 5151-5156.
116. Lee, B. F.; Kade, M. J.; Chute, J. A.; Gupta, N.; Campos, L. M.; Fredrickson, G. H.; Kramer, E. J.; Lynd, N. A.; Hawker, C. J., Poly(allyl glycidyl ether)-A versatile and functional polyether platform. *Journal of Polymer Science Part A: Polymer Chemistry* **2011**, *49* (20), 4498-4504.
117. Park, B.; Schaefer, J. L., Review—Polymer Electrolytes for Magnesium Batteries: Forging Away from Analogs of Lithium Polymer Electrolytes and Towards the Rechargeable Magnesium Metal Polymer Battery. *Journal of The Electrochemical Society* **2020**, *167* (7), 070545.
118. Hiller, M. M.; Joost, M.; Gores, H. J.; Passerini, S.; Wiemhöfer, H. D., The influence of interface polarization on the determination of lithium transference numbers of salt in polyethylene oxide electrolytes. *Electrochimica Acta* **2013**, *114*, 21-29.

119. Fu, J., Superionic conductivity of glass-ceramics in the system Li₂O-Al₂O₃-TiO₂-P₂O₅. *Solid State Ionics* **1997**, *96* (3), 195-200.
120. Kamaya, N.; Homma, K.; Yamakawa, Y.; Hirayama, M.; Kanno, R.; Yonemura, M.; Kamiyama, T.; Kato, Y.; Hama, S.; Kawamoto, K.; Mitsui, A., A lithium superionic conductor. *Nature Materials* **2011**, *10* (9), 682-686.
121. Murugan, R.; Thangadurai, V.; Weppner, W., Fast lithium ion conduction in garnet-type Li₇La₃Zr₂O₁₂. *Angewandte Chemie (International ed. in English)* **2007**, *46* (41), 7778-81.
122. Zhang, W.; Richter, F. H.; Culver, S. P.; Leichtweiss, T.; Lozano, J. G.; Dietrich, C.; Bruce, P. G.; Zeier, W. G.; Janek, J., Degradation Mechanisms at the Li₁₀GeP₂S₁₂/LiCoO₂ Cathode Interface in an All-Solid-State Lithium-Ion Battery. *ACS Applied Materials & Interfaces* **2018**, *10* (26), 22226-22236.
123. Ning, Z.; Jolly, D. S.; Li, G.; De Meyere, R.; Pu, S. D.; Chen, Y.; Kasemchainan, J.; Ihli, J.; Gong, C.; Liu, B.; Melvin, D. L. R.; Bonnin, A.; Magdysyuk, O.; Adamson, P.; Hartley, G. O.; Monroe, C. W.; Marrow, T. J.; Bruce, P. G., Visualizing plating-induced cracking in lithium-anode solid-electrolyte cells. *Nature Materials* **2021**, *20* (8), 1121-1129.
124. Yuan, C.; Lu, W.; Xu, J., Unlocking the Electrochemical–Mechanical Coupling Behaviors of Dendrite Growth and Crack Propagation in All-Solid-State Batteries. *Advanced Energy Materials* *n/a* (n/a), 2101807.
125. Cabana, J.; Kwon, B. J.; Hu, L., Mechanisms of Degradation and Strategies for the Stabilization of Cathode–Electrolyte Interfaces in Li-Ion Batteries. *Accounts of Chemical Research* **2018**, *51* (2), 299-308.

126. Keller, M.; Varzi, A.; Passerini, S., Hybrid electrolytes for lithium metal batteries. *Journal of Power Sources* **2018**, *392*, 206-225.
127. Merrill, L. C.; Chen, X. C.; Zhang, Y.; Ford, H. O.; Lou, K.; Zhang, Y.; Yang, G.; Wang, Y.; Wang, Y.; Schaefer, J. L.; Dudney, N. J., Polymer–Ceramic Composite Electrolytes for Lithium Batteries: A Comparison between the Single-Ion-Conducting Polymer Matrix and Its Counterpart. *ACS Applied Energy Materials* **2020**, *3* (9), 8871-8881.
128. Agapov, A. L.; Sokolov, A. P., Decoupling Ionic Conductivity from Structural Relaxation: A Way to Solid Polymer Electrolytes? *Macromolecules* **2011**, *44* (11), 4410-4414.
129. Wang, Y.; Agapov, A. L.; Fan, F.; Hong, K.; Yu, X.; Mays, J.; Sokolov, A. P., Decoupling of Ionic Transport from Segmental Relaxation in Polymer Electrolytes. *Physical Review Letters* **2012**, *108* (8), 088303.
130. Singh, M.; Odusanya, O.; Wilmes, G. M.; Eitouni, H. B.; Gomez, E. D.; Patel, A. J.; Chen, V. L.; Park, M. J.; Fragouli, P.; Iatrou, H.; Hadjichristidis, N.; Cookson, D.; Balsara, N. P., Effect of Molecular Weight on the Mechanical and Electrical Properties of Block Copolymer Electrolytes. *Macromolecules* **2007**, *40* (13), 4578-4585.
131. Kim, O.; Kim, K.; Choi, U. H.; Park, M. J., Tuning anhydrous proton conduction in single-ion polymers by crystalline ion channels. *Nature Communications* **2018**, *9* (1), 5029.
132. Lascaud, S.; Perrier, M.; Vallee, A.; Besner, S.; Prud'homme, J.; Armand, M., Phase Diagrams and Conductivity Behavior of Poly(ethylene oxide)-Molten Salt Rubbery Electrolytes. *Macromolecules* **1994**, *27* (25), 7469-7477.

133. Keith, J. R.; Ganesan, V., Ion transport mechanisms in salt-doped polymerized zwitterionic electrolytes. *Journal of Polymer Science* **2020**, *58* (4), 578-588.
134. Irfan, M.; Zhang, Y.; Yang, Z.; Su, J.; Zhang, W., Novel conducting solid polymer electrolytes with a zwitterionic structure boosting ionic conductivity and retarding lithium dendrite formation. *Journal of Materials Chemistry A* **2021**.
135. Lu, F.; Gao, X.; Wu, A.; Sun, N.; Shi, L.; Zheng, L., Lithium-Containing Zwitterionic Poly(Ionic Liquid)s as Polymer Electrolytes for Lithium-Ion Batteries. *The Journal of Physical Chemistry C* **2017**, *121* (33), 17756-17763.
136. Lu, F.; Li, G.; Yu, Y.; Gao, X.; Zheng, L.; Chen, Z., Zwitterionic impetus on single lithium-ion conduction in solid polymer electrolyte for all-solid-state lithium-ion batteries. *Chemical Engineering Journal* **2020**, *384*, 123237.
137. Taylor, M. E.; Panzer, M. J., Fully-Zwitterionic Polymer-Supported Ionogel Electrolytes Featuring a Hydrophobic Ionic Liquid. *The Journal of Physical Chemistry B* **2018**, *122* (35), 8469-8476.
138. D'Angelo, A. J.; Panzer, M. J., Design of Stretchable and Self-Healing Gel Electrolytes via Fully Zwitterionic Polymer Networks in Solvate Ionic Liquids for Li-Based Batteries. *Chemistry of Materials* **2019**, *31* (8), 2913-2922.
139. Sun, J.; MacFarlane, D. R.; Byrne, N.; Forsyth, M., Zwitterion effect in polyelectrolyte gels based on lithium methacrylate-N,N-dimethyl acrylamide copolymer. *Electrochimica Acta* **2006**, *51* (19), 4033-4038.
140. Guzmán, G.; Nava, D. P.; Vazquez-Arenas, J.; Cardoso, J., Design of a Zwitterion Polymer Electrolyte Based on Poly[poly (ethylene glycol) methacrylate]: The

Effect of Sulfobetaine Group on Thermal Properties and Ionic Conduction. *Macromolecular Symposia* **2017**, 374 (1), 1600136.

141. Makhlooghiyazad, F.; O'Dell, L. A.; Porcarelli, L.; Forsyth, C.; Quazi, N.; Asadi, M.; Hutt, O.; Mecerreyes, D.; Forsyth, M.; Pringle, J. M., Zwitterionic materials with disorder and plasticity and their application as non-volatile solid or liquid electrolytes.

Nature Materials **2021**.

142. Mei, W.; Rothenberger, A. J.; Bostwick, J. E.; Rinehart, J. M.; Hickey, R. J.; Colby, R. H., Zwitterions Raise the Dielectric Constant of Soft Materials. *Physical Review Letters* **2021**, 127 (22), 228001.

143. Walden, P., Innere Reibung und deren Zusammenhang mit dem Leitvermögen. *Z. Phys. Chem* **1906**, 55 (2), 207-249.

144. Floudas, G.; Placke, P.; Stepanek, P.; Brown, W.; Fytas, G.; Ngai, K. L., Dynamics of the "Strong" Polymer of n-Lauryl Methacrylate below and above the Glass Transition. *Macromolecules* **1995**, 28 (20), 6799-6807.

145. Floudas, G.; Štěpánek, P., Structure and Dynamics of Poly(n-decyl methacrylate) below and above the Glass Transition. *Macromolecules* **1998**, 31 (20), 6951-6957.

146. Köberle, P.; Laschewsky, A.; Tsukruk, V., The structural order of some novel ionic polymers, 1. X-ray scattering studies. *Die Makromolekulare Chemie* **1992**, 193 (8), 1815-1827.

147. Galin, M.; Marchal, E.; Mathis, A.; Galin, J.-C., Poly(ammonioalkanesulfonate) Blends with Polar Organic Species and Alkali Metal Salts:

Structure, Glass Transition and Ionic Conductivity. *Polymers for Advanced Technologies* **1997**, 8 (2), 75-86.

148. Lee, C.-U.; Li, A.; Ghale, K.; Zhang, D., Crystallization and Melting Behaviors of Cyclic and Linear Polypeptoids with Alkyl Side Chains. *Macromolecules* **2013**, 46 (20), 8213-8223.

149. Robeson, L. M., Correlation of separation factor versus permeability for polymeric membranes. *Journal of Membrane Science* **1991**, 62 (2), 165-185.

150. Seamus D. Jones, N. S. S., Glenn H. Fredrickson, Rachel A. Segalman, The Role of Polymer-Ion Interaction Strength on the Viscoelasticity and Conductivity of Solvent-Free Polymer Electrolytes. *Macromolecules* **2020**.

151. Chen, Q.; Huang, C.; Weiss, R. A.; Colby, R. H., Viscoelasticity of Reversible Gelation for Ionomers. *Macromolecules* **2015**, 48 (4), 1221-1230.

152. Bergstrom, H. K.; Fong, K. D.; McCloskey, B. D., Interfacial Effects on Transport Coefficient Measurements in Li-ion Battery Electrolytes. *Journal of The Electrochemical Society* **2021**, 168 (6), 060543.

153. Anderson, O. L.; Stuart, D. A., Calculation of Activation Energy of Ionic Conductivity in Silica Glasses by Classical Methods. *Journal of the American Ceramic Society* **1954**, 37 (12), 573-580.

154. McElfresh, D.; Howitt, D. G., Activation Enthalpy for Diffusion in Glass. *Journal of the American Ceramic Society* **1986**, 69 (10), C-237-C-238.

155. Stacy, E. W.; Gainaru, C. P.; Gobet, M.; Wojnarowska, Z.; Bocharova, V.; Greenbaum, S. G.; Sokolov, A. P., Fundamental Limitations of Ionic Conductivity in Polymerized Ionic Liquids. *Macromolecules* **2018**, 51 (21), 8637-8645.

156. Osaka, A.; Takahashi, K.; Ariyoshi, K., The elastic constant and molar volume of sodium and potassium germanate glasses and the germanate anomaly. *Journal of Non-Crystalline Solids* **1985**, *70* (2), 243-252.
157. Tian, Y.; Shi, T.; Richards, W. D.; Li, J.; Kim, J. C.; Bo, S.-H.; Ceder, G., Compatibility issues between electrodes and electrolytes in solid-state batteries. *Energy & Environmental Science* **2017**, *10* (5), 1150-1166.
158. Ohno, H.; Yoshizawa-Fujita, M.; Kohno, Y., Design and properties of functional zwitterions derived from ionic liquids. *Physical Chemistry Chemical Physics* **2018**, *20* (16), 10978-10991.
159. Phan, T. N. T.; Ferrand, A.; Ho, H. T.; Liénafa, L.; Rollet, M.; Maria, S.; Bouchet, R.; Gigmes, D., Vinyl monomers bearing a sulfonyl(trifluoromethane sulfonyl) imide group: synthesis and polymerization using nitroxide-mediated polymerization. *Polymer Chemistry* **2016**, *7* (45), 6901-6910.